R-08-14

Radionuclide release calculations for SAR-08

Gavin Thomson, Alex Miller, Graham Smith, Duncan Jackson
Enviros Consulting Ltd

April 2008

Svensk Kärnbränslehantering AB
Swedish Nuclear Fuel
and Waste Management Co
Box 250, SE-101 24 Stockholm
Tel +46 8 459 84 00

ISSN 1402-3091
SKB Rapport R-08-14

Radionuclide release calculations for SAR-08

Gavin Thomson, Alex Miller, Graham Smith, Duncan Jackson
Enviros Consulting Ltd

April 2008

Keywords: dokID 1169703, SFR 1 SAR-08, Radionuclide transport.

Preface

This document describes the radionuclide release calculations that have been undertaken as part of the safety analysis SFR 1 SAR-08 and the document constitutes one of the references to the safety analysis.

Gavin Thomson, Alex Miller, Graham Smith and Duncan Jackson have conducted the modelling work and compiled the report.

This document has been reviewed and all comments have been documented in accordance with SKIFS 2004:1.

Stockholm, May 2008

Anna Gordon

Project leader, SFR 1 SAR-08

Executive summary

Following a review by the Swedish regulatory authorities of the post-closure safety assessment of the SFR 1 disposal facility for low and intermediate waste (L/ILW), SAFE, the SKB has prepared an updated assessment called SAR-08.

This report describes the radionuclide release calculations that have been undertaken as part of SAR-08. The information, assumptions and data used in the calculations are reported and the results are presented.

The calculations address issues raised in the regulatory review, but also take account of new information including revised inventory data.

The scenarios considered include the main case of expected behaviour of the system, with variants; low probability releases, and so-called residual scenarios. Apart from these scenario uncertainties, data uncertainties have been examined using a probabilistic approach.

Calculations have been made using the AMBER software. This allows all the component features of the assessment model to be included in one place. AMBER has been previously used to reproduce results the corresponding calculations in the SAFE assessment. It is also used in demonstration of the IAEA's near surface disposal assessment methodology ISAM and has been subject to very substantial verification tests and has been used in verifying other assessment codes.

Results are presented as a function of time for the release of radionuclides from the near field, and then from the far field into the biosphere. Radiological impacts of the releases are reported elsewhere. Consideration is given to each radionuclide and to each component part of the repository. The releases from the entire repository are also presented.

The peak releases rates are, for most scenarios, due to organic C-14. Other radionuclides which contribute to peak release rates include inorganic C-14, Ni-59 and Ni-63.

Contents

1 Introduction

1.1 Background

SFR 1 is situated in the northern part of Uppland, close to the Forsmark nuclear power plant and is the central Swedish repository for operational solid radioactive waste from the country's nuclear power plants (NPPs) and for solid low and intermediate waste (L/ILW) from operations at the Studsvik Research Site.

This report describes the radionuclide release calculations that have been undertaken as part of SAR-08. The information, assumptions and data used in the calculations are reported and the results are presented which are an update of the most recent safety assessment calculations of the SFR 1 facility (Project SAFE) /Lindgren et al. 2001/ following the authorities' review of the safety case documentation /SKI and SSI 2004/. It is intended to undertake this update by performing new safety assessment calculations in response to comments received in the authorities' review and also on the basis of new and additional data and information. This will result in a new safety assessment and safety case for SFR 1 ("SAR-08").

The radionuclide release calculations have been undertaken in order to quantitatively assess differing scenario variants through the use of targeted calculation cases. The calculation cases seek to address specific questions related to the assessment of the performance of the SFR 1 repository.

The following areas have been reviewed and updated following Project SAFE.

- Assessment timescales have been extended beyond 10,000 years post-closure.
- The possible impacts of climate change have been considered.
- A revised set of scenarios and calculation cases has been derived.
- An updated radionuclide disposal inventory has been estimated.
- Uncertainties in the calibration of the supporting hydrogeological models are considered.
- The time-dependent failure of the engineering barrier system is considered.
- The impacts of uncertainties in key parameters are considered through undertaking calculations using parameters sampled from distributions.

1.2 Structure of report

Section 2 summarises the scenarios and calculation cases considered within the near-field and geosphere calculations for SAR-08.

Section 3 presents the assumptions and data used in the near-field and geosphere models.

Section 4 presents the near-field and geosphere results for all calculation cases.

Section 5 provides a summary.

References are included and supporting information and data are appended.

2 Scenarios and calculation cases for SFR 1 SAR-08

2.1 Selection of calculation cases

Calculation cases treated in this report constitutes one part of the all calculation cases treated within the safety analysis SAR-08. The calculation cases in this report were compiled mainly using the following information sources:

- Experience from previous safety assessments,
- Knowledge of the initial state of SFR at closure, and
- Description of climate changes and the resultant effect.

The calculation cases presented in this report is however only a subset of the assessment calculations in SAR-08.

2.1.1 Experience from previous safety assessments

SKB is able to use the experience it has gained from previous calculations in the safety assessments it has undertaken to date. These safety assessments include the following

- Previous safety assessments for SFR 1 /SKB 2001a, 1993/.
- The SR-Can and SR97 safety assessments for spent fuel /SKB 2006a, 1999a/.
- Safety assessments for long-lived LILW /SKB 1999b/.

The safety assessments provide a useful reference to previous safety assessment iterations in order that cycles of hazard identification and assessment can be reviewed and considered for inclusion within SAR-08. Additionally, several of these assessments benefit from having been subject to regulatory review and therefore also provide further information beneficial SAR-08.

The most recent assessment for SFR 1, Project SAFE, /SKB 2001a/ contained several calculations to assess the following situations.

- Intact near-field barriers.
- Degraded near-field barriers.
- Initially degraded barriers.
- Complexants.
- Permafrost.
- Human intrusion.

This list of calculations, combined with consideration of the Authorities review /SKI and SSI 2004/ therefore provides a useful checklist for the calculation cases to be included both within the present report and for the SAR-08 assessment as a whole.

2.1.2 Knowledge of the initial state of SFR 1 at closure

For the purposes of the long-term safety assessment, the repository is considered to be operated and closed in a manner similar to that assumed for Project SAFE, i.e.

- The waste disposed in the Silo is mainly composed of ion-exchange resins in a concrete or bitumen matrix. The waste packages are placed in the shafts and the voids between the waste packages are gradually backfilled with porous concrete. The Silo will be closed with a 1 m thick concrete lid (with gas vents), the top of the lid will be covered with a thin layer of sand and then 1.5 m of sand/bentonite mixture (90/10). The remaining void above the sand/bentonite in the top will be filled with sand or gravel.
- The BMA waste consists of ion exchange resins, scrap metal and trash in a concrete or bitumen matrix packaged similarly to the Silo, i.e. moulds and drums. The BMA structure is divided into 15 compartments separated by concrete walls. The waste is stacked on top of the concrete floor so that the concrete moulds act as support for prefabricated concrete lids. Lids are emplaced as soon as the individual compartments are filled and a layer of concrete is cast on top of the lid. Between the concrete structure and the rock the void space will be filled with sand or gravel.
- The two rock vaults for concrete tanks, 1BTF and 2BTF contain de-watered low-level ion exchange resin in concrete tanks. In addition, some drums with ashes have been disposed in 1BTF. The concrete tanks, each with a volume of 10 m^3, are stacked in two levels with four tanks in each row. A concrete lid is placed on top of each stack once it has been completed. The space between the different tanks is backfilled with concrete and the space between the tanks and the rock wall will be filled with sand stabilised in cement.
- The waste deposited in BLA is mainly low level scrap metal and refuse placed in standard steel containers. Some of the waste inside the containers is placed in steel drums and others in bales. The containers are placed two in a row and three full height containers in height on the concrete base slab. Most of the containers are half height and these are piled to a height of six. No backfill is planned.
- The access points to the disposal tunnels and Silo are sealed with plugs. Similar plugs are also placed in the access ramps. The plugs are comprised of a 1 m thick bentonite seal.

2.2 Summary of near-field and geosphere calculation cases

Table 2-1 below summarises the near-field and geosphere calculation cases in the present report. Within the table a brief overview of the aspects relevant to near-field and geosphere is given with a reference to a fuller description in the sections below.

A subset of the calculation cases presented here include several improvements over those previously presented in Project SAFE, including the following.

- The assessment timescale is not truncated to 10,000 years post-closure
- The implications of climate change are considered. The climate evolution is assumed to correspond to that used in the SR-Can assessment where two equally likely climate evolutions, the Weichselian variant which is a repetition of the last glaciation and the greenhouse variant which assumes that the present temperate period is extended due to anthropogenic releases of green house gases /SKB 2006ab/.
- The evolution of the total barrier system (including the geosphere) is considered.

Table 2-1. Overview of calculation cases presented in the current report.

Calculation case		Near field and geosphere aspects
CC1	Weichselian climate evolution	The evolution of the climate is assumed to be a repetition of the last glaciation (the Weichselian). The periods of continuous permafrost are considered to be sufficient to inhibit the transfer of radionuclides and movement of ground water flow. The assumptions regarding closure design, disposal inventory and system performance follow best estimates. See subsection 2.2.1
CC2	Weichselian climate evolution with taliks	Identical to CC1, except that radionuclide release and transport to taliks is assumed during periods of continuous permafrost. See subsection 2.2.2
CC3	Weichselian climate evolution with an alternative inventory	Identical to CC1, except that the disposal inventory considered to be maximum allowable under licence conditions. See subsection 2.2.3
CC4	Weichselian climate evolution with early BMA degradation	Identical to CC1, except that the barriers in BMA degrade after 23,000 years post-closure. See subsection 2.2.4
CC5	Weichselian climate evolution with taliks and early BMA degradation	Identical to CC2, except that the barriers in BMA degrade after 23,000 years post-closure. See subsection 2.2.4
CC6	Greenhouse climate evolution	The evolution of the climate is assumed to follow that described within the Greenhouse variant of the SR-Can main scenario /SKB 2006ab/. The periods of continuous permafrost are considered to be sufficient to inhibit the transfer of radionuclides and movement of ground water flow. The assumptions regarding closure design and disposal inventory follow best estimates. See subsection 2.2.5
CC7	Extreme Permafrost climate evolution	The evolution of the climate is assumed to follow that described within the Permafrost Variant. The periods of continuous permafrost are considered to be sufficient to inhibit the transfer of radionuclides and movement of ground water flow. The assumptions regarding closure design and disposal inventory follow best estimates. See subsection 2.2.6
CC8	Extreme Permafrost climate evolution with taliks	Identical to CC7, except that radionuclide release and transport to taliks is assumed during periods of continuous permafrost. See subsection 2.2.7
CC9	Weichselian climate evolution with high concentrations of complexing agents	Identical to CC1, except that the high concentrations of complexing agents such as ISA are assumed to result in the reduction in sorption of some elements. See subsection 2.2.8
CC10	Weichselian climate evolution with initial releases from the Silo affected by bulk gas generation	Identical to CC1, except that the impacts of enhanced levels of bulk gas generation on radionuclide transport are considered for the Silo. See subsection 2.2.9
CC11	Intrusion wells	Considers the radionuclide concentrations in gravel for use in estimating the potential impacts from human intrusion into the facility at some point in the future. This is calculated for CC1 and CC9. See subsection 2.2.10
CC12	Near-field barriers I	Identical to CC1, except that sorption onto near-field materials is excluded. See subsection 2.2.11
CC13	Geosphere barriers	Identical to CC1, except that the geosphere is excluded. See subsection 2.2.12
CC14	Near-field barriers II	Identical to CC, except that the failure of Silo and BMA occurs at 3,000 years post-closure. See subsection 2.2.13

2.2.1 Calculation Case 1: Weichselian climate evolution

The purpose of Calculation Case 1 (CC1) is to present an estimate of radionuclide release and migration and consequent exposure associated with a probable evolution of SFR 1 during a repetition of the Weichselian glaciation cycle.

Description of climate evolution

The climate considered in the Weichselian climate evolution is a repeat of the previous glacial cycle from cooling of the current temperate climate to colder permafrost and glacial conditions /Vidstrand et al. 2007/. The anticipated climate evolution is a period of temperate conditions at the Forsmark site for approximately 23,000 years, although a shorter periglacial period with sporadic (and relatively shallow) permafrost occurs around 8,000 to 10,000 years after present (AP). Following this, the temperate conditions are gradually replaced by periglacial periods with permafrost conditions between 23,000 and 37,000 years AP and from 42,000 to 56,000 years AP. The period 37,000 to 42,000 years AP is characterised by a temperate period. From 56,000 years AP glacial conditions exist until the retreat of the ice at 66,000 years AP at which time the area of the site is considered to be submerged and remains below sea-level, most likely under cold climate conditions, until 75,000 years AP. Cold climate conditions continue and permafrost returns from 75,000 to 91,000 years AP and glacial conditions are re-established from 91,000 years to the end of the assessment period (100,000 years AP).

The evolution of the climate for the Weichselian climate evolution is summarised below in Figure 2-1 and Table 2-2, supplied by SKB.

Near-field

The repository is considered to be operated and closed in the manner previously described in subsection 2.1.2. The disposal inventory is that resulting from 50 years of reactor operations and disposal of the 50 years of operating wastes is assumed complete at 2040 at which time the repository is closed.

One of the primary assumptions of this calculation case is that the initial properties of the engineered barrier system are at least equivalent to its design specification. This implies that concrete floor, walls and lids in the different repository facilities do not contain large intersecting fractures. The same assumption is made of the porous concrete or concrete grout surrounding the waste packages. Small fractures in the concrete may be formed due to stress in the material but these are assumed to be so small as to not form an interconnected network. Bentonite and sand/bentonite barriers in the Silo and the bentonite plugs are assumed to be homogeneous. The concrete moulds and concrete tanks are assumed to be intact at closure, i.e. they do not contain large intersecting fractures. Although it may be considered that the steel packages may be sealed at closure, they are not considered to be completed impermeable to water or gases and there is also the potential that they may have been damaged during the operational period, for example due to corrosion. Steel packages are therefore not considered to act as a barrier to either water or dissolved radionuclides.

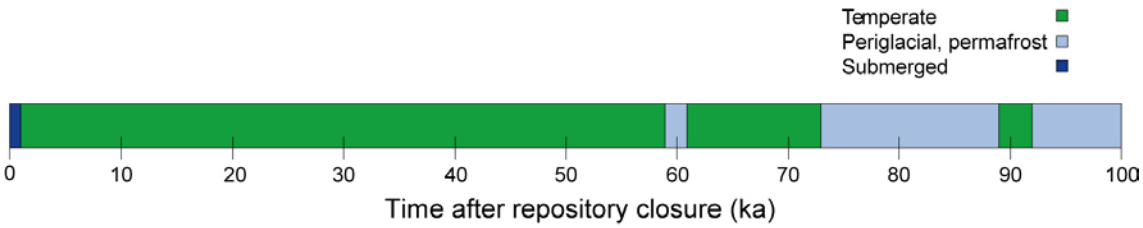

Figure 2-1. *Duration of climate domains for CC1, Weichselian climate evolution.*

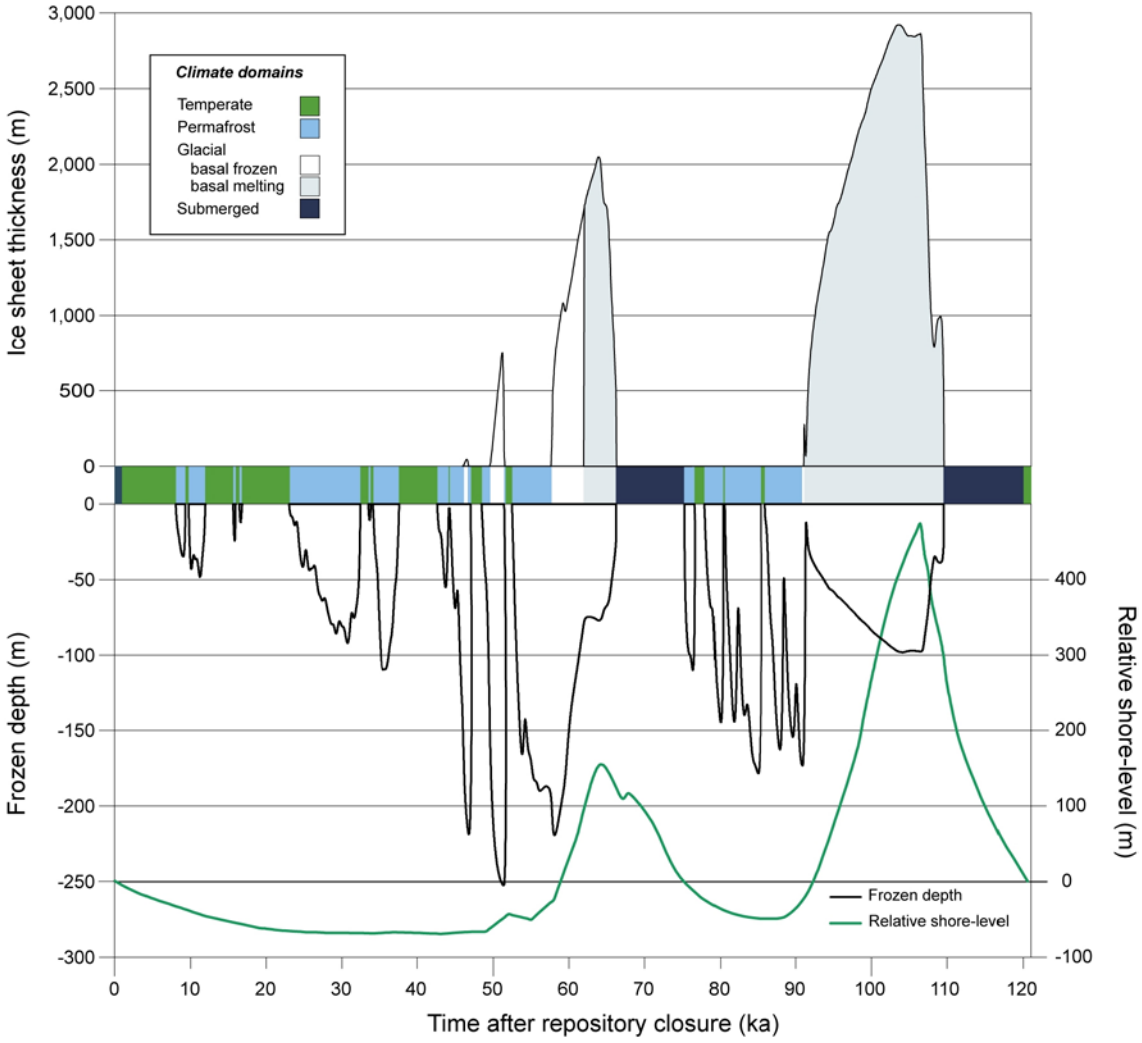

Figure 2-2. *Summary of climate variables for CC1, Weichselian climate evolution.*

Table 2-2. Chronological summary of climate domains for CC1, Weichselian climate evolution.

Climate domain	Time [kyears, AP]
Temperate	0–8
Periglacial with sporadic permafrost	8–10
Temperate	10–23
Periglacial with continuous permafrost	23–37
Temperate	37–42
Periglacial with continuous permafrost	42–56
Glacial, ice sheet cover	56–66
Submerged	66–75
Periglacial with continuous permafrost	75–91
Glacial, ice	91–109

After closure the operational drainage system will be decommissioned and so groundwater will flow into the different repository parts from the surrounding rock and fill up pore volumes and empty space in the repository. The time from repository closure to a water filled repository is considered to be relatively short, some few years for the vaults (i.e. BMA, 1BTF, 2BTF, BLA) and some tens of years for the Silo /Holmén and Stigsson 2001a/. In the calculations the time to saturate the repository is neglected as not significant for groundwater release and saturation is assumed immediately after closure.

Radionuclide release

Once groundwater has saturated the different repository facilities it may come into contact with waste and the radionuclides in the waste will dissolve in the water. No limitations by solubility or availability are assumed for the radionuclides in either cement or bitumen matrices, or in any other parts of the system. Dissolved radionuclides are then able to be transported through the waste matrix, walls of waste packages and surrounding concrete, bentonite and gravel barriers out from the different repository parts. The transport occurs by diffusion and advective groundwater flow but the release is delayed by sorption in the barrier materials. The quantity of the radionuclides that are released from the different repository parts is dependent on: the concentration of radionuclides in the water in contact with the waste; the diffusion and sorption properties of the barrier materials; and the size and distribution of the water flow in the barriers and how these change with time.

In most cases it is assumed that no release of radionuclides occurs in the release of gas from the near field, however gas release is included in CC10.

Performance of barriers

The engineered barrier system within SFR 1 has been designed to both limit the migration of radionuclides within groundwater and to provide a controlled pathway for the release of gases. Following the emplacement of the engineered barrier system it is assumed to operate during the initial post-closure period in line with the specifications of its design. Studies have been undertaken to investigate the degradation of the barriers due to chemical reactions between the barrier material and components in influent groundwaters /Höglund 2001, Cronstrand 2007/. These studies indicate that the barriers within the BMA and Silo are likely to perform extremely well for a significant period of time in excess of 10,000 years post-closure.

Different FEPs have the potential to impact on the performance of the barriers. The facility may be subject to mechanical stresses associated with different climate states. For example, freeze/thaw cycles associated with the development and retreat of permafrost and ice sheets in the region of the site may induce differential stresses on the repository components due to the different porosities exhibited by the materials. The BMA barriers are considered to fail at the beginning of the second period of continuous permafrost at 42,000 years post-closure /Emborg et al. 2007/. Additionally the advance and retreat of large bodies of ice above the site can be expected to exert significant stresses on the repository. Thus within the Silo the barriers are considered to fail following the retreat of the ice-sheet across the site at 66,000 years post-closure which results in the degradation of the Silo encapsulation and the discharge of a significant flux of glacial meltwaters breaching the bentonite backfill.

The thickness of barriers within the 1BTF and 2BTF is less than those of the BMA and Silo and it is therefore considered that these barriers will perform well for a period of 1,000 years post-closure and thereafter will be degraded. No barriers are considered for the BLA[1].

[1] The BTF and BLA require less engineered controls in their closure due to the lower radionuclide contents of wastes disposed within them.

Other calculation cases are considered, in which the consequences of a more rapid degradation of the engineered barrier system (e.g. CC4, CC12, CC14). A further calculation case is considered in which human intrusion into the facility occurs, by drilling activities, in the future (CC11).

The magnitude and direction of groundwater flow within the different repository facilities will change in response to those FEPs outlined above. Supporting studies have been undertaken in order to provide a basis for the values used in the assessment calculations; stepwise changes in the magnitude and direction of the groundwater flow are made in the assessment model in accordance with the results from the supporting hydrogeological calculations /Holmén and Stigsson 2001ab/. The magnitude and direction of the groundwater flow calculated for the time 2,000 AD is assumed to be valid from repository closure to 1,000 years post-closure. Stepwise changes to the groundwater flows are then made at 1,000, 2,000 and 3,000 years post-closure. These assumed stepwise changes in flow result in corresponding abrupt changes in the radionuclide releases. The repository groundwater flow fields also take account of the potential uncertainty in the calibration of the models through the use of uncertainty factors that were derived from an inverse modelling study which investigated the sensitivities to uncertainties in the calibration /Holmén 2005, 2007/. Uncertainty factors have been used for the groundwater flow regimes at closure and 2,000 years post-closure.

In order to support the longer-term hydrogeological conditions additional studies have been undertaken in order to investigate the potential groundwater flow regime under changed climatic conditions /Vidstrand et al. 2007/. This study considered the potential changes to the groundwater flows estimated for the near-future that could occur for the climate states identified in Table 2-2. The flows are provided as estimates of the potential changes to the groundwater flow that can be expected to occur within the vicinity of the repository and are considered an appropriate means of assessing the potential hydrogeological conditions that may be established under different environmental states.

Gaseous generation

Bulk gases such as hydrogen, carbon dioxide and methane are generated within the disposal facilities, due to the anaerobic corrosion of metals and degradation of organic materials. Radiolysis of water contributes negligible amounts to the total volumes of gas generated over time and is not included in the calculation. In addition the degradation of ion-exchange resins and bitumen is so slow that such contributions can also be neglected /Moreno 2001/. The corrosion of the metals is not possible without the presence of water but the amounts of water are small such that water availability may be considered the limiting factor during the re-saturation period.

The design of repository and its waste-forms also takes account of the need to provide a means to prevent the build up of gases within the repository components. The largest volumes of gas will be generated within the BLA and Silo. The wastes within the BLA are not grouted and limited engineered barriers are included within this disposal facility so the gases produced are therefore readily able to escape. It is considered that the corrosion of steel waste containers will begin soon after waste emplacement and so will provide a means of escape for gas from the waste-form. As an additional feature the concrete lid of the Silo has been designed to include sand filled evacuation pipes which provides a means of reducing the potential for the build-up of gases within the Silo. The waste-forms within the BMA and BTF are packaged similarly and the concrete lids used to enclose the compartments will not from an impermeable gas seal.

These bulk gases are not thought capable of producing an impact on the environment given their low bulk compared with the wider biosphere. An alternative calculation case has been undertaken to assess the potential impacts on groundwater flow of higher generation rates of gas within the Silo (CC10).

Retardation by sorption

The transport of radionuclides in the near field will be delayed by sorption in cement and concrete as well as in bentonite barriers and gravel backfill. In cement and concrete barriers the influent water will quickly obtain a high pH, and the ion strength will be high since the penetrating water is saline and additionally the concrete contributes dissolved salts /Höglund 2001, Cronstrand 2007/. With time the leaching of cement components may result in some decrease in pH and ion strength in cement and concrete barriers, but alkaline conditions are expected to be maintained for significant periods. Following the degradation of the concrete and cement the sorption capacity of the materials is assumed to be reduced to levels similar to that for sand and gravel. Sorption is also considered possible on the bentonite backfill around the Silo.

Products from corrosion of iron and steel can be of importance for the release of radionuclides as there is strong evidence that iron oxides and iron hydroxides bind many elements. However, sorption onto corrosion products is not taken into account.

The waste disposed within SFR 1 contains chemicals that may form complexes with the radionuclides and thereby influence the sorption of radionuclides. Cellulose in the waste and as additive in cement and concrete may degrade forming isosaccarinic acid (ISA), which is a strong complexing agent. A review has previously been undertaken to estimate the potential concentrations of complexing agents within SFR 1 /Fanger et al. 2001/. This review concluded that the concentration of complexing agents inside the waste packages for a few waste types may be sufficiently high that it can not be disregarded and that sorption inside the packages may be influenced. The highest concentrations of ISA were estimated for the wastes stabilised with bitumenised waste in steel packaging, however, sorption is not considered for bitumenised wastes.

Regarding the expected small effects from complexing agents on the sorption and that the data representing the sorption in the system without complexing agents are already conservatively chosen, the possible effects from complexing agents are considered in CC1 in so far as they are considered within the uncertainty ranges of the sorption coefficients. The presence of high concentrations of complexing agents may however be of importance for the safety of the repository. Thus this is illustrated as a separate calculation case where the presence of complexing agents results in a further reduction of the sorption in the near-field barriers (CC9).

Geosphere

Radionuclides released from the different repository facilities are transported within the rock by the flowing water. The transport occurs mainly by advection in the open fractures in the rock. The ability of the rock to delay and through radioactive decay, reduce the total release as well as peak release rates of radionuclides to the biosphere compared to the release from the near field depends upon the magnitude of the groundwater flow, the path length and the exchange of radionuclides between the flowing water and the rock matrix.

During the period following closure when the repository is submerged the migration routes from the repository to the surface are relatively short and are orientated in the vertical direction with the discharge anticipated to occur at a point on the seabed above the repository. However, the hydraulic gradients are relatively low and so the travel times are relatively long. The ongoing land rise displaces the shoreline (passing over the repository at approximately 2,800 AD /Holmén and Stigsson 2001a/) and thus both the distance travelled and the groundwater flow change with time which results in an increase in the groundwater flow paths. The area of discharge is considered to be an area of low lying topography to the north-west of the repository in which the formation of a lake is considered highly likely. The continued shoreline displacement corresponds with a change of flow direction to the horizontal and an increase in the hydraulic gradients which results in a reduction in travel times.

Estimates of geosphere path length and travel time for the near-future have been taken from the inverse modelling studies /Holmén 2007/. The correlations between the rate of groundwater

flow through the near-field and the migration paths through the geosphere have been found to be strong. Radionuclides are assumed to retarded by the rock matrix through by sorption and matrix diffusion.

These conditions are assumed to continue throughout the assessment, although during the periods of continuous permafrost the geosphere is assumed to freeze and so radionuclide migration is prevented /Vidstrand et al. 2007, Emborg et al. 2007/. During the period in which the site is covered by an ice sheet the geosphere flow paths are expected to be extremely long and the groundwater will discharge at the snout of the glacier which could be many 10's (or even 100's) of kilometres from the site. However, it is conservatively assumed that the groundwater continues to discharge at a location closer to the repository. Estimates of the relative increase in regional groundwater flow regime have been based on the same estimates used to support the near-field groundwater flow and are again considered to be adequate for the purposes of the assessment.

The groundwater is initially assumed to be saline in nature but the ongoing land rise and shoreline displacement means that by 1,000 years post-closure the groundwater has become non-saline /Holmén and Stigsson 2001a/. Values of sorption coefficients and effective diffusivity have been selected for both saline and non-saline conditions. Following the retreat of the ice-sheet and the re-submergence of the site 66,000 and 75,000 years post-closure the groundwater is assumed to return to saline conditions.

2.2.2 Calculation Case 2: Weichselian climate evolution with taliks

Calculation Case 2 (CC2) is a variant of CC1 which considers uncertainty in the behaviour of the repository and the surrounding area during periods of continuous permafrost.

In CC2 the situation is considered that during periods of continuous permafrost the groundwater within the repository remains un-frozen as does areas of the geosphere between the repository and the ground surface such that a migration route for radionuclides is developed. Groundwater may remain unfrozen (with zones called cryopegs) at temperatures below 0°C for different reasons, such as pressure, composition or its position relative to the main permafrost body /Vidstrand et al. 2007, McEwen and de Marsily 1991/.

Estimates of the potential hydrogeological response to this situation has been undertaken within /Vidstrand et al. 2007/. These are the only changes and the remainder of CC2 is identical to CC1.

2.2.3 Calculation Case 3: Weichselian climate evolution with alternative inventory

Calculation Case CC3 (CC3) is a variant of CC1 which considers uncertainty in the radionuclide inventory that will have been emplaced within the repository at the time of closure.

SFR 1 is an operational facility and therefore will not have a fixed final disposal inventory until disposal operations have been completed. In order to undertake periodic safety assessments of the facility and to demonstrate compliance with repository licence conditions it is necessary to produce estimates of the radionuclide disposal inventory that will have been emplaced at the time of closure.

It is commonplace that during the operational lifetime of repositories the estimates of the final disposal inventory vary over time in response to several factors such as management practices at the waste producers' sites, management practices at the repository and the results of safety assessment cycles.

In CC3 the radionuclide inventory disposed of in SFR 1 is considered to be the maximum allowable under licence conditions. These are the only changes and the remainder of CC3 is identical to CC1.

2.2.4 Calculation Case 4 and 5: Weichselian climate evolution with early BMA degradation

Calculation Case 4 (CC4) and Calculation Case 5 (CC5) consider uncertainty in the behaviour of the BMA during periods of continuous permafrost within the Base Variant climate evolution.

The barriers that form the BMA encapsulation are assumed to be sufficient to withstand the consequences of the first period of continuous permafrost within CC1 but insufficient to withstand the second period of continuous permafrost which develops to a greater depth more quickly (Figure 2-2). CC6 considers the possibility that the BMA may be insufficient to withstand the consequences of the first period of permafrost and the encapsulation may fail at the start of the first period of continuous permafrost (i.e. at 23,000 years post-closure).

At this point the BMA barriers are considered to fail in a similar manner to that described previously for CC1 with increases in groundwater flow rates and the effective diffusivity of concrete and reductions in the sorption capacity of concrete and cement. Furthermore within this calculation case consideration is also given to the uncertainty in the existence of a migration pathway between the repository and ground surface during periglacial periods of continuous permafrost, as outlined in the description of CC2.

The differences between the following two calculation cases:

CC4 – Early degradation of the BMA encapsulation with Weichselian climate evolution.

CC5 – Early degradation of the BMA encapsulation with Weichselian climate evolution and taliks.

These are the only changes to CC4 and CC5 and the remainder of these calculations is identical to CC1 and CC2, respectively.

2.2.5 Calculation Case 6: Greenhouse climate evolution

Calculation Case 6 (CC6) considers human influences on climate that are not included within the Weichselian climate evolution and therefore adopts the Greenhouse climate evolution. Such a change is considered just as likely as the Weichselian climate evolution.

/Vidstrand et al. 2007/ suggest that for the purpose of a safety assessment, the impact of greenhouse warming on climate-related conditions in Sweden can be regarded as being expressed through a long period of temperate domain.

In the Greenhouse climate evolution, it is assumed that the temperate domain will prevail for approximately another 50,000 years until the first, restricted, ice advance in Fennoscandia takes place. After that, the first 70,000 years of the Weichselian climate evolution is assumed to follow. The first major ice advance will thus occur after approximately 100,000 years in the Greenhouse climate evolution /Vidstrand et al. 2007/.

The evolution of the climate for the Greenhouse climate evolution is summarised below in Figure 2-3 and Table 2-3.

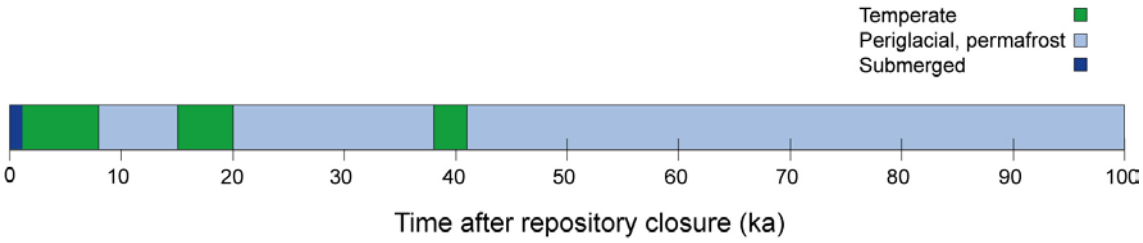

Figure 2-3. *Duration of climate domains for CC6, Greenhouse climate evolution.*

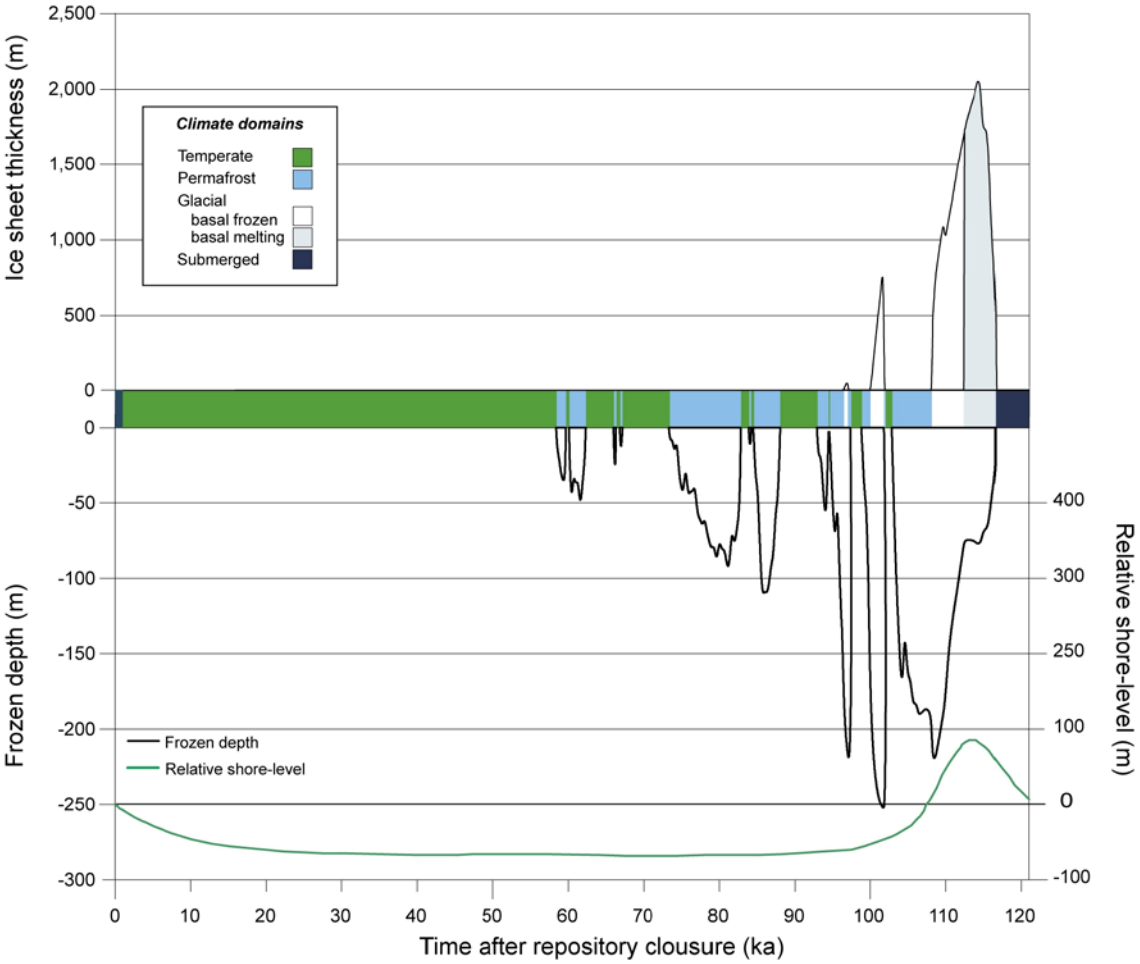

Figure 2-4. *Summary of climate variables for CC6, Greenhouse climate evolution.*

Table 2-3. Chronological summary of climate domains for CC6, Greenhouse climate evolution.

Climate domain	Time [kyears, AP]
Temperate	0–73
Periglacial, continuous permafrost	73–100

The anticipated climate evolution is a significant period of temperate conditions at the site until approximately 73,000 years AP and thereafter a period of continuous permafrost at repository depth occurs[2].

The majority of the remainder of the calculation case follows those described previously for CC1. However, the following differences exist.

- Degradation of the BMA is assumed to take place at 73,000 years post-closure, the Silo remains intact through the assessment timescale.
- The tunnel plugs are assumed to remain intact throughout the assessment timescale.
- The geosphere changes from saline to non-saline at 1,000 years post-closure as in CC1 and remains non-saline from here on.

[2] No radionuclide migration is assumed to occur during the period of continuous permafrost in CC6 and therefore the calculation is truncated at 73,000 years post-closure.

2.2.6 Calculation Case 7: Permafrost climate evolution

Calculation Case 7 (CC7) considers a less likely set of climate variables which are not included within the Base Variant climate evolution and result in more extensive development of permafrost within the Permafrost Variant climate evolution.

The Permafrost Variant of climate evolution assumes that air temperatures fall according to the glacial cycle temperature curve of the reference evolution, but in an extremely dry climate which does not support ice sheet growth. To further enhance permafrost growth the effects of snow cover and vegetation were excluded from consideration, and the site was assumed to always remain above sea level /Vidstrand et al. 2007, SKB 2006b/.

The evolution of the climate for the Permafrost Variant is summarised below in Figure 2-5 and Table 2-4.

The anticipated climate evolution comprises alternating periods of temperate conditions and continuous permafrost at the Forsmark site until approximately 41,000 years AP and thereafter a period of continuous permafrost at repository depth occurs[3].

The majority of the remainder of the calculation case follows those described previously for CC1. However, the following differences exist.

- Degradation of the BMA is assumed to take place at 20,000 years post-closure.
- Degradation of the Silo concrete structure is assumed to take place at 20,000 years post-closure, however, the bentonite backfill remains intact throughout the assessment timescale.
- The tunnel plugs are assumed to remain intact throughout the assessment timescale.
- The geosphere changes from saline to non-saline at 1,000 years post-closure as in CC1 and remains non-saline from here on.

Table 2-4. Chronological summary of climate domains for CC7, Permafrost climate evolution.

Climate domain	Time [kyears, AP]
Temperate	0–8
Periglacial, continuous permafrost	8–15
Temperate	15–20
Periglacial, continuous permafrost	20–37
Temperate	37–41
Periglacial, continuous permafrost	41–100

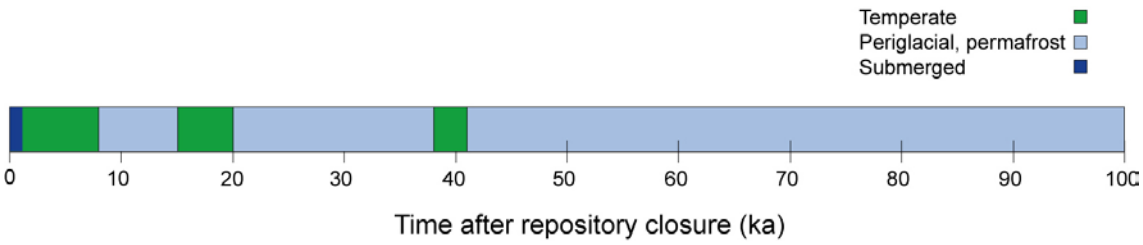

Figure 2-5. *Duration of climate domains for CC7, Permafrost climate evolution.*

[3] No radionuclide migration is assumed to occur during the period of continuous permafrost in CC7 and therefore the calculation is truncated at 41,000 years post-closure.

2.2.7 Calculation Case 8: Permafrost climate evolution with taliks

Calculation Case 8 (CC8) is a variant of CC7 which considers uncertainty in the behaviour of the repository and the surrounding area during periods of continuous permafrost. CC8 is related to CC7 in a similar manner that CC2 is related to CC1.

In CC8 the situation is considered that during periods of continuous permafrost the groundwater within the repository remains un-frozen as does areas of the geosphere between the repository and the ground surface such that a migration route for radionuclides is developed. Groundwater may remain unfrozen (with zones called cryopegs) at temperatures below 0°C for different reasons, such as pressure, composition or its position relative to the main permafrost body /Vidstrand et al. 2007, McEwen and de Marsily 1991/.

Estimates of the potential hydrogeological response to this situation has been undertaken within /Vidstrand et al. 2007/. These are the only changes and the remainder of CC8 is identical to CC7.

2.2.8 Calculation Case 9: Near-field complexants

Calculation Case 9 (CC9) considers the potential consequences for radionuclide release from the repository under conditions in which the levels of complexants within the near-field are significantly higher than those considered in CC1.

/Fanger et al. 2001/ have previously undertaken a review and concluded that there is a low probability that the concentration of the complexants such as ISA may reach levels within the repository such that reductions in the sorption of elements may be possible.

CC9 therefore considers the potential impacts of a reduction in the values of near-field sorption coefficients for those elements which are sensitive to concentrations of complexing agents.

2.2.9 Calculation Case 10: Enhanced bulk gas generation

Calculation Case 10 (CC10) considers the potential consequences for radionuclide release from the Silo during periods of enhanced bulk gas generation.

A review of the potential for the generation gases within SFR 1 has previously identified that the most likely processes are anaerobic corrosion, degradation of organic materials and hydrolysis /Moreno et al. 2001/. The bulk gases that will be produced are hydrogen, carbon dioxide and methane, which generated dominantly by the anaerobic corrosion of metals and degradation of organic materials. Radiolysis of water contributes negligible amounts to the total volumes of gas generated over time and it is considered that the degradation of ion-exchange resins and bitumen is so slow that such contributions can also be neglected /Moreno et al. 2001/.

The corrosion of the metals is not possible without the presence of water but the amounts of water required are small such that water availability is not considered a limiting factor in CC10. This is due to the fact that as noted previously in the description of CC1 it has been cautiously assumed that the repository is saturated immediately on closure. A similar assumption of instantaneous saturation is assumed here.

The corrosion of steel is estimated to result in the generation of the largest gas volumes but the corrosion of aluminium and zinc is considered to result in the highest initial rates of generation. The BLA and the Silo are estimated to generate the largest volumes of gases and 2BTF the lowest.

The design of repository and its wasteforms also takes account of the need to provide a means to prevent the build up of gases within the repository components. As noted previously the largest volumes of gas will be generated within the BLA and Silo. The wastes within the BLA are not grouted and the limited engineering of this disposal facility enables the gases produced to

escape readily. As noted previously in the description of CC1 it is considered that corrosion of the steel containers begins soon after waste emplacement and so will provide a means of escape for gas from the individual wasteforms.

The wasteforms within the BMA and BTF are packaged similarly and the concrete lids used to enclose these disposal compartments within these facilities will not from a seal which is impermeable to gas. However, the void between the Silo walls and the excavated caverns will be backfilled with low-permeability bentonite and the area beneath the base and directly above the lid will be backfilled with a low-permeability sand-bentonite mixture. Therefore as an additional feature the concrete lid of the Silo has been designed to include sand filled evacuation pipes which provides a means of reducing the potential for the build-up of gases within the Silo.

The likely sequence of events with the Silo following closure and concerning the generation of bulk gases has been previously described in /Moreno et al. 2001/ and is considered within CC10 as follows.

The Silo is operated and closed in a manner consistent with that considered in CC1.

Upon closure the Silo is immediately saturated and the generation of bulk gases also commences immediately through the anaerobic corrosion of steel and the degradation of organics.

The bulk gases generated cannot travel through the water saturated Silo materials and therefore a volume of porewater is expelled in order to create a means of escape for the gases. The expulsion of water takes place vertically upwards from the Silo encapsulation through the concrete lid. It was estimated that sufficient gas generation occurs immediately on closure for this release to take place over a period of approximately 1 year /Moreno et al. 2001/.

Following this initial release an overpressure is required to be developed within the Silo encapsulation in order to overcome the relatively low hydraulic conductivity in the sand-bentonite layer above the Silo lid to enable the gas to escape /Moreno et al. 2001/. The overpressure required is assumed to be 15 kPa which results in a lowering of the water level within the Silo encapsulation and the expulsion the displaced porewater through the walls and base of the Silo over a period of approximately 10 years /Moreno et al. 2001/.

The assumption of instantaneous saturation and maximum gas generation within CC10 is conservative when considering the effects of bulk gas generation on radionuclide release because saturation of the facilities will only be completed once gas generation has completed[4]. However, it is also considered to be unlikely.

2.2.10 Calculation Case 11: Intrusion wells

Calculation Case 11 (CC11) is a calculation case which considers the potential impacts from human intrusion into the facility at some point in the future.

Following closure of the repository it is possible that as time passes knowledge of the repository and/or its contents may be lost. As land uplift and shoreline migration continues the position of the coastline will pass over the repository (at approximately year 3,000 AD) and it will become accessible from the ground surface above from this point.

Review of the EFEPs relevant to Future Human Actions /Gordon et al. 2008/ suggests that the most likely cause of human intrusion will be the construction of a borehole from the ground surface that intercepts the waste within the repository.

[4] The presence of pockets of gas resulting from the corrosion and degradation of materials will delay the full saturation of the facility and therefore decrease the rates of advective and diffusive radionuclide transport.

In order to assess the potential dose consequences of intrusion into the repository knowledge is required of the estimated radionuclide concentrations within the gravel at the time of intrusion. This is calculated for CC1 and CC9.

2.2.11 Calculation Case 12: Near-field barriers I

Calculation Case 12 (CC12) is a calculation case which considers the contribution of the near-field barrier system in retarding the release of radionuclides by providing a matrix for them to sorb onto.

CC12 is based on CC1 and is identical to it in all aspects except that no sorption onto near-field materials is considered.

2.2.12 Calculation Case 13: Geosphere barriers

Calculation Case 13 (CC13) is a calculation case which considers the contribution of the geosphere to act as part of the barrier system and retard the release of radionuclides.

CC13 is assessed by comparing aspects of the CC1 near-field radionuclide release profile with those from the geosphere.

2.2.13 Calculation Case 14: Near-field barriers II

Calculation Case 14 (CC14) is a calculation case which considers the impact of the Silo and BMA barrier system in retarding the release of radionuclides at early times.

CC14 is based on CC1 and is identical to it in all aspects except that the failure of both the Silo and BMA are assumed to occur at 3,000 years post-closure.

The failure time of 3,000 years post-closure is chosen as this coincides with the time at which releases from the geosphere cease to be to a marine ecosystem and instead occur to a lacustrine or terrestrial ecosystem.

3 Development of AMBER models for SAR-08

3.1 AMBER

AMBER is a flexible, graphical-user-interface based tool that allows users to build their own dynamic compartmental models to represent the migration, degradation and fate of contaminants in an environmental system. AMBER allows the user to assess routine, accidental and long-term contaminant releases. It allows the user the flexibility to define:

- Any number of compartments
- Any number of contaminants and associated rates of degradation (both compartment dependent and independent)
- Any number of transfers between compartments
- Sub-models within larger models
- Algebraic expressions to represent transfer processes operating between compartments
- Algebraic expressions to represent the uptake of contaminants by humans and other output quantities of interest
- Non-linear transfer processes (e.g. solubility-limited leaching)
- Deterministic, probabilistic and time varying parameter values.

Within any given compartment in AMBER, a contaminant is assumed to be uniformly mixed. Each transfer is 'donor controlled', depending directly on the amount of material present in the compartment from which the contaminant is moving (the donor compartment), and can change with time. AMBER allows contaminants to decay or degrade with time into other contaminants, if required. For example, one radionuclide may decay into another.

An AMBER compartment model will usually contain compartments, transfers between compartments and sources providing input of contaminants to compartments.

Mathematically, the amount of contaminant in any compartment is determined by Equation 3-1.

If the total amount of contaminant m in compartment i is I_i^m (moles) then this satisfies:

$$\frac{dI_i^m}{dt} = -\left[\lambda_r^m + \sum_j \lambda_{ij}\right] I_i^m + \lambda_r^{m+1} I_i^{m+1} + \sum_j \lambda_{ji} I_j^m \qquad \text{Equation 3-1}$$

where

λ_{ij} is the exchange rate between compartment i and compartment j (y^{-1})

λ_r^{m+1} is the decay rate of the parent contaminant $m+1$ (y^{-1})

λ_r^m is the decay rate of contaminant m (y^{-1}).

These equations are linear, so that, for example, if there is twice as much contaminant in the system initially, then the calculated concentrations in the various compartments will all be doubled at each time of interest.

Although the models which can be set up in AMBER are generally limited to those of the linear donor controlled compartment type, this class of models can be applied to a very wide range of problems as a result of the flexibility with which transfers between compartments can be specified. For example, some diffusive-like processes depend upon the concentrations of contaminants in both the donor and receiving compartments, but these can readily be represented in AMBER by including a 'forward' transfer from the donor to the receiving compartment and

a ‘backward’ transfer from the receiving compartment to the donor. The combination of these two transfers will correctly model the net transfer between compartments. Certain non-linear problems, such as those arising from solubility limitations, can also be solved using AMBER.

AMBER has been applied to a wide range of problems concerned with the way that radionuclides and other contaminants move through different parts of the environment. AMBER is used by 59 organisations in 24 different countries. Most of these users have focussed their application on performance assessments of nuclear waste facilities (including surface and deep facilities). Further description of AMBER can be found in the AMBER Reference Guide 5.1 /Enviros and Quintessa 2007/.

3.2 Implementation of Project SAFE in AMBER

The implementation of Project SAFE in AMBER have been described by /Thomson et al. 2008/. This report documents an exercise in which AMBER has been used to represent the models used in Project SAFE, the previous safety assessment undertaken on SFR 1[5].

AMBER was used to undertake assessment calculations on all of the disposal system, including all disposal tunnels and the Silo, the geosphere and several biosphere modules.

- The near-field conceptual models were implemented with minimal changes to the approach undertaken previously in Project SAFE. Model complexity varied significantly between individual disposal facilities increasing significantly from the BLA to the BTF and BMA tunnels and Silo.
- Radionuclide transport through the fractured granite geosphere was approximated using a compartment model approach in AMBER.
- Several biosphere models were implemented in AMBER including Reasonable Biosphere Development, which considered the evolution of the Forsmark area from coastal to lacustrine to agricultural environments in response to land uplift. Parameters were sampled from distributions and simulations were run for 1,000 realisations.

In undertaking the comparison of AMBER with the various codes and calculation tools used in Project SAFE it was necessary to undertake a detailed analysis of the modelling approach previously adopted, with particular focus given to the near-field models. The exercise demonstrates that AMBER is fully capable of representing the features of the SFR 1 disposal system in a safety assessment.

Figure 3-1 shows a comparison of the estimated flux from the Silo for AMBER and NUCFLOW /Thomson et al. 2008/. The open symbols are NUCFLOW and the lines are AMBER. For the majority of radionuclide the output times for NUCFLOW and AMBER are identical, however, as NUCFLOW simulations are undertaken individually for each radionuclide some radionuclides have different output times[6].

Table 3-1 also summarises the results for each simulation. For each radionuclide reported the first value is the maximum radionuclide flux (Bq y^{-1}) and the second value in parentheses is the time of the maximum radionuclide flux (y). Differences in the models are highlighted in bold. Generally it can be seen that the agreement between the two simulations is very good.

[5] As Enviros would use AMBER in supporting SKB it was first necessary to replicate the existing Project SAFE model in AMBER, so that the uncertainty that any changes to calculated performance are due to differences in modelling approaches or assumptions between Project SAFE and the AMBER model is removed.

[6] In situations in which it was necessary to undertake detailed comparisons of individual radionuclides, the AMBER simulation was re-run using radionuclide-specific output times derived from the corresponding NUCFLOW simulation.

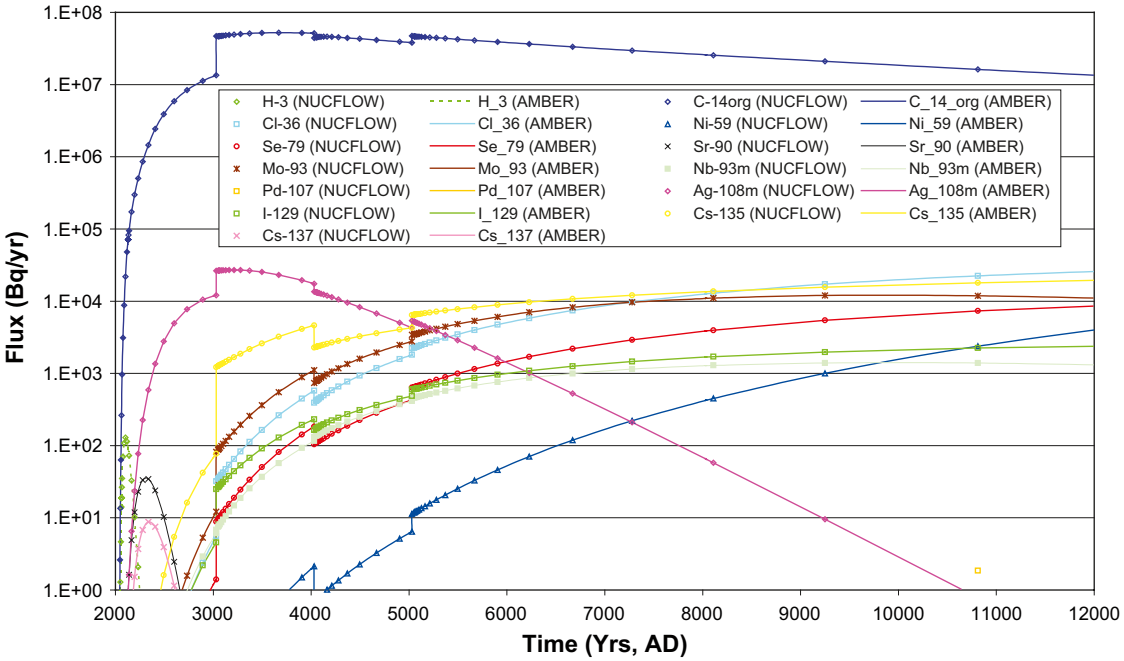

Figure 3-1. *Comparison of Silo near-field flux for selected radionuclides from AMBER and NUCFLOW /Thomson et al. 2008/.*

Table 3-1. Summary of comparisons of maximum radionuclide flux and time of maximum for AMBER and NUCFLOW Silo models.

Radionuclide	Maximum radionuclide flux, Bq y^{-1} (time of max, y)	
	AMBER	NUCFLOW
H-3	$1.290 \cdot 10^{2}$ ($7.2 \cdot 10^{1}$)	$1.289 \cdot 10^{2}$ ($7.2 \cdot 10^{1}$)
Inorganic C-14	3.617 ($1.3 \cdot 10^{4}$)	3.616 ($1.3 \cdot 10^{4}$)
Organic C-14	$5.229 \cdot 10^{7}$ ($1.6 \cdot 10^{3}$)	$5.228 \cdot 10^{7}$ ($1.6 \cdot 10^{3}$)
Cl-36	$3.263 \cdot 10^{4}$ ($1.3 \cdot 10^{4}$)	$3.263 \cdot 10^{4}$ ($1.3 \cdot 10^{4}$)
Ni-59	$1.122 \cdot 10^{4}$ ($1.3 \cdot 10^{4}$)	$1.122 \cdot 10^{4}$ ($1.3 \cdot 10^{4}$)
Se-79	$1.163 \cdot 10^{4}$ ($1.3 \cdot 10^{4}$)	$1.163 \cdot 10^{4}$ ($1.3 \cdot 10^{4}$)
Sr-90	$3.441 \cdot 10$ ($3.1 \cdot 10^{2}$)	$3.442 \cdot 10$ ($3.1 \cdot 10^{2}$)
Nb-93m	$1.393 \cdot 10^{3}$ ($7.2 \cdot 10^{3}$)	$1.392 \cdot 10^{3}$ ($7.2 \cdot 10^{3}$)
Mo-93	$1.198 \cdot 10^{4}$ ($7.2 \cdot 10^{3}$)	$1.198 \cdot 10^{4}$ ($7.2 \cdot 10^{3}$)
Tc-99	$3.402 \cdot 10^{-3}$ ($1.3 \cdot 10^{4}$)	$3.400 \cdot 10^{-3}$ ($1.3 \cdot 10^{4}$)
Pd-107	8.906 ($1.3 \cdot 10^{4}$)	8.904 ($1.3 \cdot 10^{4}$)
Ag-108m	$2.706 \cdot 10^{4}$ ($1.2 \cdot 10^{3}$)	$2.706 \cdot 10^{4}$ ($1.2 \cdot 10^{3}$)
I-129	$2.625 \cdot 10^{3}$ ($1.3 \cdot 10^{4}$)	$2.625 \cdot 10^{3}$ ($1.3 \cdot 10^{4}$)
Cs-135	$2.319 \cdot 10^{4}$ ($1.3 \cdot 10^{4}$)	$2.318 \cdot 10^{4}$ ($1.3 \cdot 10^{4}$)
Cs-137	8.787 ($3.1 \cdot 10^{2}$)	8.786 ($3.1 \cdot 10^{2}$)

The detailed review and comparison of the Project SAFE near-field model identified some discrepancies in the implementation of the models and documentation which have been corrected here and are summarised in Appendix A. Also contained in Appendix A are some other changes that have been made to the bitumen release model and the level of discretisation used within the geosphere model.

3.3 Configuration of AMBER models for SAR-08

The starting point for the near-field and geosphere models for SAR-08 is the conceptual models previously described for Project SAFE /Lindgren et al. 2001, Thomson et al. 2008/ that are informed by the SAR-08 calculation cases described in Chapter 2.

This section presents the data used in the configuration of AMBER for SAR-08 to implement the SAR-08 calculation cases described in Chapter 2.

3.3.1 Near-field

Repository dimensions and materials

The repository dimensions reported in the SAFE Data report /SKB 2001b/ and those used in the safety assessment calculations undertaken in Project SAFE /Lindgren et al. 2001/ are used here.

The mixing proportions of the cementitious materials and structural concrete are assumed to be identical to those reported in the SAFE Data report /SKB 2001b/. The base of the Silo uses a mixture of 90% sand 10% bentonite as a backfill and in line with Project SAFE it is assumed that the same mixture will be used above the facility on closure. It is also assumed that sand and/or gravel with be used as a backfill in other areas of the Silo and disposal tunnels.

Disposal inventories

Estimates of the radionuclide inventory that will be emplaced in SFR 1 at repository closure have been undertaken for 59 radionuclides /Almkvist and Gordon 2007/. However, it is expected that not all of these radionuclides will be important in the evaluation of the safety of the repository (due to differences in half-life, mobility, bioavailability, radiotoxicity etc…).

Therefore a preliminary screening exercise has been undertaken to focus the main set of calculations on a subset which comprises those radionuclides considered to be the most important with regards to the overall safety of SFR 1. This is reported in Appendix B.

The 24 radionuclides screened for consideration within the near-field and geosphere calculations are reported below in Table 3-2. Comments are also provided on specifics of their treatment, where necessary. For example,

- Sr-90 decays to Y-90 which has a half-life of 64.1 hours and it is therefore not considered necessary to include this decay chain within the near-field and geosphere calculations.
- Pu-239 is part of the 4N+3 Series (decaying to U-235, its parent is Am-243)
  Decay of Pu-239 (it would take in excess of 240,000 y to achieve 10 half-lives) adds < 1% to U-235 inventory which is insufficient to increase U-235 above the screening cut-off. Inclusion of U-235 and its daughters is therefore not considered necessary.

Within SAR-08 two different disposal inventories are to be considered

- The revised reference disposal inventory (“Akt 2040”)

The reference disposal inventory which is used in all the calculation cases (except CC3) is based on 50 years of reactor operations /Almkvist and Gordon 2007/. Radionuclides highlighted in italics are not included in the calculations. The treatment of these radionuclides has been discussed previously in Table 3-2.

Table 3-2. Short-list of radionuclides for consideration within near-field and geosphere calculations of SAR-08.

Radionuclide	Comment
H-3	
C-14	Organic and inorganic forms both considered
Cl-36	
Ni-59	
Co-60	
Ni-63	
Se-79	
Sr-90	Decay chain not required.
Mo-93	
Nb-94	
Tc-99	
Ag-108m	
Sn-126	
I-129	
Cs-135	
Cs-137	Decay chain not required.
Ho-166m	
Np-237	
Pu-239, Pu-242	Decay chains not required.
Pu-240	Add Cm-244 disposal inventory. Decay chain not required.
Am-241	Add Pu-241 disposal inventory. Include decay to Np-237.
Am-243	Include decay to Pu-239.

The reference disposal inventory has been subject to a continuing programme of review and update and during the course of the SAR-08 safety calculations a revised reference disposal inventory was developed in which the data for a small number of radionuclides was updated; C-14, Cl-36, Mo-93, Tc-99, I-129, Cs-135. In Table 3-3 the revised inventory is given. After the completion of the radionuclide transport calculations the inventory for Cs-135 was reviewed again. This change is not reflected in this report, but accounted for in the dose assessment /Bergström et al. 2008/.

- Alternative disposal inventory (“Fullt Förvar”).

The alternative disposal inventory is used calculation case CC3 and is the maximum allowable under the licence conditions, Table 3-4 taken from /Almkvist and Gordon 2007/.

Two fundamental assumptions have been made regarding the disposal inventories:

- The radionuclides are distributed similarly to Project SAFE. Np-237 and Am-243 were not included within Project SAFE and are assumed to be distributed identically to Pu-239.
- The facilities are volumetrically full.

Table 3-3. Revised reference disposal inventory (Bq) based on 50 years of reactor operations.

Radionuclide	Silo	BMA	1 BTF	2 BTF	BLA
H-3	$3.49 \cdot 10^{10}$	$3.78 \cdot 10^{9}$	$1.63 \cdot 10^{8}$	$3.96 \cdot 10^{8}$	$2.19 \cdot 10^{7}$
C-14 organic	$1.39 \cdot 10^{12}$	$3.19 \cdot 10^{11}$	$7.39 \cdot 10^{9}$	$5.55 \cdot 10^{10}$	$1.16 \cdot 10^{9}$
C-14 inorganic	$3.23 \cdot 10^{12}$	$7.45 \cdot 10^{11}$	$1.73 \cdot 10^{10}$	$1.30 \cdot 10^{11}$	$2.70 \cdot 10^{9}$
Cl-36	$1.08 \cdot 10^{9}$	$2.31 \cdot 10^{8}$	$1.06 \cdot 10^{7}$	$3.08 \cdot 10^{7}$	$1.04 \cdot 10^{6}$
Ni-59	$7.31 \cdot 10^{12}$	$2.09 \cdot 10^{12}$	$2.09 \cdot 10^{10}$	$4.16 \cdot 10^{10}$	$5.26 \cdot 10^{9}$
Co-60	$8.54 \cdot 10^{13}$	$7.00 \cdot 10^{12}$	$2.87 \cdot 10^{11}$	$3.71 \cdot 10^{11}$	$3.57 \cdot 10^{10}$
Ni-63	$8.86 \cdot 10^{14}$	$2.59 \cdot 10^{14}$	$2.31 \cdot 10^{12}$	$2.80 \cdot 10^{12}$	$6.61 \cdot 10^{11}$
Se-79	$1.03 \cdot 10^{9}$	$2.14 \cdot 10^{8}$	$5.95 \cdot 10^{6}$	$2.35 \cdot 10^{7}$	$4.93 \cdot 10^{5}$
Sr-90	$1.08 \cdot 10^{13}$	$1.69 \cdot 10^{12}$	$6.44 \cdot 10^{10}$	$2.08 \cdot 10^{11}$	$4.69 \cdot 10^{9}$
Mo-93	$2.86 \cdot 10^{9}$	$6.84 \cdot 10^{8}$	$4.41 \cdot 10^{7}$	$8.90 \cdot 10^{7}$	$2.00 \cdot 10^{7}$
Nb-94	$1.61 \cdot 10^{10}$	$3.60 \cdot 10^{9}$	$8.46 \cdot 10^{7}$	$4.16 \cdot 10^{8}$	$1.32 \cdot 10^{7}$
Tc-99	$3.58 \cdot 10^{11}$	$3.72 \cdot 10^{10}$	$6.96 \cdot 10^{9}$	$7.61 \cdot 10^{9}$	$4.98 \cdot 10^{8}$
Ag-108m	$9.19 \cdot 10^{10}$	$2.00 \cdot 10^{10}$	$4.84 \cdot 10^{8}$	$2.32 \cdot 10^{9}$	$4.16 \cdot 10^{8}$
Sn-126	$1.28 \cdot 10^{8}$	$2.68 \cdot 10^{7}$	$7.43 \cdot 10^{5}$	$2.94 \cdot 10^{6}$	$6.16 \cdot 10^{4}$
I-129	$8.08 \cdot 10^{8}$	$1.83 \cdot 10^{8}$	$3.07 \cdot 10^{6}$	$1.90 \cdot 10^{7}$	$3.14 \cdot 10^{5}$
Cs-135*	$1.23 \cdot 10^{9}$	$8.89 \cdot 10^{7}$	$8.53 \cdot 10^{6}$	$1.07 \cdot 10^{7}$	$3.24 \cdot 10^{5}$
Cs-137	$1.12 \cdot 10^{14}$	$2.04 \cdot 10^{13}$	$6.67 \cdot 10^{11}$	$1.84 \cdot 10^{12}$	$4.84 \cdot 10^{10}$
Ho-166m	$7.04 \cdot 10^{9}$	$1.63 \cdot 10^{9}$	$5.85 \cdot 10^{7}$	$1.87 \cdot 10^{8}$	$1.67 \cdot 10^{7}$
Np-237	$1.30 \cdot 10^{8}$	$2.52 \cdot 10^{7}$	$4.06 \cdot 10^{5}$	$1.93 \cdot 10^{6}$	$2.67 \cdot 10^{4}$
Pu-239	$8.94 \cdot 10^{9}$	$1.98 \cdot 10^{9}$	$1.49 \cdot 10^{8}$	$1.99 \cdot 10^{8}$	$1.30 \cdot 10^{7}$
Pu-240	$1.79 \cdot 10^{10}$	$3.95 \cdot 10^{9}$	$2.98 \cdot 10^{8}$	$3.98 \cdot 10^{8}$	$2.61 \cdot 10^{7}$
Pu-241	$6.63 \cdot 10^{11}$	$1.39 \cdot 10^{11}$	$7.54 \cdot 10^{9}$	$8.60 \cdot 10^{9}$	$4.84 \cdot 10^{8}$
Pu-242	$7.89 \cdot 10^{7}$	$2.31 \cdot 10^{7}$	$1.49 \cdot 10^{6}$	$1.61 \cdot 10^{6}$	$8.99 \cdot 10^{4}$
Am-241	$4.89 \cdot 10^{11}$	$6.90 \cdot 10^{9}$	$8.42 \cdot 10^{8}$	$4.86 \cdot 10^{8}$	$5.02 \cdot 10^{7}$
Am-243	$8.37 \cdot 10^{8}$	$2.32 \cdot 10^{8}$	$1.48 \cdot 10^{7}$	$1.59 \cdot 10^{7}$	$8.96 \cdot 10^{5}$
Cm-244	$8.50 \cdot 10^{9}$	$1.35 \cdot 10^{9}$	$1.02 \cdot 10^{8}$	$1.13 \cdot 10^{8}$	$2.18 \cdot 10^{7}$

*The inventory of Cs-135 has been altered after the completion of the radionuclide transport calculations.

3.3.2 Near-field flow fields

This section describes the use of hydrogeological data to represent the migration of radionuclides within the SFR 1 disposal facilities.

The near-field flow fields in AMBER comprise the following datasets.

- The basic flow fields used in Project SAFE /Holmén and Stigsson 2001ab, SKB 2001b/.
- The uncertainty in the calibration of the supporting hydrogeological models /Holmén 2005, 2007/.
- The degradation of the engineered near-field barriers /Holmén and Stigsson 2001ab/.
- The long-term hydrogeological response to environmental change /Vidstrand et al. 2007/.

Table 3-4. Maximum disposal inventory (Bq) allowable under licence conditions.

Radionuclide	Silo	BMA	1 BTF	2 BTF	BLA
H-3	$2.42 \cdot 10^{11}$	$2.62 \cdot 10^{10}$	$1.13 \cdot 10^{9}$	$2.75 \cdot 10^{9}$	$1.52 \cdot 10^{8}$
C-14 organic	$9.61 \cdot 10^{12}$	$2.22 \cdot 10^{12}$	$1.20 \cdot 10^{11}$	$3.85 \cdot 10^{11}$	$8.05 \cdot 10^{9}$
C-14 inorganic	$2.24 \cdot 10^{13}$	$5.17 \cdot 10^{12}$	$5.14 \cdot 10^{10}$	$8.98 \cdot 10^{11}$	$1.88 \cdot 10^{10}$
Cl-36	$7.53 \cdot 10^{9}$	$1.61 \cdot 10^{9}$	$7.34 \cdot 10^{7}$	$2.13 \cdot 10^{8}$	$7.18 \cdot 10^{6}$
Ni-59	$5.07 \cdot 10^{13}$	$1.45 \cdot 10^{13}$	$1.99 \cdot 10^{12}$	$2.89 \cdot 10^{11}$	$3.65 \cdot 10^{10}$
Co-60	$5.93 \cdot 10^{14}$	$4.86 \cdot 10^{13}$	$1.45 \cdot 10^{11}$	$2.58 \cdot 10^{12}$	$2.48 \cdot 10^{11}$
Ni-63	$6.15 \cdot 10^{15}$	$1.80 \cdot 10^{15}$	$1.61 \cdot 10^{13}$	$1.95 \cdot 10^{13}$	$4.59 \cdot 10^{12}$
Se-79	$7.14 \cdot 10^{9}$	$1.49 \cdot 10^{9}$	$4.13 \cdot 10^{7}$	$1.63 \cdot 10^{8}$	$3.42 \cdot 10^{6}$
Sr-90	$7.52 \cdot 10^{13}$	$1.17 \cdot 10^{13}$	$4.47 \cdot 10^{11}$	$1.44 \cdot 10^{12}$	$3.25 \cdot 10^{10}$
Mo-93	$1.99 \cdot 10^{10}$	$4.75 \cdot 10^{9}$	$3.06 \cdot 10^{8}$	$6.17 \cdot 10^{8}$	$1.38 \cdot 10^{8}$
Nb-94	$1.12 \cdot 10^{11}$	$2.50 \cdot 10^{10}$	$5.88 \cdot 10^{8}$	$2.89 \cdot 10^{9}$	$9.19 \cdot 10^{7}$
Tc-99	$2.50 \cdot 10^{12}$	$2.59 \cdot 10^{11}$	$4.83 \cdot 10^{10}$	$5.28 \cdot 10^{10}$	$3.46 \cdot 10^{9}$
Ag-108m	$6.38 \cdot 10^{11}$	$1.39 \cdot 10^{11}$	$3.36 \cdot 10^{9}$	$1.61 \cdot 10^{10}$	$2.88 \cdot 10^{9}$
Sn-126	$8.92 \cdot 10^{8}$	$1.86 \cdot 10^{8}$	$5.16 \cdot 10^{6}$	$2.04 \cdot 10^{7}$	$4.28 \cdot 10^{5}$
I-129	$5.60 \cdot 10^{9}$	$1.27 \cdot 10^{9}$	$2.14 \cdot 10^{7}$	$1.31 \cdot 10^{8}$	$2.18 \cdot 10^{6}$
Cs-135*	$8.55 \cdot 10^{9}$	$6.62 \cdot 10^{6}$	$5.93 \cdot 10^{7}$	$7.44 \cdot 10^{7}$	$2.25 \cdot 10^{6}$
Cs-137	$7.78 \cdot 10^{14}$	$1.41 \cdot 10^{14}$	$4.63 \cdot 10^{12}$	$1.28 \cdot 10^{13}$	$3.36 \cdot 10^{11}$
Ho-166m	$4.89 \cdot 10^{10}$	$1.13 \cdot 10^{10}$	$4.06 \cdot 10^{8}$	$1.30 \cdot 10^{9}$	$1.16 \cdot 10^{8}$
Np-237	$9.03 \cdot 10^{8}$	$1.75 \cdot 10^{8}$	$2.82 \cdot 10^{6}$	$1.34 \cdot 10^{7}$	$1.85 \cdot 10^{5}$
Pu-239	$6.21 \cdot 10^{10}$	$1.37 \cdot 10^{10}$	$1.03 \cdot 10^{9}$	$1.38 \cdot 10^{9}$	$9.06 \cdot 10^{7}$
Pu-240	$1.24 \cdot 10^{11}$	$2.75 \cdot 10^{10}$	$2.07 \cdot 10^{9}$	$2.77 \cdot 10^{9}$	$1.81 \cdot 10^{8}$
Pu-241	$4.60 \cdot 10^{12}$	$9.66 \cdot 10^{11}$	$5.23 \cdot 10^{10}$	$5.97 \cdot 10^{10}$	$3.36 \cdot 10^{9}$
Pu-242	$5.48 \cdot 10^{8}$	$1.60 \cdot 10^{8}$	$1.04 \cdot 10^{7}$	$1.12 \cdot 10^{7}$	$6.24 \cdot 10^{5}$
Am-241	$3.55 \cdot 10^{12}$	$8.01 \cdot 10^{10}$	$7.59 \cdot 10^{9}$	$3.37 \cdot 10^{9}$	$3.48 \cdot 10^{8}$
Am-243	$5.81 \cdot 10^{9}$	$1.61 \cdot 10^{9}$	$1.03 \cdot 10^{8}$	$1.10 \cdot 10^{8}$	$6.22 \cdot 10^{6}$
Cm-244	$5.90 \cdot 10^{10}$	$9.40 \cdot 10^{9}$	$7.08 \cdot 10^{8}$	$7.82 \cdot 10^{8}$	$1.52 \cdot 10^{8}$

*The inventory of Cs-135 has been altered after the completion of the radionuclide transport calculations.

Project SAFE flow fields

The groundwater flow rate through the different repository parts of SFR 1 was estimated during Project SAFE and is discussed in detail elsewhere /Holmén and Stigsson 2001a/. The total groundwater flow rate through the different repository parts of SFR 1 as estimated in the detailed hydrogeology modelling during Project SAFE is given in Table 3-5. The results from the detailed hydrogeology modelling were then adjusted in accordance with the discretisation used in the near-field model /Holmén and Stigsson 2001b/. This data was then transferred as input data to the near-field model such that a three-dimensional water flow is assigned to each compartment in the model. The representation of this within AMBER has been previously described /Thomson et al. 2008/.

There is uncertainty in the calibration of the hydrogeological models used to the support the groundwater flow fields that were derived in Project SAFE. Therefore a study was undertaken to investigate the uncertainty in the calibration and assess its potential impacts on the data reported in Table 3-5 /Holmén 2005/.

Table 3-5. Total groundwater flow rates through disposal facilities calculated during Project SAFE.

Disposal facility	Total groundwater flow rates [m³/y] years post-closure			
	0	1,000	2,000	3,000
Silo: top backfill	0.53	1.4	2.2	2.2
Silo: Encapsulation	0.23	0.22	0.16	0.23
BMA: Encapsulation	0.07	0.13	0.26	0.28
BMA: Total	8.7	36.7	52.7	54.7
1BTF Waste	2.4	2.7	6.8	7.8
1BTF Total	7.5	19.4	26.4	30.7
2BTF Waste	2.4	3.0	6.0	6.8
2BTF Total	6.7	17.6	27.7	29.6
BLA: Waste	9.6	19.4	35.0	38.4
BLA: Total	13.6	33.1	50.2	54.2

The uncertainties that were identified for consideration included /Holmén 2005/.

- Uncertainty in the conductivity and heterogeneity of the rock mass between fracture zones.
- Uncertainty in the transmissivity of local and regional fracture zones.
- Uncertainty in the properties of a hydraulic skins that surrounds the tunnels.
- Uncertainty in the measured inflow of groundwater to the SFR 1 tunnels.
- Uncertainty in the combination of the above.

The study adopted what it termed an inverse modelling approach where random realisations where generated from plausible datasets and the realisations that produced an acceptable match to measured tunnel inflow were accepted.

Values of near-field uncertainty factors (*"U-factors"*) resulting from the inverse modelling study have been provided for each disposal facility (i.e. Silo, BMA, 1BTF, 2BTF, BLA) for closure and 2,000 years post-closure /Holmén 2005, 2007/. The U-factors are a simple means of relating the results of the calibration uncertainty study to the corresponding values in the original model /Holmén 2005/[7]. These values are the 60 accepted realisations that passed the constraining tests in the study. These data are used directly in the SAR-08 calculations to modify the near-field flow fields by multiplying the basic Project SAFE flow fields /Holmén 2005, 2007/.

Median values of the U-factors are given in Table 3-6. The U-factors for closure are assumed to be valid for the period from closure up to 2,000 years post-closure, when the values for 2,000 years post-closure become valid.

The median value of U-factors for the Silo in Table 3-6 will result in slightly reduced rates of groundwater flow through the facility for closure relative to Project SAFE and little change for 2,000 years post-closure. Similarly the values for the BMA are increased closure and 2,000 years post-closure and so will both result in a relative increase in flows compared to Project SAFE. Data for the BTF and BLA tunnels will result in flows that are little changed at closure and increased at 2,000 years post-closure.

However, it is important to note that the data reported in Table 3-6 are the median values. Further information on the distributions of data can be found in Appendix D.

[7] The U-factors are calculated as the flow from the inverse modelling study divided by the flow from the original Project SAFE model.

Table 3-6. Median values of uncertainty factors calculated from /Holmén 2007/.

Disposal facility	U-factors [–] years post-closure	
	0	2,000
Silo	0.69	0.97
BMA	3.4	3.4
1BTF	0.90	4.9
2BTF	0.85	4.0
BLA	1.0	3.6

Representation of barrier failure

Within SAR-08 the consideration of the evolution of the engineered barrier is to be assessed, including the failure of the barriers. The basic near-field flow fields considered within Project SAFE are valid only for intact barriers and therefore there is a need to assess radionuclide migration from the disposal facilities following the failure of the barriers (and tunnel plugs).

The hydrogeological modelling studies carried out in support of Project SAFE included a case in which the Silo barriers were considered to have failed (but the plugs were considered to remain intact). The side walls and associated bentonite backfill were considered to either be breached or to have collapsed. The flow fields developed for this case could therefore be used to represent a failed Silo for the purposes of the SAR-08 assessment. However, in order to do this it is necessary to convert the reported flow fields /Holmén and Stigsson 2001a/ to those required for input to AMBER (i.e. using a similar technique to that used to derive the NUCFLOW input). This is described in more detail in Appendix E.

Table 3-7 provides a comparison of the axial and radial flow components through the Silo for the base case at Closure and the failed case at Closure and 3,000 years post-closure based on data from the hydrogeological modelling studies /Holmén and Stigsson 2001a/. It can be seen that for the failed Silo case the flow direction is still estimated to be dominantly in the vertical direction at Closure, whereas at 3,000 years post-closure the dominant direction appears to be horizontally. The results for the failed case at Closure seems to be consistent with the general findings that when the Silo is beneath the sea bed the small hydraulic gradients result in low magnitude groundwater flow vertically upwards. The results for the failed case at 3,000 years post-closure reflect both the changes in regional groundwater flow patterns to a more horizontal orientation with larger gradients and also the absence of the low permeability Silo structures (which moderate the regional groundwater flow in the intact base case simulation in /Holmén and Stigsson 2001a/).

Within the hydrogeological modelling studies /Holmén and Stigsson 2001a/ sensitivity studies were also undertaken in which sections of the BMA and 1BTF were assumed to have failed in the areas that they are intersected by a near vertical NNW striking fracture zone (zone 6). The simulations that were undertaken considered that the hydraulic conductivities of these sections were increased to 10^{-5} m s^{-1} in all directions. It is important to note therefore that these studies considered that an isolated section of a tunnel was breached, not the entire tunnel.

Table 3-7. Comparison of flow components [m^3 y^{-1}] for intact and failed Silo.

	Axial flow		Radial flow	
	K–1	K+1	Inflow	Outflow
Intact: Closure	1.86	–2.11	0.27	–0.011
Failed: Closure	3.57	–3.80	0.53	–0.30
Failed: 3,000 years post-closure	–2.07	0.48	2.96	–1.37

Table 3-8 provides a summary of groundwater flow components for the BMA base case and the partially failed case. The data in Table 3-8 report the total groundwater flows through the encapsulation (i.e. areas with waste) and also the total flow through the tunnel. A more detailed breakdown of flow through different parts of the encapsulation is given for the partially failed case.

The total flow through the encapsulation is around 30–40 times higher for the partially breached case with over 95% flow through the encapsulation occurring within the breached section. However, the overall total tunnel flow is unaltered for both cases suggesting that the groundwater is simply re-routed through different sections of the tunnel.

Table 3-9 provides a summary of groundwater flow components for the 1BTF base case and the partially failed case. Two cases for 1BTF were considered, the second case is considered here which includes the failure of the encapsulation, floor and side fillings. The data reported is the same as presented previously for the BMA.

The total flow through the encapsulation is around 5–6 times higher for the partially breached case with over 50% flow through the encapsulation occurring within the breached section. The overall total tunnel flow is higher for the partially breached case but by less than a factor of 2.

Table 3-8. Comparison of groundwater flow components [$m^3\ y^{-1}$] for intact base case and partially failed BMA.

	Years post-closure			
	0	1,000	2,000	3,000
Base case (intact)				
Encapsulation	0.07	0.13	0.26	0.28
Tunnel flow	8.7	36.7	52.7	54.7
Failed containment in section 12				
Intact parts of encapsulation	0.04	0.16	0.29	0.30
Breached part of encapsulation	2.4	3.7	9.2	10.1
All encapsulation	2.4	3.86	9.5	10.4
Tunnel flow	8.7	36.6	52.6	54.6
Ratio Failed:Base case	1.0	1.0	1.0	1.0

Table 3-9. Comparison of groundwater flow components [$m^3\ y^{-1}$] for base case and failed 1BTF.

	Years post-closure			
	0	1,000	2,000	3,000
Base case (intact)				
Encapsulation	2.4	2.7	6.8	7.8
Tunnel flow	7.5	19.4	26.4	30.7
Failed containment				
Intact parts of encapsulation	1.2	1.9	4.0	4.7
Breached part of encapsulation	12.0	15.1	30.7	33.9
All encapsulation	13.2	17.0	34.7	38.6
Tunnel flow	14.5	24.1	45.0	50.2
Ratio Failed:Base case	1.94	1.24	1.71	1.64

The simple approach adopted within SAR-08 for the BMA and BTF disposal facilities uses a multiplier as a means of enhancing the rate of flow through the whole system with the primary purpose of increasing flow rates and the removal of radionuclides from the waste. This is schematically shown in Figure 3-2 (the relative thicknesses of the arrows signifying advective transport represent areas of relatively higher and lower flow rates).

The values used in the calculations are summarised below in Table 3-10 and are applied in each calculation at the facility–dependent time at which failure is considered (e.g. in CC1 66,000 years post-closure for the Silo, 42,000 years post-closure for the BMA and 1,000 years post-closure for 1BTF and 2BTF).

It should be noted that for the BMA a value of 30 is considered to be conservative in terms of radionuclide release. This is due to the fact that following the failure of the BMA encapsulations. However, it may be argued that this represents an appropriate means of estimating the potential consequences of such a failure as the radionuclide flux from the near-field may be considered to be an overestimate.

Table 3-10. Tunnel flow factors for degraded barriers.

	Flow factor (–)	Comment
Silo	–	Alternative flow fields derived, see text and Appendix E.
BMA	30	Based on potential increases in groundwater flow rate through the encapsulation area that would result in flows through the waste comparable to those in 1BTF.
1BTF	2	Assumes breached encapsulation, floor and side filling. Long term average value.
2BTF	2	Assumed to be the same as 1BTF.
BLA	–	No barriers considered within BLA.

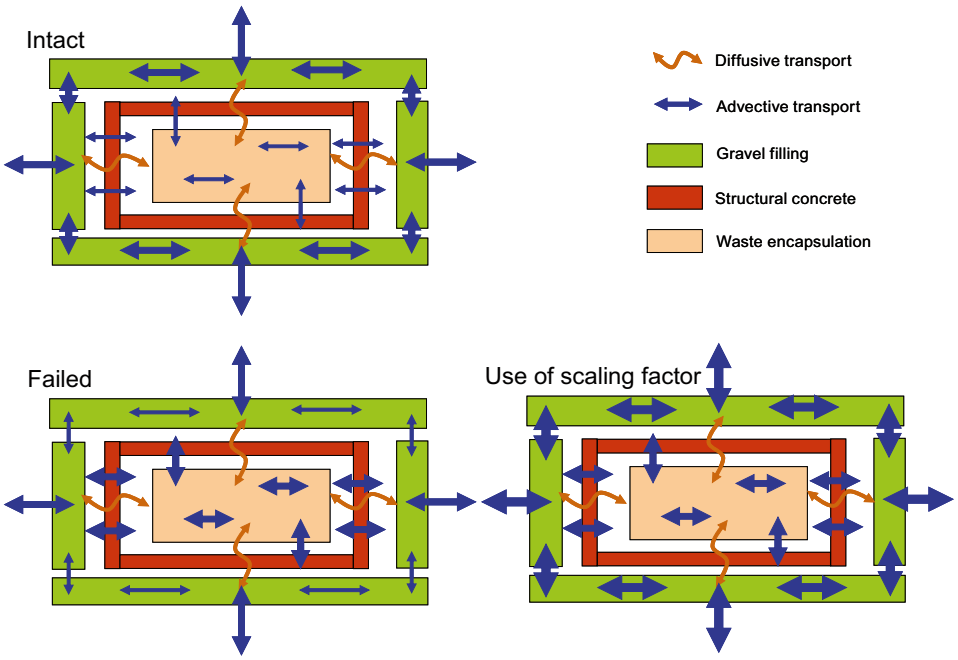

Figure 3-2. *Schematic representation of simplified approach to barrier failure.*

The hydrogeological modelling studies /Holmén and Stigsson 2001a/ also included an analysis of groundwater flows through the repository components following the failure of the tunnel plugs. The results of this analysis was used as basis to deriving scaling factors to represent the relative increase in total groundwater flow through the disposal facilities in a manner similar to that described above for the BMA and BTF to represent barrier failure. The facility-dependent values are summarised below in Table 3-11 and these are applied in the calculations from the point at which the plugs are assumed to fail (i.e. from 66,000 years onwards in CC1).

The appropriate values for the BMA, BTF and BLA tunnels are considered to be the long term relative tunnel flow. The value used for the Silo is the long term relative flow through the waste. This value is used in preference to the relative tunnel flow because Holmén and Stigsson /Holmén and Stigsson 2001a/ estimated that the majority of the flow in Silo was directed through the sand/gravel backfill above the Silo and therefore using the relative tunnel flow as a scaling factor for the Silo flow fields would overestimate the groundwater flow through the encapsulation.

Hydrogeological response to long-term environmental change

Previous hydrogeological studies in support of Project SAFE /Holmén and Stigsson 2001ab/ considered the evolution of the regional and local groundwater systems for several thousand years post-closure. However, subsequent studies have been carried out in order to estimate the potential changes to regional flow fields under changed climate conditions, in particular under colder climate conditions such as permafrost and glacial environments which can be applied to the original Project SAFE data as a multiplier /Vidstrand et al. 2007/. Values for the Weichselian, Greenhouse and Periglacial climate evolutions are tabulated in Tables 3-12, 3-13 and 3-14, respectively.

Impacts of bulk gas generation on flow fields

The final consideration for the near-field flow fields is the effect on groundwater flow from the generation of bulk gases within the Silo at increased rates which is considered in CC10 as a two step process. Firstly, in order for the gases to escape from the Silo it is necessary for them to expel porewater to create a migration route. Secondly, it is also necessary to create an overpressure in the Silo in order that the gas can migrate through the sand/bentonite layer above the Silo lid. An overpressure of 15–50 kPa has been estimated to be required /Moreno et al. 2001/ and calculations have been undertaken on the basis of 15 kPa which amounts to a lowering of the water level in the Silo by 1.5 m.

/Moreno et al. 2001/ estimated that during the initial stages 72.5 m^3 of porewater would be forced upwards through the Silo lid to expel water from gas evacuation pipes and sand immediately above and below the Silo lid. It was further concluded that the initial gas generations were sufficient for this expulsion to take place in the initial year following closure of the repository. A review of the inventory for SAR-08 suggests that sufficient gas generation is still possible for this step to take place in the initial year post-closure.

Table 3-11. Tunnel flow factors for degraded plugs.

	Flow factor (–)	Comment
Silo	1.3	Long term relative flow through waste
BMA	2	Long term relative waste flow
1BTF	2	Long term relative tunnel flow
2BTF	2	Long term relative tunnel flow
BLA	2	Long term relative tunnel flow

Table 3-12. Flow multipliers from long-term hydrogeological modelling studies for Weichselian climate evolution.

Climate domain	Time [kyears AP]	Comment
Temperate	0–8	Flow multiplier of 1 [–].
Periglacial, sporadic permafrost	8–10	
Temperate	10–23	
Periglacial, continuous permafrost	23–37	Flow multiplier of 0 [–] for CC1, as system assumed frozen and so no radionuclide transport is considered within the near-field or geosphere in CC1. Flow multiplier of 10 for CC2 [–].
Temperate	37–42	Flow multiplier of 1 [–].
Periglacial, continuous permafrost	42–56	Flow multiplier of 0 [–] for CC1, as system assumed frozen and so no radionuclide transport is considered within the near-field or geosphere in CC1. Flow multiplier of 10 for CC2 [–].
Glacial, ice sheet covered	56–66	Flow multiplier of 0.5 [–].
Submerged	66–75	Flow multiplier of 0.01 [–] from DarcyTools modelling used for tunnels. Value of 1 [–] used for the Silo and geosphere.*
Periglacial, continuous permafrost	75–91	Flow multiplier of 0 [–] for CC1, as system assumed frozen and so no radionuclide transport is considered within the near-field or geosphere in CC1. Flow multiplier of 10 for CC2 [–].
Glacial, ice sheet covered	91–109	Flow multiplier of 0.2 [–].

* Value of 1 used here for the Silo and geosphere models:
– The Silo has individual flow fields resolved for this time period which account for the location of the repository below the sea.
– The geosphere is configured to use the data which represent conditions at Closure.

Table 3-13. Flow multipliers from long-term hydrogeological modelling studies for the Greenhouse climate evolution.

Climate domain	Time [kyears AP]	Comment
Temperate	0–73	Flow multiplier of 1 [–].
Periglacial, continuous permafrost	73–100	Flow multiplier of 0 for CC1 [–], as system assumed frozen and so no radionuclide transport is considered.

Table 3-14. Chronological summary of climate domains for Periglacial climate evolution.

Climate domain	Time [kyears AP]	Comment
Temperate	0–8	Flow multiplier of 1 [–]
Periglacial, continuous permafrost	8–15	Flow multiplier of 0 [–] for CC7, as system assumed frozen and so no radionuclide transport is considered within the near-field or geosphere in CC7. Flow multiplier of 10 for CC8 [–]
Temperate	15–20	Flow multiplier of 1 [–]
Periglacial, continuous permafrost	20–37	Flow multiplier of 0 [–] for CC7, as system assumed frozen and so no radionuclide transport is considered within the near-field or geosphere in CC7. Flow multiplier of 10 for CC8 [–]
Temperate	37–41	Flow multiplier of 1 [–]
Periglacial, continuous permafrost	41–100	Flow multiplier of 0 [–] for CC7, as system assumed frozen and so no radionuclide transport is considered within the near-field or geosphere in CC7. Flow multiplier of 10 for CC8 [–]

/Moreno et al. 2001/ estimated that a further 60 m^3 of porewater would be require displacing from the Silo to reduce the water level by 1.5 m in order to create an overpressure of 15 kPa and to establish gas flow through the sand/bentonite above the Silo lid. This volume of water will be expelled through the base and sides of the Silo and requires 10 years to discharge (assuming a hydraulic conductivity of concrete of around 10^{-9} m/s).

Therefore in order to these groundwater fluxes in the Silo model for CC10 it was necessary to change some of groundwater flow parameters for the initial period. This is described further in Appendix E.

3.3.3 Near-field chemical data

No account is taken of solubility limits in the model, nor of radionuclides being inaccessible for dissolution in local water. Radionuclides stabilised in both cement and bitumen matrices are assumed to be immediately available for release, subject to sorption on local solid media.

Reference sorption coefficients

The sorption coefficients for concrete and cement and sand and gravel for all calculations except CC9 /Cronstrand 2005/ are shown below in Table 3-15. These values were input as log-triangular distributions.

The values for concrete and cement are representative of fresh materials and the parameter ranges are considered sufficient to include any changes to elements such as Ni and Cs under changes from saline to non-saline conditions.

Following the degradation of concrete and cement the sorption capacity will be reduced due to leaching of constituent materials which reduces the ability of the concrete and cement to maintain an alkaline pH which promotes the sorption of many species. Therefore values for sand and gravel will be used for the construction concrete and cement grout media when they are considered to have been degraded (e.g. in CC1 this is 66,000 years post-closure for the Silo, 42,000 years post-closure for the BMA and 1,000 years post-closure for BTF).

The Sorption coefficients for bentonite for all calculations except CC9 are those that were used in the SR-Can assessment for the system open to CO_2 /Ochs and Talerico 2004/. These values were derived for MX-80 bentonite but are considered to be applicable to GEKO/QI bentonite which is used within the SFR 1 as the buffer adjacent to the Silo side walls[8]. Values for the sand-bentonite mixture are calculated as a weighted average of the end member values (90% sand and 10% bentonite). These values are shown below in Table 3-16 and were input as log-triangular distributions[9].

Effects of complexing agents

This section presents a review of the effects of enhanced levels of complexants such as ISA on sorption coefficients in order to support the parameterisation of CC9.

[8] Following the washout of the side-wall bentonite by the retreating ice sheet within CC1 sorption onto bentonite is not considered.

[9] Values of 0 m^3/kg for Ag were assumed to be 10^{-10} m^3/kg for the purposes of defining the probability distribution function within AMBER.

Table 3-15. Sorption coefficients [m³/kg] for concrete and cement and sand and gravel.

	Concrete and cement			Sand and gravel		
	Min.	Max.	Recommended	Min.	Max.	Recommended
H	0	0	0	0	0	0
Inorganic C	0.01	4	0.2	0.00002	0.01	0.0005
Organic C	0	0	0	0	0	0
Cl	0.0006	0.06	0.006	0	0	0
Co	0.004	0.4	0.04	0.001	0.1	0.01
Ni	0.008	0.2	0.04	0.002	0.05	0.01
Se	0.0001	0.4	0.006	0.00001	0.03	0.0005
Sr	0.0005	0.05	0.001	0.00002	0.0005	0.0001
Mo	0.0001	0.4	0.006	0	0	0
Nb	0.1	2.5	0.5	0.1	2.5	0.5
Tc(IV)	0.05	5	0.5	0.03	3	0.3
Ag	0.00002	0.05	0.001	0.0002	0.5	0.01
Sn	0.025	10	0.5	0	0.01	0
I	0.0003	0.03	0.003	0	0	0
Cs	0.0001	0.01	0.001	0.001	0.12	0.01
Ho	1	25	5	0.2	5	1
Np(IV)	1	25	5	0.2	5	1
Pu(IV)	1	25	5	0.2	5	1
Am	0.2	5	1	0.2	5	1

Table 3-16. Sorption coefficients [m³/kg] for bentonite and sand and bentonite.

	Bentonite			Sand-Bentonite mixture		
	Min.	Max.	Recommended	Min.	Max.	Recommended
H	0	0	0	0	0	0
C (inorganic)	0	0	0	0.000018	0.009	0.00045
C (organic)	0	0	0	0	0	0
Cl	0	0	0	0	0	0
Co	0.03	3.3	0.3	0.0039	0.42	0.039
Ni	0.03	3.3	0.3	0.0048	0.375	0.039
Se	0.003	0.4	0.04	0.000309	0.067	0.00445
Sr	0.0009	0.031	0.005	0.000108	0.00355	0.00059
Mo	0	0	0	0	0	0
Nb	0.2	45	3	0.11	6.75	0.75
Tc	2.3	1,764	63	0.257	179	6.57
Ag	0	15	0	0.00018	1.95	0.009
Sn	2.3	1,764	63	0.23	176	6.3
I	0	0	0	0	0	0
Cs	0.018	0.6	0.11	0.0027	0.168	0.02
Ho	0.8	93	8	0.26	13.8	1.7
Np	4	1,113	63	0.58	116	7.2
Pu	4	1,111	63	0.58	116	7.2
Am	10	378	61	1.18	42.3	7

Tetravalent actinides

A few experimental studies exist on the complexation of tetravalent actinides by ISA and its effect on the increase of solubility and decrease in sorption. The list of experimental data available is not very long, although from some of the studies very interesting conclusions can be extracted. Most studies have been undertaken under hyper-alkaline media, which is due to the fact that the highest ISA concentrations are expected to occur in the low and intermediate level repositories, where concrete is a very common material used in the stabilisation and/or immobilisation of the waste.

Pu(IV)

/Greenfield et al. 1997/ studied the sorption of Pu(IV) onto NIREX Reference Vault Backfill (NRVB) material under hyperalkaline conditions. In the presence of 10^{-2} M of ISA, the authors determined a K_d value of 0.1 m^3/kg. Most of the experimental studies under these conditions are those conducted in the frame of the NIREX Safety Assessment Research Programme (NSARP).

Under similar experimental conditions but when no ISA is present in the system, Bayliss et al. /Bayliss et al. 1996/ obtained an average K_d value of 70 m^3/kg. This would imply a reduction factor of 700. Although some authors have reported a significant sorption of ISA onto cement phases this factor was not verified in the works here discussed.

The effect of ISA is expected to be higher in the absence of Ca in the medium, given that Ca forms the following complexes with ISA /Hummel et al. 2005/:

$Ca(ISA)^+$

Ca(OH)ISA(aq)

That compete for ISA in solution, although the calcium effect at Ca concentrations in the level of those in equilibrium with portlandite at pH = 12.5 are not important for ISA concentrations below 0.01 M (see Figure 3-3).

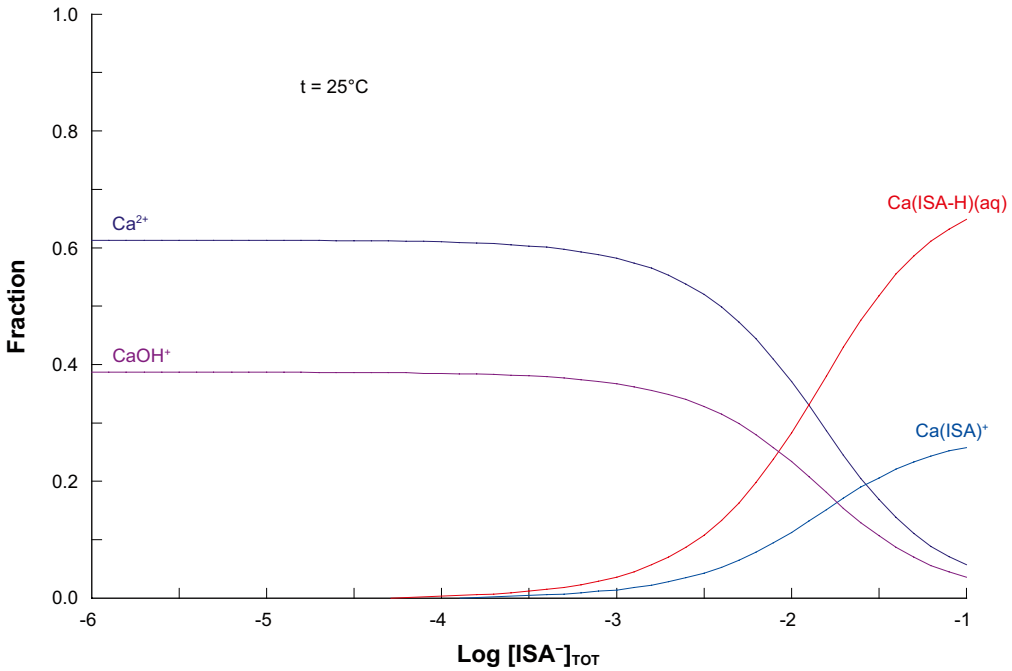

Figure 3-3. *Fractional diagram of the speciation of Ca when adding 0.01 M of Ca to the system.*

Np(IV)

/Vercammen et al. 2001/ studied the effect of ISA on the reduction of the sorption of Np(IV) onto cement by conducting sorption experiments in the presence and in the absence of Ca and at different pH values. They observed that for ISA concentrations of 0.01 M, the sorption reduction factors recommended are shown in Table 3-17.

The original reference quoted for the former values is /Rai et al. 1998/ and from review of the values we can see that Np(IV) is likely to be less affected by ISA complexation than Pu(IV).

Summary of reduction factors for tetravalent actinides

A summary of reduction factors for tetravalent actinides derived from experimental measurements is shown in Table 3-18.

A way of calculating a theoretical reduction factor for sorption at different ISA concentrations and at different pH values is to derive the speciation scheme of the radionuclides in the presence and in the absence of ISA. In principle, the reduction in the sorption of a given radionuclide when ISA is present will be due to the formation of Radionuclide–ISA complexes which compete with the hydrolysis and with the sorption reactions.

For tetravalent actinides, and under hyperalkaline conditions in the absence of ISA, the main aqueous species present in solution will be the neutral tetrahydroxo species $An(OH)_4(aq)$.

In the presence of ISA, species of the type $An(OH)_{(4-m)}(ISA)_n^{n-}$ may form. The stoichiometry, that is, the values of *m* and *n*, as well as the stability of the different species will depend on the studied actinide.

A preliminary selection of the stability of these species, based on the data available in the literature has been conducted, and values shown in Table 3-19 have been considered, in agreement with solubility and sorption data. The values of the stability constants given in Table 3-19 correspond to the reaction:

$$An(OH)_4(aq) + nISA^- + m\ H^+ = An(OH)_{(4-m)}(ISA)_n^{n-} + mH_2O \qquad \text{Equation 3-2}$$

With the associated reaction constants as expressed by Equation 3-3

$$K_n^m = \frac{[An(OH)_{4-m}(ISA)_n^{n-}]}{[An(OH)_4(aq)]\cdot[ISA^-]\cdot[H^+]} \qquad \text{Equation 3-3}$$

Table 3-17. Sorption reduction factors [–] for Np(IV) in the presence of 0.01 M ISA /Vercammen et al. 2001/.

pH	Np(IV) sorption reduction factors [–]
10.7	170
12	8.7
13.3	0.44

Table 3-18. Summary of experimental reduction factors for tetravalent actinides.

An(IV)	Reduction factor for [ISA] = 0.01 M	[ISA] = 10^{-4} M	Reference
Pu	1,000	3	/Greenfield et al. 1997, Bayliss et al. 1996, Rorif et al. 2004/.
Np	10		/Rai et al. 1998/.

Table 3-19. Speciation scheme used for tetravalent actinides in the presence of ISA.

Species	**$Np(OH)_3(ISA)(aq)$**	**$Np(OH)_3(ISA)_2^-$**	**$Np(OH)_4(ISA)^-$**	**$Np(OH)_4(ISA)_2^{2-}$**
Log*K*	11.57	13.68	4.1	6.1
Comment		Recalculated from /Rai et al. 2003/		
Species	**$Pu(OH)_3(ISA)(aq)$**	**$Pu(OH)_3(ISA)_2^-$**	**$Pu(OH)_4(ISA)^-$**	**$Pu(OH)_4(ISA)_2^{2-}$**
Log*K*	13.25	15.36	4.9	9.2
Comment	Estimated by correlation with tetravalent actinides		/Moreton et al. 2000/	

The total aqueous concentration of the actinide in the absence of ISA will be:

$$[An(IV)]_{aq}\,(withoutISA) = [An(OH)_4(aq)] \qquad \text{Equation 3-4}$$

While in the presence of ISA:

$$[An(IV)]_{aq}\,(withISA) = \left[[An(OH)_4(aq)] + \sum_{m,n}[An(OH)_{4-m}(ISA)_n^{n-}]\right] = \qquad \text{Equation 3-5}$$

$$= [An(OH)_4(aq)]\cdot\left(1 + \sum_{n,m} K_n^m [ISA^-]^n [H^+]^m\right)$$

Dividing Equation 3-5 by Equation 3-4 gives the ratio between the aqueous actinide in the presence over the absence of ISA, that is, a way of calculating the ratio between the K_d in the absence and the K_d in the presence of ISA, that is, a theoretical sorption reduction factor:

$$\frac{[An(IV)]_{aq}\,(withISA)}{[An(IV)]_{aq}\,(withoutISA)} = \left(1 + \sum_{n,m} K_n^m [ISA^-]^n [H^+]^m\right) \qquad \text{Equation 3-6}$$

and by calculating the value of Equation 3-6 for each actinide by using the selected constants shown in Table 3-19, we obtain the theoretical calculated sorption reduction factors shown in Table 3-20, from where a reasonable agreement is found when comparing with the experimental factors that have been presented in Table 3-18.

Table 3-20. Comparison between calculated sorption reduction factors and experimental values for tetravalent actinides.

pH	**[ISA]**	**Calculated sorption reduction factors**	**Experimental sorption reduction factors**
Pu(IV)			
12.5	10^{-4}	9	3
12.5	10^{-3}	80	
12.5	10^{-2}	795	1,000
Np(IV)			
12.5	10^{-4}	3	
12.5	10^{-3}	20	
12.5	10^{-2}	301	10

Am(III) and trivalent lanthanides

Tits et al. /Tits et al. 2005/ conducted a rather complete study on the complexation of Am by ISA. The influence of ISA on the sorption of Am onto the surface of calcite under hyperalkaline conditions was studied. The only Am-ISA species considered to form in solution was $Am(ISA_{-3H})^{-}$, which is equivalent to the following formulation:

$$Am^{3+} + 3\ H_2O + ISA^{-} = Am(OH)_3ISA^{-} + 3\ H^{+}$$

Tits et al. /Tits et al. 2005/ determined β_{AmISA} value by modelling sorption data, and obtained a value of $\log K = -21.4 \pm 1$ for the former reaction.

Taking into consideration the formation of the former species, the speciation of Am under hyperalkaline pH value at different ISA concentrations can be calculated (see Figure 3-4) from where it can be seen that the effect of ISA is important from concentrations as low as 10^{-5} M.

Nevertheless, if the same exercise is conducted for a ISA concentration of 10^{-4} M at different pH values (Figure 3-5), the ISA species is not important until pH values exceed 10, so that the reduction of the sorption of Am due to the presence of ISA would only be effective under alkaline conditions.

The maximum reduction factor for the sorption of Am onto cement under the presence of ISA by considering the system previously presented can be estimated in 500 for a concentration of ISA of 0.01 M.

/Rorif et al. 2004/ measured the effect of ISA on the sorption of Pu(IV) and Am(III) onto Boom Clay undisturbed and disturbed by an hyperalkaline plume. The maximum reduction factor for the sorption of Am(III) both onto undisturbed boom clay and under the hyperalkaline perturbed one was of 2.5 for ISA concentrations between 10^{-4} and 10^{-3} M.

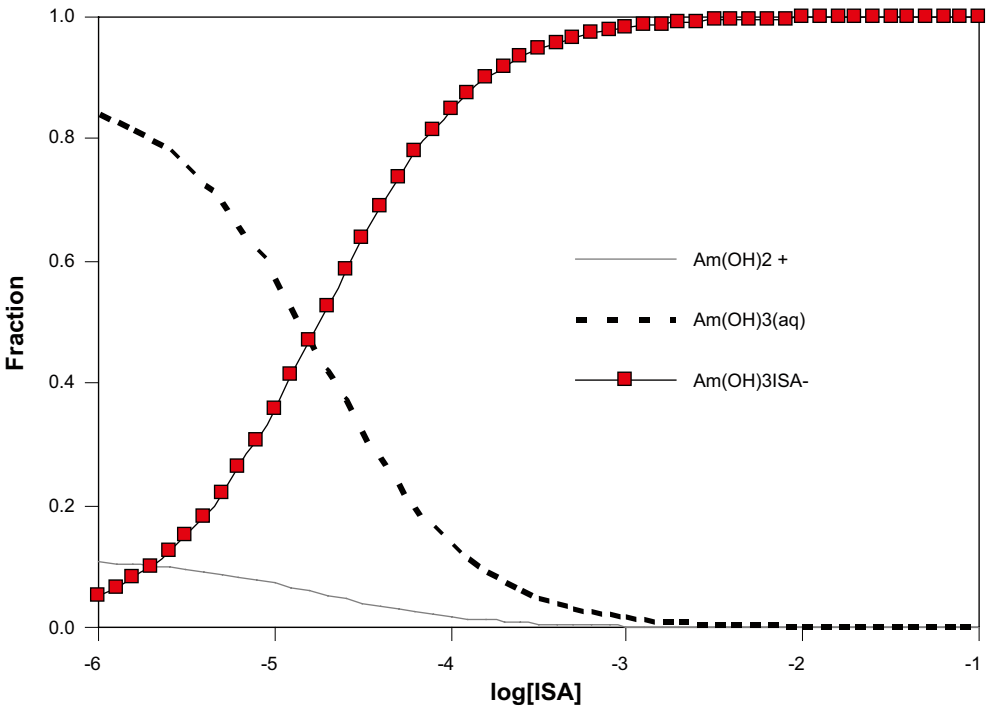

Figure 3-4. *Fractional diagram of Am aqueous species in the presence of different ISA concentrations at pH 12.5.*

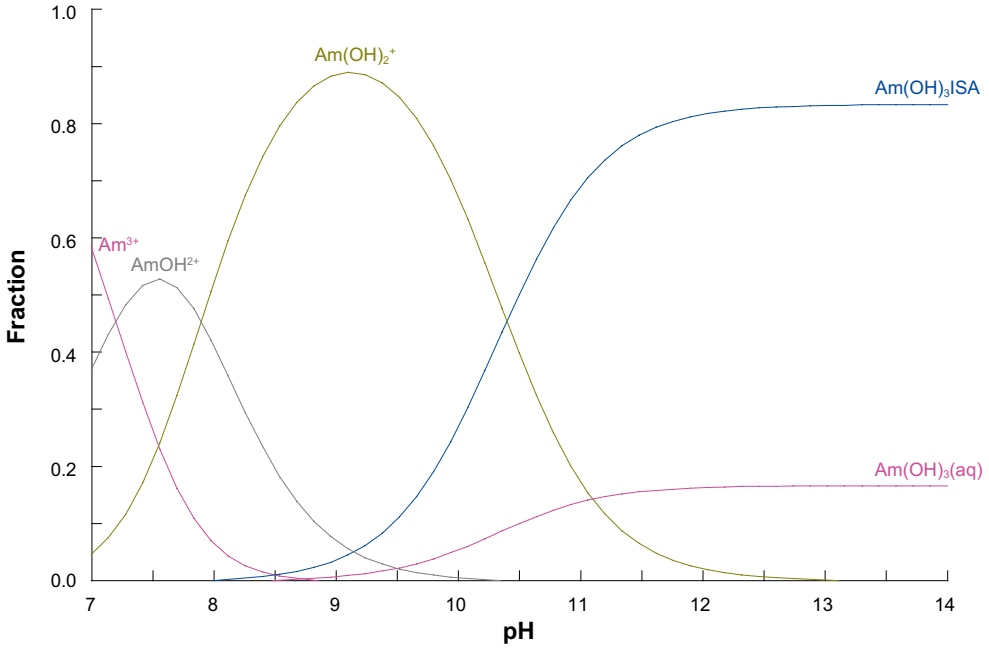

Figure 3-5. *Speciation of Am in the presence of 10^{-4} M ISA at different pH values.*

/Tits et al. 2005/ also studied the sorption of Eu onto cement under different ISA concentrations. The reduction factors obtained for a concentration of ISA of 10^{-2} M is of 1,000, while for a concentration of ISA of 10^{-4} M, a sorption reduction factor of 7 is obtained, which is in agreement with data reported by /Bradbury and Van Loon 1998/.

Following a similar approach to that described for the tetravalent actinides theoretical sorption reduction factors can be calculated for Am in the presence and in the absence of ISA we obtain the following values (Table 3-21). Again the data are considered show reasonable agreement given the uncertainties.

Divalent and monovalent metals

The influence of ISA on the sorption of divalent metals is not expected to be as important due to the lower stability of the complexes formed by ISA with divalent in comparison to those formed with tri- and tetravalent elements.

Data gathered by /Warwick et al. 2006/ indicated that the reduction factor for the sorption of Cobalt and Cadmium onto cement due to the presence of ISA was insignificant for ISA concentrations in the order of 10^{-4} M, and a maximum reduction of 1 order of magnitude in the sorption was observed for Co(II) when the ISA level was of 0.01 M.

Table 3-21. Comparison between calculated sorption reduction factors and experimental values for Am and Eu.

pH	[ISA]	Calculated sorption reduction factors	Experimental sorption reduction factors
		6	2.5 (Am) 7 (Eu)
12.5	10^{-4}	51	
12.5	10^{-3}	502	1,000 (Eu)
12.5	10^{-2}	6	2.5 (Am) 7 (Eu)

For the sorption of Ni onto cement, /Wieland et al. 1998/ observed no sorption reduction under a concentration of ISA of 10^{-4} M, and the same was suggested for Sr(II).

A concentration of 10^{-4} M of ISA in solution had no effect on the sorption of Cs(I) onto cement phases according to /Wieland et al. 1998/.

Conclusions on sorption reduction factors

The simplified approach presented previously could be used to assess the sorption reduction factor of any radionuclide onto different solid surfaces at different concentrations of organic complexants.

In Table 3-22 the values of K_d compiled in /Cronstrand 2005/, both recommended and minimum, are compared with the minimum K_d value resulting from applying the experimental reduction factors outlined above to the recommended K_d value in /Cronstrand 2005/. Bold data stands for original experimental values. The other values have been taken by chemical analogy.

In general, the minimum value in /Cronstrand 2005/ covers the ISA effect expected for an ISA concentration of 10^{-4} M. When considering circumstances with higher ISA concentrations (i.e. 0.01 M), such as in CC9, the K_d values should be decreased (highlighted in the table).

Table 3-22. Comparison between minimum K_d [kg/m^3] values recommended in /Cronstrand 2005/ for concrete and cement and those resulting from applying the experimental reduction factors.

		Best estimate /Cronstrand 2005/	Minimum value /Cronstrand 2005/	Sorption reduction factor	Comment
M(I)	H	0	0	n/a	No sorption considered
	Cs	0.001	0.0001	10	Based on Ag
	Ag	0.001	0.00002	10	Considered in initial parameter range
M(II)	Ni	0.04	0.008	10	Considered in initial parameter range
	Co	0.04	0.004	**10**	Considered in initial parameter range
	Sr	0.001	0.0005	10	Outwith initial parameter range
	Sn	0.5	0.025	10	Considered in initial parameter range
M(III)	Am	1	0.2	**500**	Outwith initial parameter range
	Ho	5	1	1,000	Based on Eu Outwith initial parameter range
M(IV)	Pu	5	1	**1,000**	Outwith initial parameter range
	Np	5	1	**10**	Outwith initial parameter range
	Tc	0.5	0.05	10	Considered in initial parameter range
	C	0.2	0.01	10	Considered in initial parameter range
M(V)	Nb	0.5	0.1	1	No significant reduction in sorption anticipated
M(VI)	Mo	0.006	0.0001	30	Considered in initial parameter range
M(-I)	Cl	0.006	0.0006	1	No significant reduction in sorption anticipated
	^{129}I	0.003	0.0003	1	No significant reduction in sorption anticipated
M(-II,IV,VI)	^{79}Se	0.006	0.0001	1	No significant reduction in sorption anticipated

Sorption reductions factors for sand and gravel and bentonite have also been considered as follows.

- Tetravalent elements considered to undergo a similar in reduction in sorption as observed for cement.
- Trivalent elements, such as Am, Ho and Eu would present lower influence of ISA at pH values below 9, especially in the presence of carbonate in the system, which is expected in the presence of bentonite and/or sand-gravel. Therefore, for trivalent elements, a reduction factor of 5 can be applied for waters with average carbonate contents of 0.001 M in the presence of 0.01 M ISA.
- Divalent elements are not expected to exhibit a reduction in sorption.
- Monovalent elements are not expected to exhibit a reduction in sorption.

Tables 3-23 and 3-24 summarise the best estimate and minimum values of sorption coefficient used within CC1 sand and gravel and bentonite, also indicating the sorption reduction factor in each instance for use in CC10.

The sorption reduction factors for CC9 are summarised in Table 3-25.

Table 3-23. Sorption coefficients [kg/m^3] and reduction factors for sand and gravel.

		Best estimate /Cronstrand 2005/	Minimum value /Cronstrand 2005/	Sorption reduction factor	Comment
M(I)	H	0	n/a	n/a	No sorption considered
	Cs	0.01	0.001	1	Considered in initial parameter range
	Ag	0.01	0.0002	1	Considered in initial parameter range
M(II)	Ni	0.01	0.002	1	Considered in initial parameter range
	Co	0.01	0.001	1	Considered in initial parameter range
	Sr	0.0001	0.00002	1	Considered in initial parameter range
	Sn	0	n/a	1	Considered in initial parameter range
M(III)	Am	1	0.2	5	Considered in initial parameter range
	Ho	1	0.2	5	Considered in initial parameter range
M(III,IV)	Pu	1	0.2	1,000	Outwith initial parameter range
M(IV)	Np	1	0.2	10	Outwith initial parameter range
	Tc	0.3	0.03	10	Considered in initial parameter range
	C	0.0005	0.00002	10	Considered in initial parameter range
M(V)	Nb	0.5	0.1	1	No significant reduction in sorption anticipated
M(VI)	Mo	0	n/a	n/a	No sorption considered
M(-I)	Cl	0	n/a	n/a	No sorption considered
	^{129}I	0	n/a	n/a	No sorption considered
M(-II,IV,VI)	^{79}Se	0.0005	0.00001	1	No significant reduction in sorption anticipated

Table 3-24. Sorption coefficients [kg/m^3] and reduction factors for bentonite.

		Best estimate /Cronstrand 2005/	Minimum value /Cronstrand 2005/	Sorption reduction factor	Comment
M(I)	H	0	n/a	n/a	No sorption considered
	Cs	0.11	0.018	10	Considered in initial parameter range
	Ag	0	n/a	n/a	No sorption considered
M(II)	Ni	0.3	0.03	1	Considered in initial parameter range
	Co	0.3	0.03	1	Considered in initial parameter range
	Sr	0.005	0.0009	1	Considered in initial parameter range
	Sn	63	2.3	1	Considered in initial parameter range
M(III)	Am	61	10	5	Considered in initial parameter range
	Ho	8	0.8	5	Considered in initial parameter range
M(III,IV)	Pu	63	4	1,000	Outwith initial parameter range
M(IV)	Np	63	4	10	Considered in initial parameter range
	Tc	63	2.3	10	Considered in initial parameter range
	C	0	n/a	n/a	No sorption considered
M(V)	Nb	3	0.2	1	No significant reduction in sorption anticipated
M(VI)	Mo	0	n/a	n/a	No sorption considered
M(-I)	Cl	0	n/a	n/a	No sorption considered
	^{129}I	0	n/a	n/a	No sorption considered
M(-II,IV,VI)	^{79}Se	0.04	0.003	1	No significant reduction in sorption anticipated

Table 3-25. Summary of sorption reduction factors [–] for CC9.

	Concrete and cement	Sand and gravel	Bentonite
H	1	1	1
C_in	10	10	10
C_org	1	1	1
Cl	1	1	1
Co	10	1	1
Ni	10	1	1
Se	1	1	1
Sr	10	1	1
Mo	30	1	1
Nb	1	1	1
Tc	10	10	10
Ag	10	1	1
Sn	10	1	1
I	1	1	1
Cs	10	1	1
Ho	1,000	5	5
Np	10	10	10
Pu	1,000	1,000	1,000
Am	500	5	5

3.3.4 Near-field physical data

The majority of parameter values for effective diffusivities, particle density and porosities was taken from the data compilation produced for Project SAFE /SKB 2001b/.

The effective diffusivity selected for fresh structural concrete is $3 \cdot 10^{-12}$ m^2/s and $3 \cdot 10^{-11}$ m^2/s for aged structural concrete. These effective diffusivity[10] values were based on a porosity of 15% together with the assumptions of a geometric factor of 0.01 for fresh structural concrete and 0.1 for aged structural concrete and a diffusivity in unconfined water of $2 \cdot 10^{-9}$ m^2/s /SKB 2001b/. A higher value of the geometric factor in aged concrete than in fresh concrete was selected since the internal pore structure may change towards a less complex structure due to recrystallisation of the calcium silicate hydrate gel during ageing. However, /Höglund and Bengtsson 1991/ noted that a geometric factor of 0.1 for aged concrete is probably too high since this value is a reasonable value for a homogeneous porous material with distributed pore sizes.

In previous assessments an effective diffusivity of $3 \cdot 10^{-10}$ m^2/s in the Silo grout was assumed, i.e. a ten times higher value than in aged structural concrete /Wiborgh and Lindgren 1987/. The reason to the selection of a higher diffusivity is the higher w/c ratio and thus higher capillary porosity in the Silo grout. This value is retained for use in SAR-08. This value is also selected for the effective diffusivity in the BTF grout in line with the assumptions in Project SAFE /SKB 2001b/.

The porosity of gravel is assumed to be 30% (from a range 25–40% e.g. /Freeze and Cherry 1979/). Furthermore, it is conservatively assumed that the geometric factor, GF, is 1 which gives an effective diffusivity in gravel of $6 \cdot 10^{-10}$ m^2/s in line with the assumptions in Project SAFE /SKB 2001b/.

Values for effective diffusivity for bentonite were calculated from approximations used in the SR-Can assessment /Ochs and Talerico 2004/. The best estimate value was estimated to be $4.6 \cdot 10^{-10}$ m^2/s with upper and lower limits of $4.9 \cdot 10^{-10}$ m^2/s and $4.3 \cdot 10^{-10}$ m^2/s, respectively. These are higher than the values for MX-80 (the bentonite assumed in SR-Can) due to the lower dry density of the GEKO/QI bentonite assumed in SFR 1 (1,050 kg/m^3).

The effective diffusivity for sand/bentonite was derived from a porosity of 25% and a geometric factor of 1 which gives an effective diffusivity of $5 \cdot 10^{-10}$ m^2/s in line with the assumptions in Project SAFE /SKB 2001b/.

3.3.5 Geosphere flow-related parameters

AMBER has been used in a variety of post-closure safety assessments, and the ability to represent the processes in the conceptual models has been verified according to two directions. The first is via a continuing sequence of verification procedures applied to each new version. These are reported in /Robinson et al. 2004/. Secondly, AMBER has been applied alongside and results contrasted with other assessment tools. These include notably the ISAM Vault Test Case post-disposal assessment /IAEA 2004/, which includes the same processes of advection and dispersion/diffusion which are considered in the post-closure analysis of the SFR. The results obtained from AMBER were in agreement with those obtained using other internationally recognised codes.

[10] The effective diffusivity, D_e, is defined as /SKB 2001b/ $D_e = D_w . \varepsilon \frac{\delta}{\tau^2}$, where D_w is the diffusivity in water [m^2/s], ε is the porosity [–], δ is the constrictivity factor [–] and τ is the tortuosity factor [–]. The geometric factor, GF, is defined as $GF = \frac{\delta}{\tau^2}$.

The particular approach to representing the discretisation of the geosphere within AMBER for this study has been separately presented in the AMBER verification study /Thomson et al. 2008/.

Values of geosphere pathlength and travel time have been calculated for each of the 60 accepted realisations identified within the inverse modelling studies using the results of particle tracking /Holmén 2007/. Different sets of values have been calculated for Closure and 3,000 years post-closure[11].

An important feature of the approach used in AMBER to representing the evolving geosphere is that, as the pathlength increases over time, the length of the compartments in the AMBER representation stretch in proportion, and vice versa.). This is likely to result in step-changes in estimated groundwater fluxes which are a consequence of choice made to treat the changes to the geosphere properties (e.g. path length and travel time) as occurring instantaneously. It could be argued that the change would occur over a long period of time such that they would equate to a gradual change but detailed information is not available to describe these changes dynamically, and an assumption of instantaneous change has been made. Such apparent discontinuities are often encountered when using a time-stepping approach.

The relationships between the magnitude of flow through a disposal feature and the resultant geosphere pathlength and travel time have been found to be strongly correlated and it is necessary to match the near-field and geosphere parameters derived from the inverse modelling study in order to represent these correlations /Holmén 2007/. In order to ensure the correct usage of flow related parameters the AMBER models have been developed to read in the appropriate values for predefined data samples from files which have been created by manipulating the data simply to report the near-field uncertainty factor, geosphere pathlength and travel time for each accepted realisation for each disposal facility at closure and 3,000 years post-closure.

Table 3-26 presents median values of geosphere pathlength and travel time /Holmén 2007/. Further information on the datasets is provided in Appendix D. The remaining migration-related data is presented below in Table 3-27.

3.3.6 Geosphere sorption data

Values of sorption within the geosphere are taken from the datasets recently reviewed and compiled for SR-Can /SKB 2006d/. The values are presented below in Table 3-28. A correction factor of 0.1 was applied to these data as recommended in the Sr-Can Data report /SKB 2006d/. The corrected data was then input into AMBER assuming triangular distributions.

Table 3-26. Median values of geosphere pathlength and travel time.

	Pathlength [m]		Travel time [y]	
	Closure	3,000 years post-closure	Closure	3,000 years post-closure
BMA	67	425	86	22
BLA	72	503	40	26
1BTF	78	315	317	45
2BTF	78	412	272	36
Silo	66	388	495	72

[11] It should be noted that no corresponding uncertainty factors for near-field flows have been reported for 3,000 years post-closure as it is considered that the near-field flow fields stabilise at 2,000 years post-closure. The uncertainty factors for near-field flows reported for 2,000 years post-closure are used from this time onwards.

Table 3-27. Compilation of geosphere data.

Parameter	Value	Reference
Peclet number [–]	10	/SKB 2001b/
Flow wetted surface area [$m^2\ m^{-3}$]	120	/SKB 2001b/
Matrix porosity [–]	0.005	/SKB 2001b, Holmén 2007/
Matrix density [kg m^{-3}]	2,600	/Thomson et al. 2008/
Depth of thin matrix layer [m]	0.0001	/Thomson et al. 2008/
Depth of 1st matrix compartment [m]	0.0005	/Thomson et al. 2008/
Depth of 2nd matrix compartment [m]	0.0025	
Depth of 3rd matrix compartment [m]	0.0125	
Depth of 4th matrix compartment [m]	0.0625	
Depth of 5th matrix compartment [m]	0.3125	
Depth of 6th matrix compartment [m]	1.6095	

Table 3-28. Sorption coefficients for granitic rock [m^3/kg].

Element	Non-saline			Saline		
	Minimum	Best estimate	Maximum	Minimum	Best estimate	Maximum
H	–	0	–	–	0	–
C (HCO_3^-)	$5{\cdot}10^{-4}$	$1{\cdot}10^{-3}$	$2{\cdot}10^{-3}$	$5{\cdot}10^{-4}$	$1{\cdot}10^{-3}$	$2{\cdot}10^{-3}$
Organic C	–	0	–	–	0	–
Cl	–	0	–	–	0	–
Co#	Not considered due to half life			$1{\cdot}10^{-2}$	$2{\cdot}10^{-2}$	$1{\cdot}10^{-1}$
Ni	$2.8{\cdot}10^{-2}$	$1.2{\cdot}10^{-1}$	$5.4{\cdot}10^{-1}$	$8.0{\cdot}10^{-3}$	$1.0{\cdot}10^{-2}$	$8.7{\cdot}10^{-2}$
Se	$5{\cdot}10^{-4}$	$1{\cdot}10^{-3}$	$5{\cdot}10^{-3}$	$5{\cdot}10^{-4}$	$1{\cdot}10^{-3}$	$5{\cdot}10^{-3}$
Sr#	Not considered due to half life			$1.4{\cdot}10^{-5}$	$3.1{\cdot}10^{-4}$	$2.6{\cdot}10^{-2}$
Mo	–	0	–	–	0	–
Nb	$5{\cdot}10^{-1}$	1	3	$5{\cdot}10^{-1}$	1	3
Tc(IV)	$5{\cdot}10^{-1}$	1	3	$5{\cdot}10^{-1}$	$1{\cdot}10^{0}$	3
Ag	$1{\cdot}10^{-1}$	$5{\cdot}10^{-1}$	1	$1{\cdot}10^{-2}$	$5{\cdot}10^{-2}$	$1{\cdot}10^{-1}$
Sn	0	$1{\cdot}10^{-3}$	$1{\cdot}10^{-2}$	0	$1{\cdot}10^{-3}$	$1{\cdot}10^{-2}$
I	–	0	–	–	0	–
Cs	$1.7{\cdot}10^{-3}$	$1.8{\cdot}10^{-1}$	9.6	$4.0{\cdot}10^{-4}$	$4.2{\cdot}10^{-2}$	$2.0{\cdot}10^{0}$
Ho	1	2	5	1	2	5
Np(IV)	$4.7{\cdot}10^{-2}$	$9.6{\cdot}10^{-1}$	$2{\cdot}10^{1}$	$4.7{\cdot}10^{-2}$	$9.6{\cdot}10^{-1}$	$2{\cdot}10^{1}$
Pu(IV)	1	5	$1{\cdot}10^{1}$	1	5	$1{\cdot}10^{1}$
Am(III)	$2.2{\cdot}10^{-1}$	$1.3{\cdot}10^{1}$	$1.9{\cdot}10^{2}$	$2.2{\cdot}10^{-1}$	$1.3{\cdot}10^{1}$	$1.9{\cdot}10^{2}$

The saline period comprises the initial 1,000 year period post-closure in all calculation cases.

3.3.7 Geosphere matrix diffusion data

Values of effective diffusivity within the geosphere matrix were calculated from diffusivities in free solution and formation factors (for Forsmark) reported in the SR-Can Data report /SKB 2006c/. Effective diffusivity values were obtained by multiplying the formation factor by the diffusivities in free solution. To derive values in non-saline groundwater for species subject to anion exclusion the values for inorganic C, Cl and I were divided by a factor of 10, as recommended in the SR-Can Data report /SKB 2006c/.

The resultant data are reported below in Table 3-29.

Table 3-29. Values of effective diffusivity [m^2/s] in granitic rock.

	Saline			Non-saline		
	Best estimate	Minimum	Maximum	Best estimate	Minimum	Maximum
HTO	$9.1 \cdot 10^{-14}$	$3.1 \cdot 10^{-14}$	$2.9 \cdot 10^{-13}$	–	–	–
$C(CO_3)$	$4.6 \cdot 10^{-14}$	$1.6 \cdot 10^{-14}$	$1.4 \cdot 10^{-13}$	$4.6 \cdot 10^{-15}$	$1.6 \cdot 10^{-15}$	$1.4 \cdot 10^{-14}$
Cl	$7.6 \cdot 10^{-14}$	$2.6 \cdot 10^{-14}$	$2.4 \cdot 10^{-13}$	$7.6 \cdot 10^{-15}$	$2.6 \cdot 10^{-15}$	$2.4 \cdot 10^{-14}$
Co	$2.7 \cdot 10^{-14}$	$9.1 \cdot 10^{-15}$	$8.4 \cdot 10^{-14}$	–	–	–
Ni	$2.6 \cdot 10^{-14}$	$8.8 \cdot 10^{-15}$	$8.2 \cdot 10^{-14}$	–	–	–
Sr	$3.0 \cdot 10^{-14}$	$1.0 \cdot 10^{-14}$	$9.5 \cdot 10^{-14}$	–	–	–
Ag	$6.5 \cdot 10^{-14}$	$2.2 \cdot 10^{-14}$	$2.0 \cdot 10^{-13}$	–	–	–
I	$3.2 \cdot 10^{-14}$	$1.1 \cdot 10^{-14}$	$1.0 \cdot 10^{-13}$	$3.2 \cdot 10^{-15}$	$1.1 \cdot 10^{-15}$	$1.0 \cdot 10^{-14}$
Cs	$8.0 \cdot 10^{-14}$	$2.7 \cdot 10^{-14}$	$2.5 \cdot 10^{-13}$	–	–	–
Others	$3.8 \cdot 10^{-14}$	$1.3 \cdot 10^{-14}$	$1.2 \cdot 10^{-13}$	–	–	–

3.4 Additional considerations for simulations

Two types of near-field and geosphere calculations were performed within SAR-08.

Firstly a deterministic run was undertaken in which parameters were assumed to take their best estimate values[12]. For parameters that have been defined using log-triangular distributions the best estimate value taken by AMBER is the peak value. The best estimate data for the parameters taken from the inverse modelling studies in reported below in Table 3-30.

Secondly a calculation was undertaken in which AMBER sampled parameter values using Latin Hypercube sampling.

In order to determine the number of samples required to obtain stable results a series of calculations were undertaken for CC1 with varying numbers of samples. The near-field and geosphere radionuclide fluxes were compared at set points for each of the disposal facility components and their variation with number of samples was considered. The results are presented below in Figure 3-6 and it was determined that 960 samples were sufficient in the main set of calculations to obtain stable results.

Table 3-30. Best estimate data for U-factors, geosphere pathlength and travel time.

	U_factors [–]		Pathlength [m]		Travel time [y]	
	Closure	2,000 years post-closure	Closure	2,000 years post-closure	Closure	2,000 years post-closure
BMA	3.4	3.4	67	425	86	22
BLA	1.0	3.6	72	503	40	26
1BTF	0.90	4.9	78	315	317	45
2BTF	0.85	4.0	78	412	272	36
Silo	0.69	0.97	66	388	495	72

[12] Where ‘best estimate’ occurs throughout report this refers to a deterministic approach. Where ‘sampled parameters’ occurs this refers to a probabilistic approach.

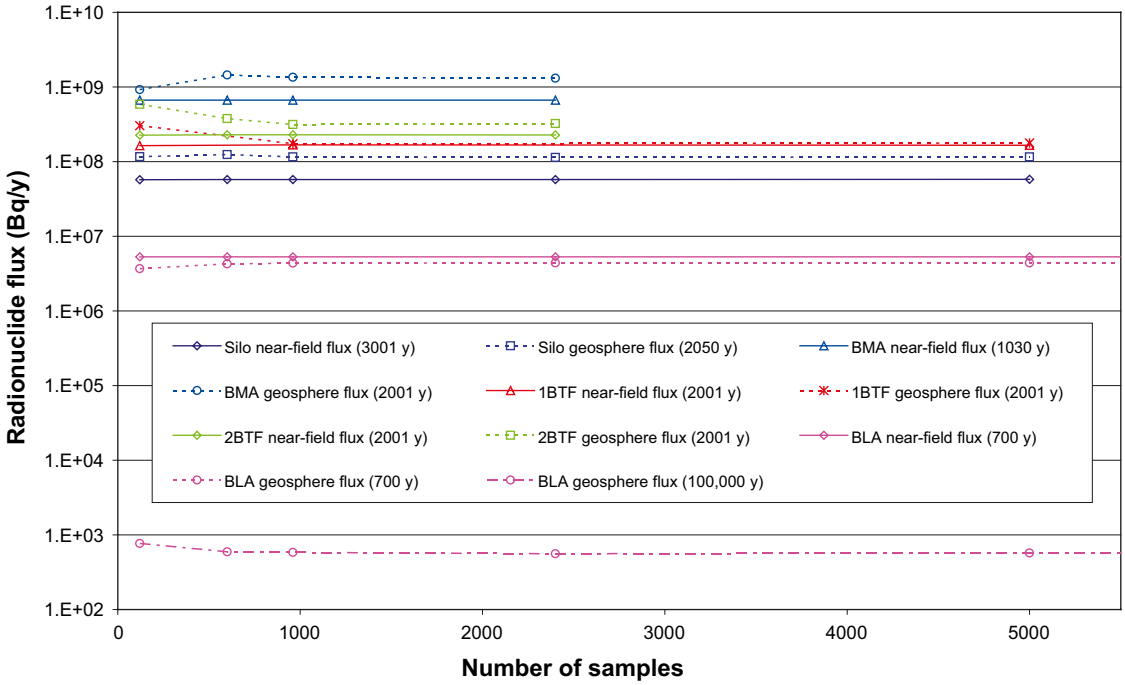

Figure 3-6. *Variation in radionuclide flux with number of samples.*

4 Results

This chapter presents the AMBER results from the different calculation cases.

The main quantities that are presented are the maximum radionuclide fluxes and the times at which these occur. These values result from simulations which represent extended time periods up to 100,000 years post-closure. For the longer time-frames, a reduced number of output times per unit time have been used for the period in the far future.

There are several time-dependent changes in model input data and modelling assumptions. These changes are assumed to occur instantaneously at the relevant times, mainly because detailed data for time dependent changes are not available. It is a cautiously pessimistic approach, tending to over-estimate the peak release rates which arise as a result of assumed instant increases in flow. The key changes are in rates of groundwater flow within the repository at 1,000, 2,000 and 3,000 years post-closure (and additionally for those far future at times when environmental changes are considered, such as development of permafrost, submergence of the site etc). The effects in the near-field are propagated to the geosphere, and so in turn effects in the geosphere will be propagated to the biosphere. Additionally changes in rates of groundwater flow and radionuclide transport within the geosphere also occur in the far future at times when environmental changes are considered such as development of permafrost, submergence of the site etc.

The results of deterministic calculations and calculations using sampled parameter values from parameter distributions are presented for each facility of SFR 1 (Silo, BMA, 1BTF, 2BTF, BLA). The calculations using sampled parameters use Latin Hypercube sampling to select parameters from distributions and other datasets. The deterministic calculations use a single best estimate value of each parameter.

Regulatory criteria are to compare the calculations of radiological dose and individual radiological risk against that have been undertaken within the SAR-08 biosphere calculations /Bergström et al. 2008/.

Therefore it is emphasised that the radionuclides that are presented here as significant in terms of radionuclide flux from the near-field and geosphere may not correspond to those radionuclides which contribute the majority of radiological exposure within the SAR-08 biosphere calculations. Parameters and processes relating to phenomena such as radionuclide transport and accumulation within the biosphere, bioavailability, radiotoxicity etc may modify the overall importance of individual radionuclides from that described for the near-field and geosphere.

Similarly information relating the to total radionuclide fluxes from the near-field and geosphere is presented below for discussion and by way of summary but it is not necessarily certain that a larger radionuclide flux will result in a larger overall impact (and vice versa). Again the parameterisation and representation of the biosphere will determine the overall importance of the radionuclide fluxes reported here.

4.1 Calculation Case CC1

The evolution of the climate in CC1 is assumed to follow that described within the Weichselian based climate evolution. The periods of continuous permafrost are considered to be sufficient to inhibit the transfer of radionuclides. The assumptions in CC1 regarding closure design, disposal inventory and system performance follow best estimates.

A detailed description of CC1 has been given previously in subsection 2.2.1. A schematic of the main features of CC1 is presented below in Figure 4-1 which provides an overview of the main features of this calculation and their variation over the assessment timescale.

4.1.1 Silo

A summary plot of the long-term best estimate near-field radionuclide flux for the Silo for CC1 is shown below in Figure 4-2. Best estimates results are calculated deterministically, assuming best estimates of the input parameters. These are determined from the input probability distribution functions as follows:

- Uniform – mean, which is equal to the median.
- Log uniform – median.
- Gaussian – mean, which is equal to the median.
- Truncated Gaussian – mean of the untruncated distribution.
- Triangular – peak.
- Beta – mean.
- General cumulative distribution function – median.

The shaded areas on the figure represent periods of continuous permafrost in which it is assumed that no transport within the Silo or release from it is possible due to the reduction in temperature. The near-field radionuclide flux is dominated by organic C-14 until 66,000 years post-closure when Ni-59 becomes the most important radionuclide.

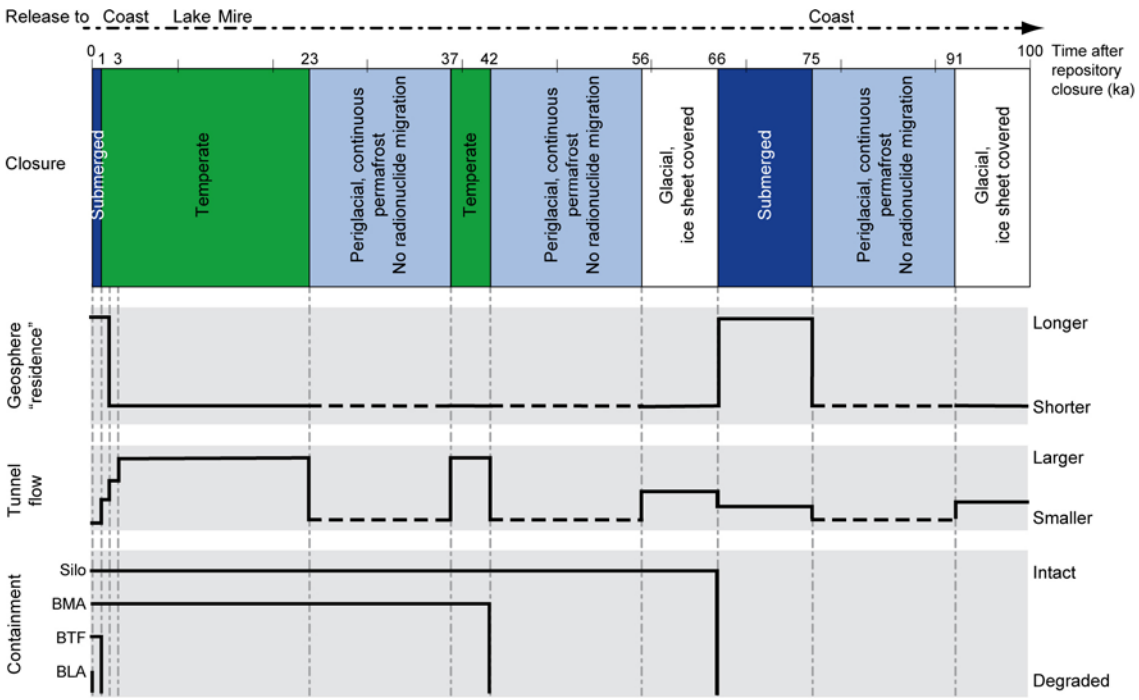

Figure 4-1. *Schematic of CC1.*

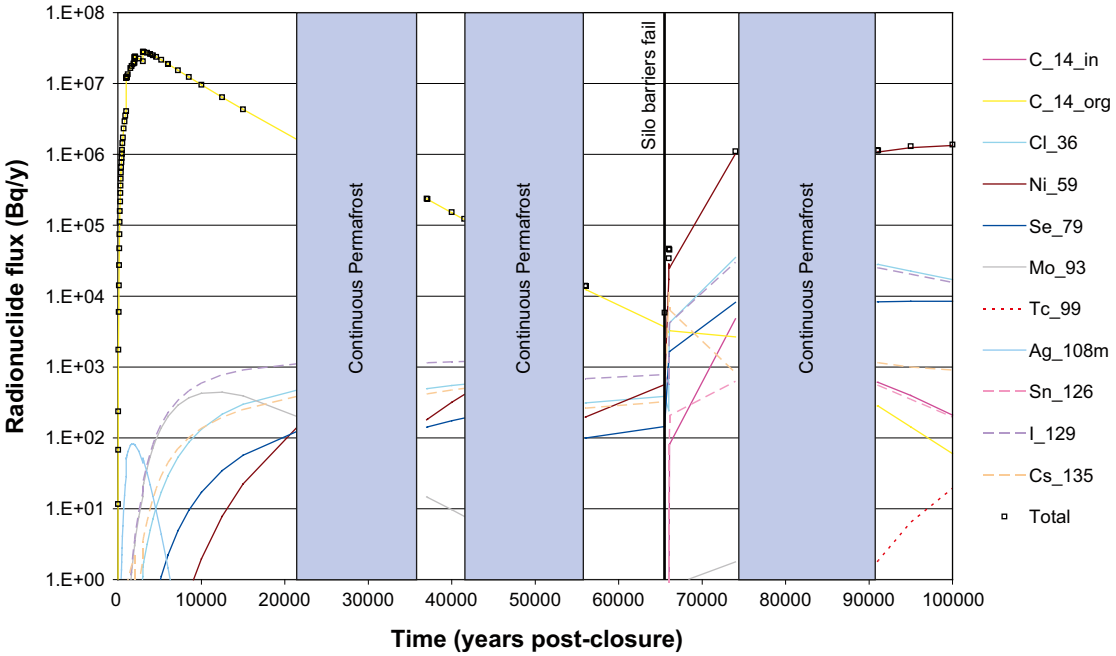

Figure 4-2. *Near-field best estimate radionuclide flux from the Silo for CC1.*

Peak releases occurring within 10,000 years and the greater detail for this timeframe are shown in Figure 4-3. The maximum total near-field radionuclide flux is estimated to be $2.8 \cdot 10^7$ Bq/y at 3,000 years post-closure and is significantly dominated by organic C-14. Peak releases of Mo-93 and Ag-108m also occur before 10,000 years and the flux of I-129 increases steadily but these are more than 4 orders of magnitude below the overall maximum flux. The radionuclide flux from the Silo is dominated by organic C-14 until around 66,000 years, by which point the organic C-14 source term has become significantly depleted and the release of Ni-59 (and other long-lived radionuclides increases) following the failure of the Silo.

Figure 4-4 shows the near-field radionuclide flux for the time period from 20,000 to 100,000 years on a linear axis in order that the latter period assessed can be seen in greater detail.

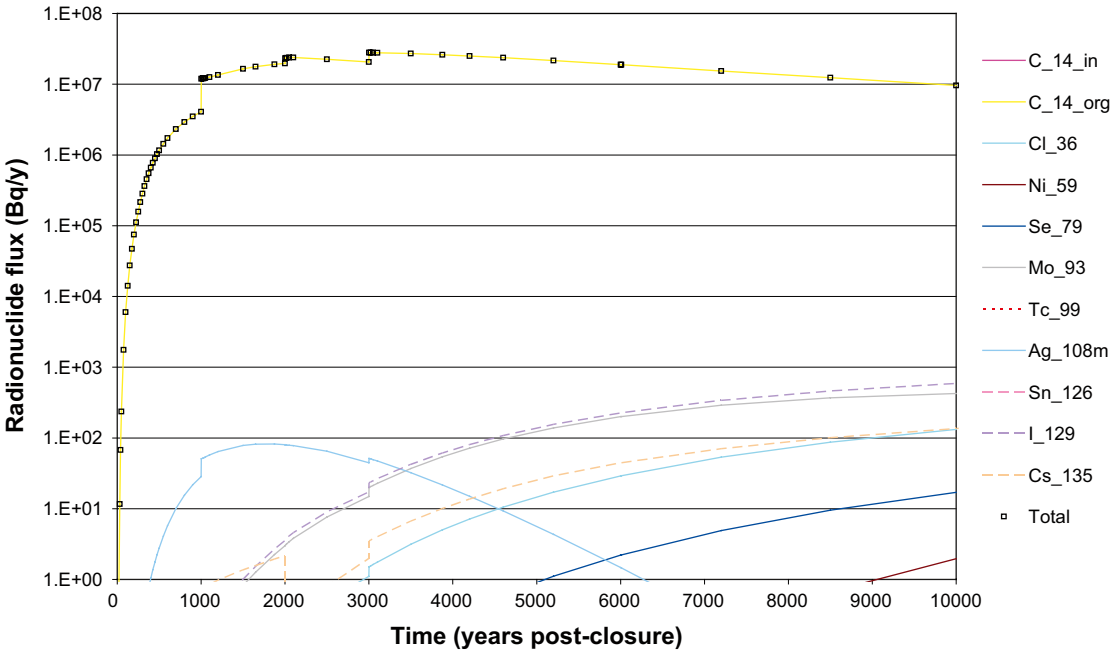

Figure 4-3. *Details of best estimate near-field radionuclide flux from the Silo for to 10,000 years for CC1.*

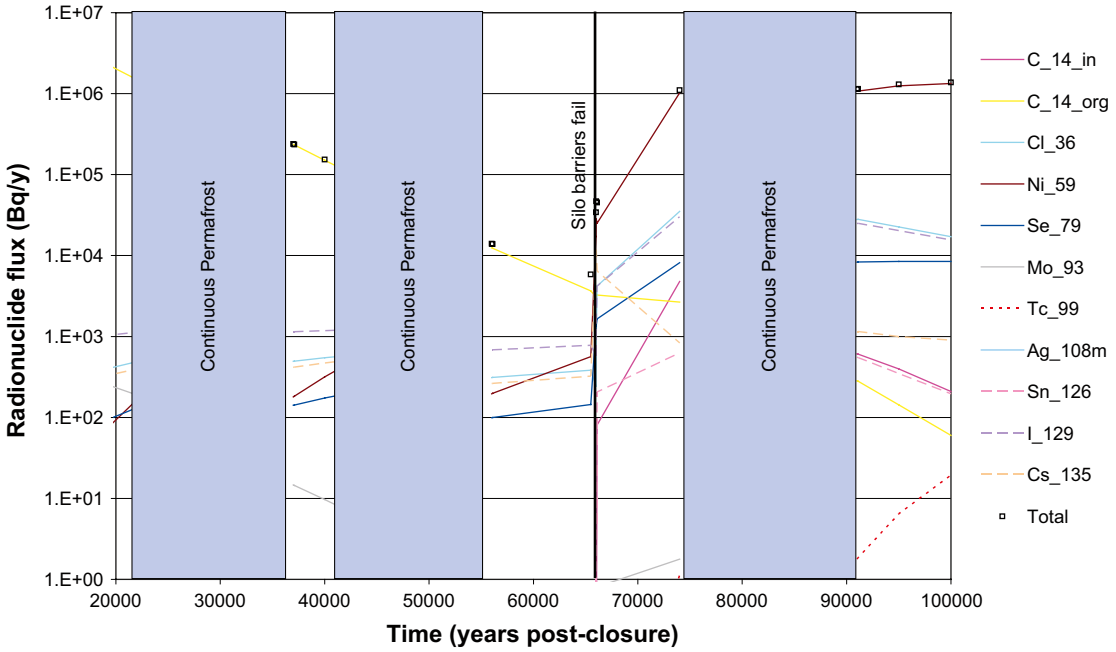

Figure 4-4. *Details of best estimate near-field radionuclide flux from the Silo for 20,000 to 100,000 years for CC1.*

At 66,000 years post-closure it is assumed that the ice-sheet which has been overlying the site retreats and in doing so generates a large amount of glacial melt waters which are assumed to remove the bentonite backfill and also degrade the concrete structure and encapsulation, resulting in substantial failure of the Silo containment. This point in time is shown in Figure 4-4 as a solid line. Thereafter it is considered possible for radionuclides to migrate through the walls of the Silo by both diffusion and advection. However, at this point the site is submerged below a marine water body and the vertical hydraulic gradients are considered to be small, similar to present day conditions at the site and the radionuclide release is proportional to the hydraulic gradient. It is also assumed that the sorption capacity of the concrete and cement becomes substantially reduced. Additionally as the bentonite backfill is removed it is assumed that no sorption capacity remains and the radionuclides which have previously sorbed and accumulated are able to be released. The long-term Silo radionuclide flux from 66,000 years onwards is dominated by Ni-59 and other weakly sorbed long-lived radionuclides Cl-36, Se-79 and I-129.

Figure 4-5 below shows a plot of the maximum total near-field radionuclide flux for the Silo from each of the 960 individual samples in the calculation using sampled parameters. This plot is included in order to illustrate how the maximum radionuclide flux and how the time at which the maximum flux occurs varies for the calculation using sampled parameter when compared to the best estimate calculation. Knowledge of the variation in the maximum radionuclide flux is considered to be important as this can have a strong control on the maximum estimates of radiological impact estimated within the biosphere. Also shown in Figure 4-5 are the mean[13] ($3.0 \cdot 10^7$ Bq/y at approximately 3,000 years post-closure) and the best estimate ($2.8 \cdot 10^7$ Bq/y at approximately 3,000 years post-closure) for comparison.

[13] The mean, which is calculated from the individual results (time of maximum radionuclide flux or maximum radionuclide flux), will show closest agreement with the corresponding best estimate value when the spread of results from the individual samples relative to the best estimate result is minimal. For the plot shown for the Silo the calculated mean therefore provides a reasonable approximation of the best estimate. For situations in which a larger variation in results from the individual samples occurs or if a bimodal distribution is observed then the mean may differ substantially from the best estimate. Therefore caution should be exercised in interpretation of the mean. However, it is included here as an aid to highlighting where variations may occur in the results from the individual samples relative to the best estimate result.

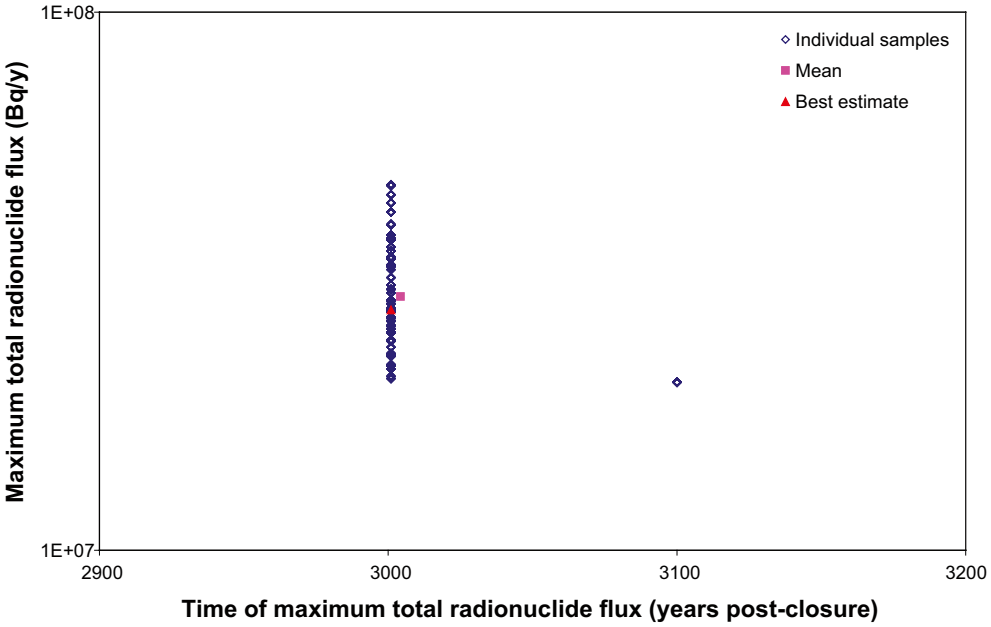

Figure 4-5. *Scatter plot of Silo maximum total near-field radionuclide flux for CC1.*

Overall little variation is evident, the maximum total flux varies between $2.0 \cdot 10^7$ and $4.8 \cdot 10^7$ Bq/y. It is very important that even the combinations of sampled parameter values which give rise to increased flux, do not result in very much higher flux estimates. In addition, the time of peak release is close to 3,000 years in all cases. This is due to the dominance of organic C-14 in determining the total radionuclide flux from the Silo. This radionuclide does not undergo sorption and is therefore not sensitive to changes in sorption coefficients (its value is assumed to be 0 [m^3/kg]). The variation in the near-field organic C-14 flux is therefore due to the Uncertainty factors used which vary over a relatively small range for the Silo.

The maximum total flux of $2.0 \cdot 10^7$ Bq/y at 3,100 years post-closure results from the use of the lowest Uncertainty factors in the calculations which reduces the rate of groundwater flow through the Silo delaying both the timing and magnitude of the maximum. Although it appears to be a single point plotted in Figure 4-5 multiple points actually exist as a result of the re-use of Uncertainty factors within the calculation[14].

Figure 4-6 is summary plot of the near-field radionuclide flux for the Silo for evaluation of CC1 using sampled parameters. Figure 4-6 shows the mean of the total near-field radionuclide flux and the 5th and 95th percentiles calculated from the distribution of data. Note that the 5th and 95th percentiles are similarly narrowly distributed around the mean, and even in the longer term showing a similar geometric range above and below the mean. Given the omission of many minor processes which would tend to reduce estimates of releases if they were included, it is anticipated that a more realistic estimate of range would extend the ranges lower than the mean but not significantly higher than those shown.

In this case the important omitted processes and parameters do not allow for organic C-14 to change chemical form to inorganic, which it may be expected to over the course of a few thousand years or earlier and then allowing for C-14 sorption.

[14] The calculation using sampled parameters uses 960 values of sampled parameters. However, the 60 accepted realisations of Uncertainty factors /Holmén 2007/ are used 16 times each (i.e. 16·60 = 960).

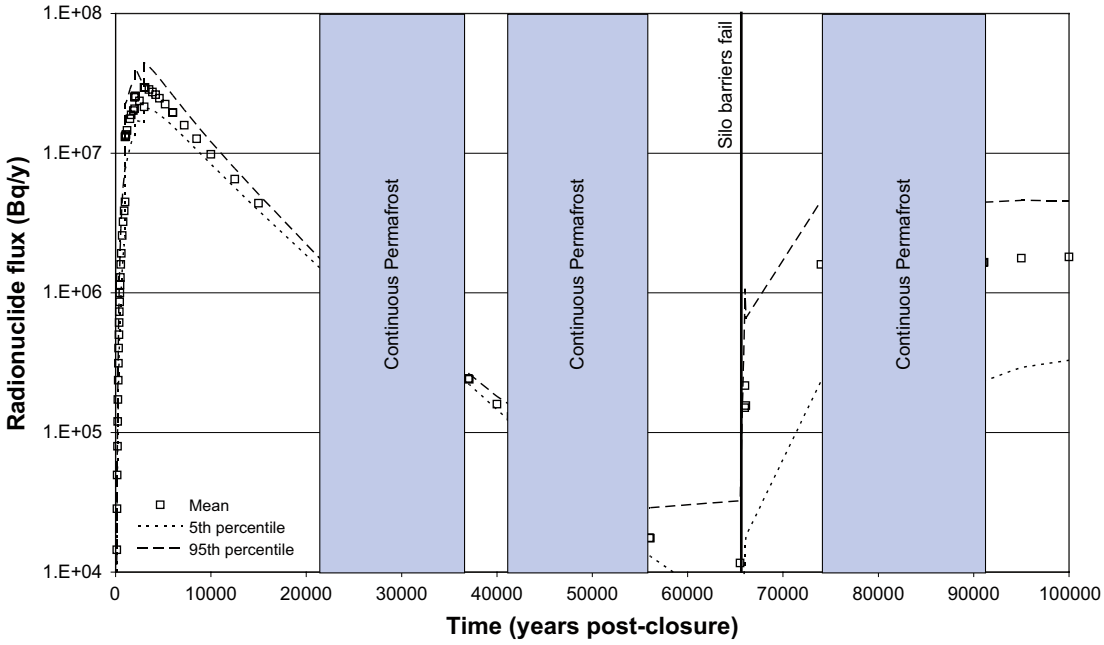

Figure 4-6. *Range of near-field total radionuclide flux from the Silo for CC1 using sampled parameters.*

Figure 4-7 is a plot of the best estimate radionuclide flux from the geosphere to the biosphere for the Silo. Generally it is evident that the breakthrough of radionuclides is delayed and lower compared to the near-field release. The peak geosphere flux of Ag-108m is reduced by almost two orders of magnitude compared to that from the near-field which is largely the result of radionuclide decay during its delay in transit through the geosphere. However, the peak radionuclide flux is estimated to be around 10^8 Bq/y at 2,000 years post-closure, predominantly from organic C-14 and is associated with a transition in hydrogeological conditions which is assumed to happen instantaneously at this time. The change in hydrogeological conditions that is represented as occurring at 2,000 years post-closure marks a transition from conditions of relatively low hydraulic gradients resulting in small vertical flows along short path lengths to higher hydraulic gradients resulting in larger horizontal flows along longer path lengths. These changes are due to the ongoing land uplift and shoreline displacement and corresponding evolution in groundwater discharge characteristics from discharge to a marine body to a terrestrial landscape.

The fact that the peak release from the geosphere occurs before the peak release from Silo warrants further consideration. The release of organic C-14 from the Silo is relatively constant for several thousand years from 1,000 years post-closure and although the maximum value for the Silo ($2.8 \cdot 10^7$ Bq/y) occurs at 3,000 years post-closure the value at 2,000 years post-closure is $2.3 \cdot 10^7$ Bq/y which is within a factor of approximately 1.2. This therefore suggests that there is a relatively high and constant flux of organic C-14 from the near-field to the geosphere between 1,000 and 3,000 years post-closure. Furthermore the Silo has the largest geosphere residence time (and so lowest transfer rate) for SFR 1 between closure and 2,000 years post-closure. These factors combine and result in the total amount of activity (primarily organic C-14) within the geosphere increasing until 2,000 years post-closure (Figure 4-8). At this point the advective rate increases markedly and this results in a corresponding increase in the transfer rate of radionuclides from the geosphere ($2.0 \cdot 10^8$ Bq/y at 2,000 years post-closure) and the release of the organic C-14 that has migrated to the geosphere over the initial period.

It is not suggested that the model assumes the accumulation of organic C-14 somehow in the geosphere; organic C-14 is not assumed to be retarded by sorption. Rather, groundwater which was carrying organic C-14 in the geosphere at one rate (already released from the near-field), suddenly starts moving more quickly, and the organic C-14 goes with it. (See discussion of

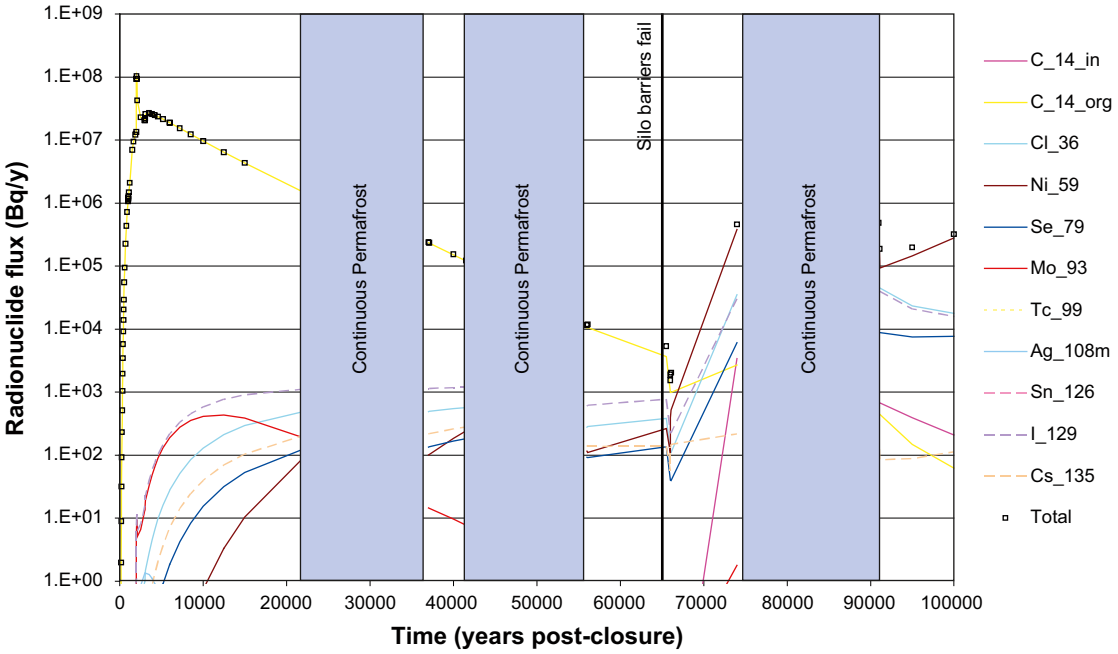

Figure 4-7. *Geosphere best estimate radionuclide flux from the Silo for CC1.*

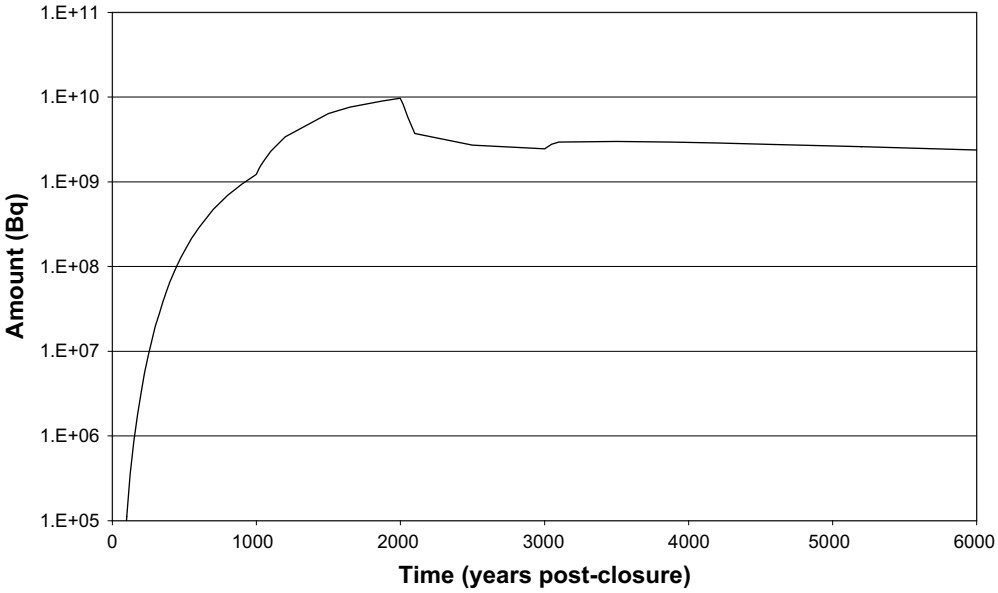

Figure 4-8. *Best estimate of total radioactivity within geosphere from the Silo for CC1.*

Figure 4-9 below). This is consistent with the conceptual understanding of the changing groundwater flow system. It could be argued that the change would occur over a period long enough so that the peaks estimated here are in fact over-estimated. However, for modelling simplicity a conservative assumption of instantaneous change has been made. A more complicated but realistic assumption of gradual change would have resulted in greater dispersion of the release.

The variation in groundwater velocity is displayed in Figure 4-9 which illustrates an increase in the groundwater Darcy velocity from less than 0.5 m/y to greater than 5 m/y. It should be noted that the variation in groundwater velocity reported in Figure 4-9 also takes into account the expected response in the hydrogeological system to environmental change (e.g. episodes of continuous permafrost result in periods of no groundwater flow).

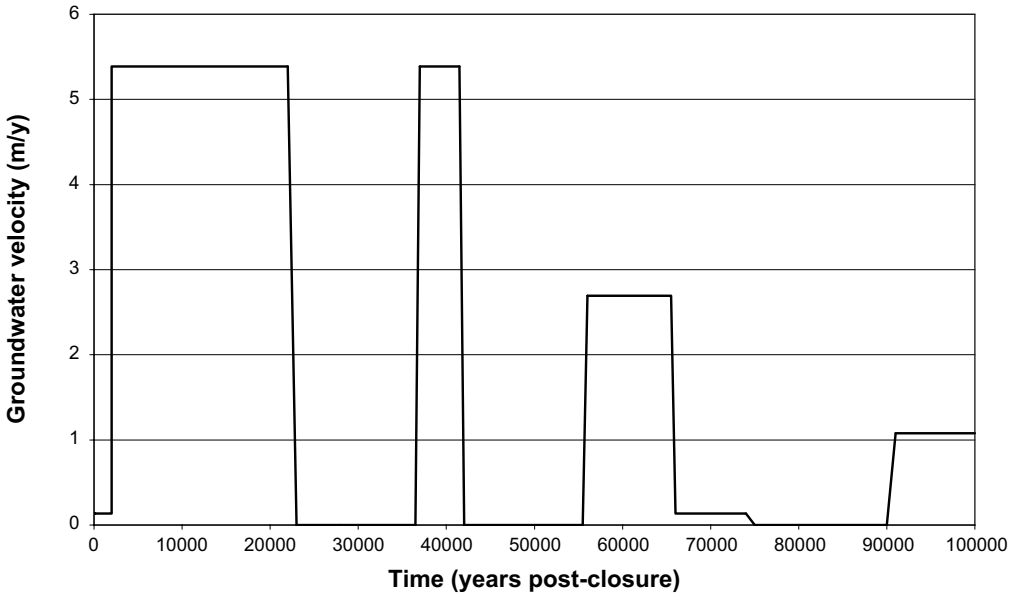

Figure 4-9. *Variation in best estimate geosphere flow velocity for Silo for CC1.*

An increase in radionuclide flux at the geosphere-biosphere interface is to be expected with an increase in groundwater velocity such as that shown in Figure 4-9 if the radionuclide concentration within the geosphere is constant. However, the timescale over which such changes take place is uncertain and it is possible that it could take place over a relatively short timescale but the assumption that it is instantaneous is likely to be conservative in terms of the radionuclide flux from the geosphere.

Discounting the effects of this transition, the peak radionuclide flux is around $3 \cdot 10^7$ Bq/y. The remainder of the geosphere flux follows a similar trend to that discussed for the near-field. Figure 4-10 shows the geosphere radionuclide flux for the time period from 20,000 to 100,000 years on a linear axis.

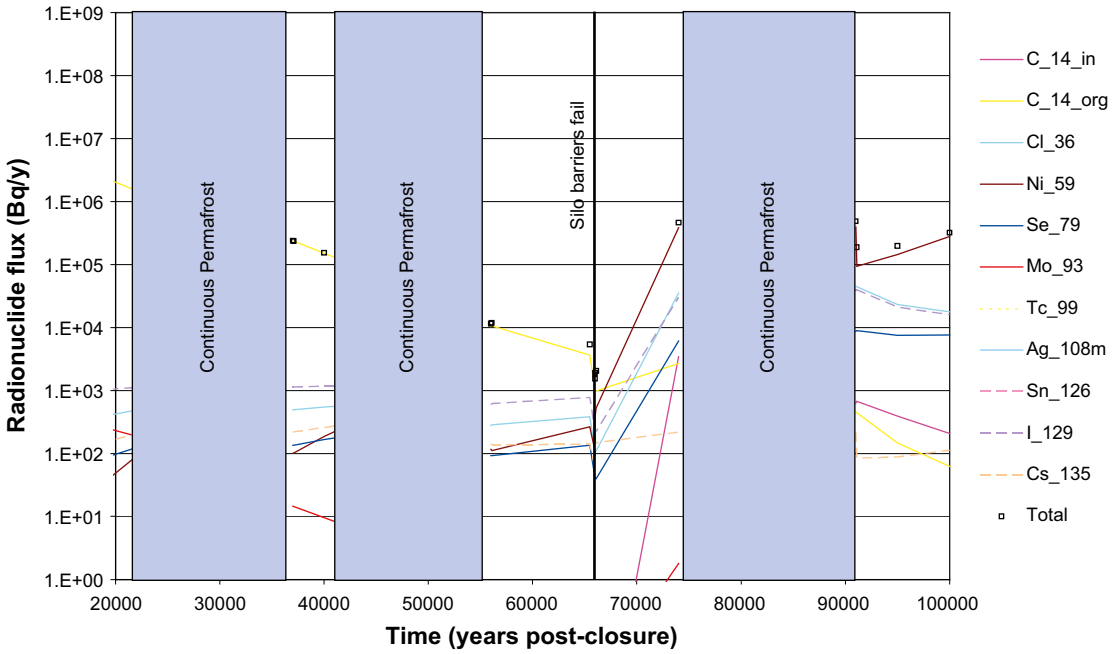

Figure 4-10. *Details of best estimate geosphere flux from the Silo for 20,000 to 100,000 years for CC1.*

Other important changes in the geosphere are the assumption of saline conditions from closure for the initial 1,000 years post-closure and also for the period from 66,000 years to 75,000 years post-closure. The sorption coefficients of Ni, Ag and Cs are reduced during the period in which the geosphere is considered to be dominated by saline groundwater whereas the values of effective diffusivity of inorganic C, Cl and I within the rock matrix are increased during this period.

Figure 4-11 below shows a plot of the maximum total geosphere radionuclide flux for the Silo from each of the individual samples run in CC1 using sampled parameters. Also shown in Figure 4-11 are the mean ($1.2 \cdot 10^8$ Bq/y at approximately 2,600 years post-closure) and the best estimate (10^8 Bq/y at approximately 2,000 years post-closure) for comparison. The mean is the average of the maximum total geosphere radionuclide flux of all the sample. The stratified nature of the spread of times of maxima within the geosphere is a consequence of the selection of output times.

More variation is evident than for the near-field flux, the maximum total flux varies between $9.4 \cdot 10^6$ and $1.3 \cdot 10^9$ Bq/y and the time of the maximum varies between 2,000 and 7,200 years post-closure, with a cluster of values around 2,000 years post-closure.

It is worthwhile noting that the highest results are only about an order of magnitude higher than either the mean or the best estimate. Given the large number of samples run, this gives confidence that the highest possible peak fluxes are not likely to be grossly higher than those which are considered more likely. On a risk calculation basis, either the mean or the best estimate appears a sensibly cautious representative results for geosphere release for CC1. As with other scenarios, a considerable number of individually minor processes have been conservatively ignored in the model, but the cumulative effect is that all the results are likely to be over-estimates, even for the mean and best estimate.

Figure 4-12 is a summary plot of the geosphere radionuclide flux for the Silo for evaluation of CC1 using sampled parameters. The figure shows the mean of the total radionuclide flux and the 5th and 95th percentiles. Comments made previously (see subsection 4.1) in relation to the over-estimate of the lower bound due to omitted processes apply here.

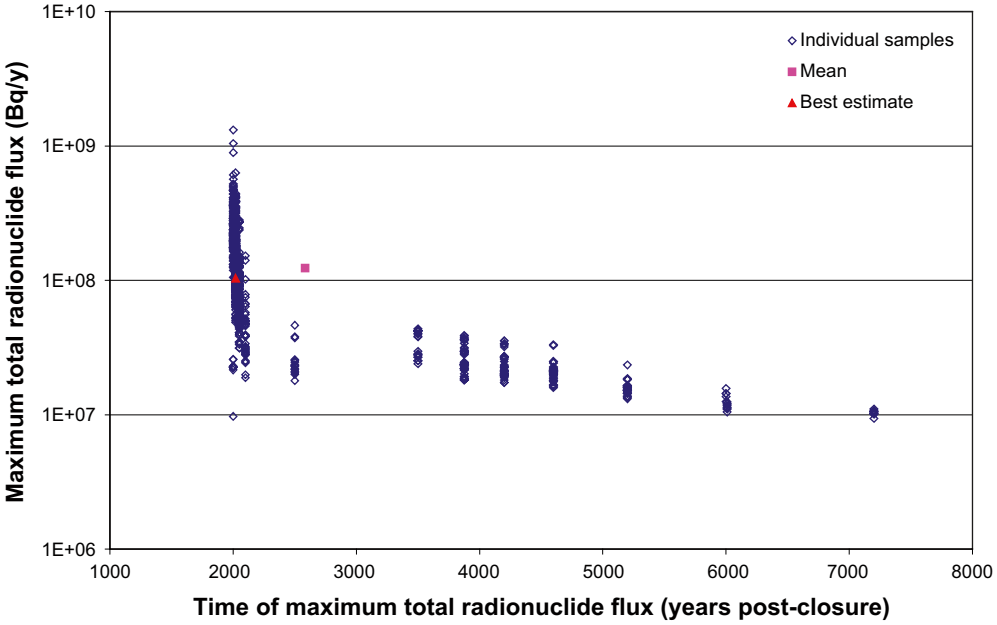

Figure 4-11. *Scatter plot of Silo maximum total geosphere radionuclide flux for CC1.*

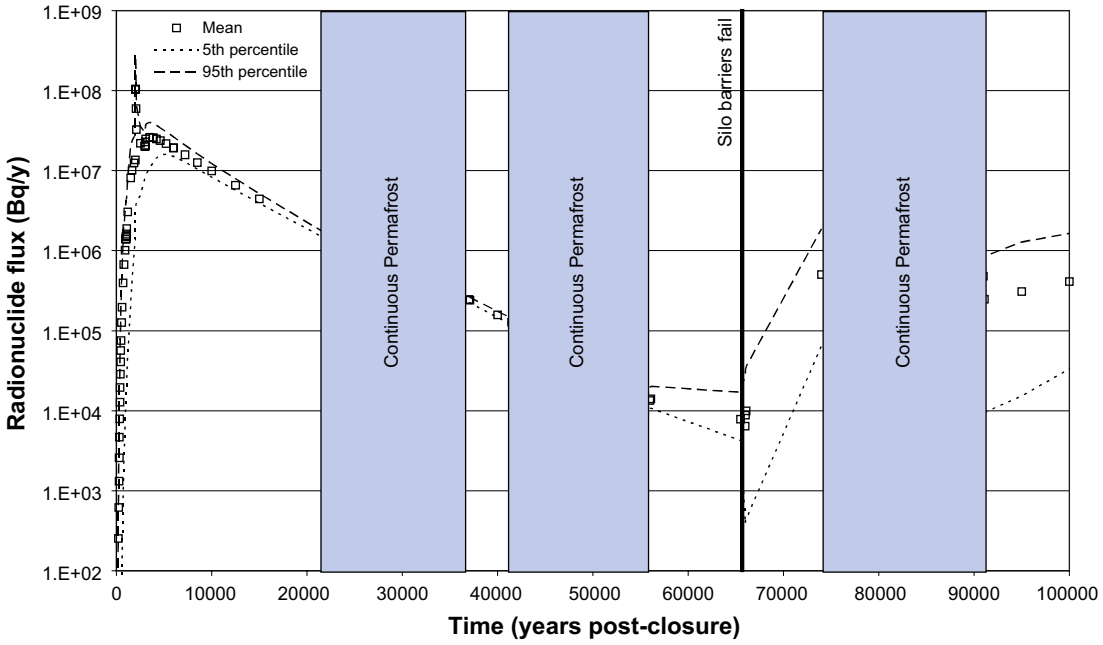

Figure 4-12. *Geosphere total radionuclide flux from the Silo for CC1 using sampled parameters.*

4.1.2 BMA

Figure 4-13 summaries the best estimate near-field radionuclide flux from the BMA disposal tunnel for CC1. Fluxes of the short-lived radionuclides H-3, Sr-90 and Cs-137 all reach their maximum values between 50 and 150 years and Ni-63 at around 300 years (Figure 4-14), they are several orders of magnitude below the total value at this time, which is dominated by organic C-14. The maximum total radionuclide flux is estimated to be approximately $2.8 \cdot 10^8$ Bq/y at 1,100 years post-closure and it is dominated by contributions from organic C-14 for the first 9,000 years of the assessment.

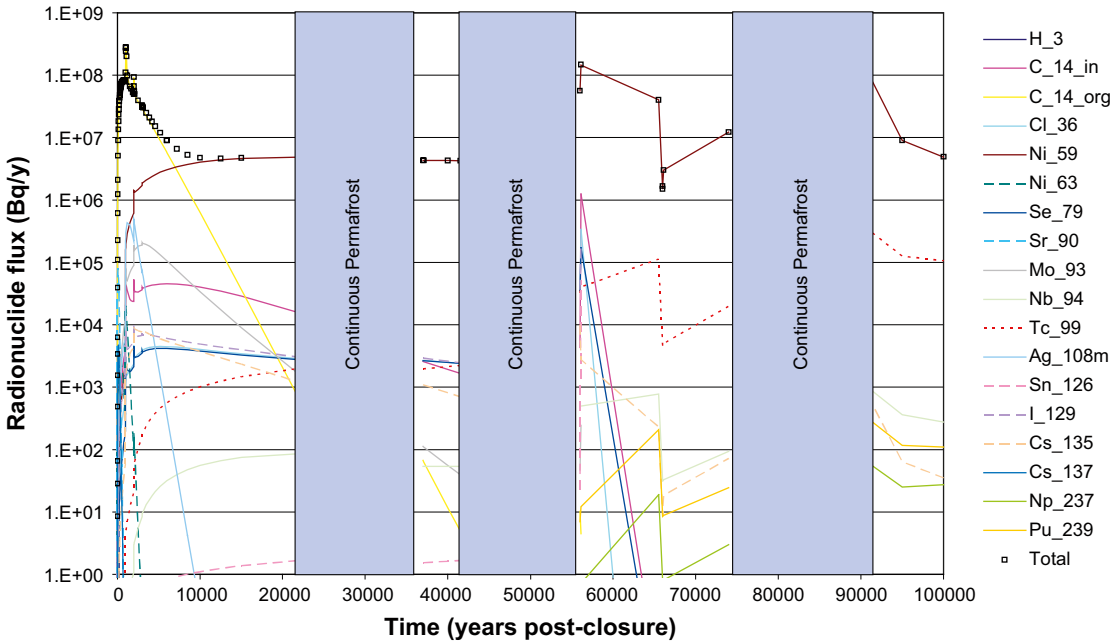

Figure 4-13. *Near-field best estimate flux from the BMA for CC1.*

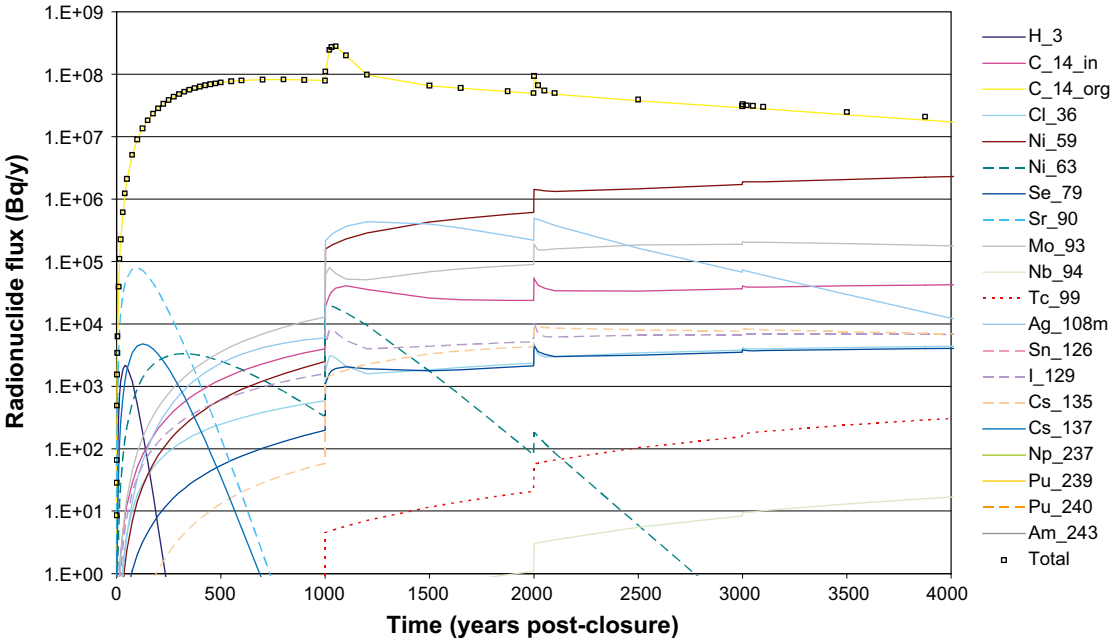

Figure 4-14. *Details of best estimate radionuclide flux from the BMA to 4,000 years for CC1.*

Beyond 9,000 years post-closure the radionuclide flux from the BMA is dominated by releases of Ni-59. Figure 4-15 shows the radionuclide flux between 20,000 and 100,000 years on a linear scale. The BMA encapsulation is assumed to fail at 42,000 years post-closure although this does not become apparent in CC1 until 56,000 years post-closure due to the fact that the disposal system is assumed to freeze during periods of continuous permafrost. At 56,000 years post-closure the flux of inorganic C-14 released increases markedly and the remaining inventory is then rapidly depleted; however, Ni-59 remains the dominant radionuclide. The release of Tc-99 also increases in the long-term, although it remains orders of magnitude below Ni-59.

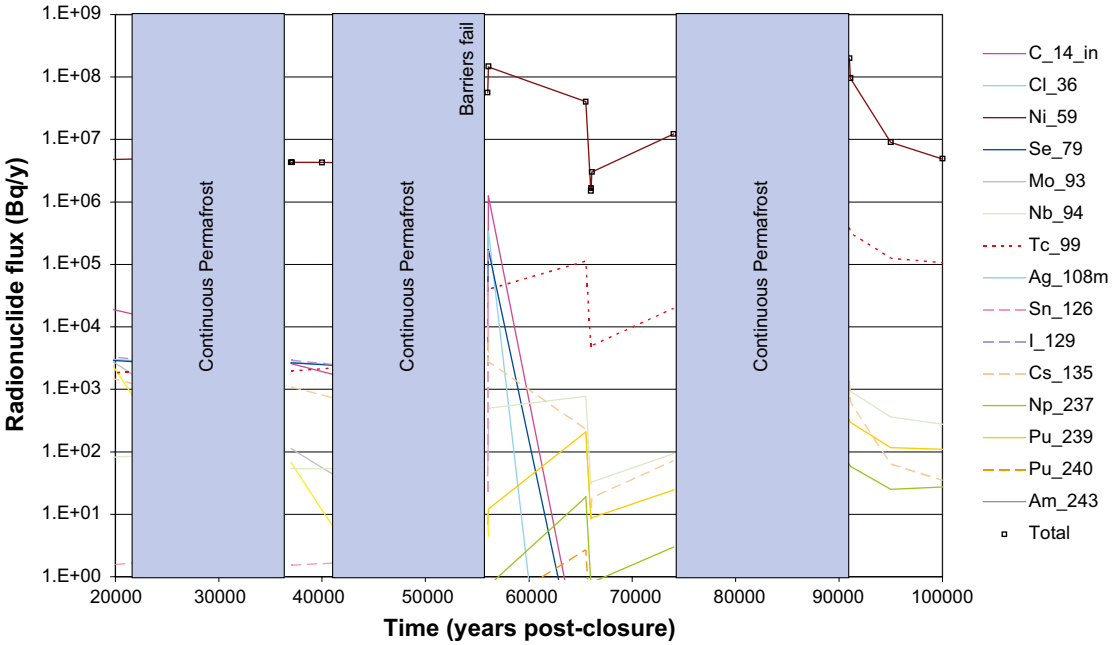

Figure 4-15. *Details of best estimate radionuclide flux from the BMA for 20,000 to 100,000 years for CC1.*

Figure 4-16 below shows a plot of the maximum total near-field radionuclide flux for the BMA from each of the individual samples run in the calculation using sampled parameters. Also shown in Figure 4-16 are the mean ($3.0 \cdot 10^8$ Bq/y at approximately 11,000 years post-closure) and the best estimate ($2.8 \cdot 10^8$ Bq/y at approximately 1,100 years post-closure) for comparison.

Overall the maximum total flux varies between $2.6 \cdot 10^8$ and $7.8 \cdot 10^8$ Bq/y and the time of the maximum varies between approximately 1,000 and 91,000 years post-closure with a significant number clustering at the end of the 2nd period of continuous permafrost.

Figure 4-17 is a summary plot of the near-field radionuclide flux for the BMA for evaluation of CC1 using sampled parameters. The figure shows the mean of the total radionuclide flux and the 5th and 95th percentiles. Comments made previously in relation to the over-estimate of the lower bound of the range due to omitted processes apply here.

Figure 4-18 shows the best estimate geosphere radionuclide flux from the BMA. The maximum radionuclide flux is estimated to be $2.0 \cdot 10^8$ Bq/y at 2,000 years post-closure and is due to organic C-14. Figure 4-19 shows a more detailed plot of the period up to 4,000 years post-closure. It should be noted that the uncertainties noted previously for the Silo regarding the duration of the transition in geosphere parameters at 2,000 years post-closure is relevant here also.

Generally the geosphere flux shows similar trends to that described for the near-field flux up to 56,000 years post-closure. The releases of the short-lived radionuclides H-3, Sr-90 and Cs-137 are reduced due to decay and their breakthrough delayed. Long term fluxes are dominated by Ni-59 but from 66,000 years post-closure a different trend is noted for the geosphere than that previously observed for the near-field.

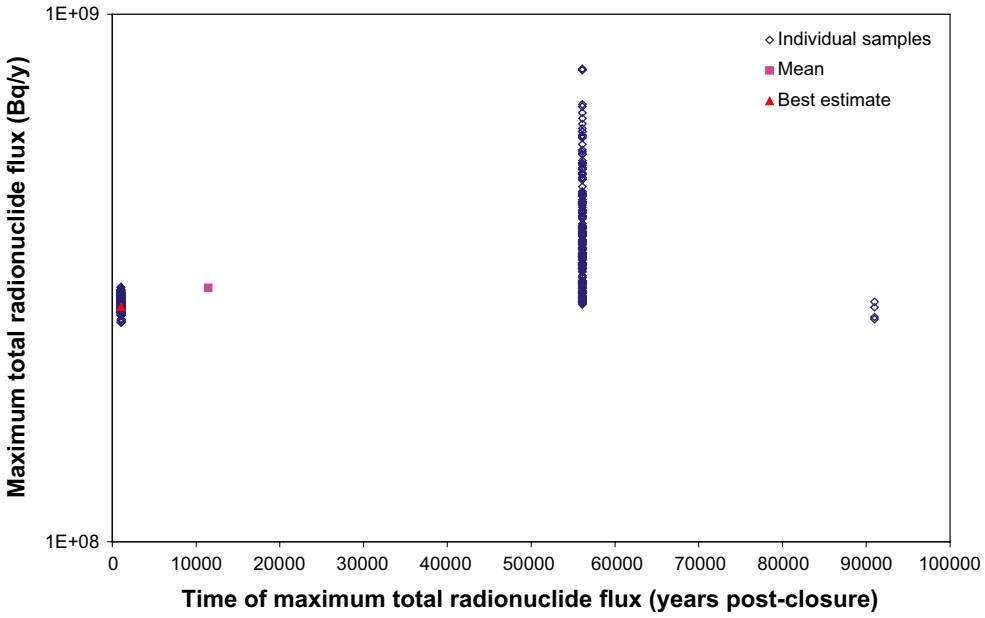

Figure 4-16. *Scatter plot of BMA maximum total near-field radionuclide flux for CC1.*

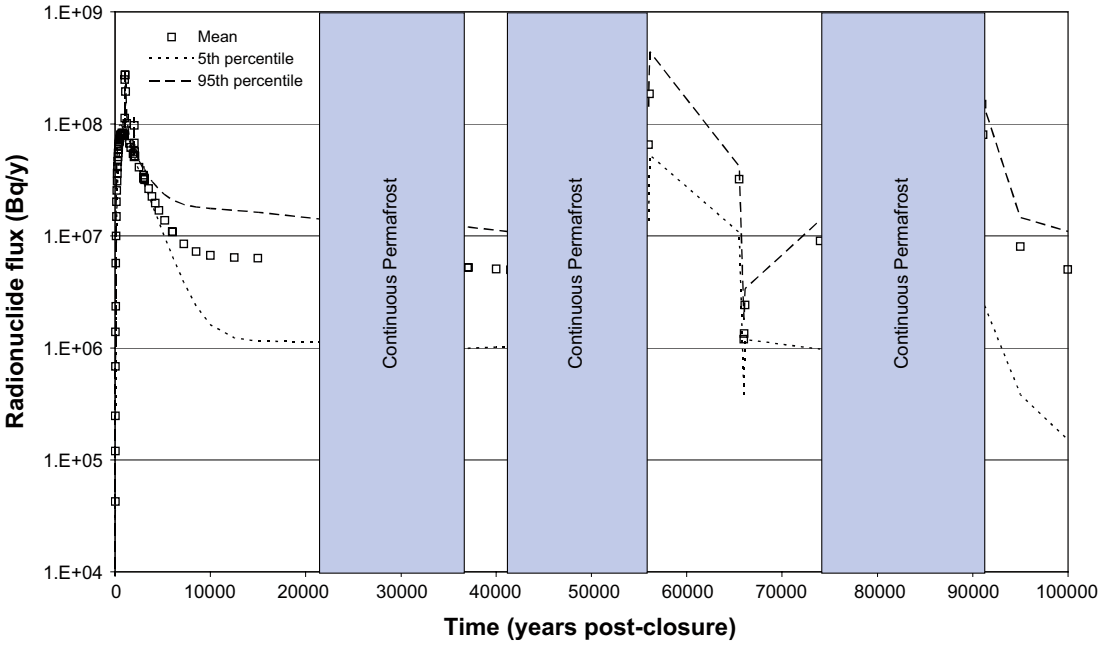

Figure 4-17. *Near-field total radionuclide flux from the BMA for CC1 using sampled parameters.*

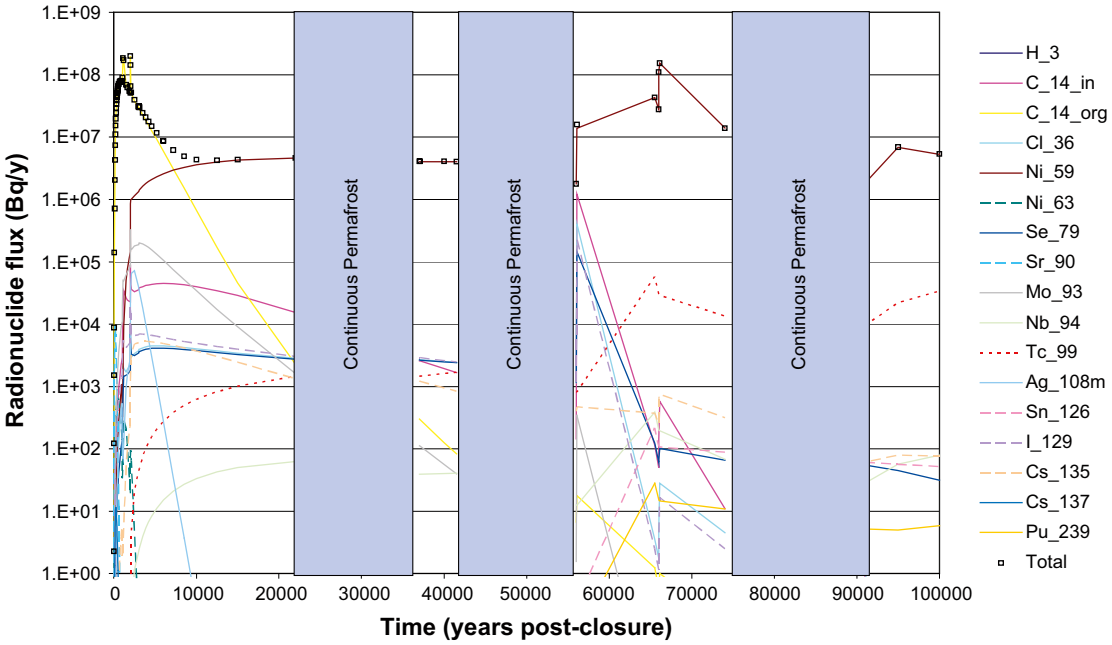

Figure 4-18. *Geosphere best estimate flux from the BMA for CC1.*

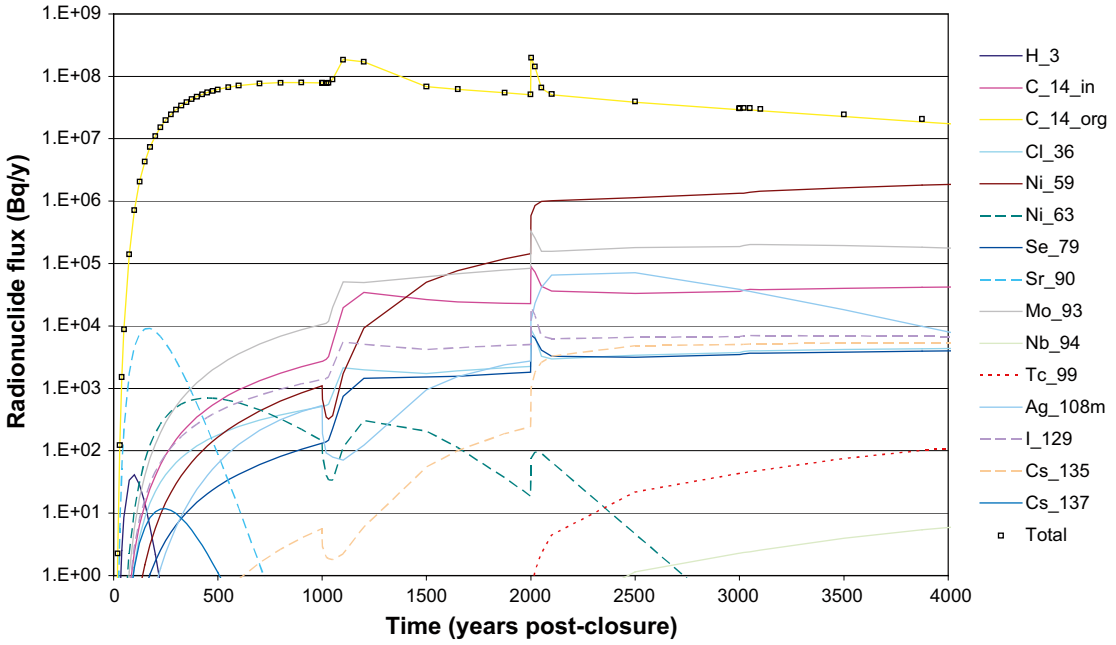

Figure 4-19. *Details of best estimate geosphere flux from the BMA to 4,000 years for CC1.*

At 66,000 years post-closure the site is assumed to become submerged beneath a marine body. The regional hydraulic gradients are assumed to be relatively small and the migration routes follow relatively short vertical pathways (similar to current conditions at the site). At the same time the geosphere is assumed to return to saline conditions and associated with this change the retention of inorganic C, Cl, Ag, I and Cs by matrix diffusion or sorption is reduced. At the same time the release of radionuclides from the near-field is reduced; both because of the reduced regional hydraulic gradients and also due to the fact that the BMA encapsulation is assumed to have failed by this point and therefore a large proportion of the radionuclides have been released from the near-field into the geosphere.

The combination of the relatively higher inventory of radionuclides within the geosphere compared to the near-field combined with the decrease in geosphere retention for some radionuclides results in the increases in fluxes for these radionuclides observed at 66,000 years post-closure.

Figure 4-20 below shows a plot of the maximum total geosphere radionuclide flux for the BMA from each of the individual samples run in the calculation using sampled parameters. Also shown in Figure 4-20 are the mean ($8.2 \cdot 10^8$ Bq/y at approximately 21,000 years post-closure) and the best estimate ($2.0 \cdot 10^8$ Bq/y at approximately 2,000 years post-closure) for comparison.

The maximum total flux varies between $1.2 \cdot 10^8$ and $8.9 \cdot 10^9$ Bq/y and the time of the maximum varies between 1,000 and 66,000 years post-closure, with a most values occurring around 2,000 years post-closure. Similarly to the near-field it can be seen that there is a significant difference between the time of the maximum radionuclide flux estimated from the best estimate calculation and that from the calculation using sampled parameters. The incidence of maximum geosphere fluxes which occur at 66,000 years post-closure in the calculation which uses sampled parameters are due to parameter combinations which result in reduced geosphere retardation (i.e. reduced travel time, matrix diffusion or sorption).

Figure 4-21 is a summary plot of the geosphere radionuclide flux for the BMA for evaluation of CC1 using sampled parameters. The figure shows the mean of the total radionuclide flux and the 5th and 95th percentiles. Comments made previously in relation to the over-estimate of the lower bound of the range due to omitted processes apply here.

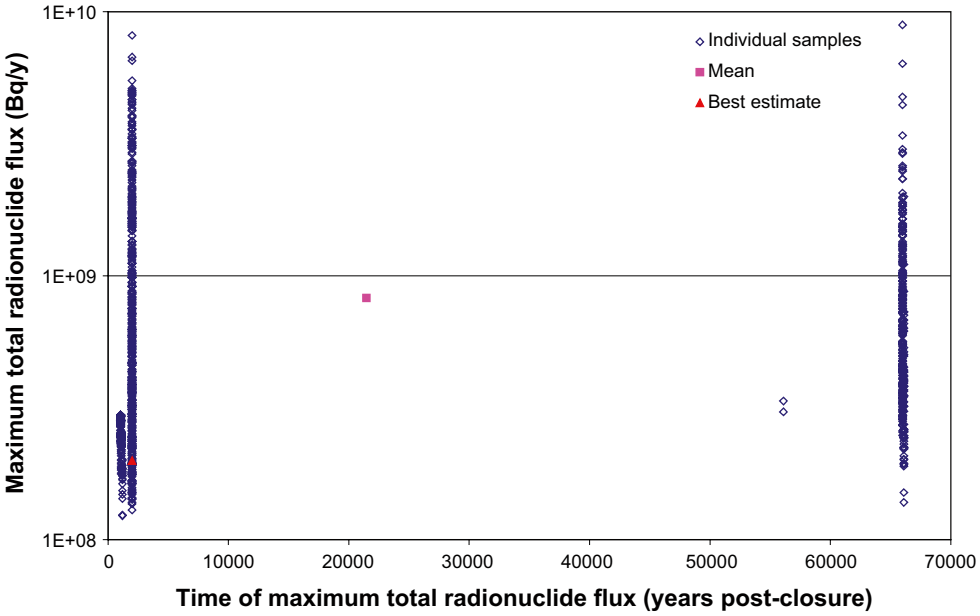

Figure 4-20. *Scatter plot of BMA maximum total geosphere radionuclide flux for CC1.*

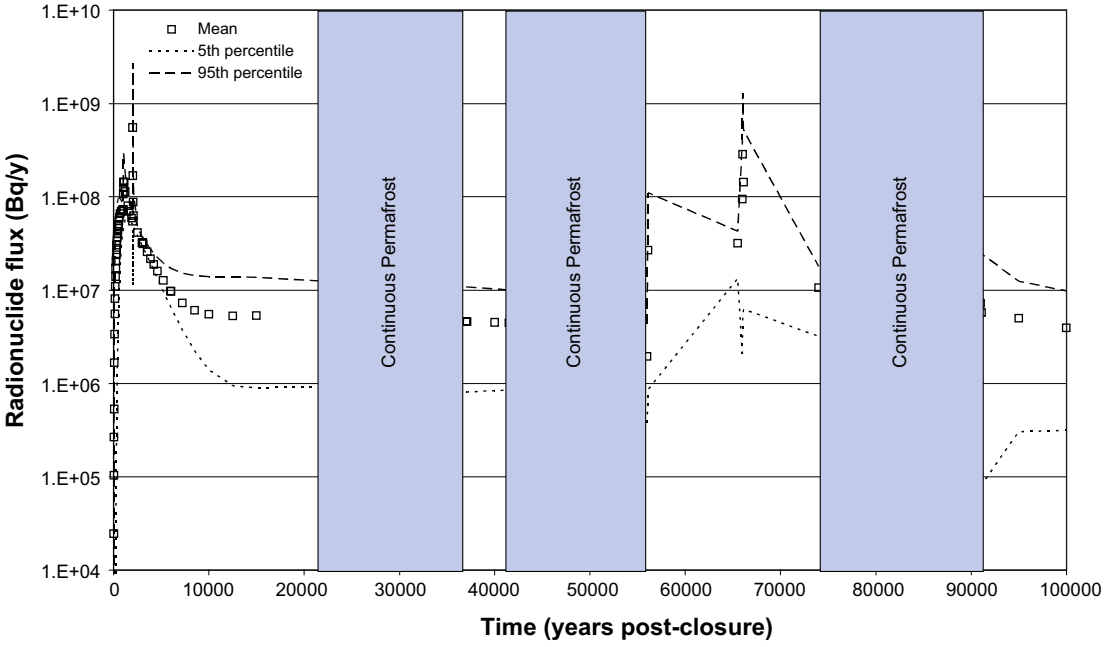

Figure 4-21. *Geosphere total radionuclide flux from the BMA for CC1 calculation using sampled parameters.*

4.1.3 1BTF

Figure 4-22 summaries the best estimate near-field radionuclide flux from the 1BTF disposal tunnel for CC1. Figure 4-23 shows a detailed plot of the period up to 4,000 years post-closure. For the initial 1,000-year period post-closure the radionuclide flux is dominated by releases of organic C-14. Fluxes of the short-lived radionuclides H-3, Sr-90 and Cs-137 reach their maximum values between 50 and 200 years, although these are orders of magnitude below the radionuclide flux of organic C-14. At 1,000 years post-closure the concrete and cement barriers are assumed to degrade and their sorption capacity is reduced to that of sand and gravel media and the groundwater flows through 1BTF also increase. This results in an increase in the release of radionuclides from 1BTF and also a change in the dominant radionuclide to inorganic C-14.

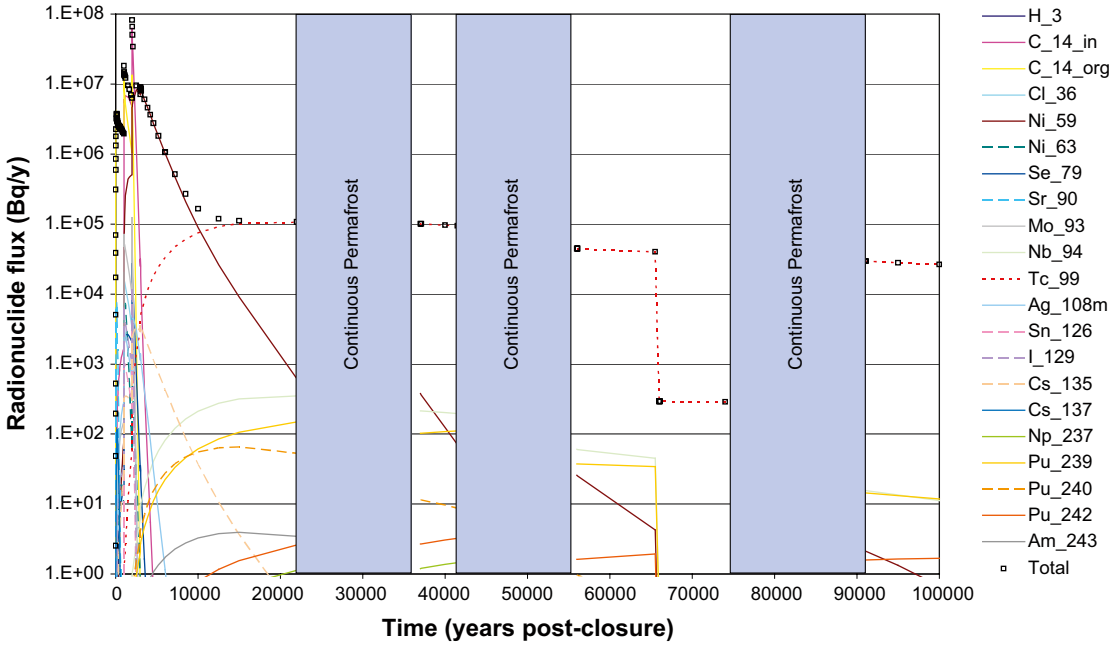

Figure 4-22. *Near-field best estimate flux from 1BTF for CC1.*

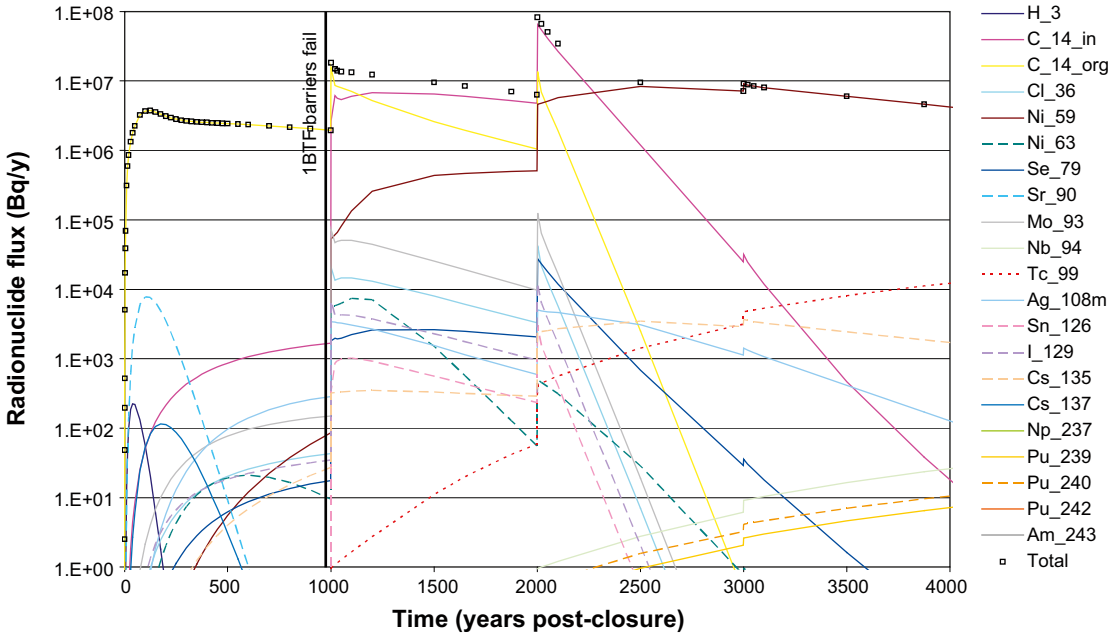

Figure 4-23. *Details of best estimate radionuclide flux from 1BTF to 4,000 years for CC1.*

The maximum total radionuclide is estimated to be $8.3 \cdot 10^7$ Bq/y at 2,000 years post-closure and is dominated by releases of inorganic C-14. At 2,000 years post-closure the groundwater flows through 1BTF increase again and this results in corresponding increases in the radionuclide flux of a number of radionuclides. The release of inorganic C-14 is completed by 5,000 years post-closure as are many other radionuclides as they become depleted. Ni-59 dominates the release profile from around 3,000 to 12,500 years post-closure and thereafter Tc-99 is the major contributor to radionuclide releases. The radionuclide flux beyond 20,000 years post-closure is three orders of magnitude less than the maximum value at 2,000 years post-closure and shows little increase in relation to the environmental changes that are assumed to occur within the latter part of the calculation.

Figure 4-24 below shows a plot of the maximum total near-field radionuclide flux for the 1BTF from each of the individual samples run in the calculation using sampled parameters. Also shown in Figure 4-24 are the mean ($7.8 \cdot 10^7$ Bq/y at approximately 2,000 years post-closure) and the best estimate ($8.3 \cdot 10^7$ Bq/y at approximately 2,000 years post-closure) for comparison.

Overall the maximum total flux varies between $1.6 \cdot 10^7$ and $1.3 \cdot 10^8$ Bq/y and the time of the maximum varies between approximately 1,000 and 2,500 years post-closure.

Figure 4-25 is a summary plot of the near-field radionuclide flux for the 1BTF for evaluation of CC1 using sampled parameters. The figure shows the mean of the total radionuclide flux and the 5th and 95th percentiles. Comments made previously in relation to the over-estimate of the lower range due to omitted processes apply here.

Figure 4-26 shows the geosphere radionuclide flux from the 1BTF. The maximum radionuclide flux is estimated to be $5.6 \cdot 10^7$ Bq/y at approximately 2,100 years post-closure and is due to contributions from inorganic C-14. Generally the geosphere flux shows similar trends to that described for the BMA. The breakthrough curves show tailing due to the effects of matrix diffusion and sorption, radioactive decay reduces the magnitude of the emergent fluxes, particularly for short-lived radionuclides. The transition in geosphere conditions at 2,000 years post-closure is evident again in the timing of the peak flux and also in the long-term behaviour at 66,000 years post-closure (Figures 4-26 and 4-27). A significant difference is the relative role of Ni-59 and Tc-99 in contributing to the long-term radionuclide flux. Tc-99 is more significant for 1BTF compare to the BMA due to the relatively higher amounts of Tc-99 compared to Ni-59 in 1BTF.

Figure 4-28 below shows a plot of the maximum total geosphere radionuclide flux for the 1BTF from each of the individual samples run in the calculation using sampled parameters. Also shown in Figure 4-28 are the mean ($8.9 \cdot 10^7$ Bq/y at approximately 2,000 years post-closure) and the best estimate ($5.6 \cdot 10^7$ Bq/y at approximately 2,100 years post-closure) for comparison. More variation is evident than for the near-field flux, the maximum total flux varies between $3.0 \cdot 10^6$ and $1.0 \cdot 10^9$ Bq/y and the time of the maximum varies between 1,000 and 3,100 years post-closure, with majority of values around 2,000 years post-closure.

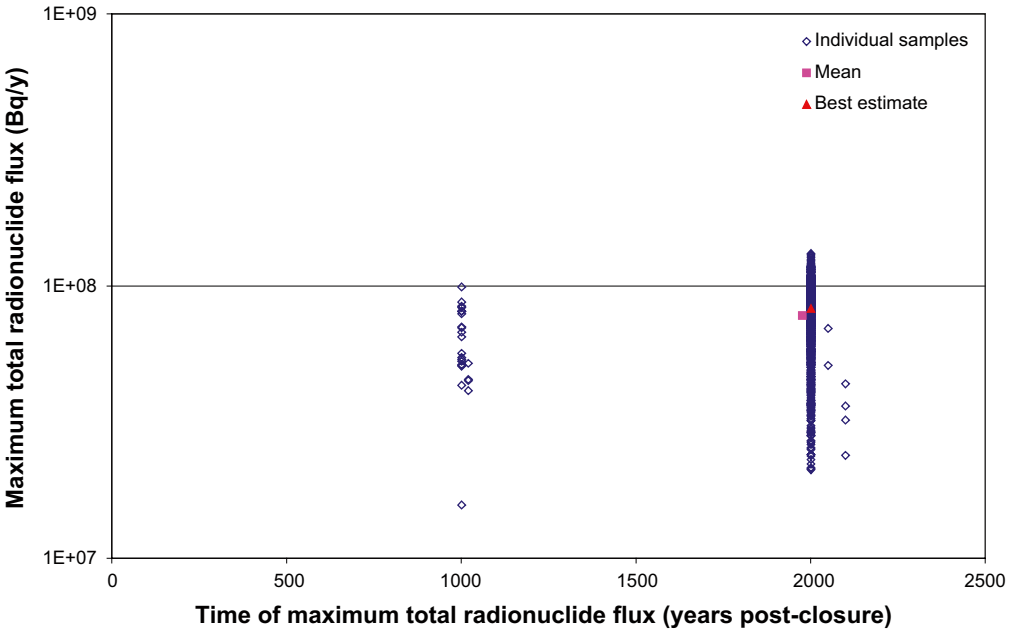

Figure 4-24. *Scatter plot of 1BTF maximum total near-field radionuclide flux for CC1.*

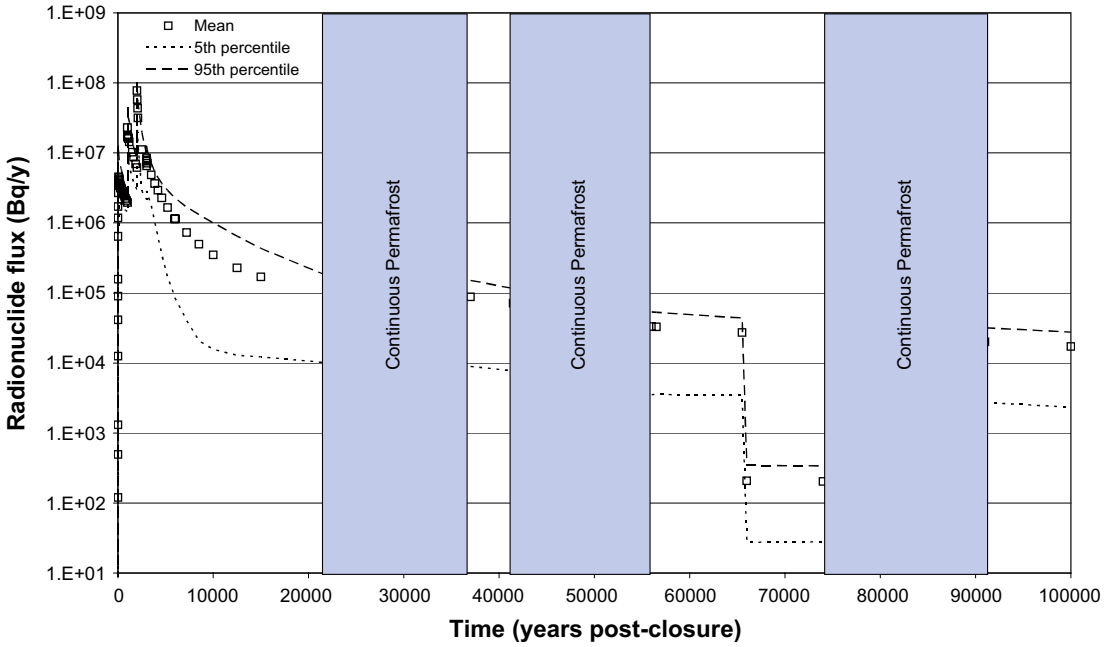

Figure 4-25. *Near-field total radionuclide flux from the 1BTF for CC1 using sampled parameters.*

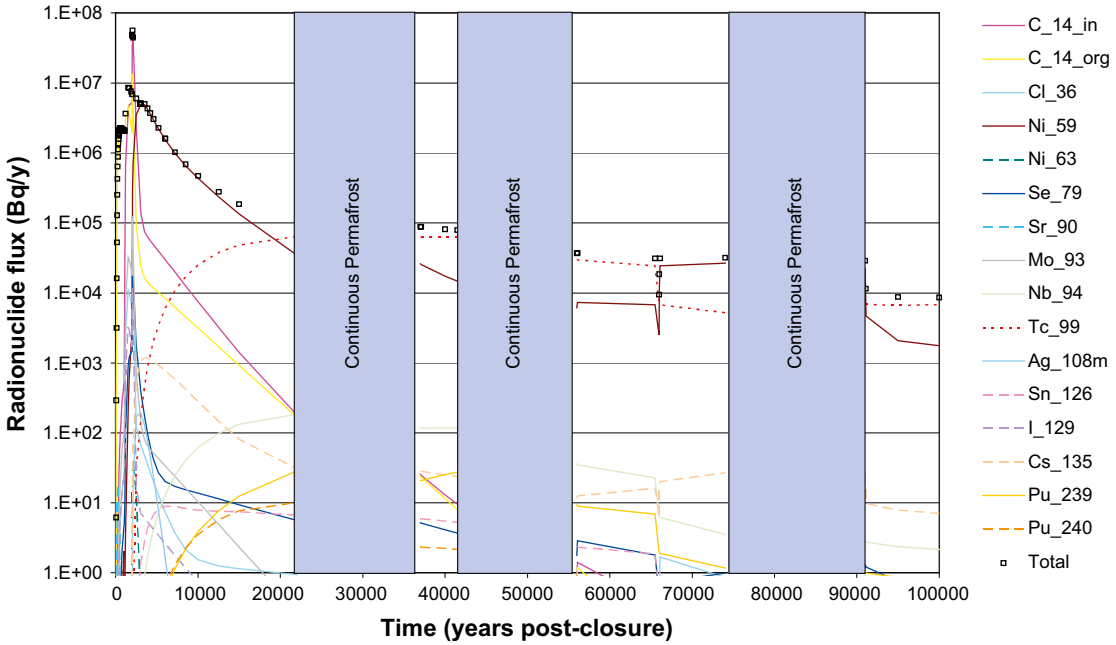

Figure 4-26. *Geosphere best estimate flux from 1BTF for CC1.*

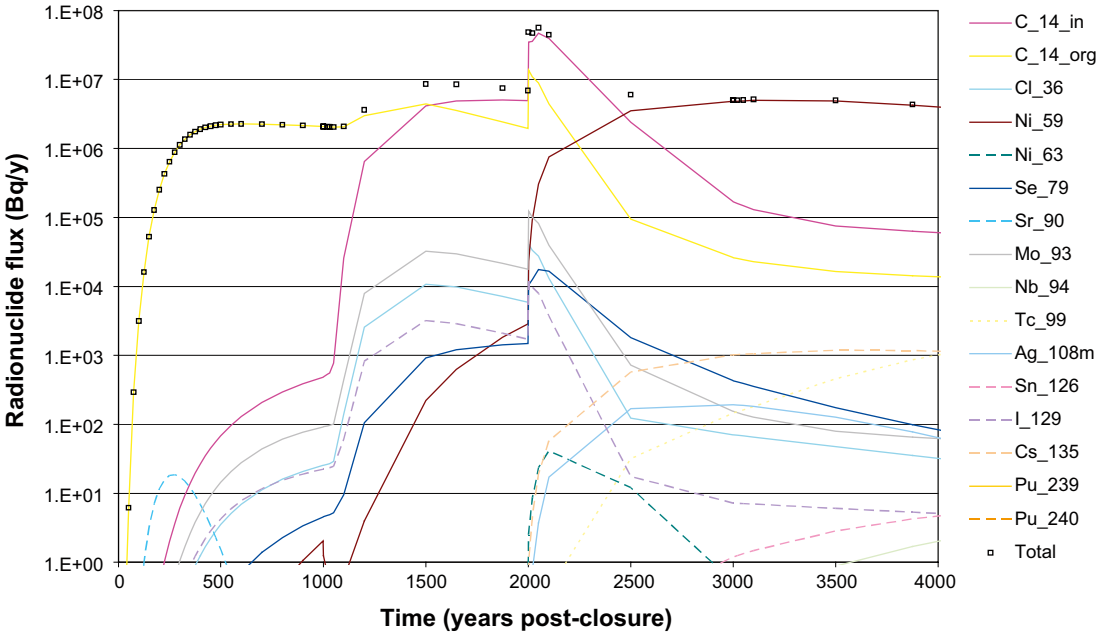

Figure 4-27. *Details of best estimate geosphere flux from 1BTF to 4,000 years for CC1.*

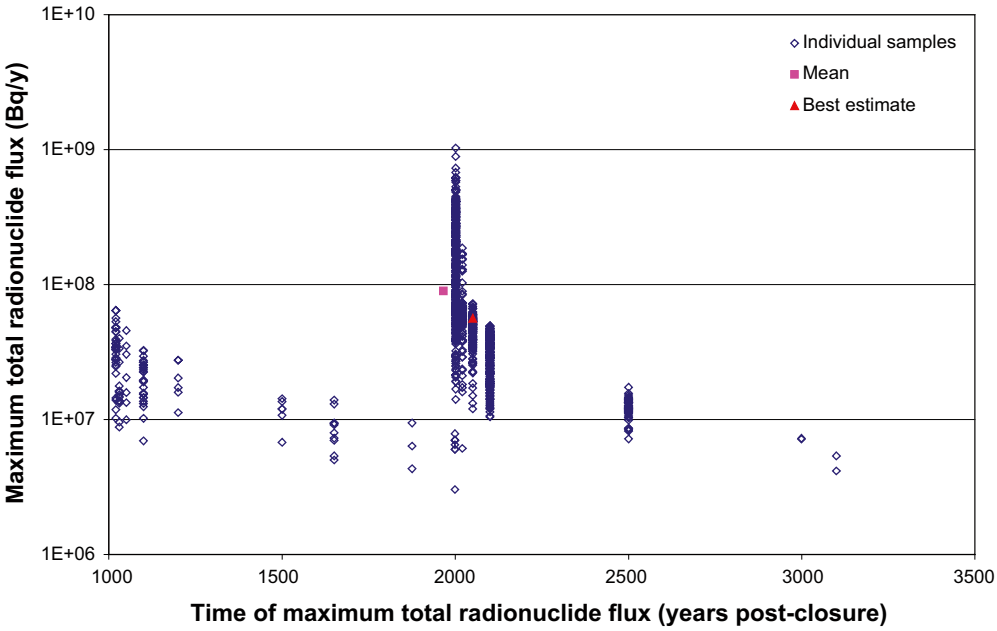

Figure 4-28. *Scatter plot of 1BTF maximum total geosphere radionuclide flux for CC1.*

Figure 4-29 is a summary plot of the geosphere radionuclide flux for the 1BTF for evaluation of CC1 using sampled parameters. The figure shows the mean of the total radionuclide flux and the 5th and 95th percentiles. Comments made previously in relation to the over-estimate of the lower range due to omitted processes apply here.

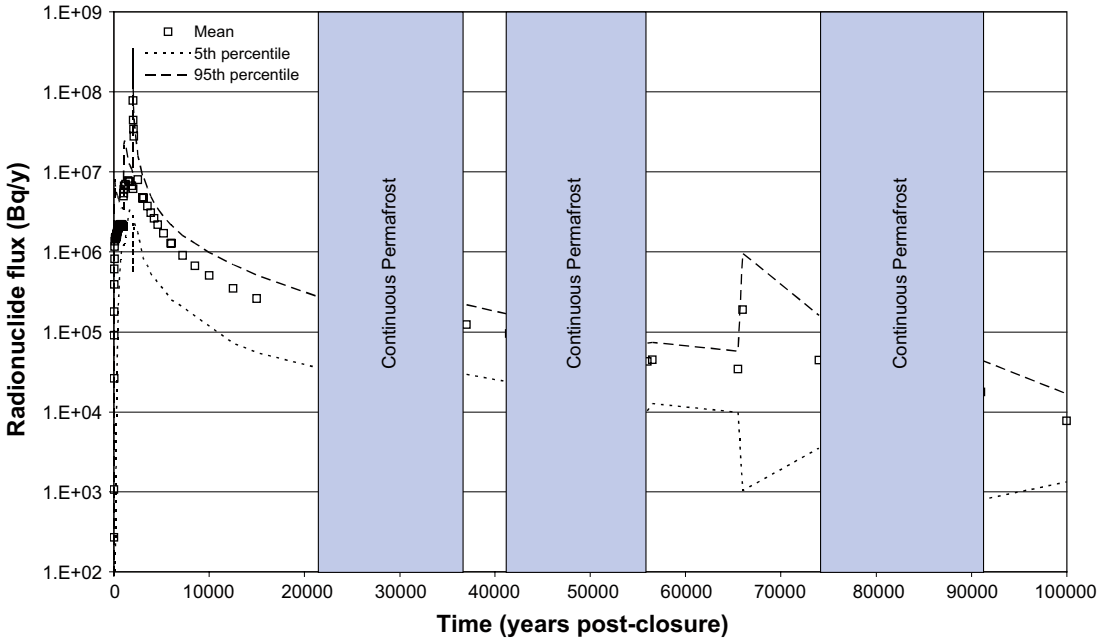

Figure 4-29. *Geosphere total radionuclide flux from the 1BTF for CC1 using sampled parameters.*

4.1.4 2BTF

Figure 4-30 summaries the best estimate near-field radionuclide flux from the 2BTF disposal tunnel for CC1. The trends show a similar pattern to those described for releases from 1BTF.

Figure 4-31 shows a detailed plot of the period up to 4,000 years post-closure. For the initial 1,000-year period post-closure the radionuclide flux is dominated by releases of organic C-14. Fluxes of the short-lived radionuclides H-3, Sr-90 and Cs-137 reach their maximum values between 50 and 200 years. At 1,000 years post-closure the concrete and cement barriers are assumed to become degraded and their sorption capacity is reduced to that of sand and gravel media and the groundwater flows through 2BTF also increase.

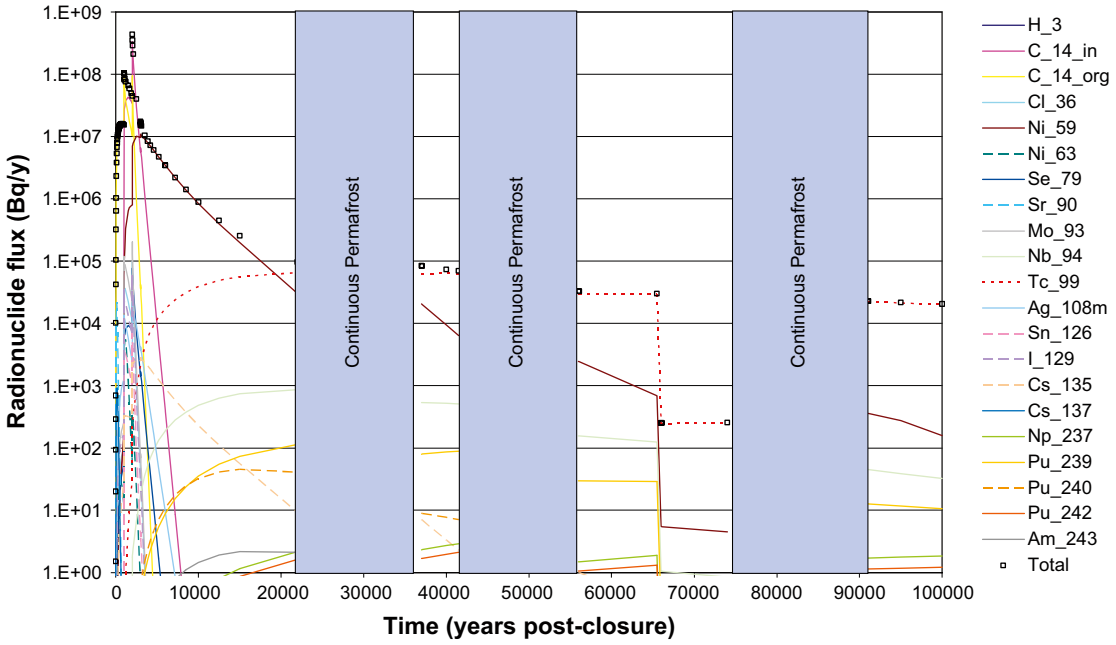

Figure 4-30. *Near-field best estimate flux from 2BTF for CC1.*

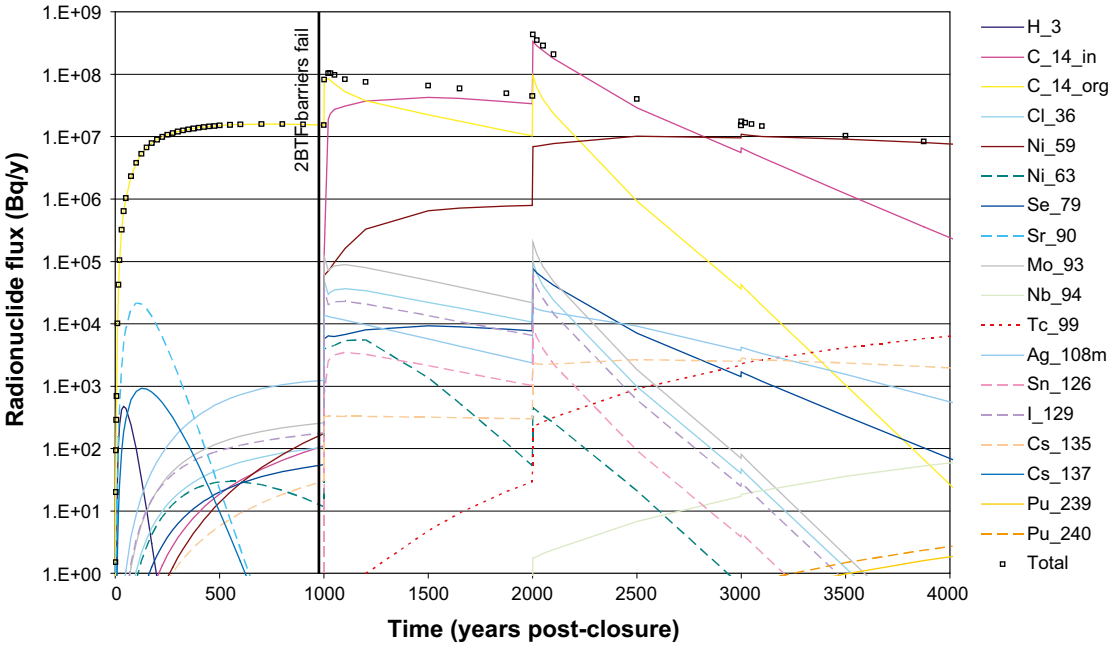

Figure 4-31. *Details of best estimate near-field radionuclide flux from 2BTF to 4,000 years for CC1.*

The maximum total radionuclide is estimated to be $4.4 \cdot 10^8$ Bq/y at 2,000 years post-closure and is dominated by releases of inorganic C-14[15]. At 2,000 years post-closure the groundwater flows through 2BTF increase significantly resulting in a significant increase in the radionuclide flux of a number of radionuclides. The release of inorganic C-14 is completed by 9,000 years post-closure as are many other radionuclides as they become depleted. Ni-59 dominates the release profile from around 3,000 to 12,500 years post-closure and thereafter Tc-99 is the major contributor to radionuclide releases. The radionuclide flux beyond 20,000 years post-closure is over three orders of magnitude below the maximum value at 2,000 years post-closure.

Figure 4-32 below shows a plot of the maximum total near-field radionuclide flux for the 2BTF from each of the individual samples in the calculation using sampled parameters. Also shown in Figure 4-32 are the mean ($3.7 \cdot 10^8$ Bq/y at approximately 2,000 years post-closure) and the best estimate ($4.4 \cdot 10^8$ Bq/y at approximately 2,000 years post-closure) for comparison. Overall the maximum total flux varies between $8.1 \cdot 10^7$ and $5.6 \cdot 10^8$ Bq/y and the time of the maximum varies between approximately 1,000 and 2,500 years post-closure. The spread of results at 2,000 years post-closure is most likely due to the variation in Uncertainty factors (2.73 to 12.8) and their effects of the near-field flow fields.

Figure 4-33 is a summary plot of the near-field radionuclide flux for the 2BTF for evaluation of CC1 using sampled parameters. The figure shows the mean of the total radionuclide flux and the 5th and 95th percentiles. Comments made previously in relation to the over-estimate of the lower range due to omitted processes apply here.

[15] This near-field radionuclide flux is higher than the maximum flux from 1BTF which is also dominated by inorganic C-14. The disposal inventory of inorganic C-14 from 50 years of reactor operations is estimated to be larger in 2BTF than 1BTF.

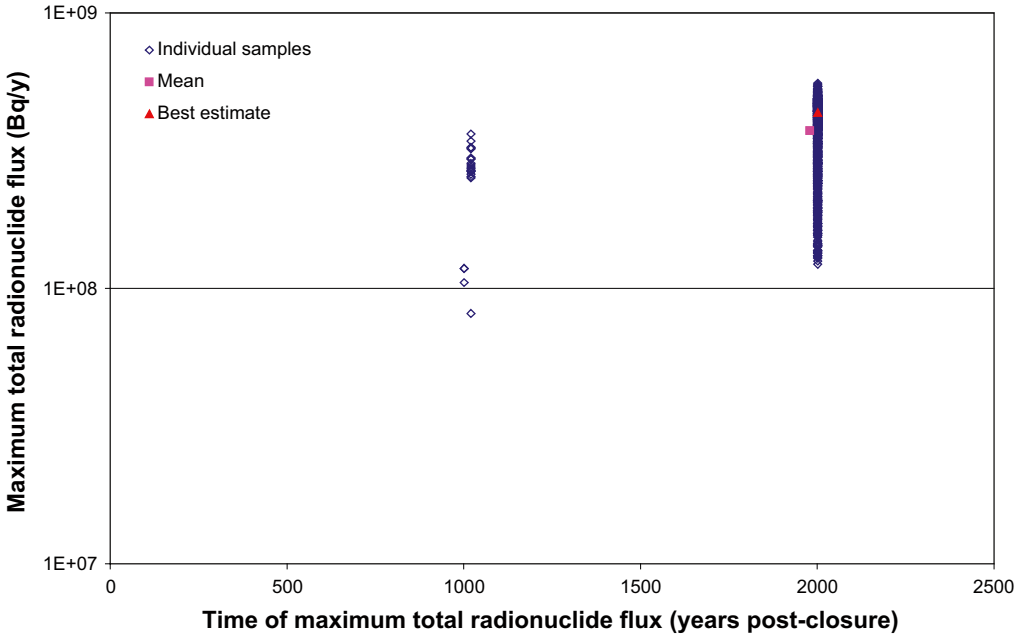

Figure 4-32. *Scatter plot of 2BTF maximum total near-field radionuclide flux for CC1.*

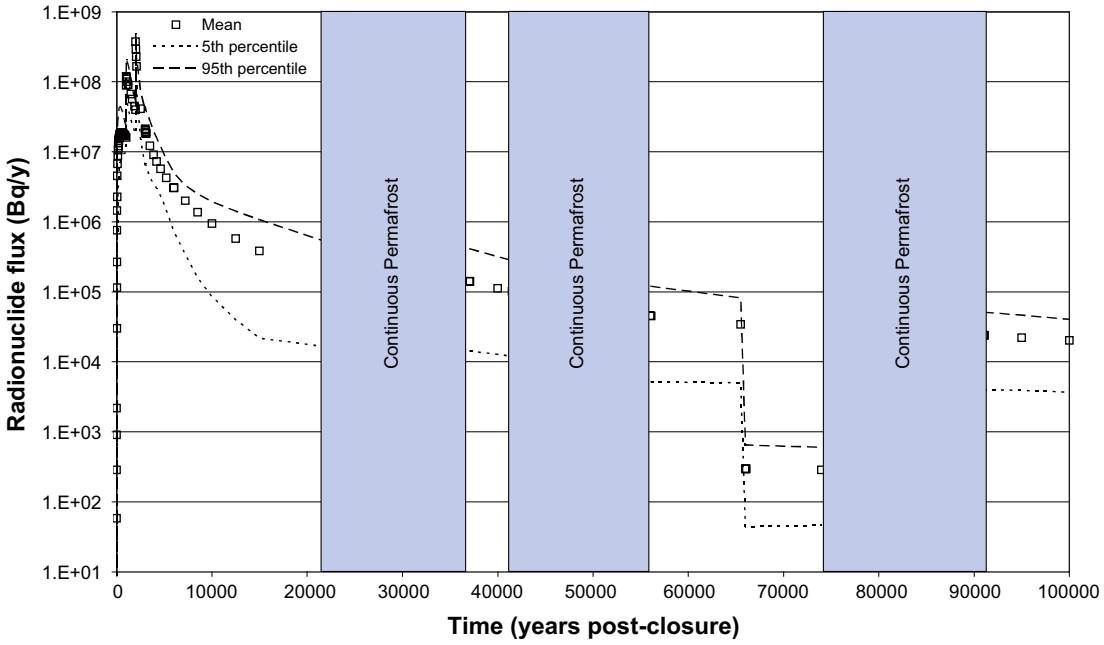

Figure 4-33. *Near-field total radionuclide flux from the 2BTF for CC1 using sampled parameters.*

Figure 4-34 shows the best estimate geosphere radionuclide flux from the 2BTF. The maximum radionuclide flux is estimated to be $3.7 \cdot 10^8$ Bq/y at 2,100 years post-closure and is due to contributions from inorganic C-14. Generally the geosphere flux shows similar trends to that described for 1BTF.

Figure 4-35 below shows a plot of the maximum total geosphere radionuclide flux for the 2BTF from each of the individual samples in the calculation using sampled parameters. Also shown in Figure 4-35 are the mean ($6.9 \cdot 10^8$ Bq/y at approximately 2,000 years post-closure) and the best estimate ($3.7 \cdot 10^8$ Bq/y at approximately 2,100 years post-closure) for comparison.

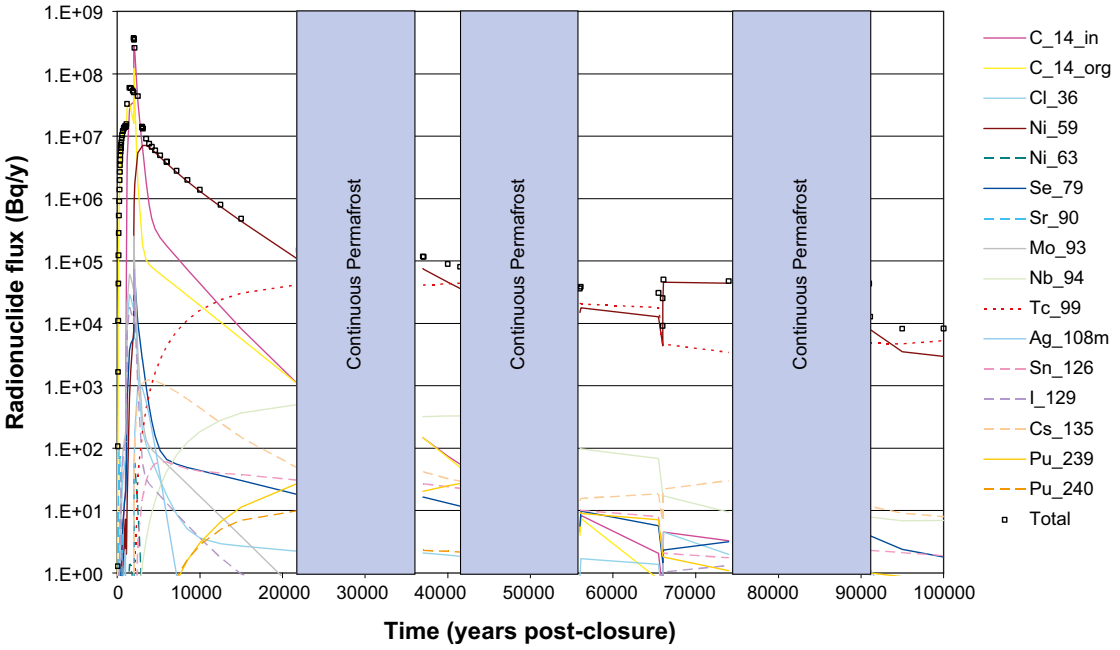

Figure 4-34. *Geosphere best estimate flux from the 2BTF for CC1.*

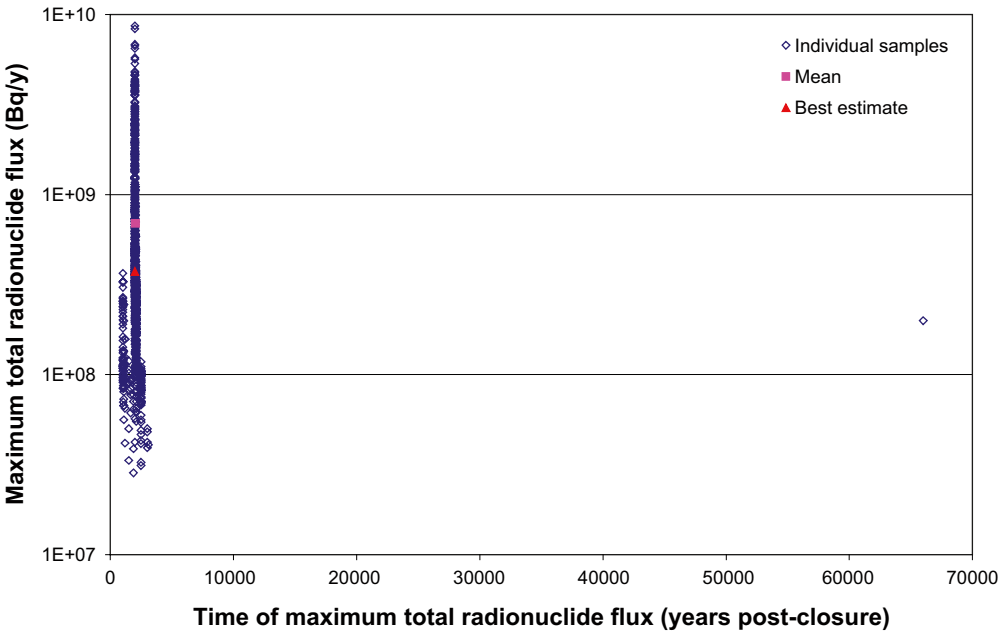

Figure 4-35. *Scatter plot of 2BTF maximum total geosphere radionuclide flux for CC1.*

More variation is evident than for the near-field flux, the maximum total flux varies between $2.9 \cdot 10^7$ and $8.7 \cdot 10^9$ Bq/y and the time of the maximum varies between 1,100 and 66,000 years post-closure, with a cluster of values around 2,000 years post-closure.

Figure 4-36 is a summary plot of the geosphere radionuclide flux for 2BTF for evaluation of CC1 using sampled parameters. The figure shows the mean of the total radionuclide flux and the 5th and 95th percentiles. Comments made previously in relation to the over-estimate of the lower bound due to omitted processes apply here.

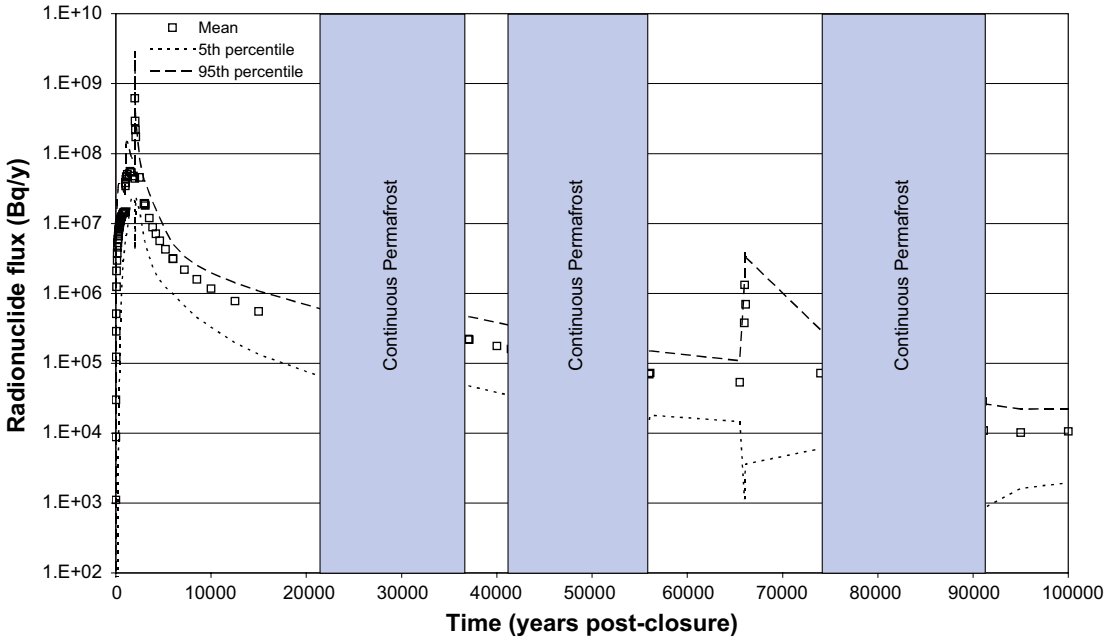

Figure 4-36. *Geosphere total radionuclide flux from the 2BTF for CC1 using sampled parameters.*

4.1.5 BLA

Figure 4-37 summaries the best estimate near-field radionuclide flux from the BLA disposal tunnel for CC1 (N.B note the truncated time period). For the purposes of the assessment calculations it has been assumed that the BLA has no barriers. Therefore the maximum total radionuclide flux occurs on closure, is estimated to be $6.3 \cdot 10^8$ Bq/y and is dominated by releases of Ni-63 for the initial 600 years. During this initial phase fluxes of Co-60 and Cs-137 are also important. Inorganic C-14 is the dominant radionuclide from approximately 700 years post-closure until 4,000 years post-closure at which point the total radionuclide flux from the BLA is below 1 Bq/y.

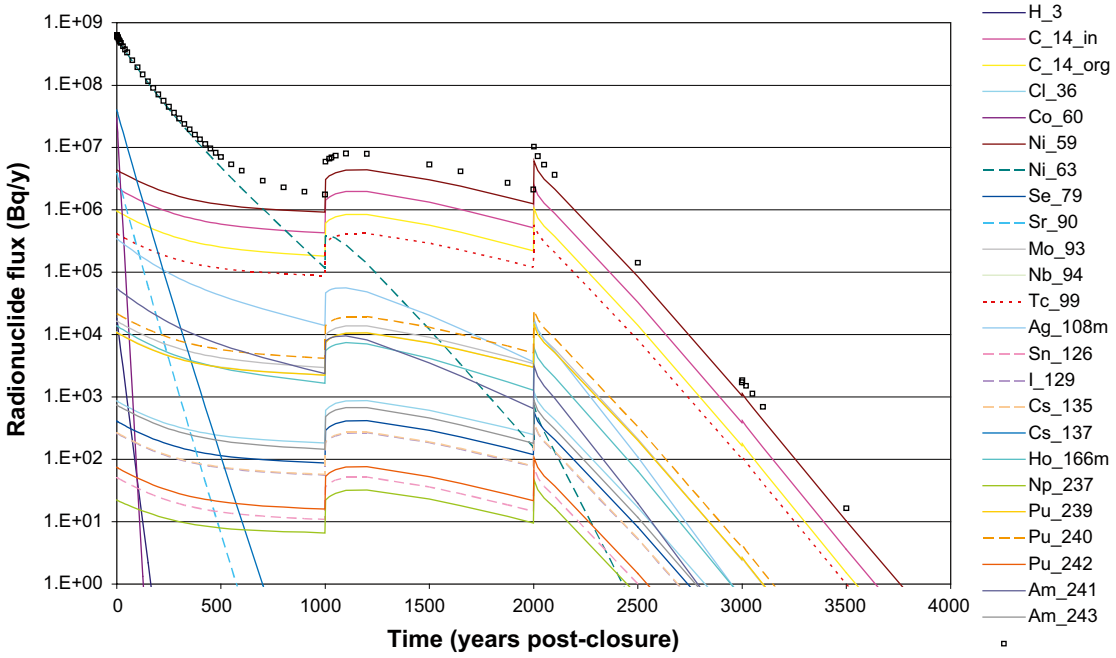

Figure 4-37. *Near-field best estimate flux from BLA for CC1.*

Overall little variation is evident in the results from the calculation using sampled parameters. The mean maximum total flux is $7.9 \cdot 10^8$ Bq/y and it varies between $3.5 \cdot 10^8$ and $1.8 \cdot 10^9$ Bq/y. In all cases the maximum value occurs on closure of the facility.

Figure 4-38 is a summary plot of the near-field radionuclide flux for the BLA for evaluation of CC1 using sampled parameters. The figure shows the mean of the total radionuclide flux and the 5th and 95th percentiles. Comments made previously in relation to the over-estimate of the lower bound due to omitted processes apply here.

Figures 4-39 and 4-40 show the best estimate geosphere radionuclide flux from the BLA. The maximum radionuclide flux is estimated to be $1.4 \cdot 10^8$ Bq/y at 75 years post-closure and is dominated by contributions from Ni-63. The dominant radionuclide continues to be Ni-63 until 600 years post-closure. From 600 to 2,500 years post-closure inorganic C-14 is the most important radionuclide in terms of the flux from the BLA, thereafter Ni-59 dominates the radionuclide release profile from the BLA.

Figure 4-41 below shows a plot of the maximum total geosphere radionuclide flux for the BLA from each of the individual samples run in the calculation using sampled parameters. Also shown in Figure 4-41 are the mean ($2.1 \cdot 10^8$ Bq/y at approximately 680 years post-closure) and the best estimate ($1.5 \cdot 10^8$ Bq/y at approximately 75 years post-closure) for comparison. The maximum total flux varies between $5.1 \cdot 10^6$ and $1.3 \cdot 10^9$ Bq/y and the time of the maximum varies between 5 and 2,500 years post-closure, with a cluster of values around the best estimate.

Figure 4-42 is a summary plot of the geosphere radionuclide flux for the BLA for evaluation of CC1 using sampled parameters. The figure shows the mean of the total radionuclide flux and the 5th and 95th percentiles. Comments made previously in relation to the over-estimate of the lower bound due to omitted processes apply here.

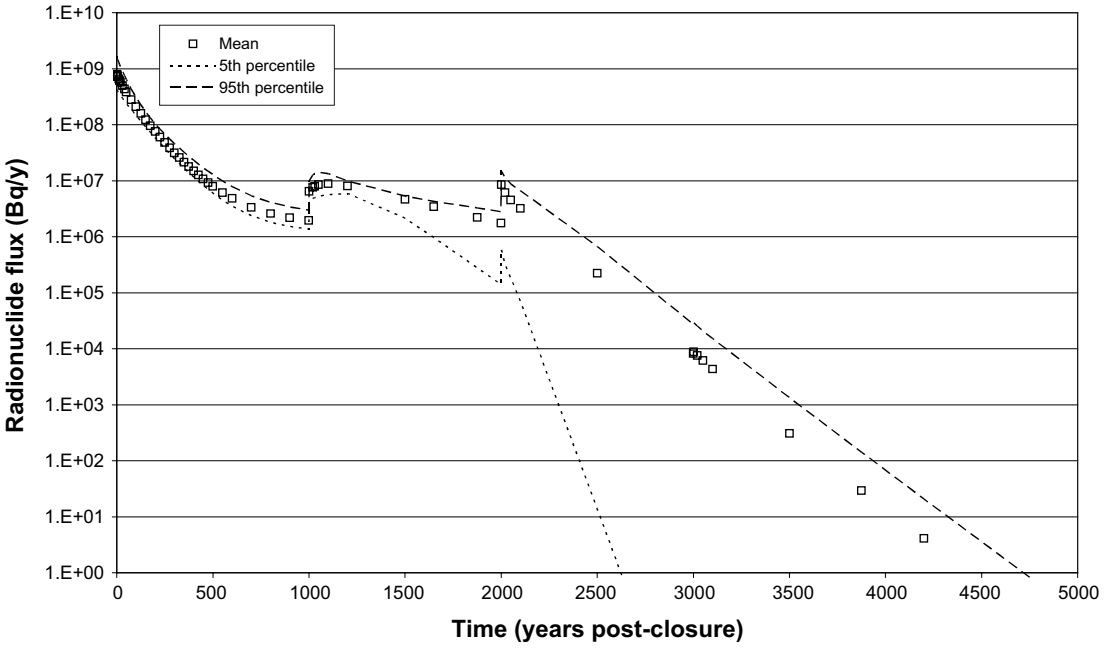

Figure 4-38. *Near-field total radionuclide flux from the BLA for CC1 using sampled parameters.*

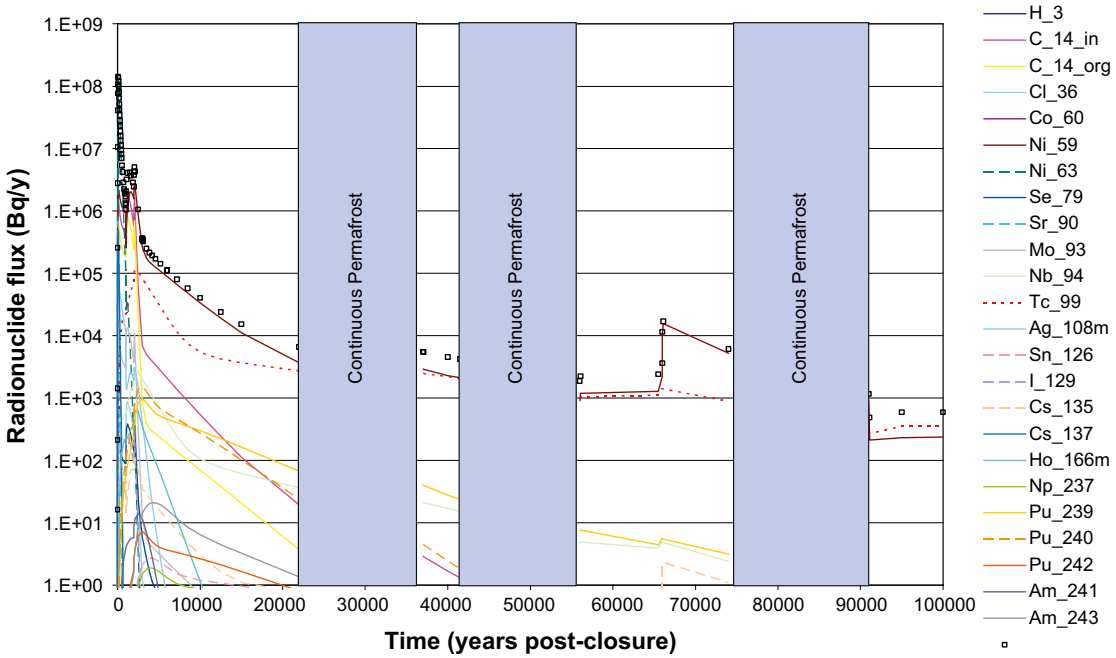

Figure 4-39. *Geosphere best estimate flux from BLA for CC1.*

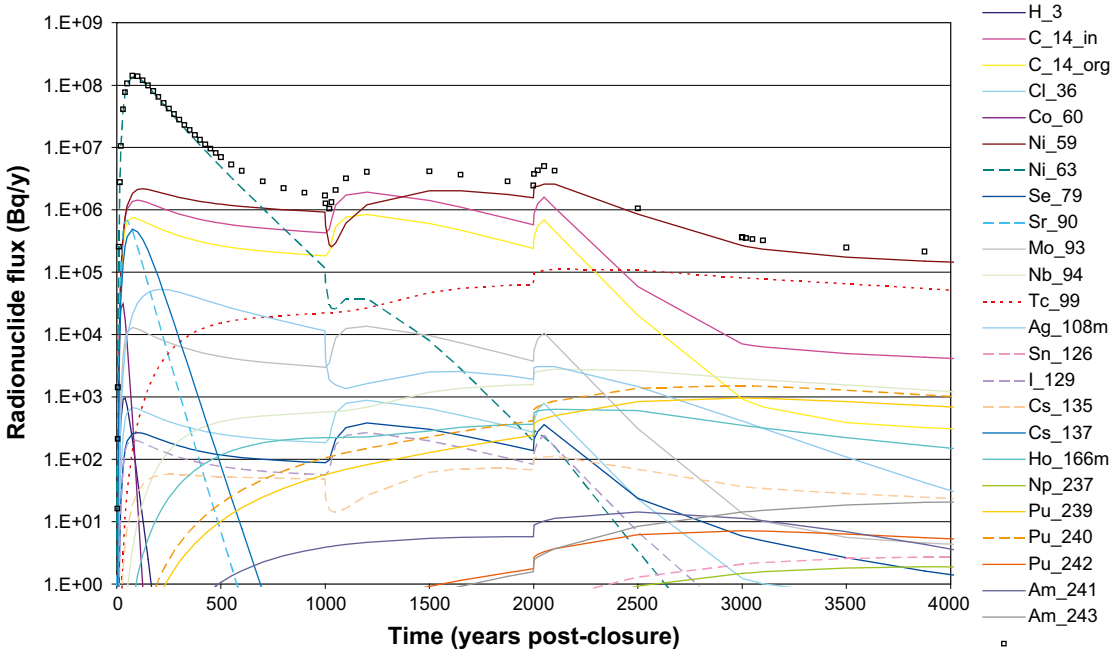

Figure 4-40. *Detail of best estimate geosphere flux from BLA to 4,000 years for CC1.*

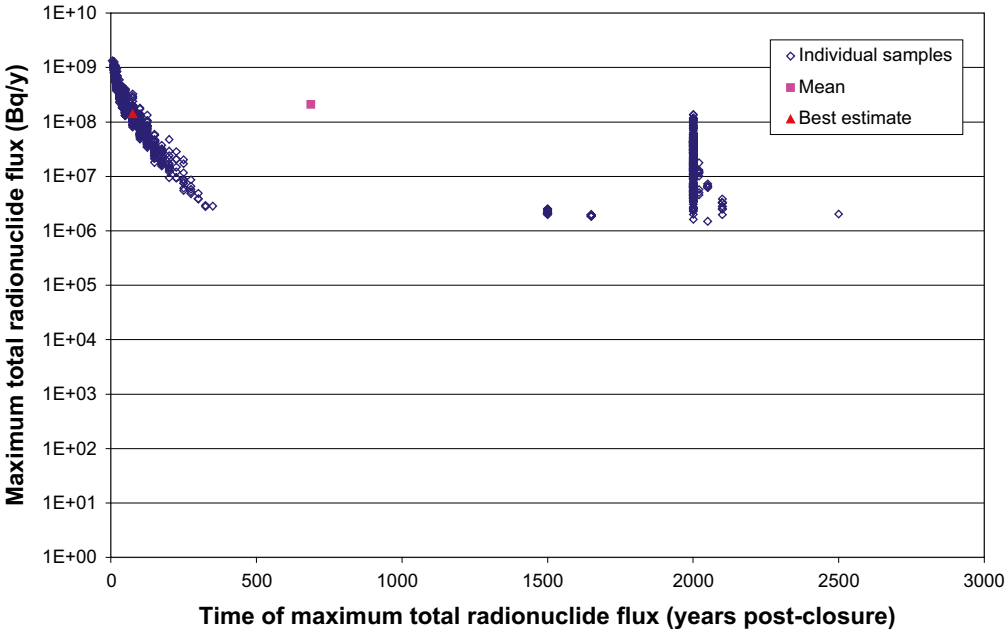

Figure 4-41. *Scatter plot of BLA maximum total geosphere radionuclide flux for CC1.*

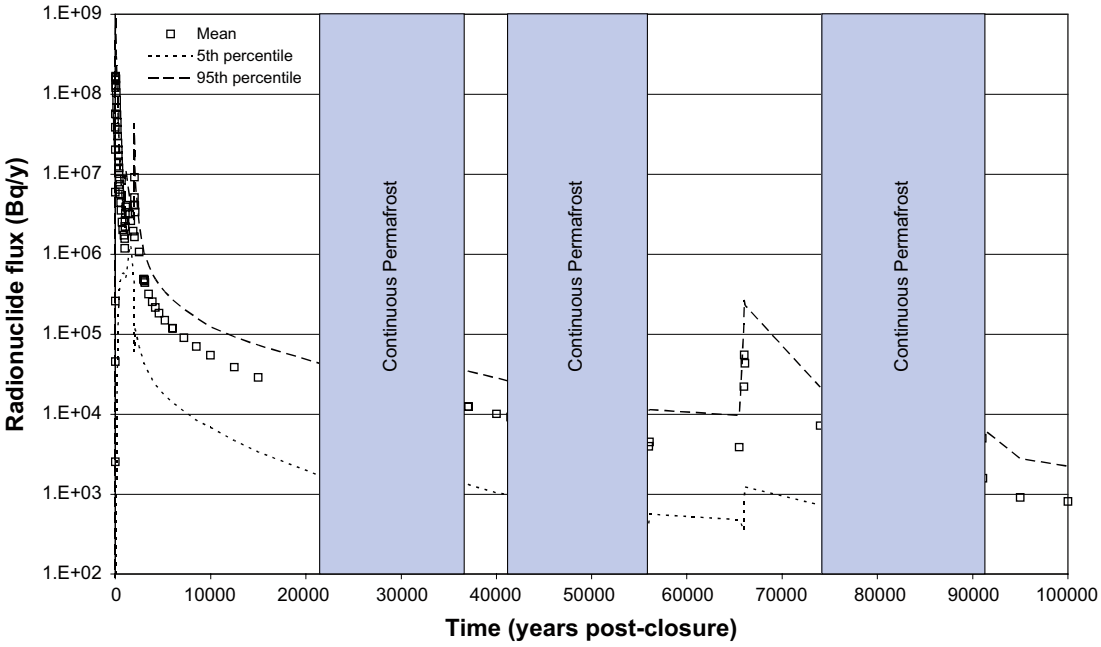

Figure 4-42. *Geosphere total radionuclide flux from the BLA for CC1 using sampled parameters.*

4.1.6 SFR 1

Table 4-1 reports the peak fluxes for the near-field and geosphere for each disposal facility; summarise the magnitude and timing of the peak and the dominant contributor. Generally it can be seen that the peak radionuclide fluxes are estimated to occur within the first 3,000 years following closure of the facility. The key factor for the Silo and BMA and BTF tunnels is the evolution of hydrogeological regime and its impact on the rate of flow through the individual disposal facilities of the repository. The BLA is not assumed to contain any barriers and the peak fluxes from this facility occur on closure.

Table 4-1. Summary of results from CC1 showing maximum flux and time of peak flux in years after closure.

	Near-field		Geosphere	
Silo	Best estimate	$2.8 \cdot 10^{7}$ Bq/y at 3,000 years (Organic C-14)	Best estimate	$1.0 \cdot 10^{8}$ Bq/y at 2,000 years (Organic C-14)
	Mean	$3.0 \cdot 10^{7}$ Bq/y at 3,000 years	Mean	$1.2 \cdot 10^{8}$ Bq/y at 2,600 years
	Range of max.	$2.0 \cdot 10^{7}$ Bq/y–$4.8 \cdot 10^{7}$ Bq/y	Range of max.	$9.4 \cdot 10^{6}$ Bq/y–$1.3 \cdot 10^{9}$ Bq/y
BMA	Best estimate	$2.8 \cdot 10^{8}$ Bq/y at 1,100 years (Organic C-14)	Best estimate	$2.0 \cdot 10^{8}$ Bq/y at 2,000 years (Organic C-14)
	Mean	$3.0 \cdot 10^{8}$ Bq/y at 11,000 years	Mean	$8.2 \cdot 10^{8}$ Bq/y at 21,000 years
	Range of max.	$2.6 \cdot 10^{8}$ Bq/y–$7.8 \cdot 10^{8}$ Bq/y	Range of max.	$1.2 \cdot 10^{8}$ Bq/y–$8.9 \cdot 10^{9}$ Bq/y
1BTF	Best estimate	$8.3 \cdot 10^{7}$ Bq/y at 2,000 years (Inorganic C-14)	Best estimate	$5.6 \cdot 10^{7}$ Bq/y at 2,100 years (Inorganic C-14)
	Mean	$7.8 \cdot 10^{7}$ Bq/y at 2,000 years	Mean	$8.9 \cdot 10^{7}$ Bq/y at 2,000 years
	Range of max.	$1.6 \cdot 10^{7}$ Bq/y–$1.3 \cdot 10^{8}$ Bq/y	Range of max.	$3.0 \cdot 10^{6}$ Bq/y–$1.0 \cdot 10^{9}$ Bq/y
2BTF	Best estimate	$4.4 \cdot 10^{8}$ Bq/y at 2,000 years (Inorganic C-14)	Best estimate	$3.7 \cdot 10^{8}$ Bq/y at 2,100 years (Inorganic C-14)
	Mean	$3.7 \cdot 10^{8}$ Bq/y at 2,000 years	Mean	$6.9 \cdot 10^{8}$ Bq/y at 2,000 years
	Range of max.	$8.1 \cdot 10^{7}$ Bq/y–$5.6 \cdot 10^{8}$ Bq/y	Range of max.	$2.9 \cdot 10^{7}$ Bq/y–$8.7 \cdot 10^{9}$ Bq/y
BLA	Best estimate	$6.3 \cdot 10^{8}$ Bq/y at 0 years (Ni-63)	Best estimate	$1.4 \cdot 10^{8}$ Bq/y at 75 years (Ni-63)
	Mean	$7.9 \cdot 10^{8}$ Bq/y at 0 years	Mean	$2.1 \cdot 10^{8}$ Bq/y at 690 years
	Range of max.	$3.5 \cdot 10^{8}$ Bq/y–$1.8 \cdot 10^{9}$ Bq/y	Range of max.	$1.5 \cdot 10^{6}$ Bq/y–$1.3 \cdot 10^{9}$ Bq/y

The barrier properties of the geosphere can be significant for the short-lived radionuclides such as H-3, Sr-90, Cs-137 and may also reduce the fluxes of Ni-63 and Ag-108m that reach the biosphere. This is particularly the case for the BLA which is not assumed to contain any barriers and therefore peak fluxes from this facility are estimated to occur on closure.

4.1.7 Comparison with Project SAFE

Figure 4-43 below shows a comparison of the best estimate radionuclides fluxes from the Silo for Project SAFE and SAR-08[16]. The main differences between the models are attributed to the combined effects of the following.

- The estimate of the amounts of organic C-14 to be disposed in the Silo inventory is decreased in SAR-08 ($1.4 \cdot 10^{12}$ Bq) by a factor of 0.8 relative to Project SAFE ($1.8 \cdot 10^{12}$ Bq).
- The estimates of disposal inventory for many other radionuclides which contribute to the overall release from the Silo inventory in SAR-08 are reduced by an order of magnitude or more; Cl-36 (reduced by a factor of approximately 40), Ni-59 (reduced by a factor of approximately 3), Se-79 (reduced by a factor of approximately 20), Mo-93 (reduced by a factor of approximately 40), Ag-108m (reduced by a factor of approximately 10), Cs-135 (reduced by a factor of approximately 20), Cs-137 (reduced by a factor of approximately 20).
- The reduced effective diffusivity of intact concrete in SAR-08 which delays the breakthrough of radionuclides.
- A reduction in the SAR-08 near-field flow fields up to 2,000 years post-closure resulting from the use of the Uncertainty factors.
- The increased sorption capacity onto bentonite for Ni, Se and Cs resulting from the use of updated values from SR-Can.

[16] It should be noted that the time axis in the figure is linear and the timescale is truncated at 10,000 years post-closure to aid comparison with the results of Project SAFE /Lindgren et al. 2001/.

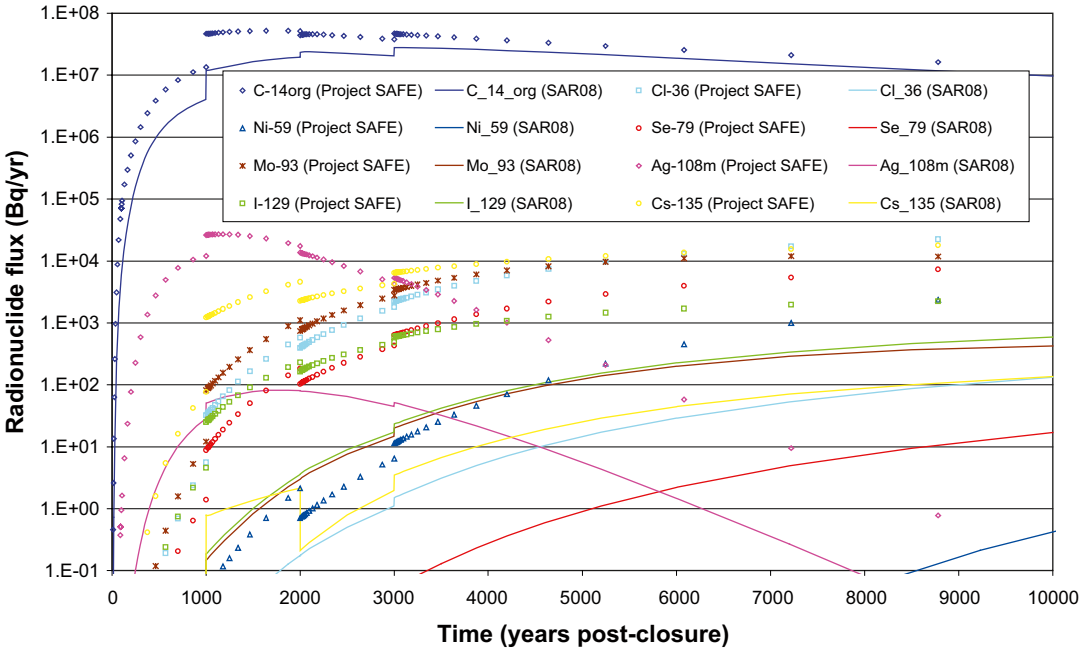

Figure 4-43. *Comparison of best estimate radionuclides fluxes from Silo for Project SAFE and SAR-08.*

- The reconfiguration of releases from the base of the model so they occur from the bottom compartment.

Additionally there have been changes to the conceptual model of release from bituminous wastes (Appendix A).

Figure 4-44 below shows a comparison of the best estimate radionuclides fluxes from the BMA for Project SAFE and SAR-08. The main differences between the models are attributed to the combined effects of the following.

- The estimates of disposal inventories in SAR-08 for inorganic C-14 have decreased by a factor of 2.5 and for organic have increased by a factor of 2.
- The estimates of disposal inventory for many other radionuclides which contribute to the overall release from the BMA inventory in SAR-08 are reduced: Se-79 (reduced by a factor of approximately 6); Sr-90 (reduced by a factor of approximately 8); Tc-99 (reduced by a factor of approximately 45); Ag-108m (reduced by a factor of approximately 6) and Cs-135 (reduced by a factor of approximately 20).
- An increase in the SAR-08 near-field flow fields resulting from the use of the Uncertainty factors.
- The reduced effective diffusivity of intact concrete in SAR-08 which delays the breakthrough of radionuclides.

Additional factors may include the changes to the conceptual model of release from wastes (see Appendix A).

Figure 4-45 below shows a comparison of the best estimate radionuclides fluxes from 1BTF for Project SAFE and SAR-08. The main differences between the models are attributed to the combined effects of the following.

- The reduced effective diffusivity of intact concrete in SAR-08 which delays the breakthrough of radionuclides.

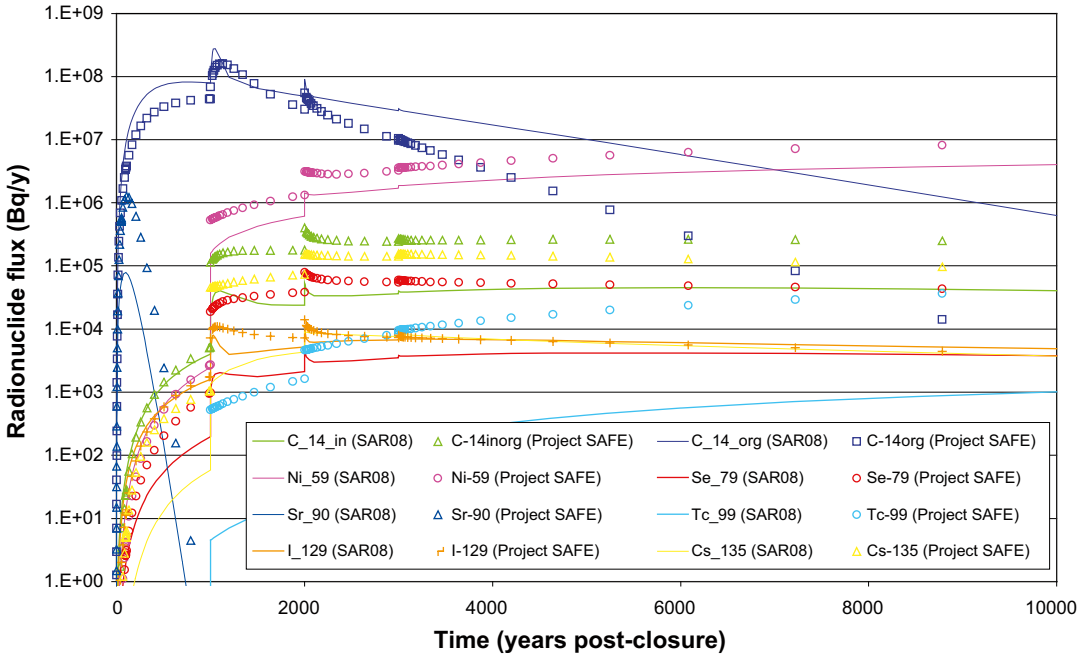

Figure 4-44. *Comparison of best estimate radionuclides fluxes from BMA for Project SAFE and SAR-08.*

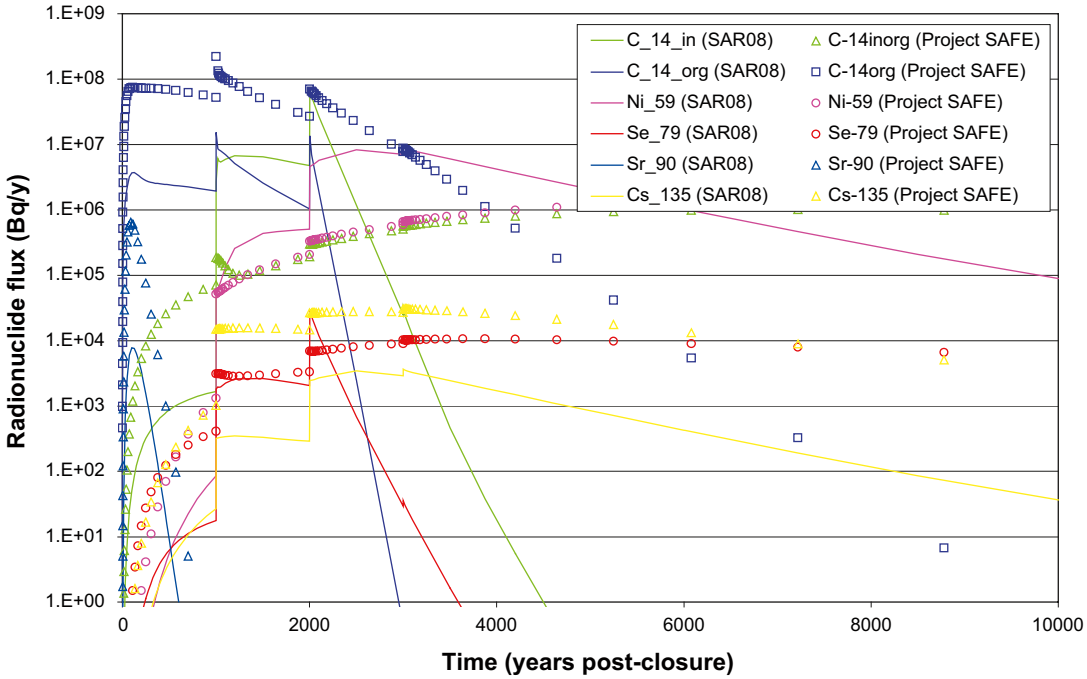

Figure 4-45. *Comparison of best estimate radionuclides fluxes from 1BTF for Project SAFE and SAR-08.*

- Changes in the estimates of disposal inventory in SAR-08; particularly for inorganic and organic forms of C-14 which are decreased by factors of 135 and 20, inventories for Se-79, Sr-90, Tc-99 and Cs-135 are all reduced in SAR-08.
- The assumption that the 1BTF encapsulation fails at 1,000 years post-closure.
- A reduction in the SAR-08 near-field flow fields up to 2,000 years post-closure and increases thereafter resulting from the use of the Uncertainty factors.

The most significant change to the SAR-08 model is the assumption of barrier failure at 1,000 years post-closure which makes explanation of the comparative radionuclide peaks after this time more difficult. However, the relative reduction in the Sr-90 maximum for SAR-08 is readily explained by a reduction in its inventory, the effective diffusivity of intact concrete and in the near-field flow fields (caused by the initial Uncertainty factors). From 1,000 years post-closure the near-field flow fields increase, the concrete diffusivity increases and the sorption onto concrete and cement reduces, meaning a larger release of activity, particularly for the less mobile radionuclides.

A comparison of results for 2BTF shows similar trends to those described above for 1BTF. The differences between the BLA results from Project SAFE and SAR-08 are explained by differences in the disposal inventory which moderates the initial fluxes from the facility (disposal inventories of inorganic C-14, Ni-63 and Cs-137 are reduced in SAR-08) and by the long-term uncertainty factors which increase the transport of radionuclides from the facility from 2,000 years post-closure onwards.

The changes to the geosphere fluxes in SAR-08 relative to Project SAFE are due to the use of time-dependent geosphere parameters (e.g. path length and travel time) and their implementation as instantaneous changes and also a reduction in matrix sorption.

4.2 Calculation Case CC2

This calculation case has been identified in order to assess the uncertainty in the assumption that during periods of continuous permafrost the SFR 1 repository and surrounding shallow and near-surface geosphere will freeze eliminating the potential for a release pathway.

In CC2 it is considered possible that during such periods of continuous permafrost it is possible that a migration pathway exists to a feature such as a talik located close to the SFR 1 at the natural discharge location. It should also be noted that in this calculation case it is assumed that the rate of transport during continuous permafrost is considered to be 10 times greater than during temperate conditions.

Table 4-2 below summarises the maximum best estimate near-field and geosphere radionuclide fluxes for CC2. Those values that differ from CC1 are highlighted in bold. These are the near-field flux from the Silo and the near-field and geosphere fluxes from the BMA.

Table 4-2. Summary of best estimate data for CC2 showing maximum flux, key radionuclide and time of peak flux in years after closure.

	Near-field (Maximum flux, time and key contributor)	**Geosphere (Maximum flux, time and key contributor)**
Silo	$7.6 \cdot 10^{7}$ Bq/y, 80,000 years Ni-59	$1.0 \cdot 10^{8}$ Bq/y, 2,000 years Organic C-14
BMA	$1.3 \cdot 10^{9}$ Bq/y, 42,000 years Ni-59	$1.2 \cdot 10^{9}$ Bq/y, 42,000 years Ni-59
1BTF	$2.0 \cdot 10^{8}$ Bq/y, 2,000 years Inorganic C-14	$5.6 \cdot 10^{8}$ Bq/y, 2,100 years Inorganic C-14
2BTF	$4.4 \cdot 10^{8}$ Bq/y, 2,000 years Inorganic C-14	$3.7 \cdot 10^{8}$ Bq/y, 2,100 years Inorganic C-14
BLA	$6.3 \cdot 10^{8}$ Bq/y, 0 years Ni-63	$1.4 \cdot 10^{8}$ Bq/y, 75 years Ni-63

The maximum Silo near-field flux increases by a factor of approximately 2.7 to $7.6 \cdot 10^7$ Bq/y and occurs at 80,000 years post-closure due to releases of Ni-59. The maximum BMA near-field flux increases by a factor of approximately 5 to $1.2 \cdot 10^9$ Bq/y and the geosphere by a factor of approximately 6 to $1.2 \cdot 10^9$ Bq/y. Both maxima occur at 42,000 years post-closure due to releases of Ni-59.

Figure 4-46 shows the near-field best estimate radionuclide flux from the Silo for CC2. Also shown on the figure are the continuous permafrost periods and the failure of the Silo encapsulation. The importance of the releases during the periods of continuous permafrost is clearly visible in Figure 4-46, particularly following failure of the Silo encapsulation at 66,000 years post-closure.

Figure 4-47 compares the total near-field radionuclide fluxes from the Silo for calculations CC1 and CC2[17]. Also shown on the figure are the contributions from organic C-14 and Ni-59 which tend to dominate in the short-term and long-term, respectively. It can be seen that the main differences for CC2 are the earlier depletion of organic C-14 and also the earlier breakthrough of Ni-59 that are due to the assumption in CC2 that radionuclide transport is possible during periods of continuous permafrost.

Figure 4-48 shows a similar plot for the geosphere radionuclide fluxes from the Silo for calculations CC1 and CC2. Although the radionuclide flux from the geosphere from 75,000 years post-closure is increased in CC2 by two orders of magnitude it still remains below the overall maximum which occurs at 2,000 years post-closure as in CC1 (which is due to the peak releases of organic C-14 occurring at a time in which the groundwater flow rate increase dramatically).

Figure 4-49 shows a plot of the maximum total near-field radionuclide flux for the Silo from each of the individual samples in the calculation using sampled parameters. Also shown on the figure are the mean ($9.7 \cdot 10^8$ Bq/y at 76,000 years post-closure) and the best estimate ($7.6 \cdot 10^7$ Bq/y at 80,000 years post-closure) for comparison.

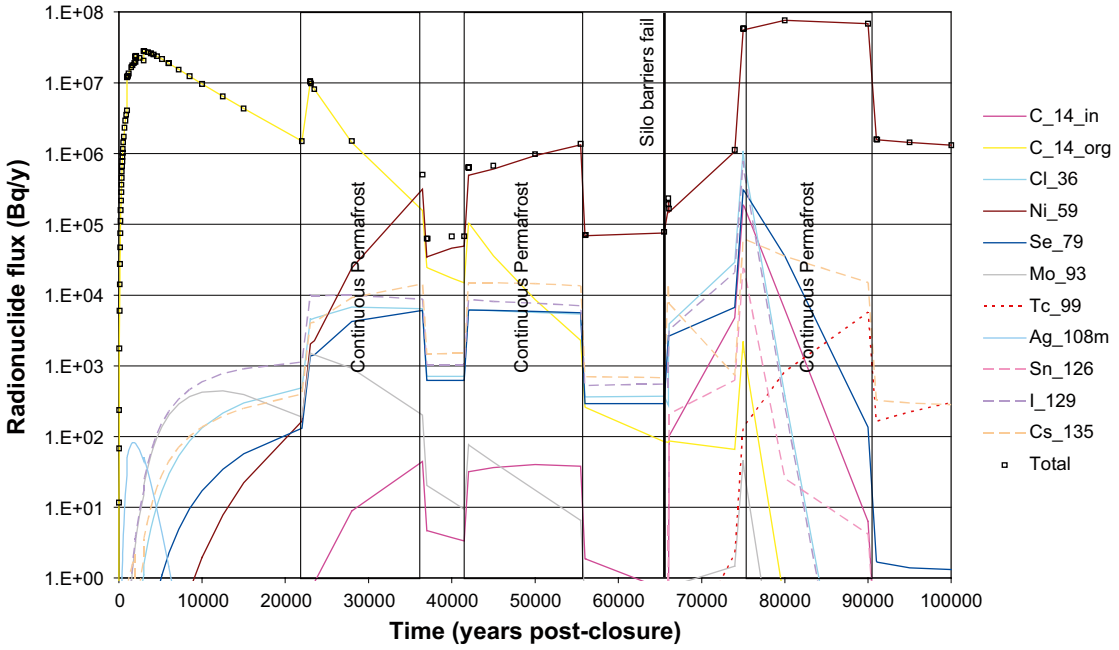

Figure 4-46. *Near-field best estimate radionuclide flux from the Silo for CC2 calculation.*

[17] No difference in radionuclide fluxes occurs for the initial 23,000 years post-closure.

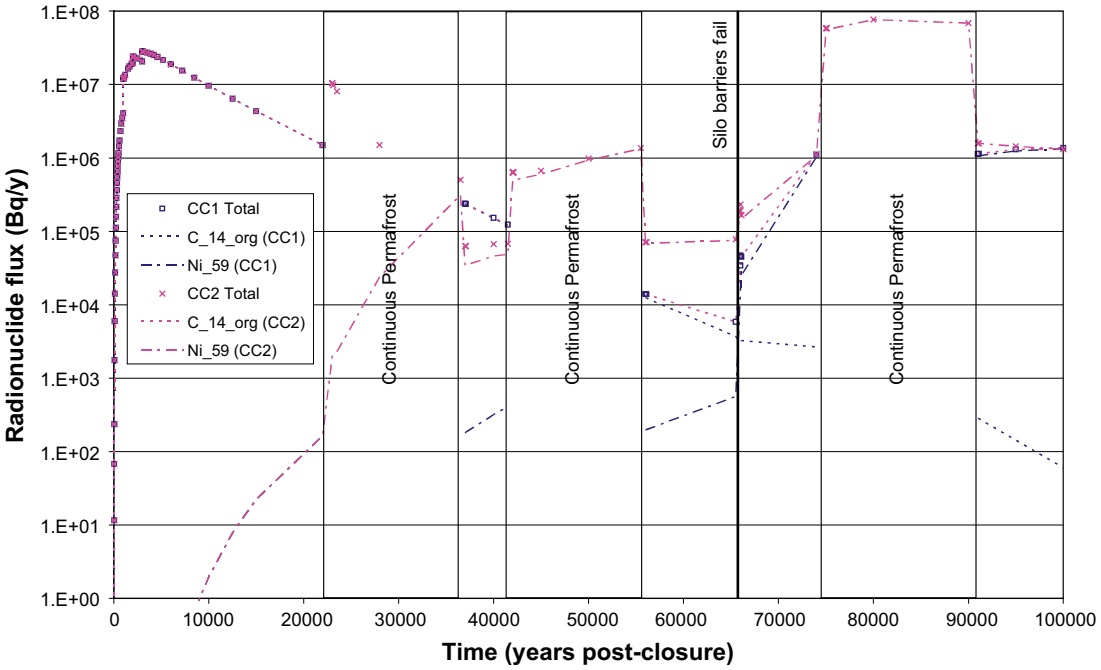

Figure 4-47. *Comparison of key contributions to Silo near-field radionuclide flux for CC1 and CC2.*

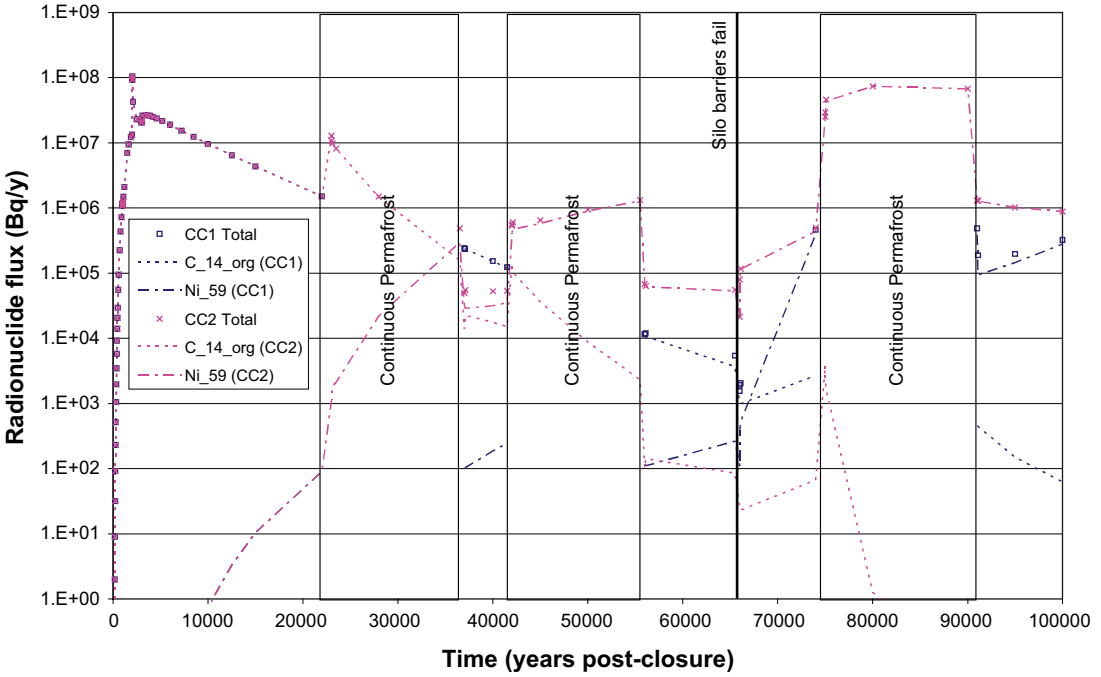

Figure 4-48. *Comparison of key contributions to Silo geosphere radionuclide flux for CC1 and CC2.*

The maximum total radionuclide flux varies between $2.0 \cdot 10^7$ and $5.2 \cdot 10^8$ Bq/y and the time varies between 3,000 and 90,000 years post-closure with the majority occurring between 75,000 and 90,000 years post-closure, within the 3rd period of continuous permafrost.

The dominance of Ni-59 in determining the overall near-field flux from the Silo for the CC2 calculation case explains the spread of data within the time of the 3rd period of continuous permafrost. This is considered to be most likely due to variations in the value of sorption coefficients for Ni selected for the various Silo materials.

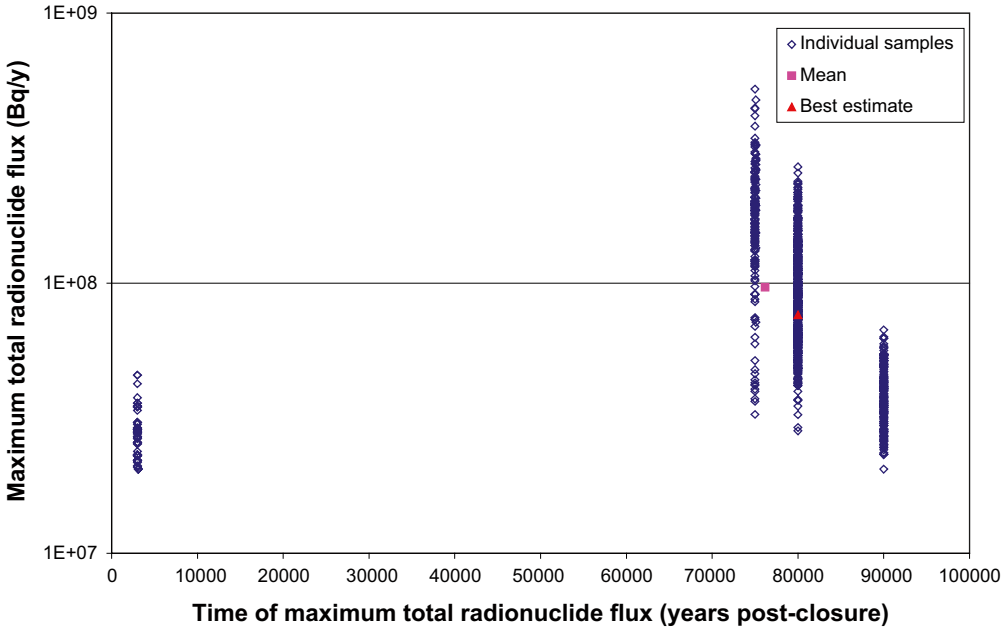

Figure 4-49. *Scatter plot of Silo maximum total near-field radionuclide flux for CC2.*

Figure 4-50 is a summary plot for the near-field radionuclide flux from the Silo for the evaluation of CC2 using sampled parameters. The figure shows the mean of the total radionuclide flux and the 5th and 95th percentiles. Comments made previously in relation to the over-estimate of the lower bound due to omitted processes apply here.

Figure 4-51 shows the near-field best estimate radionuclide flux from the BMA for CC2. Also shown on the figure are the continuous permafrost periods (failure of the BMA encapsulation occurs at the beginning of the 2nd period of permafrost). Again the importance of the releases during the periods of continuous permafrost is clearly visible in Figure 4-51, particularly following failure of the BMA encapsulation.

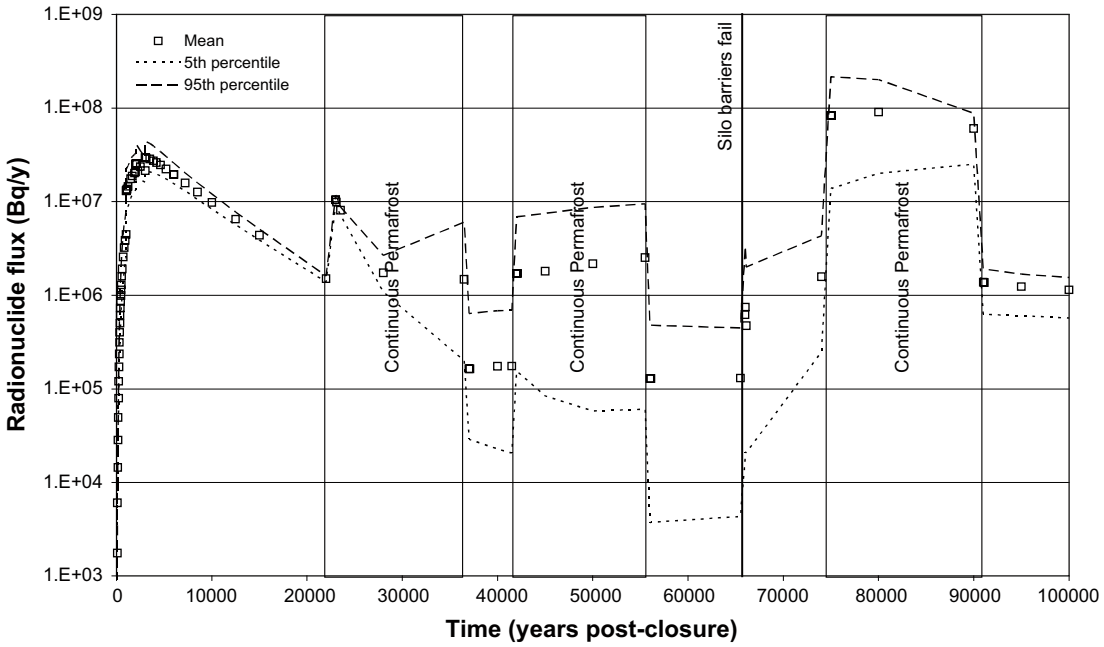

Figure 4-50. *Near-field total radionuclide flux from the Silo for CC2 using sampled parameters.*

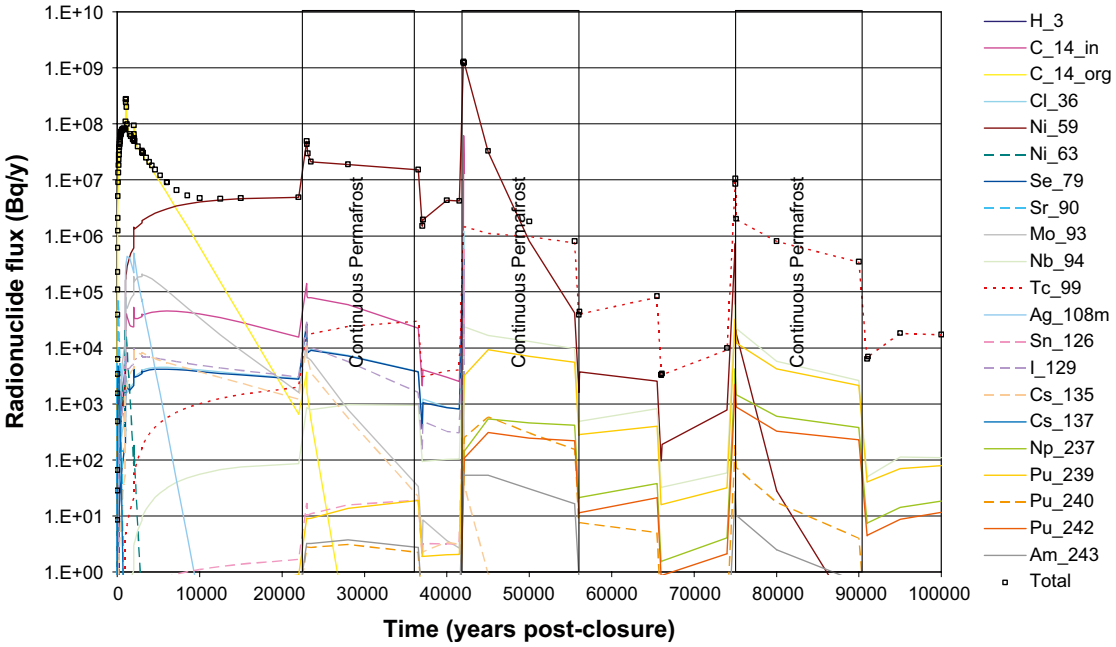

Figure 4-51. *Near-field best estimate radionuclide flux from the BMA for CC2 calculation.*

Figure 4-52 compares the total near-field radionuclide fluxes from the BMA for calculations CC1 and CC2[18]. Also shown on the figure are the contributions from organic C-14 and Ni-59 (and Tc-99 for CC2) which tend to dominate in the short-term and long-term, respectively. It can be seen that the main differences for CC2 are the earlier depletion of organic C-14 and also the earlier breakthrough of Ni-59 and a significant long-term contribution from Tc-99 in CC2.

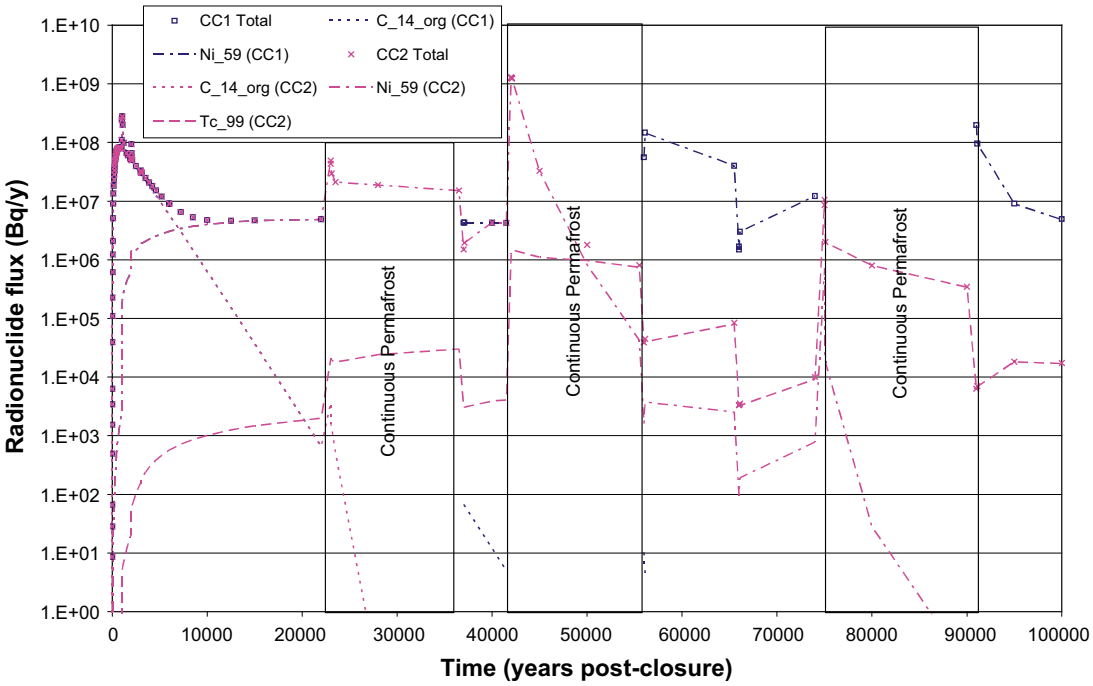

Figure 4-52. *Comparison of key contributions to BMA near-field radionuclide flux for CC1 and CC2.*

[18] No difference in radionuclide fluxes occurs for the initial 23,000 years post-closure.

Figure 4-53 shows a plot of the maximum total near-field radionuclide flux for the BMA from each of the individual samples in the calculation using sampled parameters. Also shown on the figure are the mean ($1.9 \cdot 10^9$ Bq/y at 42,000 years post-closure) and the best estimate ($1.3 \cdot 10^9$ Bq/y at 42,000 years post-closure) for comparison. The maximum total radionuclide flux varies between $5.0 \cdot 10^8$ and $8.2 \cdot 10^9$ Bq/y and the time of the maximum clusters around 42,000 years post-closure with two isolated points occurring at 1,000 years post-closure. The importance of the failure of the BMA barriers at the onset of the 2nd period of continuous permafrost explains the concentration of data around this time.

Figure 4-54 is a summary plot for the near-field radionuclide flux from the BMA for the evaluation of CC2 using sampled parameters. The figure shows the mean of the total radionuclide flux and the 5th and 95th percentiles. Comments made previously in relation to the over-estimate of the lower bound due to omitted processes apply here.

Figures 4-55 and 4-56 show similar plots for the geosphere to those described earlier. It is noted that in the case of the BMA the overall geosphere maximum also occurs at 42,000 years post-closure which therefore coincides with the near-field peak. Similar trends are noted at 66,000 years post-closure to those discussed previously for CC1. However, in CC2 the release of activity is highest during the 2nd period of continuous permafrost due to the assumed increased groundwater flow rates and failure of the BMA encapsulation.

Figure 4-57 shows a plot of the maximum total geosphere radionuclide flux for the BMA from each of the individual samples run in the calculation using sampled parameters. Also shown on the figure are the mean ($1.5 \cdot 10^9$ Bq/y at 36,000 years post-closure) and the best estimate ($1.2 \cdot 10^9$ Bq/y at 42,000 years post-closure) for comparison. The maximum total radionuclide flux varies between $1.4 \cdot 10^8$ and $8.1 \cdot 10^9$ Bq/y and the time of the maximum clusters around 2,000 and 42,000 years post-closure.

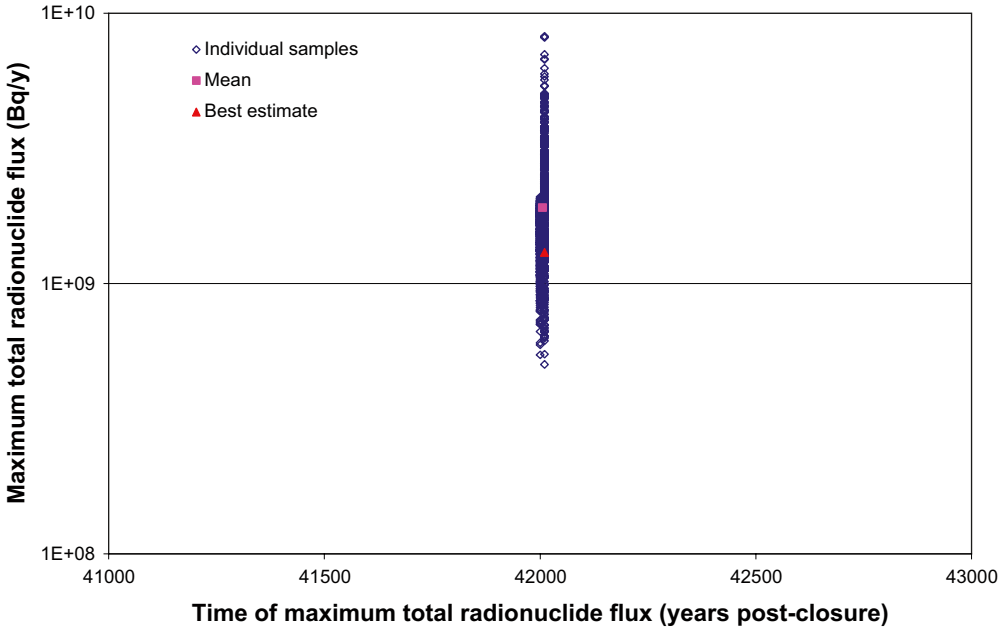

Figure 4-53. *Scatter plot of BMA maximum total near-field radionuclide flux for CC2.*

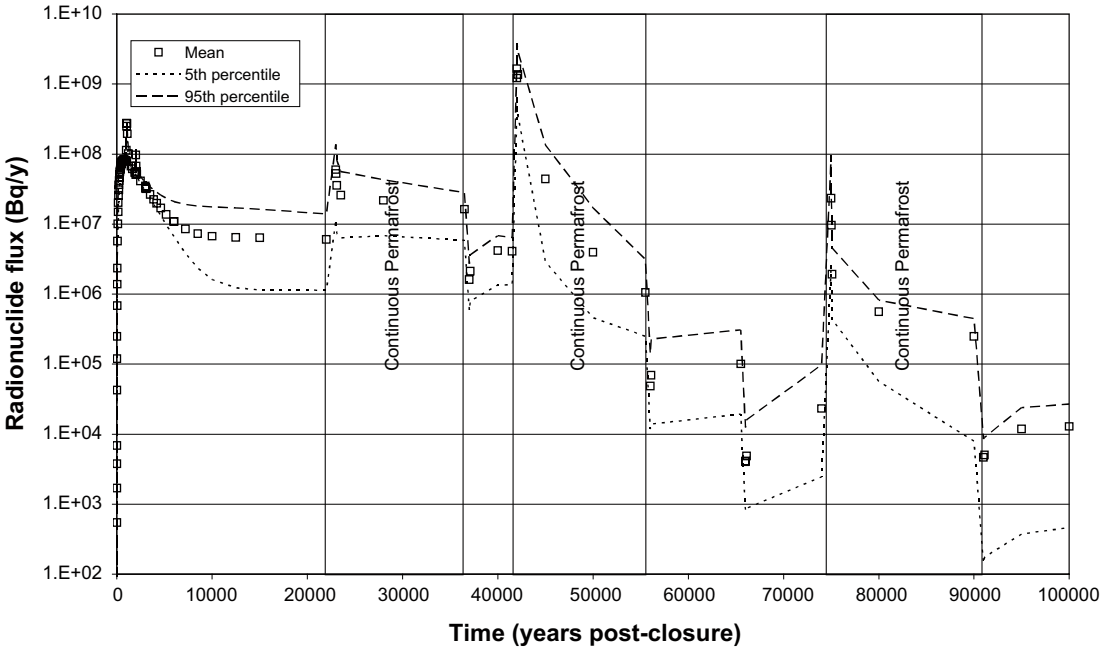

Figure 4-54. *Near-field total radionuclide flux from the BMA for CC2 using sampled parameters.*

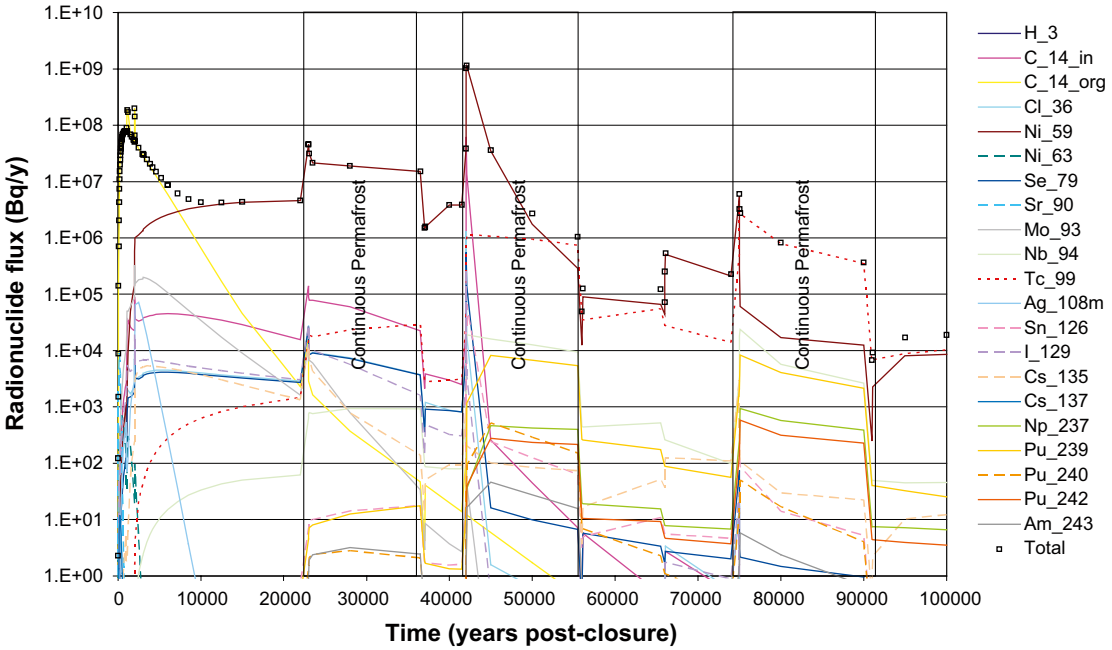

Figure 4-55. *Geosphere best estimate radionuclide flux from the BMA for CC2 calculation.*

The most likely explanation for some of the highest fluxes that are seen at around 2,000 years post-closure is that they are due to limited residence within the geosphere, either as a result of reduced travel times or diffusion (or combinations thereof). Sorption is expected to be less important in determining the magnitude of the peak at 2,000 years given the dominance of non-sorbing organic C-14 at this time.

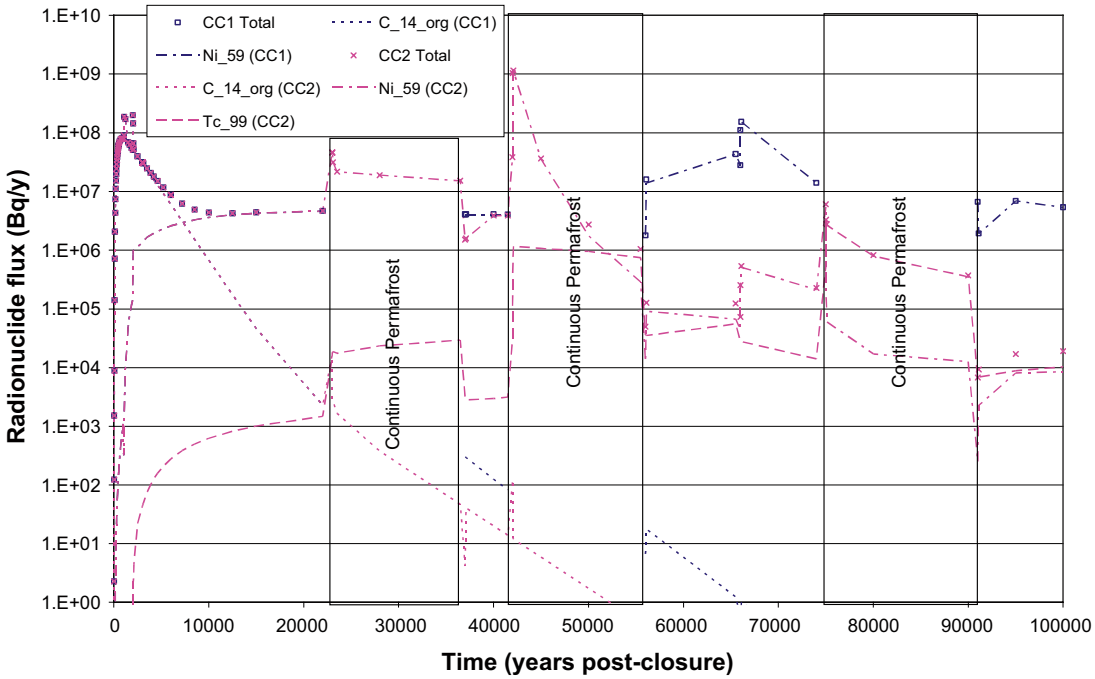

Figure 4-56. *Comparison of key contributions to BMA geosphere radionuclide flux for CC1 and CC2.*

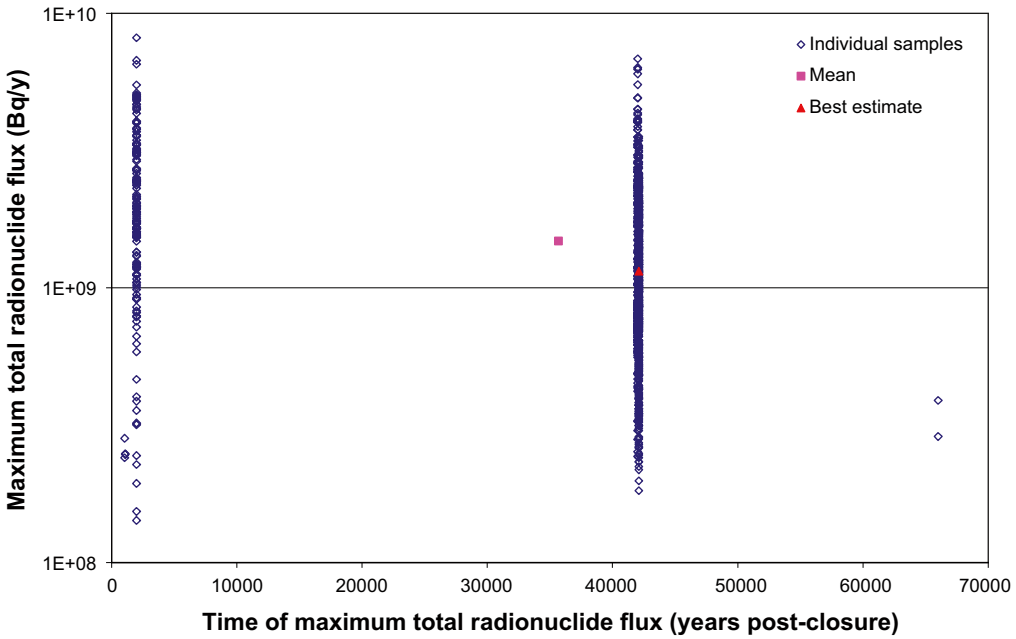

Figure 4-57. *Scatter plot of BMA maximum total geosphere radionuclide flux for CC2.*

Figure 4-58 is a summary plot for the geosphere radionuclide flux from the BMA for the evaluation of CC2 using sampled parameters. The figure shows the mean of the total radionuclide flux and the 5th and 95th percentiles. Comments made previously in relation to the over-estimate of the lower bound due to omitted processes apply here.

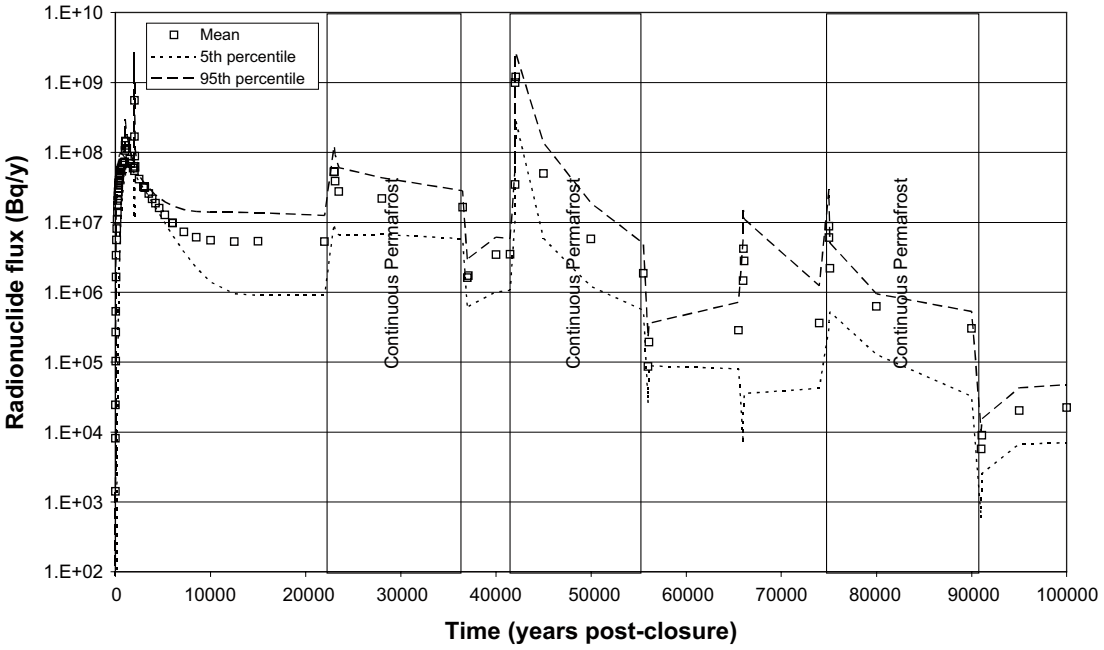

Figure 4-58. *Geosphere total radionuclide flux from the BMA for CC2 using sampled parameters.*

The best estimate radionuclide fluxes from the 1BTF, 2BTF and BLA do not vary from those reported previously for calculation case CC1. This is due to the relatively reduced amounts of engineering considered within these assessment models and therefore the tendency for these models to estimate earlier releases from these facilities. Therefore to ease the presentation the results for these facilities are not repeated here.

It can therefore be concluded that considering radionuclide transport during periods of continuous permafrost increases the best-estimate long-term maximum radionuclide fluxes by a factor of three or less. The facilities which are most sensitive are the Silo and the BMA which are anticipated to have the residual largest inventory within them due to their relatively higher level of engineered containment.

4.3 Calculation Case CC3

CC3 is identical to CC1 in all aspects except that the disposal inventory is considered to be the maximum allowable under licence conditions. For the purposes of CC3 this disposal inventory is approximately 7 times the revised reference disposal inventory.

As noted previously the equations solved by AMBER are linear and therefore it can be expected that for a constant increase in the initial amount of a radionuclide a similar increase in radionuclide flux will result. This is reflected in the results for CC3 summarised below in Table 4-3.

Table 4-3. Summary of results from CC3 showing maximum flux and time of peak flux in years after closure.

	Near-field		Geosphere	
Silo	Best estimate	$1.9 \cdot 10^{8}$ Bq/y at 3,000 years	Best estimate	$7.2 \cdot 10^{8}$ Bq/y at 2,000 years
	Mean	$2.1 \cdot 10^{8}$ Bq/y at 3,000 years	Mean	$8.5 \cdot 10^{8}$ Bq/y at 2,600 years
	Range of max.	$1.4 \cdot 10^{8}$ Bq/y–$3.3 \cdot 10^{8}$ Bq/y	Range of max.	$6.5 \cdot 10^{7}$ Bq/y–$9.1 \cdot 10^{9}$ Bq/y
BMA	Best estimate	$1.9 \cdot 10^{8}$ Bq/y at 1,100 years	Best estimate	$1.4 \cdot 10^{9}$ Bq/y at 2,000 years
	Mean	$2.1 \cdot 10^{8}$ Bq/y at 12,000 years	Mean	$5.6 \cdot 10^{9}$ Bq/y at 22,000 years
	Range of max.	$1.8 \cdot 10^{8}$ Bq/y–$5.5 \cdot 10^{8}$ Bq/y	Range of max.	$8.5 \cdot 10^{8}$ Bq/y–$6.2 \cdot 1,^{010}$ Bq/y
1BTF	Best estimate	$5.7 \cdot 10^{8}$ Bq/y at 2,000 years	Best estimate	$3.9 \cdot 10^{8}$ Bq/y at 2,100 years
	Mean	$5.0 \cdot 10^{8}$ Bq/y at 2,000 years	Mean	$2.1 \cdot 10^{8}$ Bq/y at 2,200 years
	Range of max.	$1.0 \cdot 10^{8}$ Bq/y–$8.8 \cdot 10^{8}$ Bq/y	Range of max.	$2.1 \cdot 10^{7}$ Bq/y–$7.1 \cdot 10^{9}$ Bq/y
2BTF	Best estimate	$2.3 \cdot 10^{9}$ Bq/y at 2,000 years	Best estimate	$2.6 \cdot 10^{9}$ Bq/y at 2,100 years
	Mean	$2.6 \cdot 10^{9}$ Bq/y at 2,000 years	Mean	$4.8 \cdot 10^{9}$ Bq/y at 2,000 years
	Range of max.	$5.6 \cdot 10^{8}$ Bq/y–$3.9 \cdot 10^{9}$ Bq/y	Range of max.	$2.0 \cdot 10^{8}$ Bq/y–$6.0 \cdot 10^{10}$ Bq/y
BLA	Best estimate	$4.4 \cdot 10^{9}$ Bq/y at 0 years	Best estimate	$9.9 \cdot 10^{8}$ Bq/y at 75 years
	Mean	$5.5 \cdot 10^{9}$ Bq/y at 0 years	Mean	$1.5 \cdot 10^{9}$ Bq/y at 690 years
	Range of max.	$2.5 \cdot 10^{9}$ Bq/y–$1.3 \cdot 10^{10}$ Bq/y	Range of max.	$1.0 \cdot 10^{7}$ Bq/y–$9.2 \cdot 10^{9}$ Bq/y

4.4 Calculation Cases CC4 and CC5

It has been recognised that there is the potential for the development of continuous permafrost to be more severe than considered within CC1, and as such it could result in the failure of the BMA encapsulation at this point.

Two separate calculation cases are considered here: one in which no radionuclide transport is considered during continuous permafrost (similar to CC1 conditions) “CC4”; and one which considers radionuclide transport during continuous permafrost (similar to CC2 conditions) “CC5”.

Table 4-4 summarises the results for calculation cases CC4 and CC5 (and also presents the data for CC1 and CC2 for comparison).

Limited sensitivity to early failure of the BMA at 23,000 years post-closure is shown by CC4, more changes to the radionuclide release profiles are noted for CC5.

Table 4-4. Summary of BMA best estimate results for CC4 and CC5 and comparison to CC1 and CC2.

	Near-field (Maximum flux, time and key contributor)	Geosphere (Maximum flux, time and key contributor)
CC1	$2.8 \cdot 10^{8}$ Bq/y, 1,100 years Organic C-14	$2.0 \cdot 10^{8}$ Bq/y, 2,000 years Organic C-14
CC2	$1.3 \cdot 10^{9}$ Bq/y, 42,000 years Ni-59	$1.2 \cdot 10^{9}$ Bq/y, 42,000 years Ni-59
CC4	$2.9 \cdot 10^{8}$ Bq/y, 37,100 years Organic C-14	$2.0 \cdot 10^{8}$ Bq/y, 2,000 years Organic C-14
CC5	$2.3 \cdot 10^{9}$ Bq/y, 23,000 years Ni-59	$2.8 \cdot 10^{9}$ Bq/y, 23,000 years Ni-59

For CC4, the magnitude of the maximum radionuclide fluxes remains similar to those for CC1. However, from inspection of Figures 4-59 and 4-60 it can be confirmed that the near-field peak which occurs shortly after 37,000 years post-closure (the end of the first period of continuous permafrost) are similar to the maxima for CC1 and the data in Table 4-4 suggests that the CC1 near-field value is slightly exceed for the CC4 best estimate evaluation.

The highest radionuclide flux overall is displayed by CC5 at 23,000 years post-closure which marks the failure of the BMA encapsulation and on the onset of the first period of continuous permafrost (Figure 4-59 and Table 4-4).

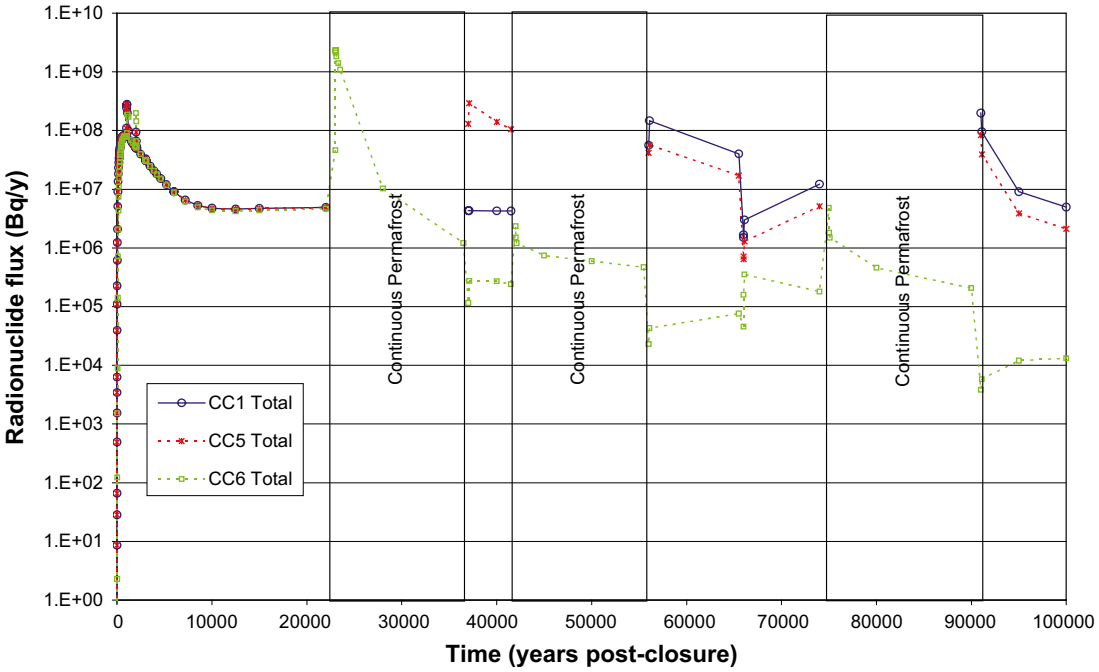

Figure 4-59. *Comparison of total BMA near-field radionuclide flux for CC1 and CC4 and CC5.*

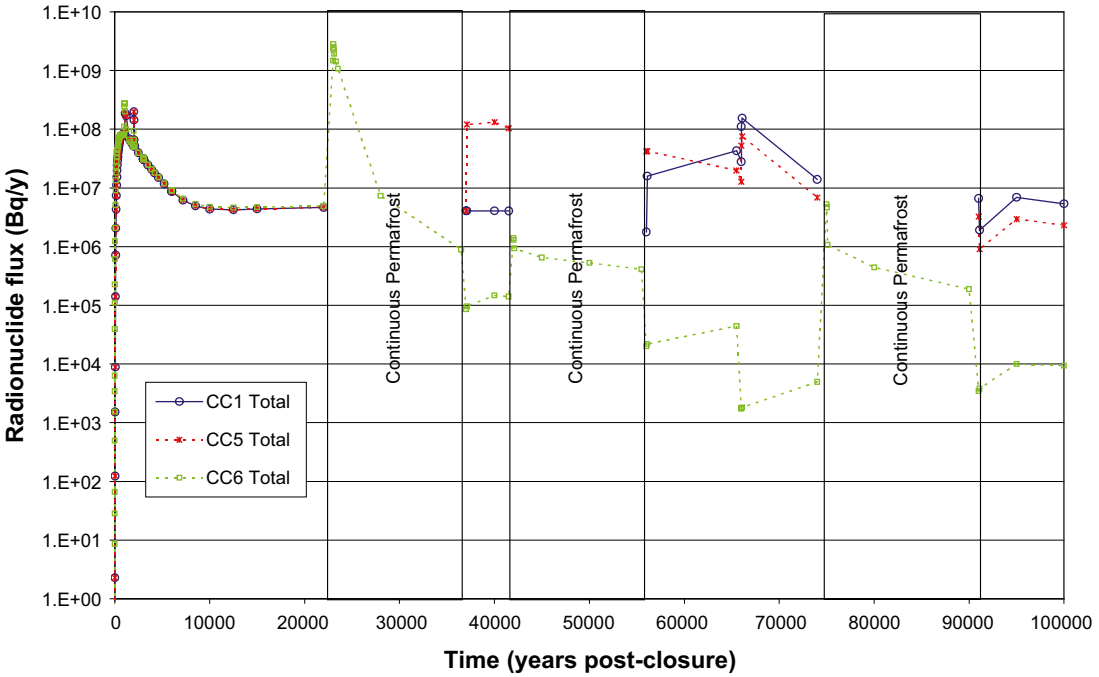

Figure 4-60. *Comparison of total BMA geosphere radionuclide flux for CC1 and CC4 and CC5.*

Figure 4-61 shows a scatter plot for the maximum total near-field radionuclide flux data for the BMA for CC4. This shows some similarities to CC1 in that there is a tight clustering of values around 1,000 years post-closure. However, a difference is the significant number of maxima that are estimated to occur at 37,000 years post-closure (following the end of the 1st period of continuous permafrost) that are associated with combinations of selections of U-factors and sorption coefficients that promote radionuclide release.

Figure 4-62 compares the total near-field radionuclide flux from the best-estimate calculation for CC1 and CC4. Also shown on the figure are the contributions from organic C-14 and Ni-59. From inspection of Figure 4-62 it can be seen that the cluster of values around 37,000 years post-closure are most likely to be associated with releases of Ni-59.

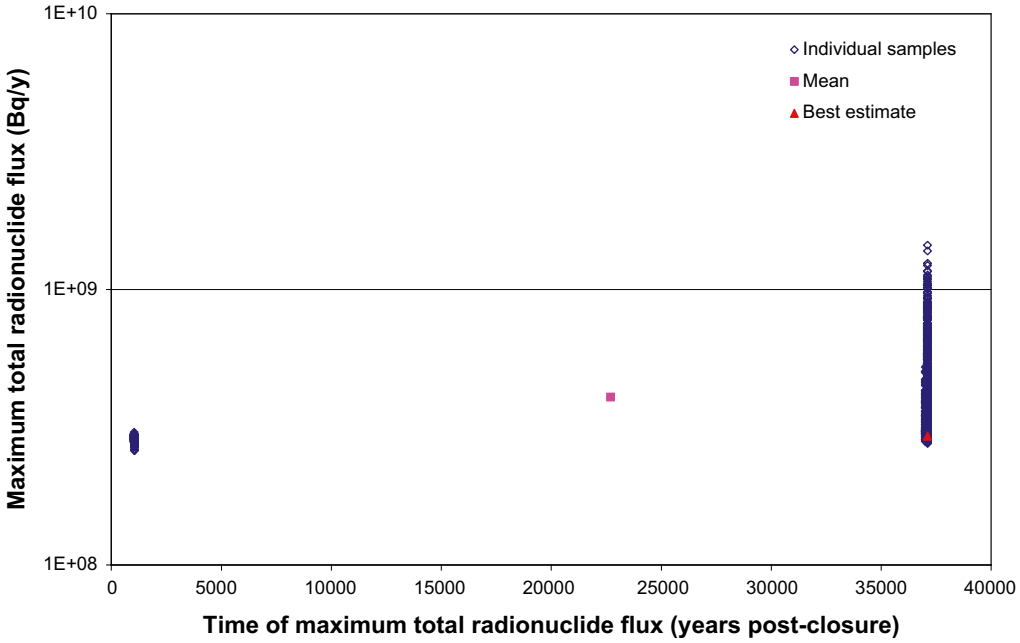

Figure 4-61. *Scatter plot of BMA maximum total near-field radionuclide flux for CC4.*

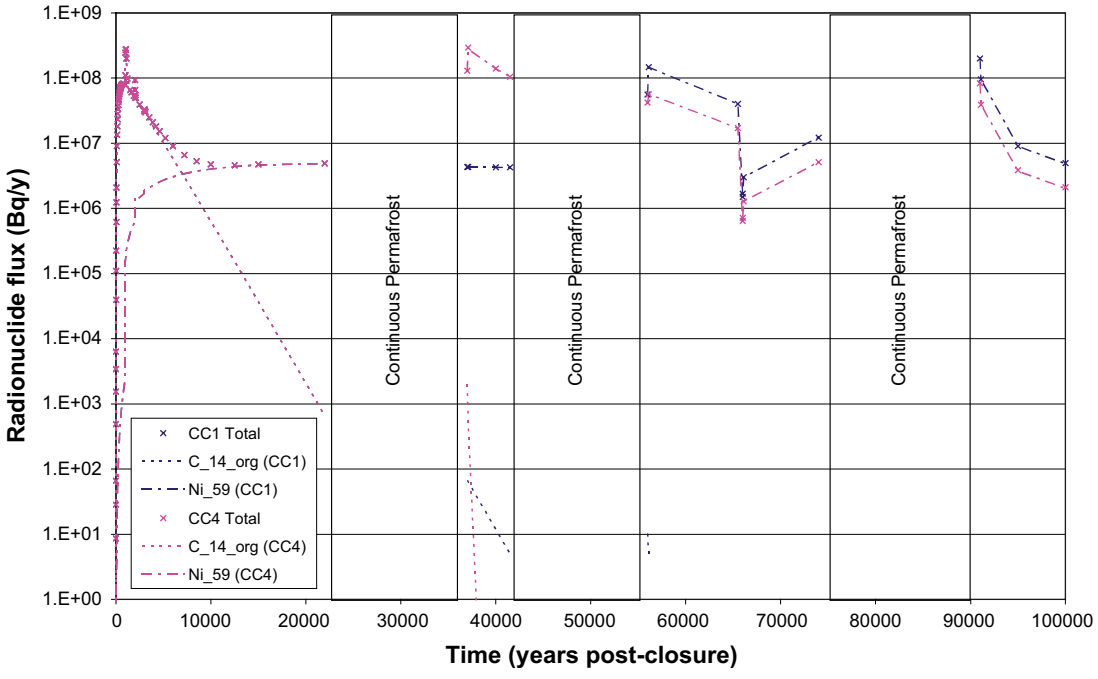

Figure 4-62. *Comparison of key contributions to BMA near-field radionuclide flux for CC1 and CC4.*

For CC5, the maximum fluxes occur at 23,000 years post-closure, earlier than those for CC2. Inspection of Figures 4-59 and 4-60 also confirms that the peaks at 23,000 years post-closure (the start of the 1st period of continuous permafrost) exceed the maxima from best estimate evaluation CC2. The best estimate near-field radionuclide flux for the BMA for CC5 is shown in Figure 4-63. Comparison of this with the complementary plot for CC2 (Figure 4-52) suggests that the reason for the higher maximum fluxes in CC2 may be associated with the earlier breakthrough of Ni-59 (and inorganic C-14) resulting from failure of the BMA at 23,000 years post-closure.

Figure 4-64 shows a plot of the maximum total near-field radionuclide flux for the BMA from each of the individual samples run in the calculation using sampled parameters for CC5. Also shown on the figure are the mean ($3.6 \cdot 10^{9}$ Bq/y at 23,000 years post-closure) and the best estimate ($2.3 \cdot 10^{9}$ Bq/y at 23,000 years post-closure) for comparison. The maximum total radionuclide flux varies between $7.3 \cdot 10^{8}$ and $1.3 \cdot 10^{10}$ Bq/y and the time of the maximum clusters around 23,000 years post-closure. The importance of the failure of the BMA barriers at the onset of the 2nd period of continuous permafrost explains the concentration of data around this time.

Figure 4-65 is a summary plot for the near-field radionuclide flux from the BMA for the evaluation of CC5 using sampled parameters. The figure shows the mean of the total radionuclide flux and the 5th and 95th percentiles. Comments made previously in relation to the over-estimate of the lower bound due to omitted processes apply here.

The maximum total geosphere radionuclide flux for CC5 varies between $4.5 \cdot 10^{8}$ and $1.5 \cdot 10^{10}$ Bq/y and the mean is $2.7 \cdot 10^{9}$ Bq/y at 22,000 years post-closure. The time of the maximum shows a bimodal distribution with clusters around 2,000 years post-closure and 23,000 years post-closure, with the majority at 23,000 years post-closure. The most likely explanation for some of the highest fluxes that are seen at around 2,000 years post-closure is that they are due to limited residence within the geosphere, either as a result of reduced travel times or diffusion (or combinations thereof). Sorption is expected to be less important in determining the magnitude of the peak at 2,000 years given the dominance of non-sorbing organic C-14 at this time.

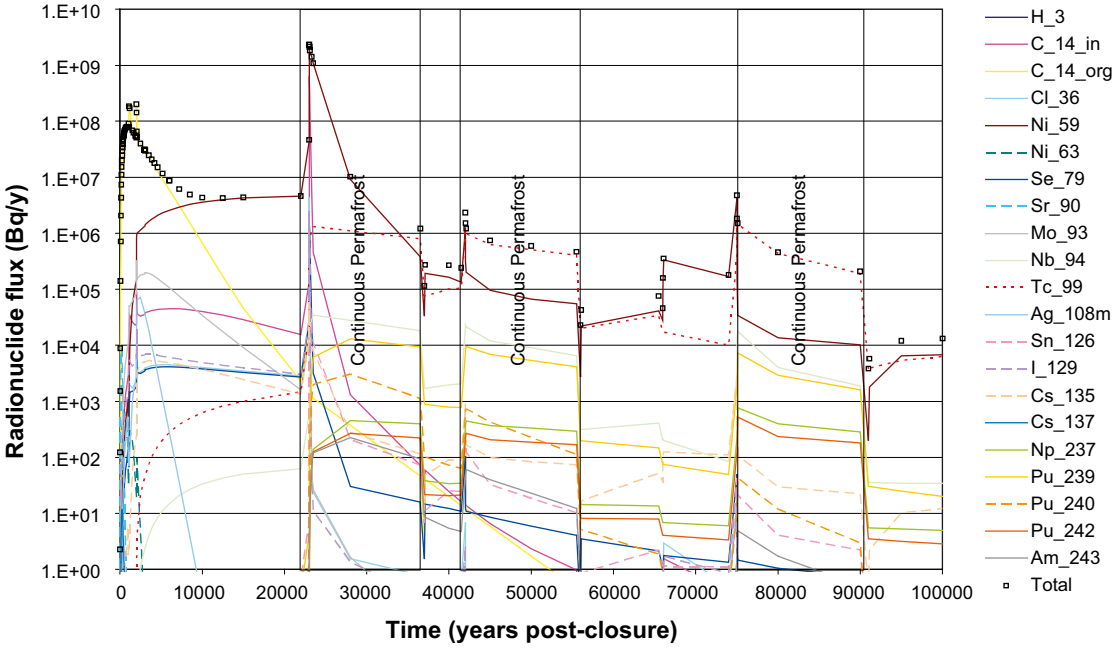

Figure 4-63. *Near-field best estimate radionuclide flux from the BMA for CC5 calculation.*

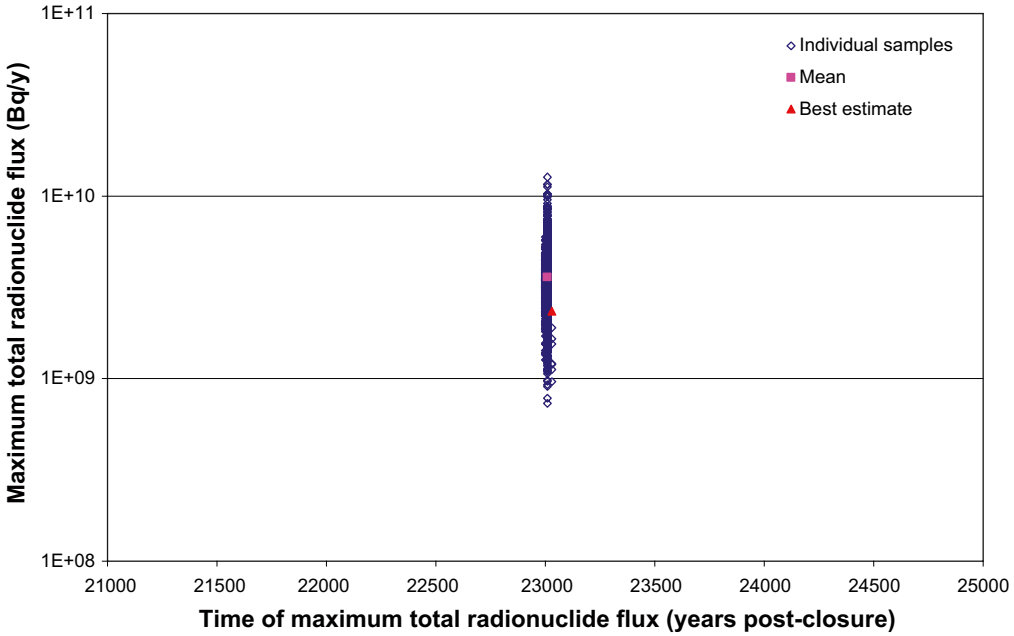

Figure 4-64. *Scatter plot of BMA maximum total near-field radionuclide flux for CC5.*

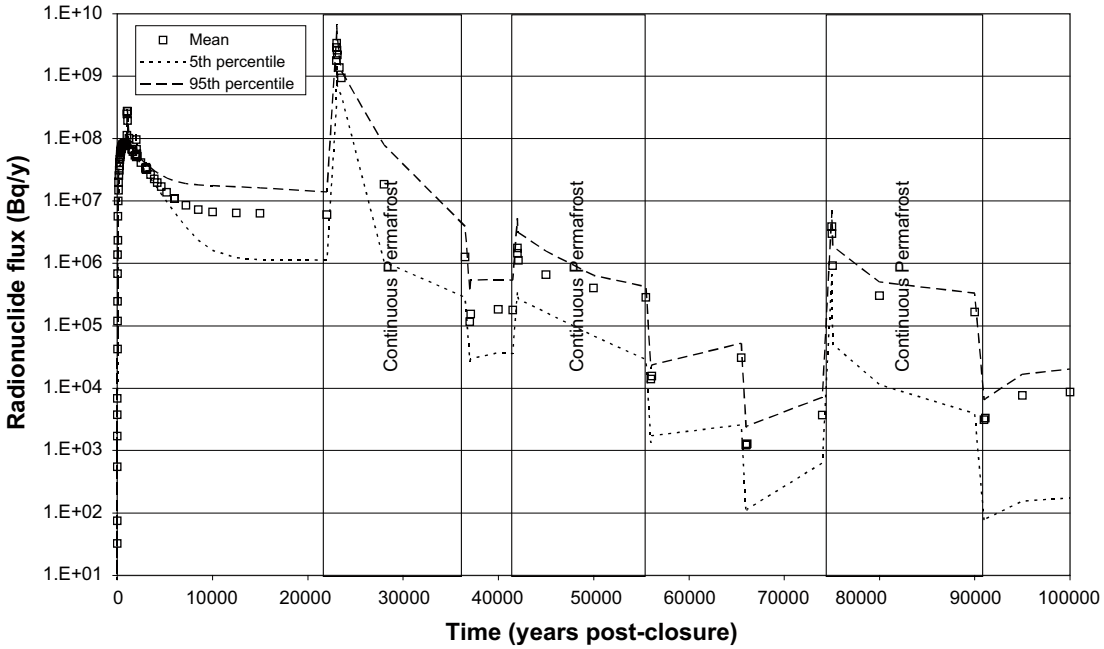

Figure 4-65. *Near-field total radionuclide flux from the BMA for CC5 using sampled parameters.*

4.5 Calculation Case CC6

This calculation case considers a variant evolution of the climate in which enhanced greenhouse warming occurs, which significantly increases the period for which a temperate climate is expected at the surface around SFR 1. There is also a subsequent delay to the cooling and development of permafrost which is anticipated to occur at approximately 73,000 years post-closure (compared to 23,000 years post-closure in CC1, CC2, CC4 and CC5). The assumptions in CC6 regarding closure design and disposal inventory follow best estimates.

A detailed description of CC6 has been given previously in subsection 2.2.5. A schematic of the main features of CC6 is presented below in Figure 4-66 which provides an overview of the main features of this calculation and their variation over the assessment timescale.

A summary of the results for CC6 is presented below in Table 4-5. The data provided in the table show the magnitudes and times of the maximum flux from the best estimate calculations and also from the calculations using sampled parameters (the latter is based on the mean of the individual results). Also shown is the range of the maximum fluxes obtained from the calculations using sampled parameters.

Table 4-5. Summary of results from CC6 showing maximum flux and time of peak flux in years after closure.

	Near-field		Geosphere	
Silo	Best estimate	$2.8 \cdot 10^{7}$ Bq/y at 3,000 years	Best estimate	$1.0 \cdot 10^{8}$ Bq/y at 2,000 years
	Mean	$3.0 \cdot 10^{7}$ Bq/y at 3,000 years	Mean	$1.2 \cdot 10^{8}$ Bq/y at 2,600 years
	Range of max.	$4.0 \cdot 10^{7}$ Bq/y–$9.3 \cdot 10^{7}$ Bq/y	Range of max.	$9.4 \cdot 10^{6}$ Bq/y–$1.3 \cdot 10^{9}$ Bq/y
BMA	Best estimate	$2.8 \cdot 10^{8}$ Bq/y at 1,100 years	Best estimate	$2.0 \cdot 10^{8}$ Bq/y at 2,000 years
	Mean	$2.8 \cdot 10^{8}$ Bq/y at 1,000 years	Mean	$6.5 \cdot 10^{8}$ Bq/y at 1,500 years
	Range of max.	$2.6 \cdot 10^{8}$ Bq/y–$3.0 \cdot 10^{8}$ Bq/y	Range of max.	$1.2 \cdot 10^{8}$ Bq/y–$8.1 \cdot 10^{9}$ Bq/y
1BTF	Best estimate	$8.3 \cdot 10^{8}$ Bq/y at 2,000 years	Best estimate	$5.6 \cdot 10^{7}$ Bq/y at 2,100 years
	Mean	$7.8 \cdot 10^{8}$ Bq/y at 2,000 years	Mean	$8.9 \cdot 10^{7}$ Bq/y at 2,000 years
	Range of max.	$1.6 \cdot 10^{7}$ Bq/y–$1.3 \cdot 10^{8}$ Bq/y	Range of max.	$3.0 \cdot 10^{6}$ Bq/y–$1.0 \cdot 10^{9}$ Bq/y
2BTF	Best estimate	$4.4 \cdot 10^{8}$ Bq/y at 2,000 years	Best estimate	$3.7 \cdot 10^{8}$ Bq/y at 2,100 years
	Mean	$3.7 \cdot 10^{8}$ Bq/y at 2,000 years	Mean	$6.9 \cdot 10^{8}$ Bq/y at 2,000 years
	Range of max.	$8.1 \cdot 10^{7}$ Bq/y–$5.6 \cdot 10^{8}$ Bq/y	Range of max.	$2.9 \cdot 10^{7}$ Bq/y–$8.7 \cdot 10^{9}$ Bq/y
BLA	Best estimate	$6.3 \cdot 10^{8}$ Bq/y at 0 years	Best estimate	$1.4 \cdot 10^{8}$ Bq/y at 75 years
	Mean	$8.0 \cdot 10^{8}$ Bq/y at 0 years	Mean	$2.1 \cdot 10^{8}$ Bq/y at 690 years
	Range of max.	$3.6 \cdot 10^{8}$ Bq/y–$1.8 \cdot 10^{9}$ Bq/y	Range of max.	$5.1 \cdot 10^{6}$ Bq/y–$1.3 \cdot 10^{9}$ Bq/y

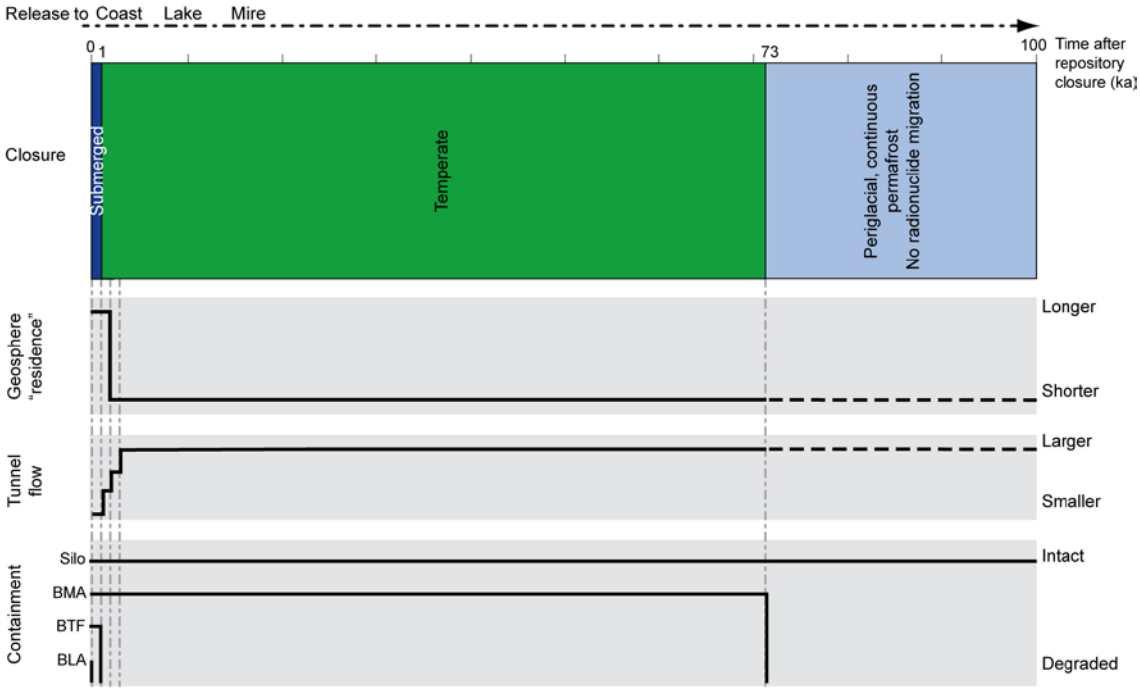

Figure 4-66. *Schematic of CC6.*

The maximum values, times and key radionuclides for the best estimate calculation are unchanged from those for CC1 for the near-field and geosphere fluxes. This is due to the fact that all these maxima occur during a period relatively near the beginning of the simulations in which the conditions represented within CC1 and CC6 are similar.

Data from the CC6 calculation using sampled parameters also shows similar trends to that undertaken for CC1. The main differences appear in the geosphere results where the effects of long-term changes to CC1 (e.g. the return to saline conditions at around 66,000 years post-closure) are not manifest in the times of maxima that are reported.

4.6 Summary of Calculation Cases CC1–CC6

The majority of the radioactive waste to be disposed within SFR 1 will be emplaced within the Silo and the BMA. These high specification facilities offer optimum environmental protection and their engineering components are estimated to afford considerable barrier properties for tens of millennia or more. The radionuclides that dominate the radionuclide flux from the Silo and the BMA are initially organic C-14 in the short-term and long-term and then Ni-59 in the very long-term. Relatively high inventories of radionuclides such as H-3, Co-60, Sr-90 and Cs-137 undergo significant retention and radioactive decay within the engineered containment. The peak radionuclide fluxes from the Silo are estimated to occur at around 3,000 years post-closure when the release of organic C-14 reaches its maximum. Account has been taken of changes in groundwater flow during the period. For the BMA this maximum is estimated to occur at around 1,100 years post-closure.

The performance of these facilities is assumed to be sensitive to large scale environmental change, the development of permafrost and the advance and retreat of ice sheets, which may result in significant degradation of these facilities in the distant future (e.g. 40,000 years AP or more). Following failure of the containment of these facilities the release rates of residual radionuclides will be increased due to increased rates of groundwater flow through the facilities and reduced sorption.

The potential for a relatively earlier failure of the BMA is not considered to result in significantly altered rates of radionuclide release (although they will occur several thousands of years earlier).

The BTF disposal facilities contain a lower radionuclide inventory and therefore require less containment. These facilities are assumed to degrade at relatively early at 1,000 years post-closure and the environmental releases from these are dominated initially by organic and inorganic C-14 and in the longer term by Ni-59 and Tc-99. Maximum releases from the facilities occur shortly after failure.

The representation of the BLA in the calculation cases excludes both engineered barriers and sorption from the assessment models. This results in the peak near-field radionuclide flux being estimated to occur immediately on closure with contributions from individual radionuclides made in proportion to their overall abundance in the disposal inventory. The dominant radionuclide is Ni-63. The highest releases of short-lived radionuclides (e.g. Co-60, Sr-90, Cs-137) are observed for the BLA due to the relative simplicity of the model.

The disposal inventory is completely removed from the BLA within the initial 5,000 year period following closure (i.e. the total radionuclide is below 1 Bq/y from this onwards). However, relatively low-level fluxes of long-lived radionuclides such as Ni-59 and Tc-99 continue from the geosphere throughout the assessment period due to retardation by matrix diffusion and sorption.

A linear relationship has been shown to exist between the amount of radionuclide disposed within a facility and the resultant maximum radionuclide release rate, i.e. the higher the disposal inventory the higher the maximum radionuclide flux.

All facilities are sensitive to assumptions on the general regional hydrogeological regime (e.g. active/in-active during continuous permafrost) and its evolution as a series of step changes. It is suggested that representing the evolution of system as a series of step changes is likely to be conservative in terms of radionuclide release.

4.7 Calculation Case CC7

This calculation case considers a variant evolution of the climate in which conditions are established which promote the development of continuous permafrost for significant periods around SFR 1. The assumptions in CC7 regarding closure design and disposal inventory follow best estimates.

A detailed description of CC7 has been given previously in subsection 2.3.6. A schematic of the main features of CC7 is presented below in Figure 4-67 which provides an overview of the main features of this calculation and their variation over the assessment timescale.

A summary of the results for CC7 is presented below in Table 4-6. The data provided in the table show the magnitudes and times of the maximum flux from the best estimate calculations and also from the calculations using sampled parameters (the latter is based on the mean of the individual results). Also shown is the range of the maximum fluxes obtained from the calculations using sampled parameters.

The maximum values, times and key radionuclides for the best estimate calculation are unchanged from those for CC1 for the near-field and geosphere fluxes except for the BMA. This is due to the fact that the majority of these maxima occur during a period relatively near the beginning of the simulations in which the conditions represented within CC1 and CC7 are similar.

The best estimate near-field radionuclide flux for the BMA for CC7 is shown in Figure 4-68. Inspection of this plot reveals several similarities to that for CC1. However, an important feature to note is the increase in radionuclide flux from 37,000 years post-closure onwards following failure of the BMA barriers at the onset of the 2nd period of continuous permafrost (and the return of radionuclide migration during temperate conditions).

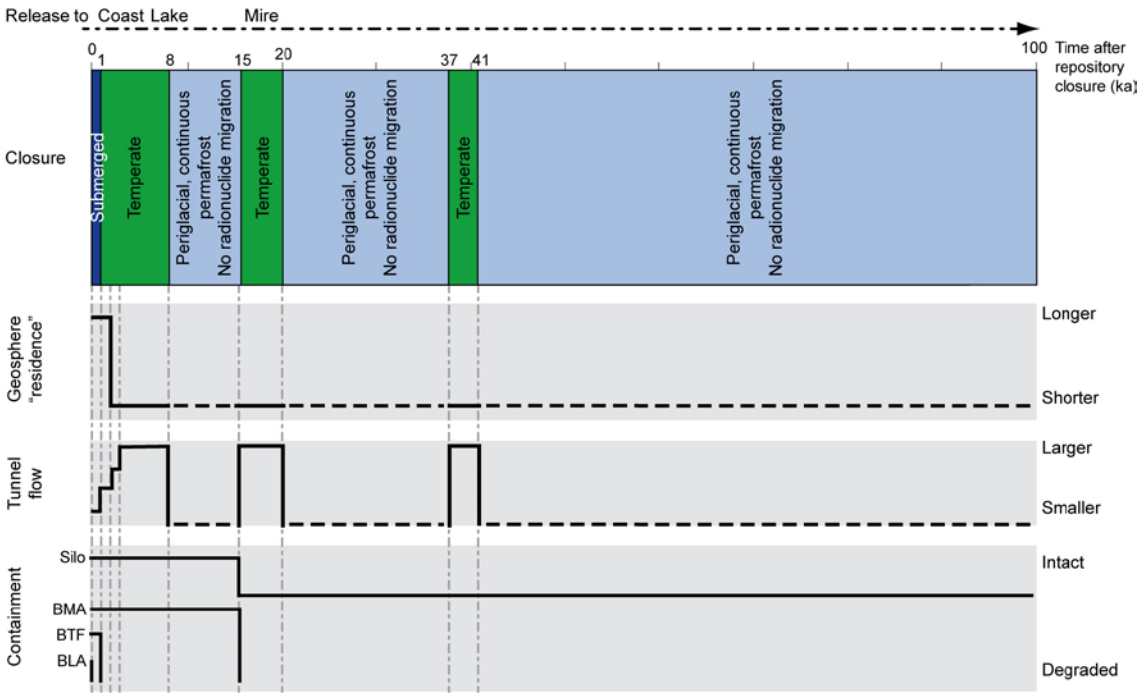

Figure 4-67. *Schematic of CC7.*

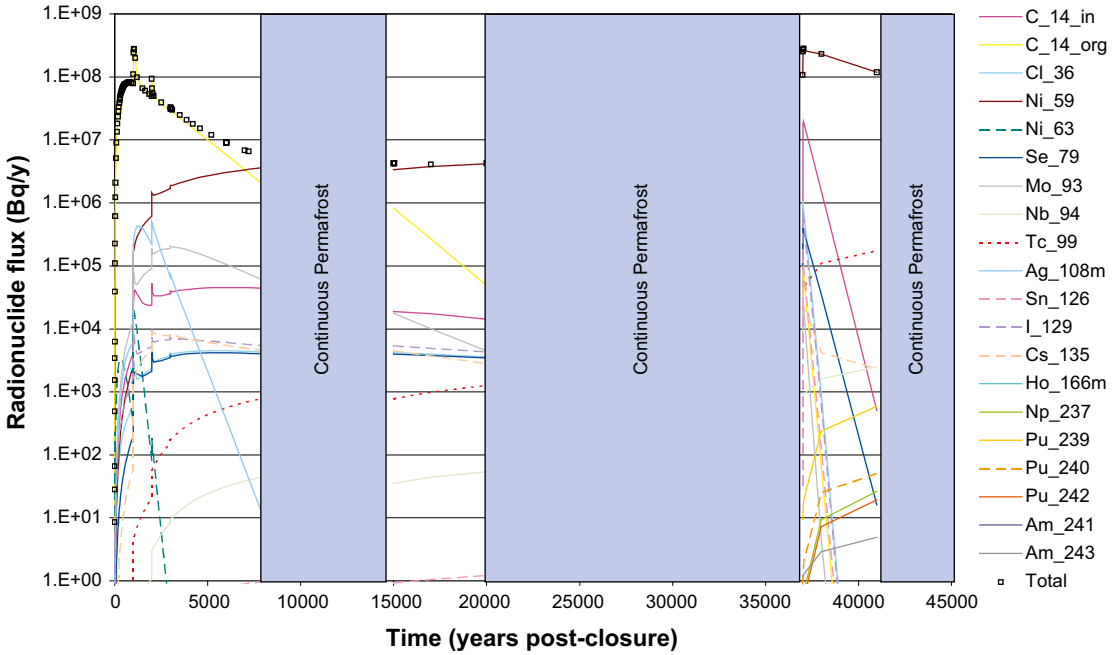

Figure 4-68. *Near-field best estimate radionuclide flux from the BMA for CC7.*

Table 4-6. Summary of results from CC7 showing maximum flux and time of peak flux in years after closure.

	Near-field		Geosphere	
Silo	Best estimate	$2.8 \cdot 10^{7}$ Bq/y at 3,000 years	Best estimate	$1.0 \cdot 10^{8}$ Bq/y at 2,000 years
	Mean	$3.0 \cdot 10^{7}$ Bq/y at 3,000 years	Mean	$1.2 \cdot 10^{8}$ Bq/y at 2,600 years
	Range of max.	$2.0 \cdot 10^{7}$ Bq/y–$4.8 \cdot 10^{7}$ Bq/y	Range of max.	$9.4 \cdot 10^{6}$ Bq/y–$1.3 \cdot 10^{9}$ Bq/y
BMA	Best estimate	$2.8 \cdot 10^{8}$ Bq/y at 37,000 years	Best estimate	$2.0 \cdot 10^{8}$ Bq/y at 2,000 years
	Mean	$4.2 \cdot 10^{8}$ Bq/y at 22,000 years	Mean	$6.6 \cdot 10^{8}$ Bq/y at 6,600 years
	Range of max.	$2.6 \cdot 10^{8}$ Bq/y–$1.6 \cdot 10^{9}$ Bq/y	Range of max.	$1.2 \cdot 10^{8}$ Bq/y–$8.1 \cdot 10^{9}$ Bq/y
1BTF	Best estimate	$8.3 \cdot 10^{8}$ Bq/y at 2,000 years	Best estimate	$5.6 \cdot 10^{7}$ Bq/y at 2,100 years
	Mean	$7.8 \cdot 10^{8}$ Bq/y at 2,000 years	Mean	$8.9 \cdot 10^{7}$ Bq/y at 2,000 years
	Range of max.	$1.6 \cdot 10^{7}$ Bq/y–$1.3 \cdot 10^{8}$ Bq/y	Range of max.	$3.0 \cdot 10^{6}$ Bq/y–$1.0 \cdot 10^{9}$ Bq/y
2BTF	Best estimate	$4.4 \cdot 10^{8}$ Bq/y at 2,000 years	Best estimate	$3.7 \cdot 10^{8}$ Bq/y at 2,100 years
	Mean	$3.7 \cdot 10^{8}$ Bq/y at 2,000 years	Mean	$6.9 \cdot 10^{8}$ Bq/y at 2,000 years
	Range of max.	$8.1 \cdot 10^{7}$ Bq/y–$5.6 \cdot 10^{8}$ Bq/y	Range of max.	$2.9 \cdot 10^{7}$ Bq/y–$8.7 \cdot 10^{9}$ Bq/y
BLA	Best estimate	$6.3 \cdot 10^{8}$ Bq/y at 0 years	Best estimate	$1.4 \cdot 10^{8}$ Bq/y at 75 years
	Mean	$7.9 \cdot 10^{8}$ Bq/y at 0 years	Mean	$2.1 \cdot 10^{8}$ Bq/y at 690 years
	Range of max.	$3.5 \cdot 10^{8}$ Bq/y–$1.8 \cdot 10^{9}$ Bq/y	Range of max.	$1.5 \cdot 10^{6}$ Bq/y–$1.3 \cdot 10^{9}$ Bq/y

Data from the CC7 calculation using sampled parameters also shows similar trends to that undertaken for CC1. The main difference is that the BMA near-field data show some sensitivity to the failure of the barriers at the 2nd period of permafrost which occurs earlier than in CC1. Additionally, differences appear in the geosphere results where the effects of some long-term changes specific to CC1 (e.g. the return to saline conditions at around 66,000 years post-closure) are not manifest in the times of maxima that are reported.

Figure 4-69 shows a plot of the maximum total near-field radionuclide flux for the BMA from each of the individual samples in the calculation using sampled parameters for CC7. Also shown on the figure are the mean ($2.8 \cdot 10^{8}$ Bq/y at 37,000 years post-closure) and the best estimate ($4.2 \cdot 10^{8}$ Bq/y at 22,000 years post-closure) for comparison. The maximum total radionuclide

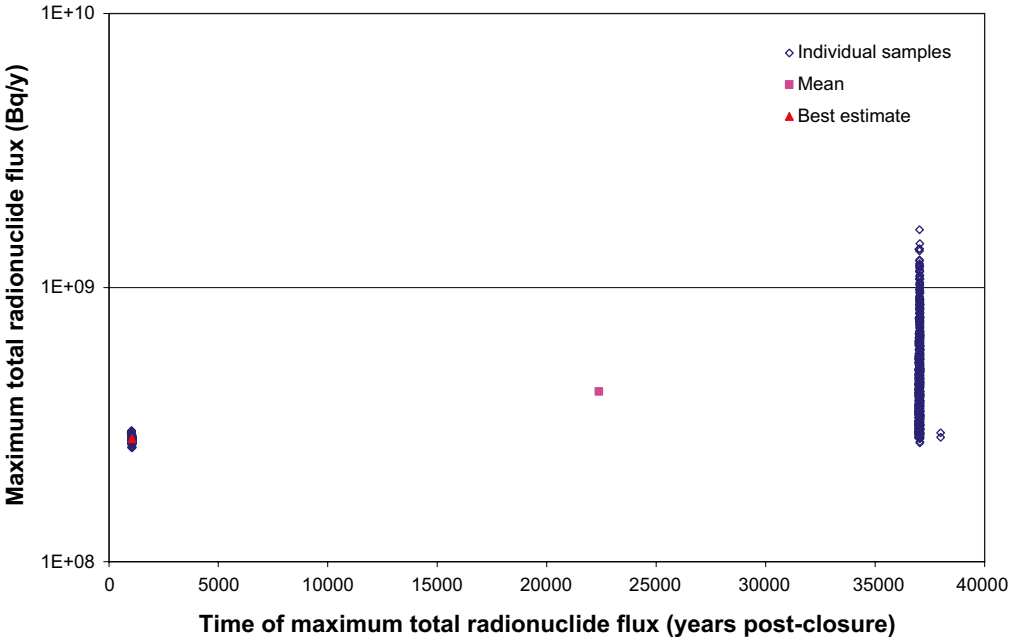

Figure 4-69. *Scatter plot of BMA maximum total near-field radionuclide flux for CC7.*

flux varies between $2.6 \cdot 10^8$ and $1.6 \cdot 10^9$ Bq/y and the time of the maximum clusters around 1,000 and 37,000 years post-closure. Figure 4-69 illustrates the increase in the total radionuclide flux following the 2nd period of continuous permafrost (failure of the BMA barriers occurs at the onset of the 2nd period of continuous permafrost). The concentration of data around this time in Figure 4-70 is most likely to be due to combinations of relatively high values of Uncertainty factors and reduced values of sorption coefficients for the dominant radionuclides (e.g. inorganic C-14, Ni-59).

Figure 4-70 is a summary plot for the near-field radionuclide flux from the BMA for the evaluation of CC7 using sampled parameters. The figure shows the mean of the total radionuclide flux and the 5th and 95th percentiles. Comments made previously in relation to the over-estimate of the lower bound due to omitted processes apply here.

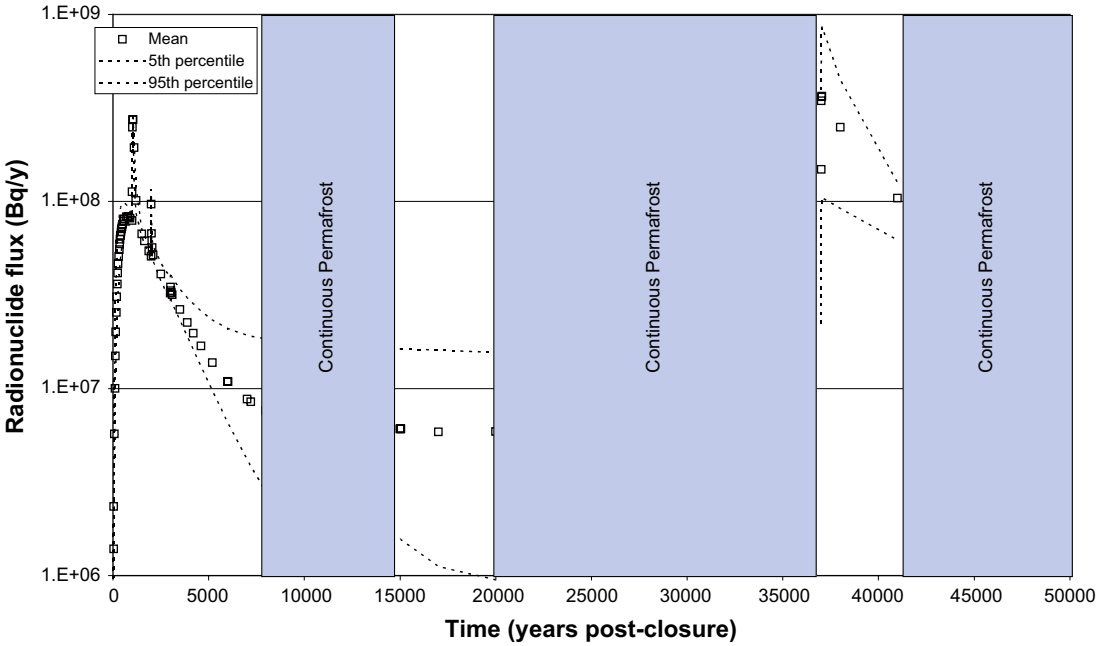

Figure 4-70. *Near-field total radionuclide flux from the BMA for CC7 using sampled parameters.*

4.8 Calculation Case CC8

This calculation case has been identified in order to assess the uncertainty in the assumption that during periods of continuous permafrost the SFR 1 repository and surrounding shallow and near-surface geosphere will freeze eliminating the potential for a release pathway.

In CC8 it is considered possible that during such periods of continuous permafrost it is possible that a migration pathway exists to a feature such as a talik located close to the SFR 1 at the natural discharge location. It should also be noted that in this calculation case it is assumed that the rate of transport during continuous permafrost is considered to be 10 times greater than during temperate conditions.

A summary of the results for CC8 is presented below in Table 4-7. The data provided in the table show the magnitudes and times of the maximum flux from the best estimate calculations and also from the calculations using sampled parameters (the latter is based on the mean of the individual results). Also shown is the range of the maximum fluxes obtained from the calculations using sampled parameters.

The results for 1BTF, 2BTF and the BLA remain unchanged from CC7 (and CC1). However, the results for the Silo and the BMA are different to CC7 (and CC1). The peak near-field radionuclide flux from the Silo for CC8 is approximately a factor of 4 higher than CC7, although it occurs later in CC8 at approximately 8,000 years post-closure (the onset of the 1st period of continuous permafrost). The peak geosphere radionuclide flux from the Silo for CC8 is little changed from CC7, although again it occurs later in CC8 at approximately 8,000 years post-closure.

The best estimate near-field radionuclide flux from the Silo for CC8 is shown in Figure 4-71. Organic C-14 dominates the initial phase of releases whilst inorganic C-14 and Ni-59 are the dominant radionuclides in the longer term. Figure 4-72 is a comparison of the key contributors to the Silo near-field radionuclide flux for CC8 and CC7. Of note here are the periods of increased radionuclide flux during continuous permafrost associated with increased groundwater fluxes and also at 20,000 years post-closure in response to the assumed partial failure of the Silo barriers at this time. The net result within CC8 is an earlier and larger cumulative radionuclide flux.

Table 4-7. Summary of results from CC8 showing maximum flux and time of peak flux in years after closure.

	Near-field		Geosphere	
Silo	Best estimate	$1.2 \cdot 10^{8}$ Bq/y at 8,000 years	Best estimate	$1.3 \cdot 10^{8}$ Bq/y at 8,000 years
	Mean	$2.3 \cdot 10^{8}$ Bq/y at 8,000 years	Mean	$3.4 \cdot 10^{8}$ Bq/y at 6,200 years
	Range of max.	$1.8 \cdot 10^{8}$ Bq/y–$3.2 \cdot 10^{8}$ Bq/y	Range of max.	$1.8 \cdot 10^{8}$ Bq/y–$2.6 \cdot 10^{9}$ Bq/y
BMA	Best estimate	$2.7 \cdot 10^{9}$ Bq/y at 20,000 years	Best estimate	$2.3 \cdot 10^{9}$ Bq/y at 20,000 years
	Mean	$8.5 \cdot 10^{9}$ Bq/y at 20,000 years	Mean	$7.8 \cdot 10^{9}$ Bq/y at 19,000 years
	Range of max.	$1.2 \cdot 10^{9}$ Bq/y–$2.5 \cdot 10^{10}$ Bq/y	Range of max.	$8.1 \cdot 10^{8}$ Bq/y–$2.3 \cdot 10^{10}$ Bq/y
1BTF	Best estimate	$2.0 \cdot 10^{8}$ Bq/y at 2,000 years	Best estimate	$1.4 \cdot 10^{8}$ Bq/y at 2,100 years
	Mean	$1.7 \cdot 10^{8}$ Bq/y at 2,000 years	Mean	$2.1 \cdot 10^{8}$ Bq/y at 2,000 years
	Range of max.	$1.9 \cdot 10^{7}$ Bq/y–$2.6 \cdot 10^{8}$ Bq/y	Range of max.	$7.9 \cdot 10^{6}$ Bq/y–$2.6 \cdot 10^{9}$ Bq/y
2BTF	Best estimate	$2.7 \cdot 10^{8}$ Bq/y at 2,000 years	Best estimate	$2.1 \cdot 10^{8}$ Bq/y at 2,100 years
	Mean	$2.3 \cdot 10^{8}$ Bq/y at 2,000 years	Mean	$3.6 \cdot 10^{8}$ Bq/y at 2,000 years
	Range of max.	$3.7 \cdot 10^{7}$ Bq/y–$3.5 \cdot 10^{8}$ Bq/y	Range of max.	$1.7 \cdot 10^{7}$ Bq/y–$5.3 \cdot 10^{9}$ Bq/y
BLA	Best estimate	$6.3 \cdot 10^{8}$ Bq/y at 0 years	Best estimate	$1.5 \cdot 10^{8}$ Bq/y at 75 years
	Mean	$7.9 \cdot 10^{8}$ Bq/y at 0 years	Mean	$2.1 \cdot 10^{8}$ Bq/y at 690 years
	Range of max.	$3.5 \cdot 10^{8}$ Bq/y–$1.8 \cdot 10^{9}$ Bq/y	Range of max.	$1.5 \cdot 10^{6}$ Bq/y–$1.3 \cdot 10^{9}$ Bq/y

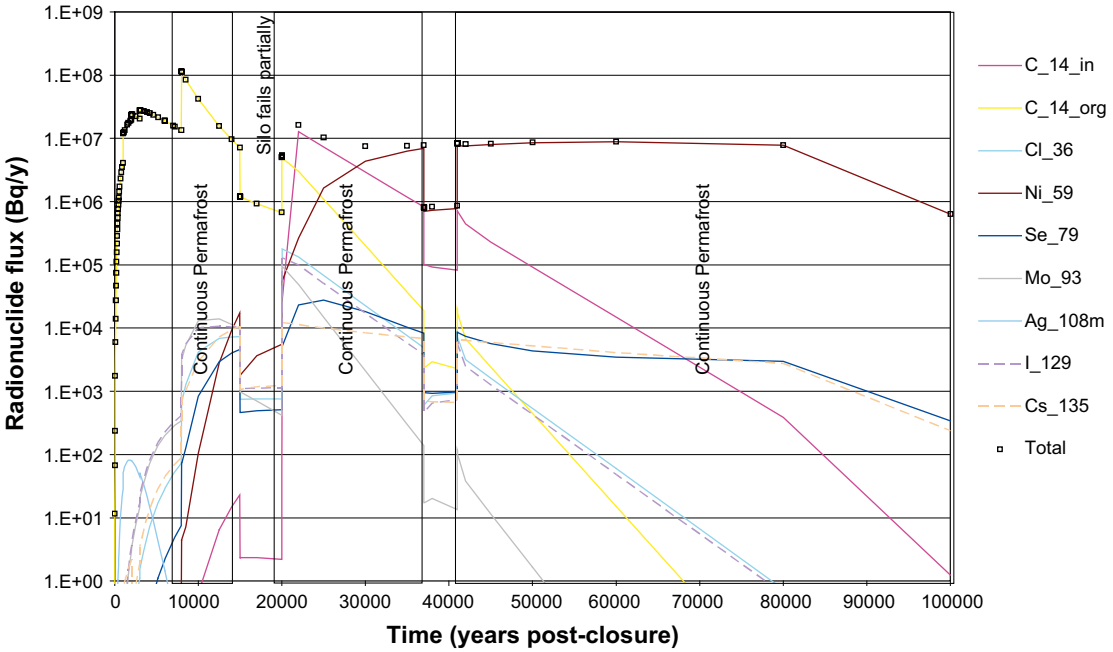

Figure 4-71. *Near-field best estimate radionuclide flux from the Silo for CC8 calculation.*

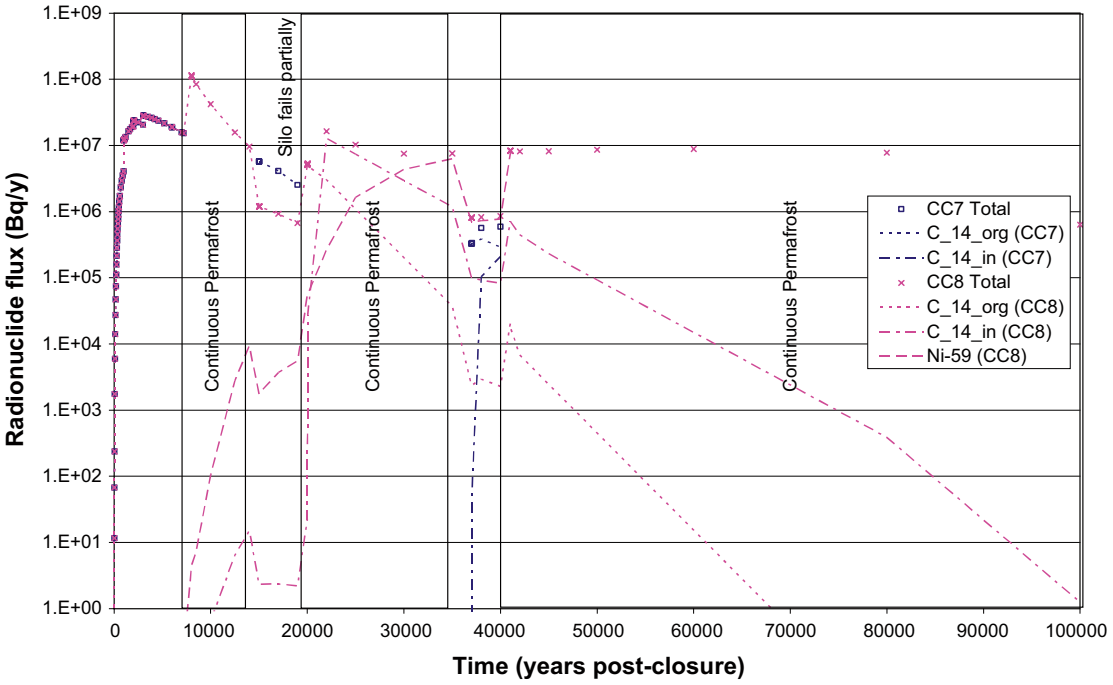

Figure 4-72. *Comparison of key contributions to Silo near-field radionuclide flux for CC7 and CC8.*

Figure 4-73 is a summary plot for the near-field radionuclide flux from the Silo for the evaluation of CC8 using sampled parameters. The figure shows the mean of the total radionuclide flux and the 5th and 95th percentiles. Comments made previously in relation to the over-estimate of the lower bound due to omitted processes apply here.

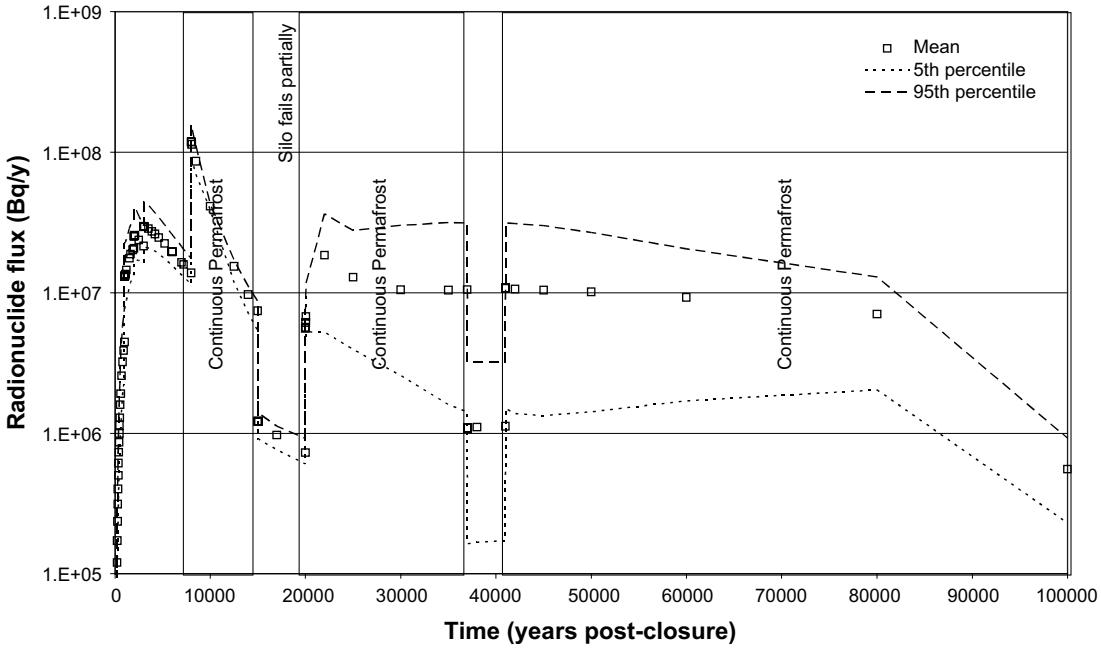

Figure 4-73. *Near-field total radionuclide flux from the Silo for CC8 using sampled parameters.*

The best estimate geosphere radionuclide flux from the Silo for CC8 is shown in Figure 4-74. Generally the geosphere trends are similar to those seen previously in the near-field; namely the periods of increased radionuclide flux during continuous permafrost associated with increased groundwater fluxes and also at 20,000 years post-closure in response to the assumed partial failure of the Silo barriers at this time.

Figure 4-75 is a summary plot for the geosphere radionuclide flux from the Silo for the evaluation of CC8 using sampled parameters. The figure shows the mean of the total radionuclide flux and the 5th and 95th percentiles. Comments made previously in relation to the over-estimate of the lower bound due to omitted processes apply here.

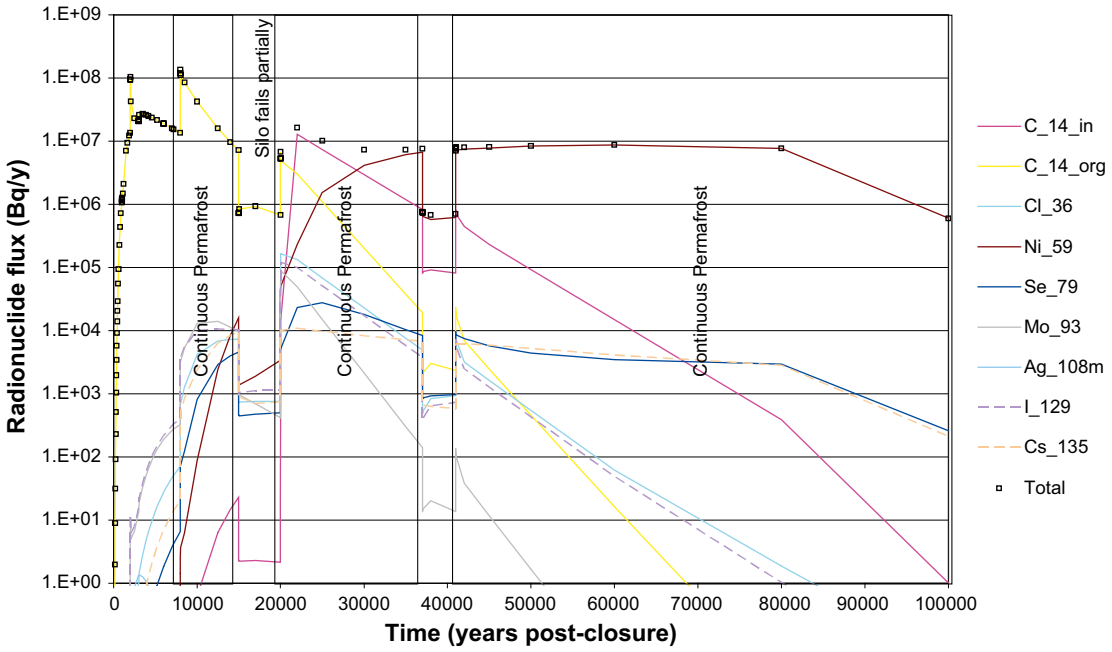

Figure 4-74. *Geosphere best estimate radionuclide flux from the Silo for CC8 calculation.*

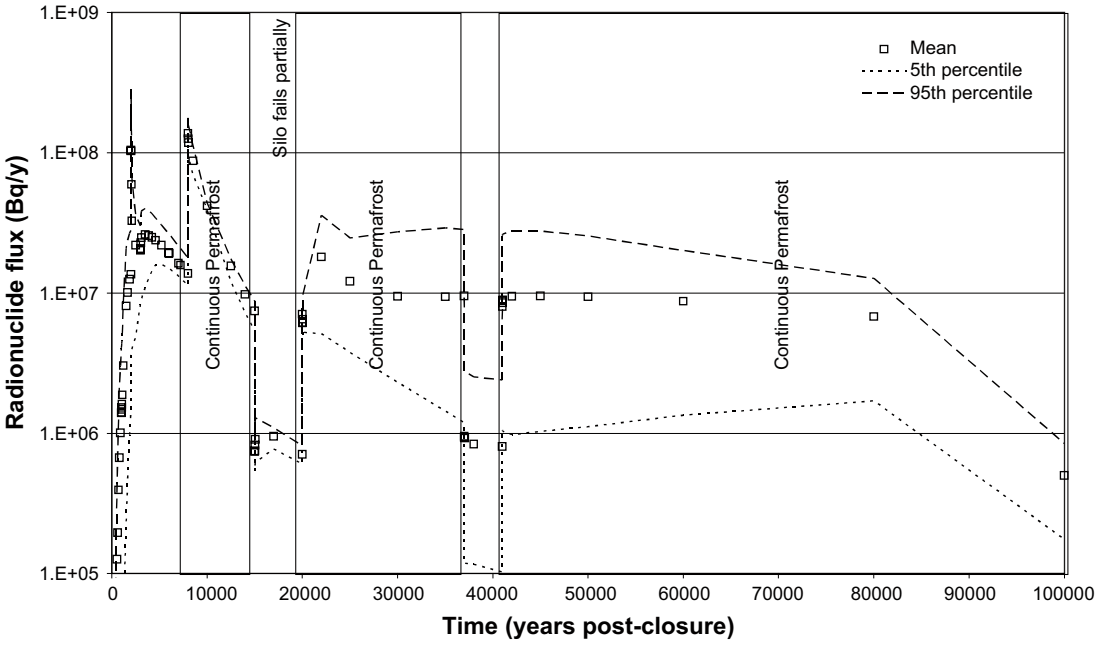

Figure 4-75. *Geosphere total radionuclide flux from the Silo for CC8 using sampled parameters.*

The peak near-field and geosphere radionuclide fluxes from the BMA for CC8 are both approximately an order of magnitude higher than those in CC7, although they occur later in CC8 at approximately 20,000 years post-closure (the onset of the 2nd period of continuous permafrost when the BMA barriers are assumed to fail).

The best estimate near-field radionuclide flux from the BMA for CC8 is shown in Figure 4-76. Of note here are the periods of increased radionuclide flux during continuous permafrost associated with increased groundwater fluxes and also at 20,000 years post-closure in response to the assumed partial failure of the BMA barriers at this time. The release of inorganic C-14 and Ni-59 at 20,000 years post-closure is important in determining the overall maximum radionuclide flux. The long-term releases are dominated by Tc-99.

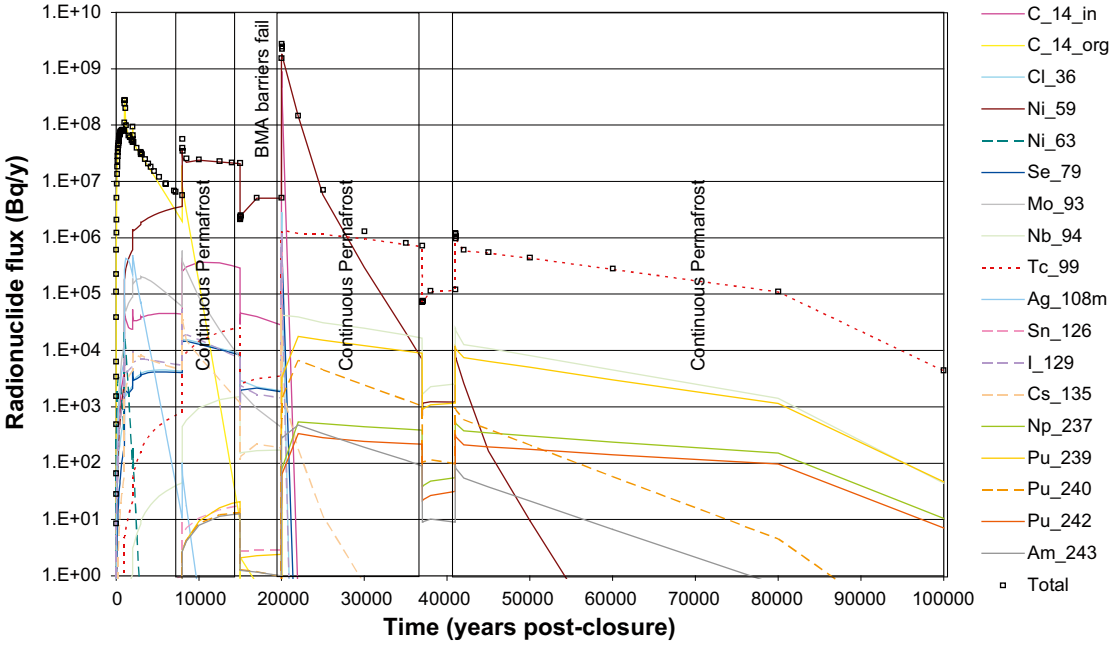

Figure 4-76. *Near-field best estimate radionuclide flux from the BMA for CC8.*

It is worth noting again the consideration that the parameterisation of groundwater flow through a failed BMA encapsulation is likely to be conservative in terms of radionuclide release.

Figure 4-77 is a summary plot for the near-field radionuclide flux from the BMA for the evaluation of CC8 using sampled parameters. The figure shows the mean of the total radionuclide flux and the 5th and 95th percentiles. Comments made previously in relation to the over-estimate of the lower bound due to omitted processes apply here.

4.9 Calculation Case CC9

CC9 considers the potential impacts of a reduction in the values of near-field sorption coefficients for those elements which are sensitive to concentrations of complexing agents. The sorption reduction factors are summarised in Table 4-8. Further description of CC9 is given in subsection 2.2.8.

Table 4-8. Summary of sorption reduction factors [–] for CC9.

	Concrete and cement	Sand and gravel	Bentonite
C_in	10	10	1
Co	10	1	1
Ni	10	1	1
Sr	10	1	1
Mo	30	1	1
Tc	10	10	10
Ag	10	1	1
Sn	10	1	1
Cs	10	1	1
Ho	1,000	5	5
Np	10	10	10
Pu	1,000	1,000	1,000
Am	500	5	5

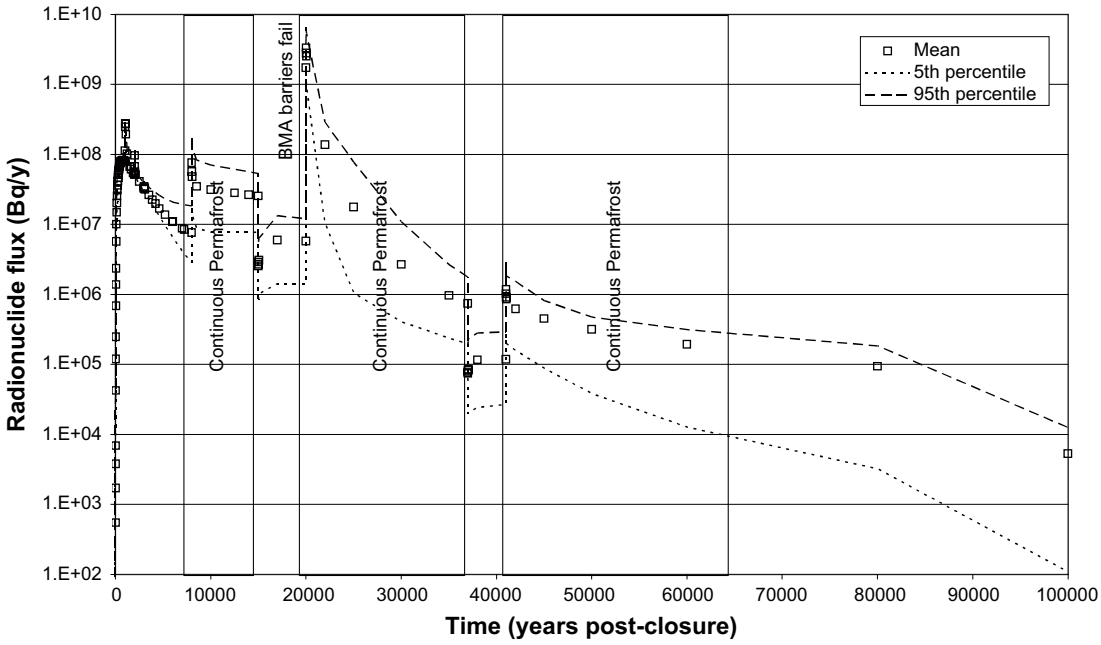

Figure 4-77. Near-field total radionuclide flux from the BMA for CC8 using sampled parameters.

Table 4-9 summarises the results for CC9. The results for the Silo are unaltered from those previously reported for CC1. The results for the BMA, 1BTF and 2BTF show slightly increased maximum radionuclide fluxes compared to those reported for CC1. The results for each facility[19] are discussed in turn below.

Silo

Table 4-10 shows a comparison of peak near-field radionuclide fluxes for the Silo for CC9 compared with CC1 for a selected subset of radionuclides which show increased peak fluxes. Figure 4-78 shows a plot of the near-field radionuclide flux from the Silo.

Table 4-9. Summary of results for CC9 showing maximum flux, key radionuclide and time of peak flux in years after closure.

	Near-field (Maximum flux, time and key contributor)	Geosphere (Maximum flux, time and key contributor)
Silo	$2.8 \cdot 10^{7}$ Bq/y, 3,000 years Organic C-14	$1.0 \cdot 10^{8}$ Bq/y, 2,000 years Organic C-14
BMA	$7.0 \cdot 10^{8}$ Bq/y, 1,100 years Organic C-14	$5.3 \cdot 10^{8}$ Bq/y, 2,000 years Organic C-14
1BTF	$2.0 \cdot 10^{8}$ Bq/y, 2,000 years Inorganic C-14	$1.6 \cdot 10^{8}$ Bq/y, 2,100 years Inorganic C-14
2BTF	$2.9 \cdot 10^{8}$ Bq/y, 2,000 years Inorganic C-14	$3.1 \cdot 10^{8}$ Bq/y, 2,100 years Inorganic C-14

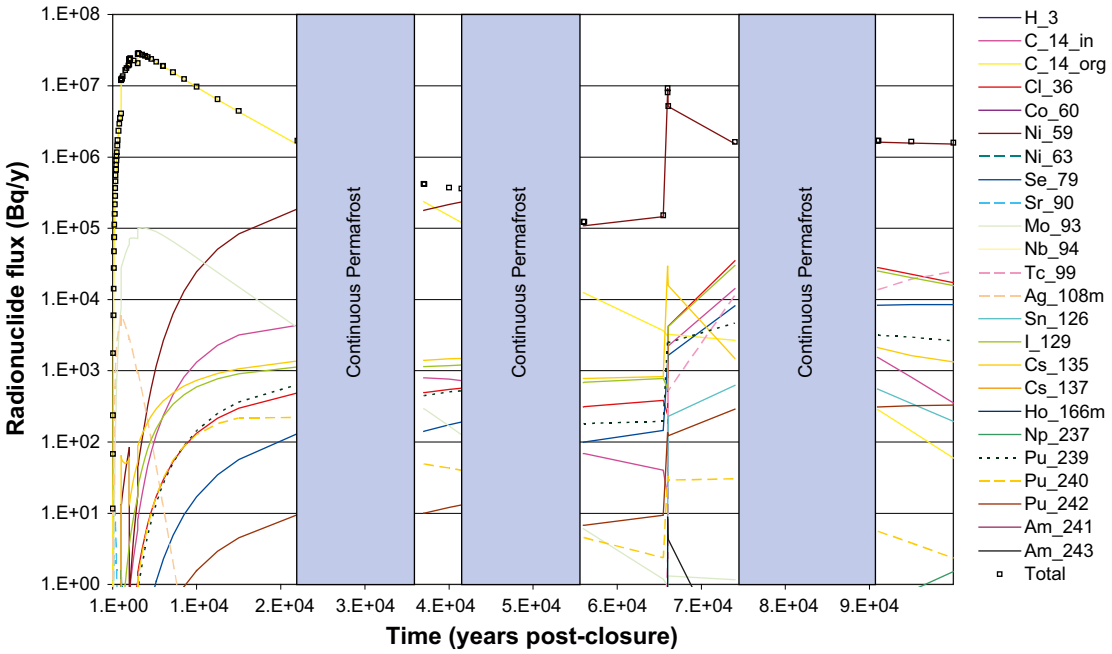

Figure 4-78. *Near-field best estimate radionuclide flux for Silo CC9.*

[19] The BLA is not included as sorption is not included in CC1 for this facility.

Table 4-10. Comparison of peak Silo near-field radionuclide fluxes for CC9.

	Peak radionuclide flux [Bq/y]	
	CC1	CC9
Inorganic C-14	4.8·103	$1.4 \cdot 10^{4}$
Ni-59	$1.3 \cdot 10^{6}$	$9.2 \cdot 10^{6}$
Ni-63	$4.0 \cdot 10^{-6}$	1.6
Mo-93	$4.4 \cdot 10^{2}$	$1.0 \cdot 10^{5}$
Tc-99	$1.9 \cdot 10^{1}$	$2.5 \cdot 10^{4}$
Ag-108m	$8.2 \cdot 10^{1}$	$6.1 \cdot 10^{3}$
Np-237	$3.3 \cdot 10^{-5}$	$1.5 \cdot 10^{0}$
Pu-239	$1.1 \cdot 10^{-4}$	$4.7 \cdot 10^{3}$
Pu-240	$9.9 \cdot 10^{-8}$	$2.2 \cdot 10^{2}$
Pu-242	$1.4 \cdot 10^{-5}$	$3.3 \cdot 10^{2}$
Am-243	$3.7 \cdot 10^{-8}$	8.8

Generally the impact of reduced sorption values results in an earlier breakthrough and a higher maximum flux. The exact details for each radionuclide depend on the degree to which sorption is affected by complexants and also the half-life of the radionuclide. For example, Ni undergoes a factor of 10 reduction in the sorption coefficient for concrete and cement. The maximum radionuclide flux of Ni-59 is increased by a factor of 9 whereas the maximum flux of Ni-63 is increased by 6 orders of magnitude. This varying behaviour is due to the increased sensitivity of the relatively short-lived Ni-63 (half-life 100 years) to retardation compared to Ni-59 (half-life 76,000 years). Under conditions reduced of reduced sorption more Ni-59 is released from the Silo before it decays even though the amount released remains negligible. Large increases in the maximum fluxes for Np-237, Pu-239, Pu-240, Pu-242 and Am-243 are also estimated as the actinide elements show the most sensitivity to complexants. However, as illustrated in Figure 4-78 the maximum fluxes of those radionuclides affected by complexants remain several orders of magnitude below the overall maximum, hence the overall results are unchanged from CC1.

BMA

Table 4-11 shows a comparison of peak near-field radionuclide fluxes for the BMA for CC9 compared with CC1 for a selected subset of radionuclides which show increased peak fluxes. Figures 4-79 and 4-80 shows the near-field radionuclide flux from the BMA, with the latter showing the initial 4,000 year period in greater detail.

Generally a similar trend is seen here to that reported previously for the Silo. An importance difference is a slight increase in overall maximum near-field and geosphere radionuclide fluxes. This is caused by increased contributions from releases of radionuclides undergoing reducing sorption, particularly inorganic C-14 and Ni-59 (Figure 4-79). Similarly to the Silo some of the largest increases are estimated for the actinides Np-237, Pu-239, Pu-240, Pu-242, Am-241 and Am-243. However, as illustrated in Figure 4-80 the maximum fluxes of these radionuclides remain several orders of magnitude below the overall maximum.

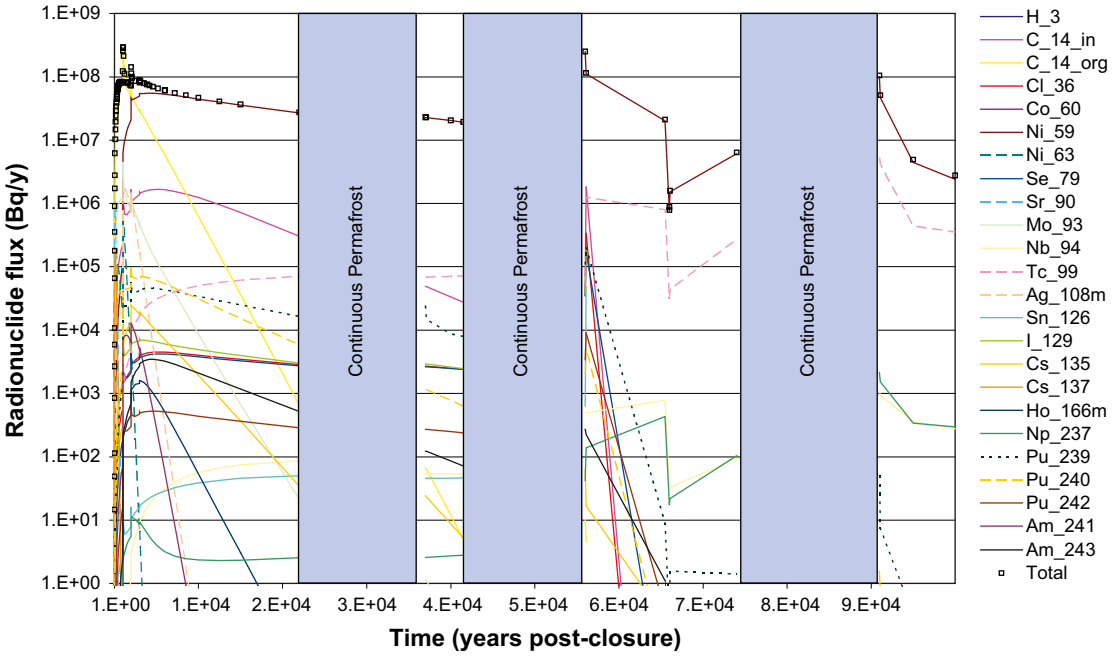

Figure 4-79. *Near-field best estimate radionuclide flux for BMA CC9.*

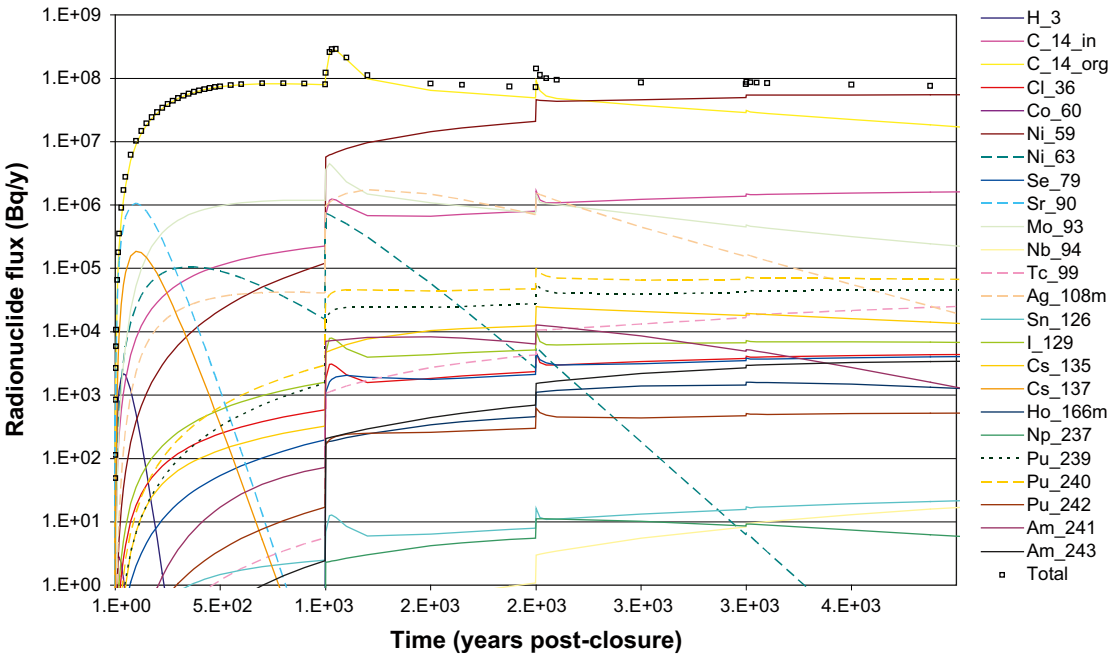

Figure 4-80. *Detail of best estimate near-field flux from BMA to 4,000 years for CC9.*

Table 4-11. Comparison of peak BMA near-field radionuclide fluxes for CC9.

	Peak radionuclide flux [Bq/y]	
	CC1	CC9
Inorganic C-14	$1.2 \cdot 10^{6}$	$1.8 \cdot 10^{6}$
Ni-59	$2.0 \cdot 10^{8}$	$2.5 \cdot 10^{8}$
Ni-63	$2.1 \cdot 10^{4}$	$7.4 \cdot 10^{5}$
Sr-90	$7.9 \cdot 10^{4}$	$1.1 \cdot 10^{6}$
Mo-93	$2.1 \cdot 10^{5}$	$4.5 \cdot 10^{6}$
Tc-99	$3.9 \cdot 10^{5}$	$5.3 \cdot 10^{5}$
Ag-108m	$4.9 \cdot 10^{5}$	$1.8 \cdot 10^{6}$
Cs-137	$4.8 \cdot 10^{3}$	$1.9 \cdot 10^{5}$
Ho-166m	$1.3 \cdot 10^{-2}$	$1.6 \cdot 10^{3}$
Np-237	$6.4 \cdot 10^{1}$	$2.1 \cdot 10^{3}$
Pu-239	$3.2 \cdot 10^{2}$	$2.0 \cdot 10^{5}$
Pu-240	$2.7 \cdot 10^{0}$	$1.0 \cdot 10^{5}$
Pu-242	$3.9 \cdot 10^{1}$	$9.0 \cdot 10^{3}$
Am-241	$3.5 \cdot 10^{-2}$	$1.3 \cdot 10^{4}$
Am-243	$3.8 \cdot 10^{-1}$	$3.5 \cdot 10^{3}$

1BTF

Table 4-12 shows a comparison of peak near-field radionuclide fluxes for the 1BTF for CC9 compared with CC1 for a selected subset of radionuclides which show increased peak fluxes for CC9. Figures 4-81 and 4-82 show plots of the near-field radionuclide flux from the 1BTF, with the latter showing the initial 4,000 year period in greater detail.

Generally a similar trend is seen here to that reported previously for the Silo and BMA. However, it is important to note that the overall maximum radionuclide flux from the near-field is unaltered from that reported for CC1. This may seem surprising considering that the dominant contribution to this are from inorganic C-14, which is assumed to undergo reduces sorption in

Table 4-12. Comparison of peak 1BTF near-field radionuclide fluxes for CC9.

	Peak radionuclide flux [Bq/y]	
	CC1	CC9
Inorganic C-14	$7.3 \cdot 10^{7}$	$7.2 \cdot 10^{7}$
Sr-90	$7.8 \cdot 10^{3}$	$1.3 \cdot 10^{5}$
Tc-99	$1.1 \cdot 10^{5}$	$1.1 \cdot 10^{6}$
Cs-137	$1.1 \cdot 10^{2}$	$2.1 \cdot 10^{3}$
Ho-166m	$2.1 \cdot 10^{-1}$	$1.4 \cdot 10^{3}$
Np-237	1.5	$2.4 \cdot 10^{1}$
Pu-239	$1.5 \cdot 10^{2}$	$4.1 \cdot 10^{5}$
Pu-240	$6.5 \cdot 10^{1}$	$7.0 \cdot 10^{5}$
Pu-242	$4.3 \cdot 10^{3}$	$7.3 \cdot 10^{3}$
Am-241	$3.9 \cdot 10^{-1}$	$3.3 \cdot 10^{2}$
Am-243	3.9	$1.1 \cdot 10^{2}$

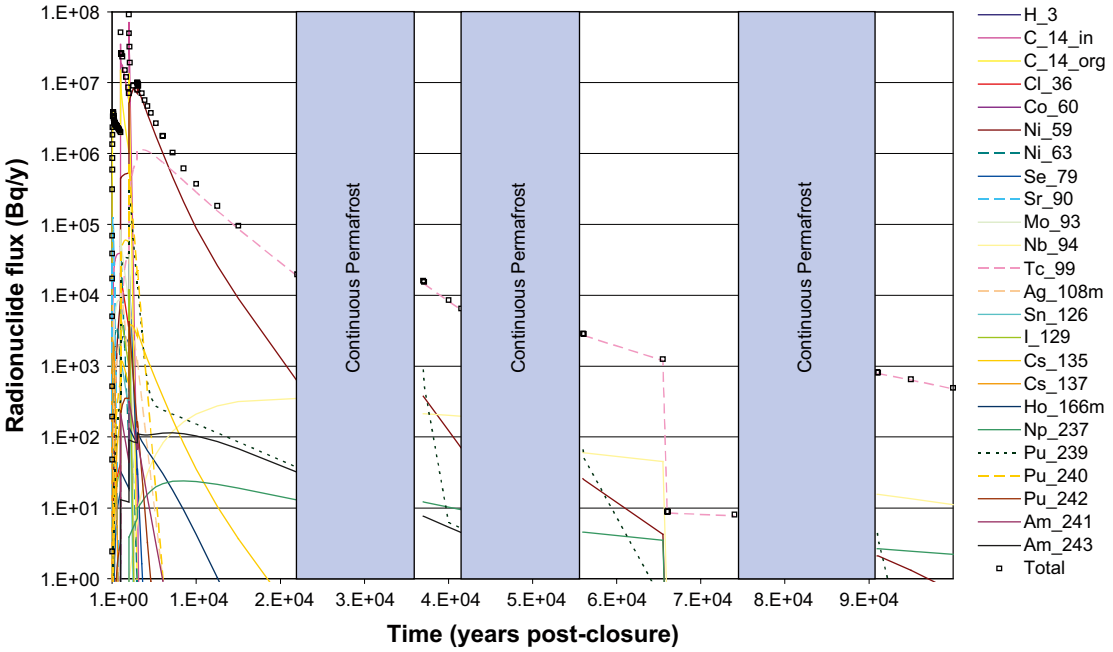

Figure 4-81. *Near-field best estimate radionuclide flux for 1BTF CC9.*

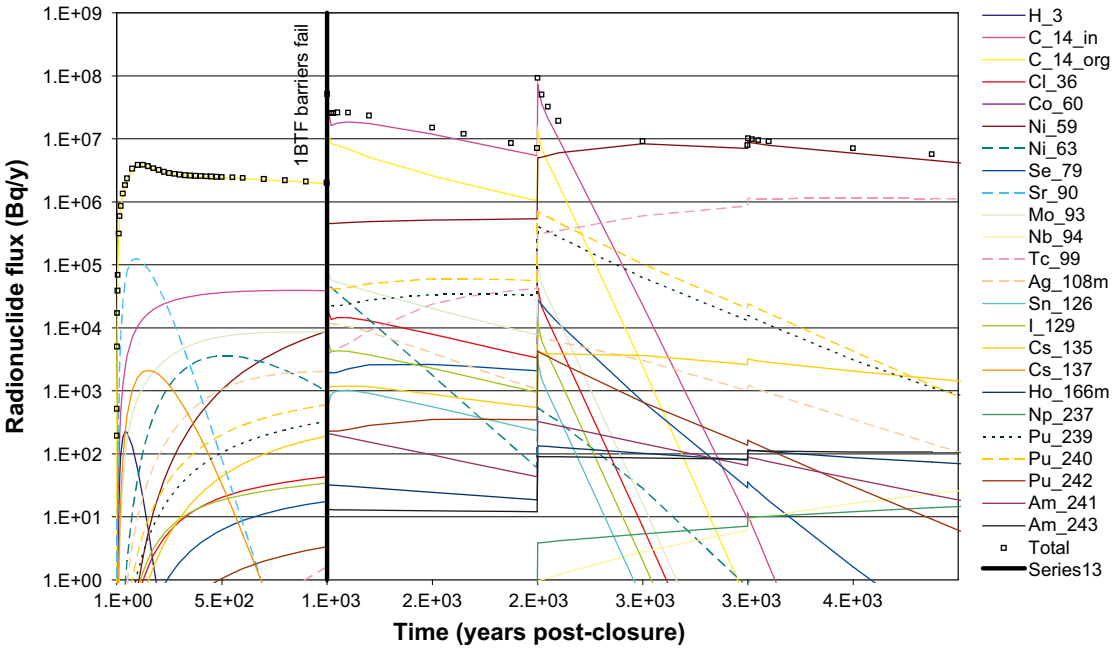

Figure 4-82. *Detail of best estimate near-field flux from 1BTF to 4,000 years for CC9.*

calculation CC9. Figure 4-83 shows a comparison of the near-field fluxes of inorganic C-14 from CC9 and CC1. Inspection of this figure reveals that within CC9 the release of inorganic C-14 is initially much higher than CC1 and therefore the depletion of the inventory also occurs earlier within CC9. This also explains the slightly higher maximum geosphere flux for CC9 reported in Table 4-9.

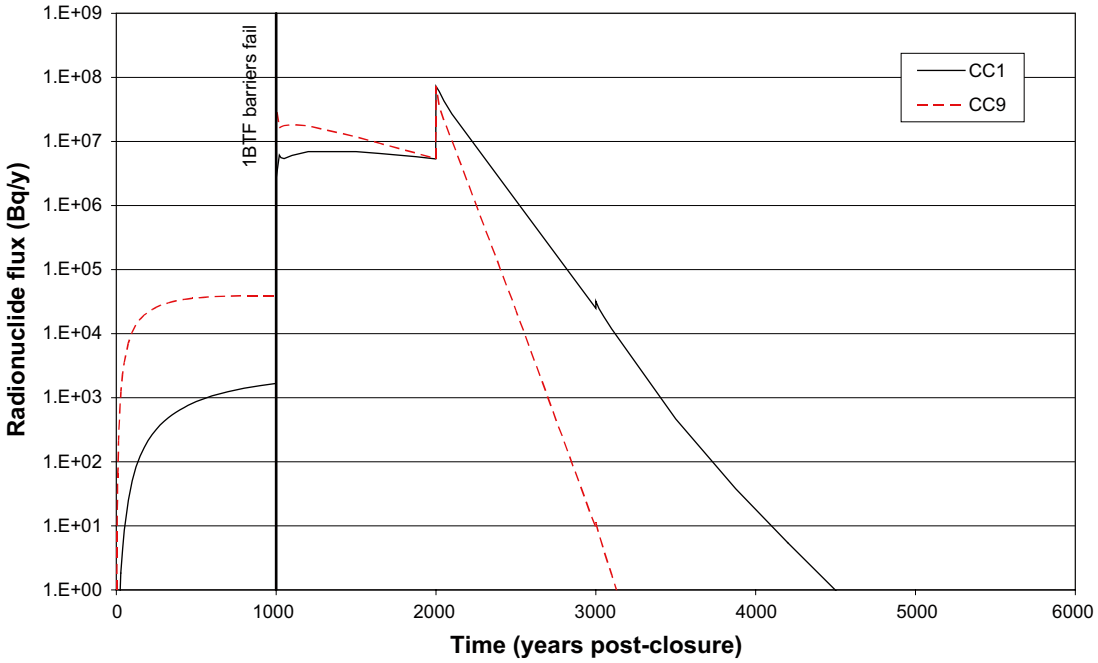

Figure 4-83. *Comparison of 1BTF near-field inorganic C-14 radionuclide flux for CC9 and CC1.*

2BTF

Table 4-13 shows a comparison of peak near-field radionuclide fluxes for the 2BTF for CC9 compared with CC1 for a selected subset of radionuclides which show increased peak fluxes. Figures 4-84 and 4-85 show plots of the near-field radionuclide flux from the 2BTF, with the latter showing the initial 4,000 year period in greater detail.

Generally similar trends are seen to those reported previously for the 1BTF. However, the maximum near-field flux of inorganic C-14 is slightly higher for CC9 than it was for CC1 which is different to that observed for 1BTF. This behaviour for 2BTF is due to the fact that inventory

Table 4-13. Comparison of peak 2BTF near-field radionuclide fluxes for CC9.

	Peak radionuclide flux [Bq/y]	
	CC1	CC9
Inorganic C-14	$3.3 \cdot 10^{8}$	$3.6 \cdot 10^{8}$
Sr-90	$2.2 \cdot 10^{4}$	$8.0 \cdot 10^{5}$
Tc-99	$6.5 \cdot 10^{4}$	$6.9 \cdot 10^{5}$
Cs-137	$9.2 \cdot 10^{2}$	$1.4 \cdot 10^{4}$
Ho-166m	$3.1 \cdot 10^{-1}$	$2.2 \cdot 10^{4}$
Np-237	2.9	$3.3 \cdot 10^{2}$
Pu-239	$1.1 \cdot 10^{2}$	$5.9 \cdot 10^{5}$
Pu-240	$4.5 \cdot 10^{1}$	$1.0 \cdot 10^{6}$
Pu-242	2.1	$5.0 \cdot 10^{3}$
Am-241	$1.7 \cdot 10^{-2}$	$1.9 \cdot 10^{4}$
Am-243	2.2	$5.3 \cdot 10^{3}$

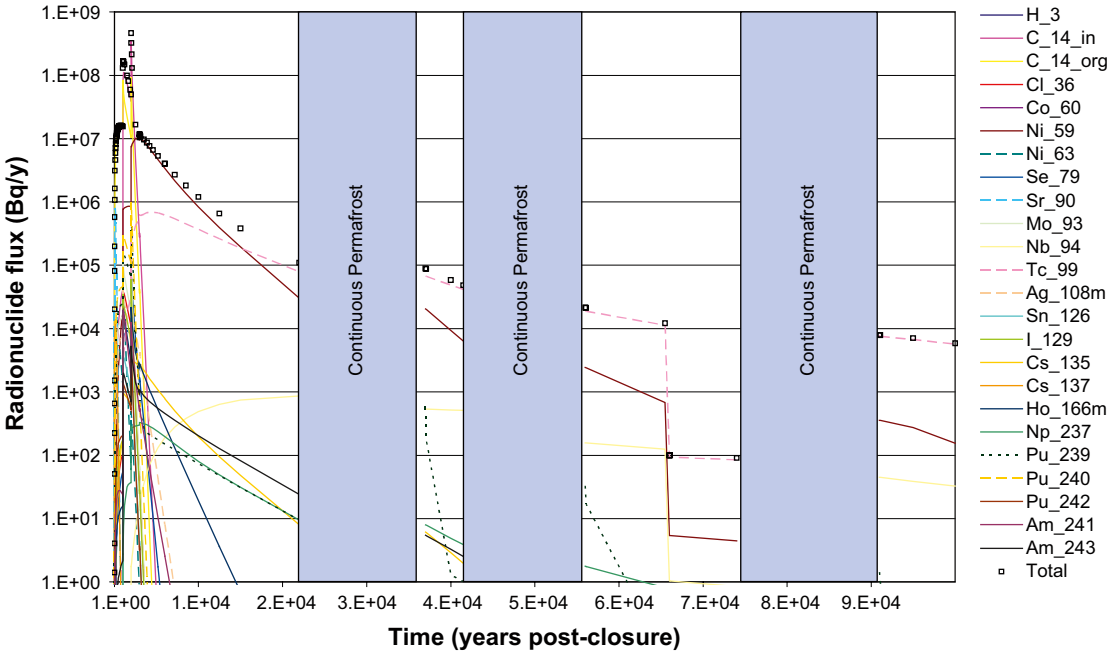

Figure 4-84. *Near-field best estimate radionuclide flux for 2BTF CC9.*

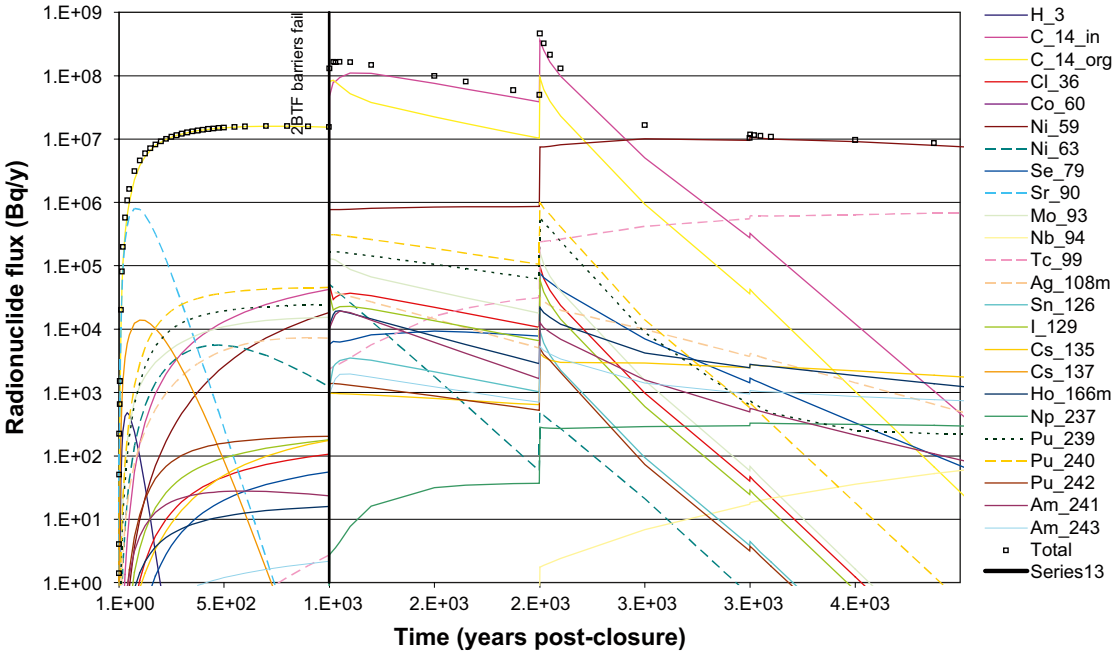

Figure 4-85. *Detail of best estimate near-field flux from 2BTF to 4,000 years for CC9.*

of inorganic C-14 within 2BTF is higher than that in 1BTF which results in the relatively higher fluxes (Figures 4-86 and 4-87). This, along with contributions from other radionuclides, also explains the slightly higher maximum near-field and geosphere fluxes reported for CC9 in Table 4-9.

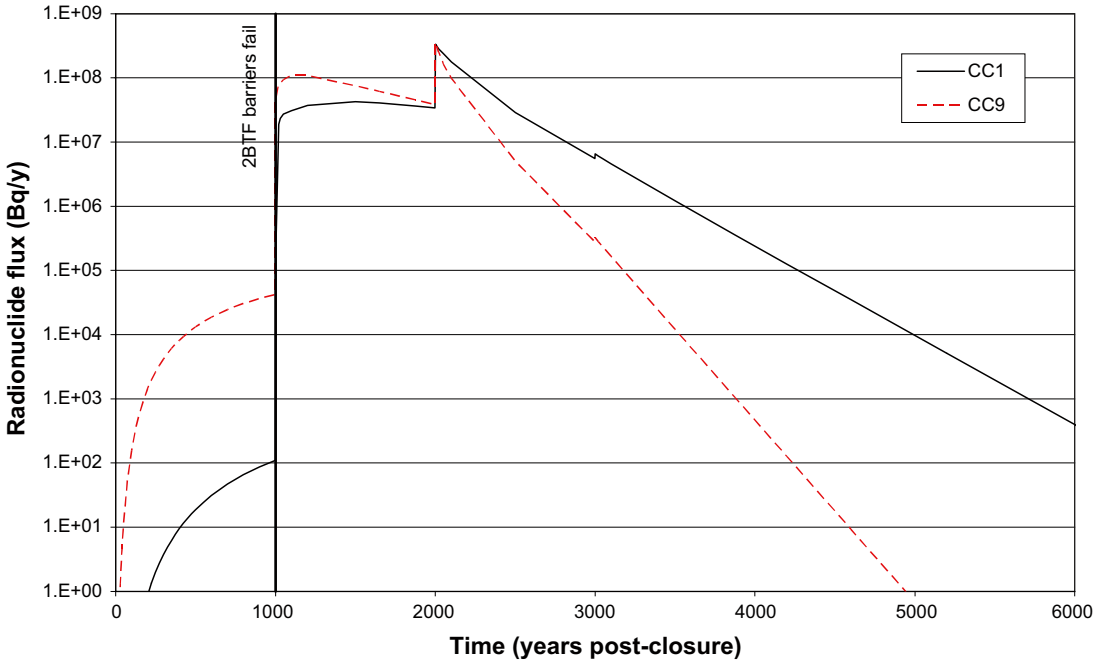

Figure 4-86. *Comparison of 2BTF near-field inorganic C-14 radionuclide flux for CC9 and CC1.*

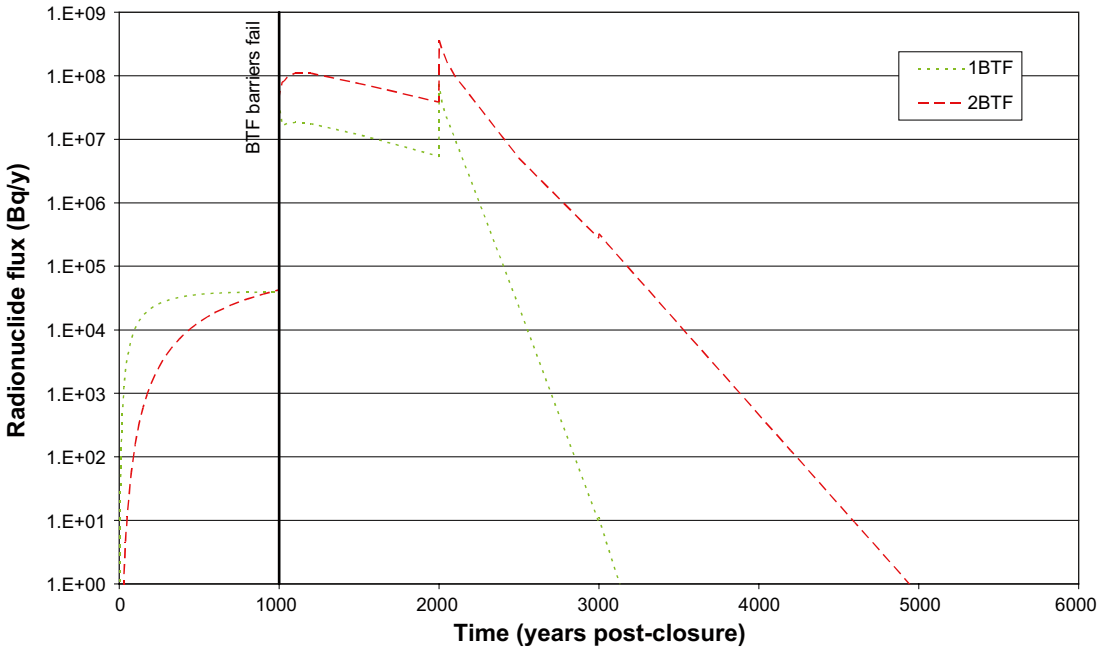

Figure 4-87. *Comparison of near-field inorganic C-14 radionuclide flux from 1BTF and 2BTF for CC9.*

4.10 Calculation Case CC10

Calculation Case 10 (CC10) considers the potential consequences for radionuclide release from the Silo during periods of enhanced bulk gas generation. A fuller description of this calculation case is given in subsection 2.2.9.

Table 4-14 below summarises the best estimate Silo results for CC1 and CC10. The effect of enhanced bulk gas generation results in a minor increase only in the maximum near-field and geosphere radionuclide fluxes for the best estimate evaluation. Data from the calculation using sampled parameters shows similar trends to those reported previously for CC1.

Figure 4-88 shows a comparison of the initial radionuclide release from the Silo for both CC1 and CC10. There is generally a higher release rate over the initial 1,000 years post-closure but these differences gradually reduce over time. Also inset in Figure 4-88 is an expanded view of the first 500 years post-closure which illustrates that the largest difference between the two calculations is evident after approximately 10 years post-closure (when it is assumed that the Silo has equilibrated and is able to passively vent gas as it is generated).

Figure 4-89 shows the breakdown of the near-field radionuclide fluxes from the best estimate calculation of CC6 for the initial 100 year period post-closure. This illustrates that the early peak at around 11 years is due to contributions from the mobile radionuclide H-3. The breakthrough of organic C-14 to the geosphere occurs slightly quicker for CC10 when compared to CC1 reaching a slightly larger value although the time of the maximum is not altered. The near-field results from the calculation using sampled parameters show a similar trend to the results from the best estimate calculation; the maximum total fluxes for CC10 are slightly higher than those from CC1, although the times of these maxima are little changed.

Table 4-14. Summary of best estimate results for Silo CC1 and CC10 showing maximum flux, key radionuclide and time of peak flux in years after closure.

	Near-field (Maximum flux, time and key contributor)	Geosphere (Maximum flux, time and key contributor)
CC1	$2.8 \cdot 10^{7}$ Bq/y, 3,000 years Organic C-14	$1.0 \cdot 10^{8}$ Bq/y, 2,000 years Organic C-14
CC10	$2.9 \cdot 10^{7}$ Bq/y, 3,000 years Organic C-14	$1.1 \cdot 10^{8}$ Bq/y, 2,000 years Organic C-14

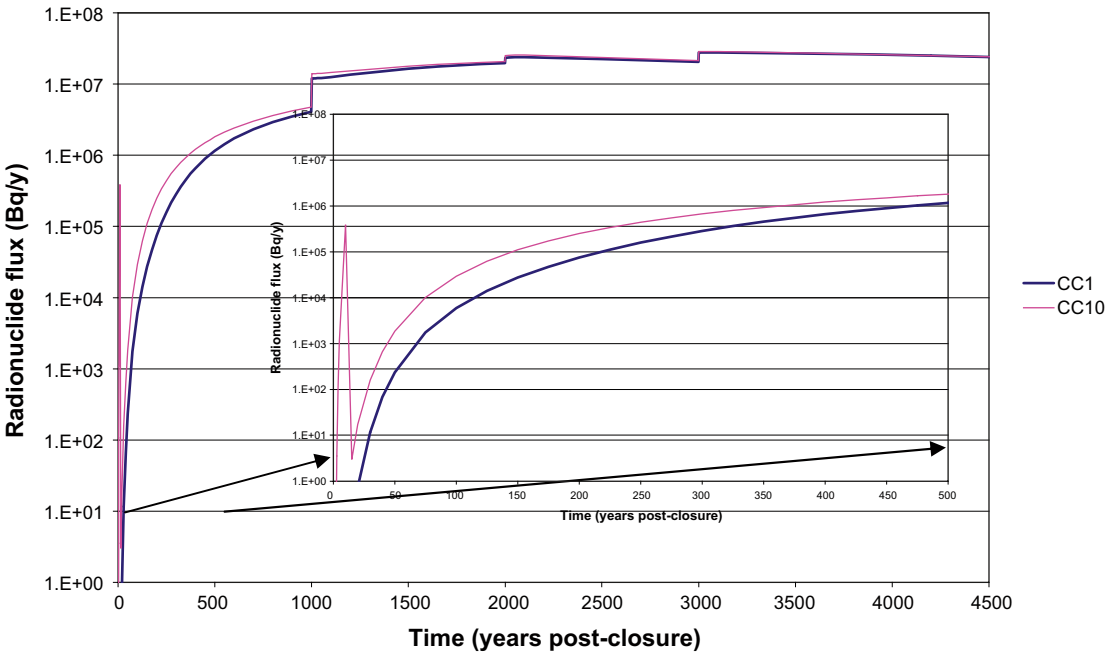

Figure 4-88. *Comparison of initial best estimate near-field release from the Silo for CC1 and CC10.*

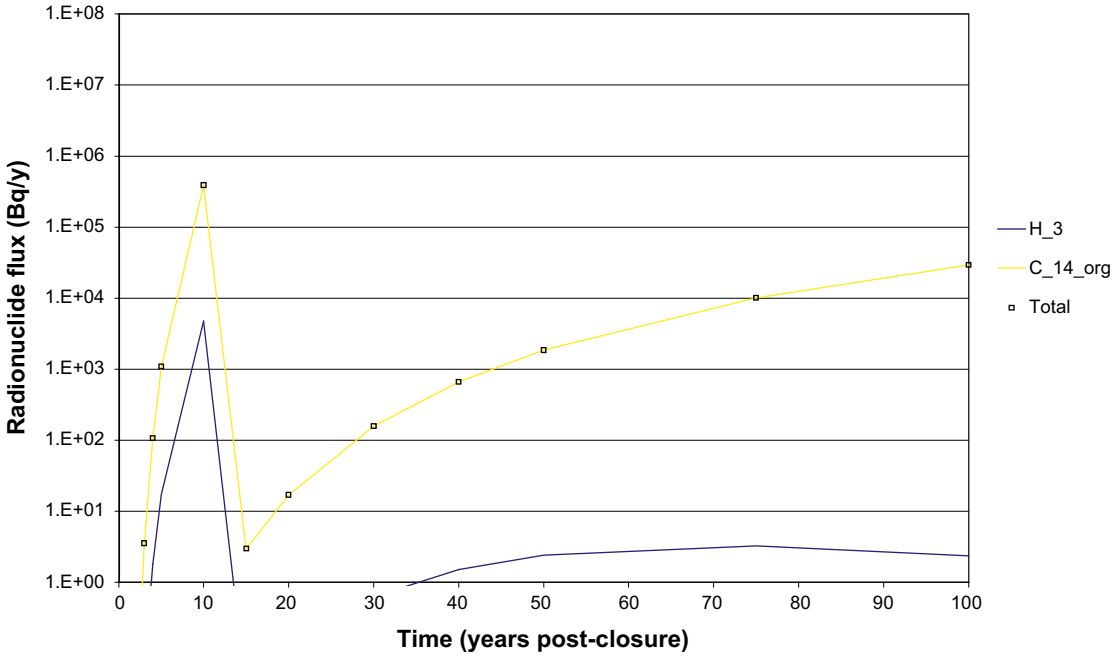

Figure 4-89. *Short-term near-field best estimate radionuclide flux for the Silo for CC10.*

Radioactive decay during transit through the geosphere results in a negligible radionuclide flux of H-3 from the geosphere to the biosphere. The breakthrough of organic C-14 to the biosphere occurs slightly quicker for CC10 when compared to CC1 reaching a slightly larger value although the time of the maximum is not altered. The geosphere results from the calculation using sampled parameters show a similar trend to the near-field results, as discussed above.

4.11 Calculation Case CC11

Figures 4-90 to 4-94 are plots of the best estimate radionuclide concentrations[20] in the gravel in the Silo, BMA, 1BTF, 2BTF and BLA, respectively for CC1. The radionuclides with the highest concentrations in the Silo and the BMA are initially organic C-14, and in the long-term Ni-59. The highest radionuclide concentrations in the BTF facilities are initially organic and inorganic C-14, and in the long-term Ni-59 and Tc-99. The highest radionuclide concentrations in the BLA are Ni-59 and Tc-99.

Figures 4-95 to 4-98 are plots of the best estimate radionuclide concentrations in the gravel in the Silo, BMA, 1BTF and 2BTF, respectively for CC9. The same radionuclides have the highest concentrations for CC9 as for CC1.

[20] Radionuclide concentrations were calculated as the amount of a radionuclide in a compartment divided by the volume of the compartment.

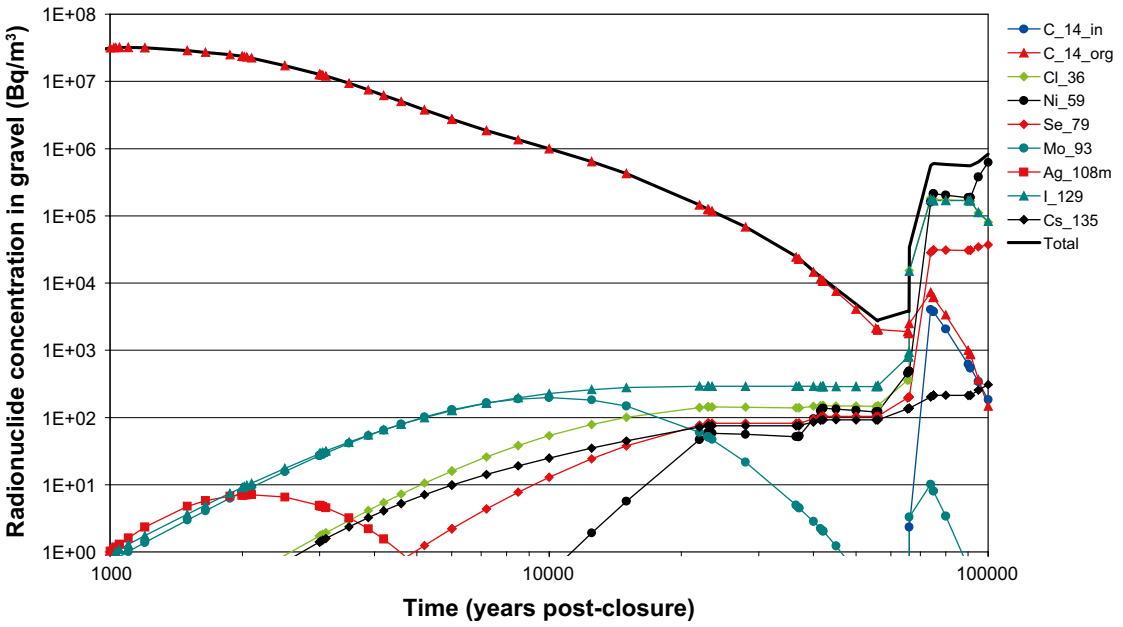

Figure 4-90. *Best estimate radionuclide concentrations within Silo gravel for CC1.*

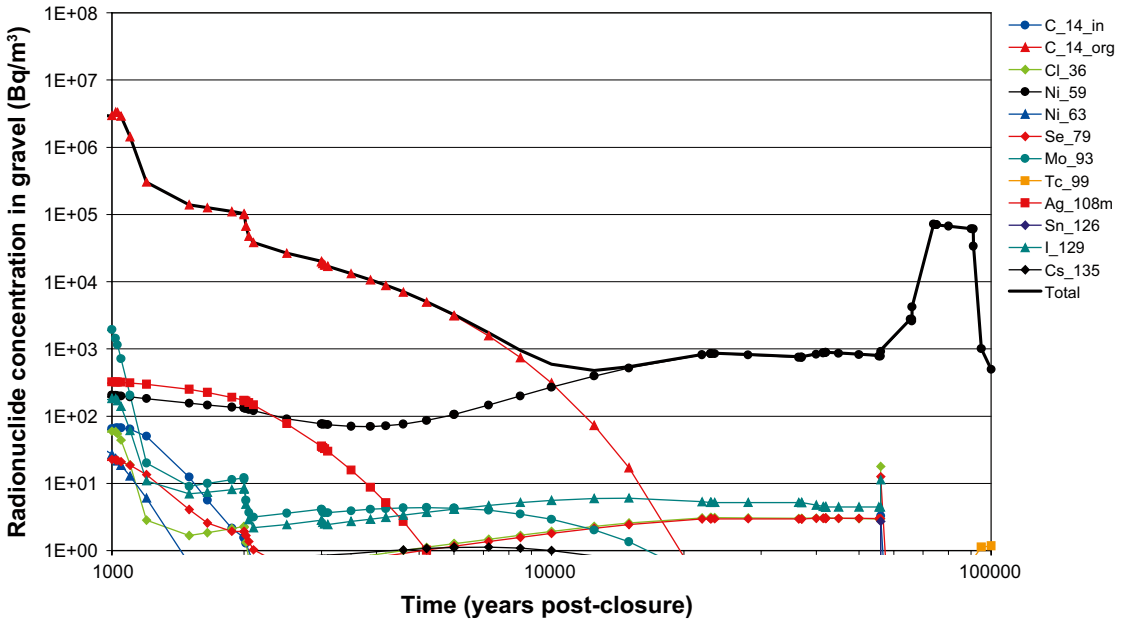

Figure 4-91. *Best estimate radionuclide concentrations within BMA gravel for CC1.*

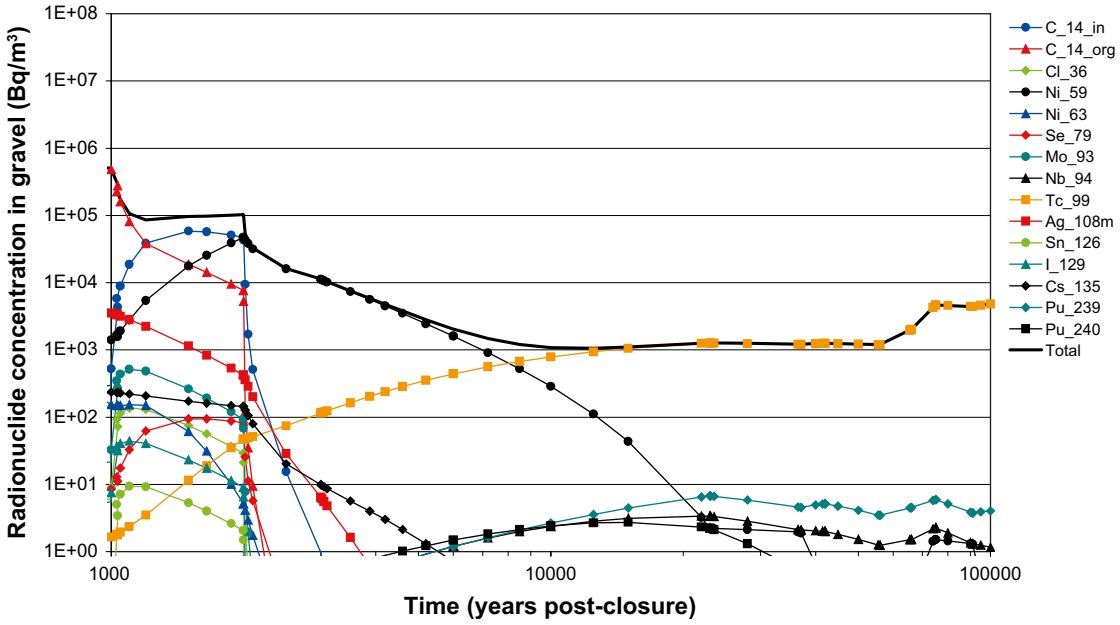

Figure 4-92. *Best estimate radionuclide concentrations within 1BTF gravel for CC1.*

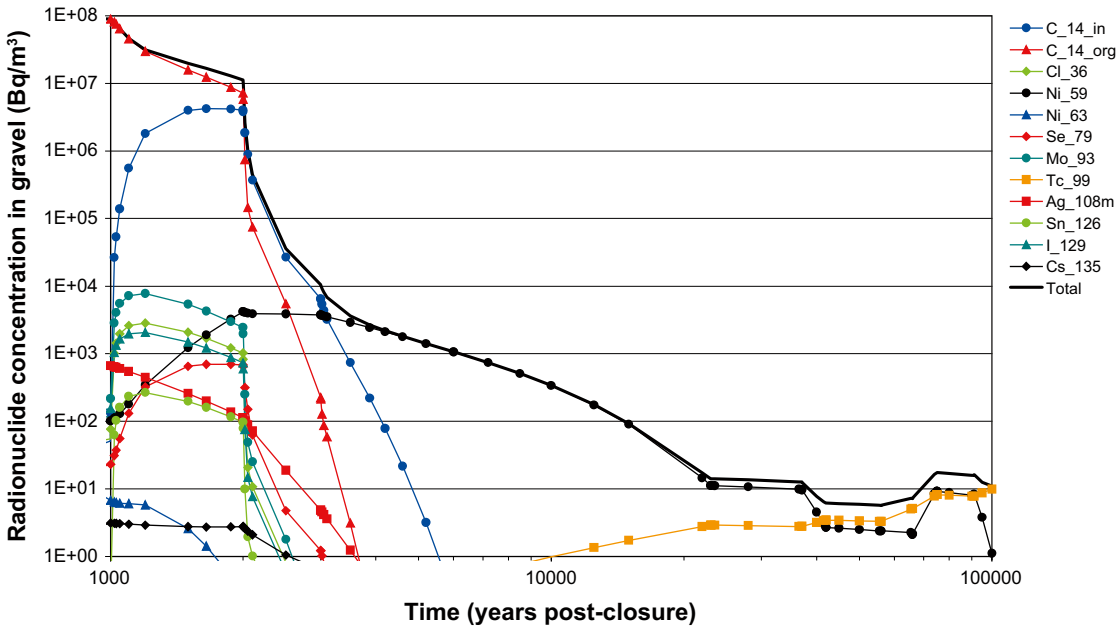

Figure 4-93. *Best estimate radionuclide concentrations within 2BTF gravel for CC1.*

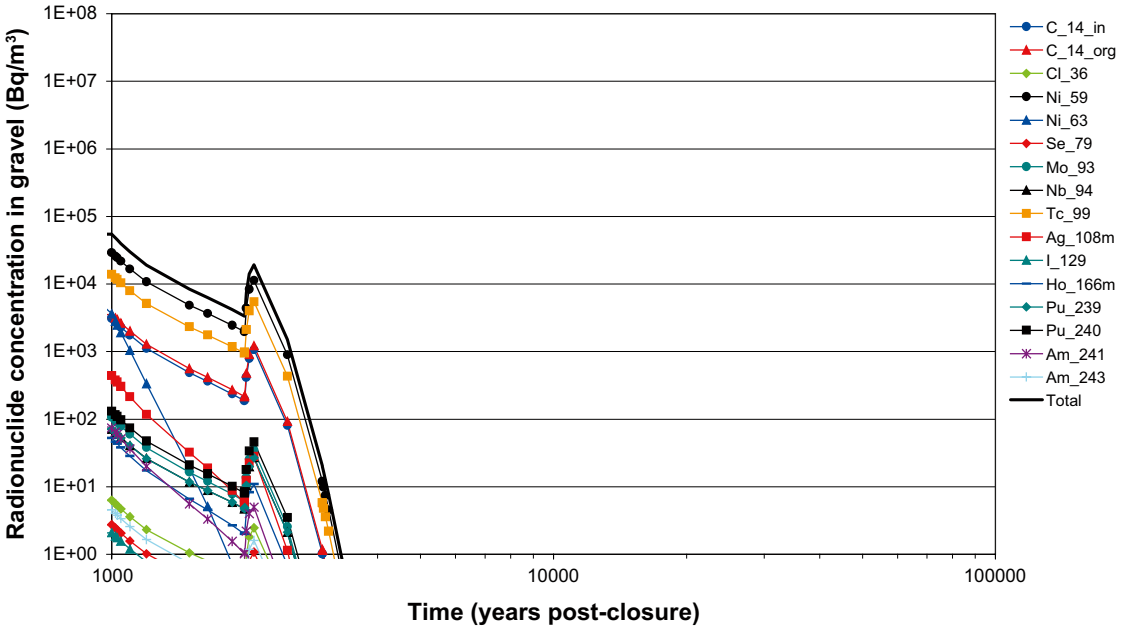

Figure 4-94. *Best estimate radionuclide concentrations within BLA gravel for CC1.*

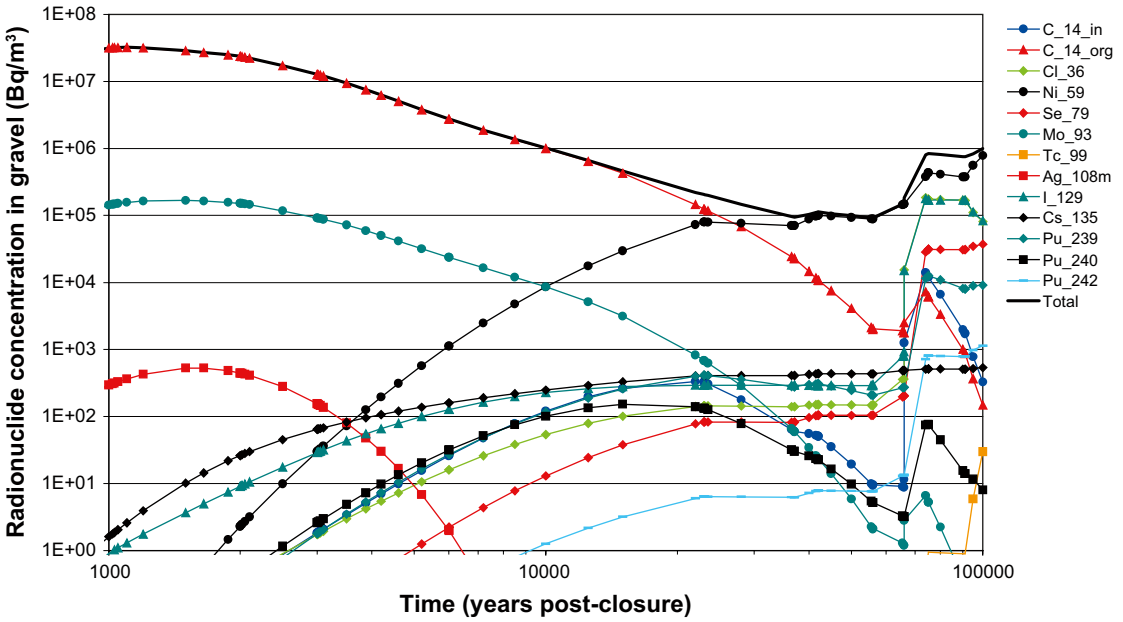

Figure 4-95. *Best estimate radionuclide concentrations within Silo gravel for CC9.*

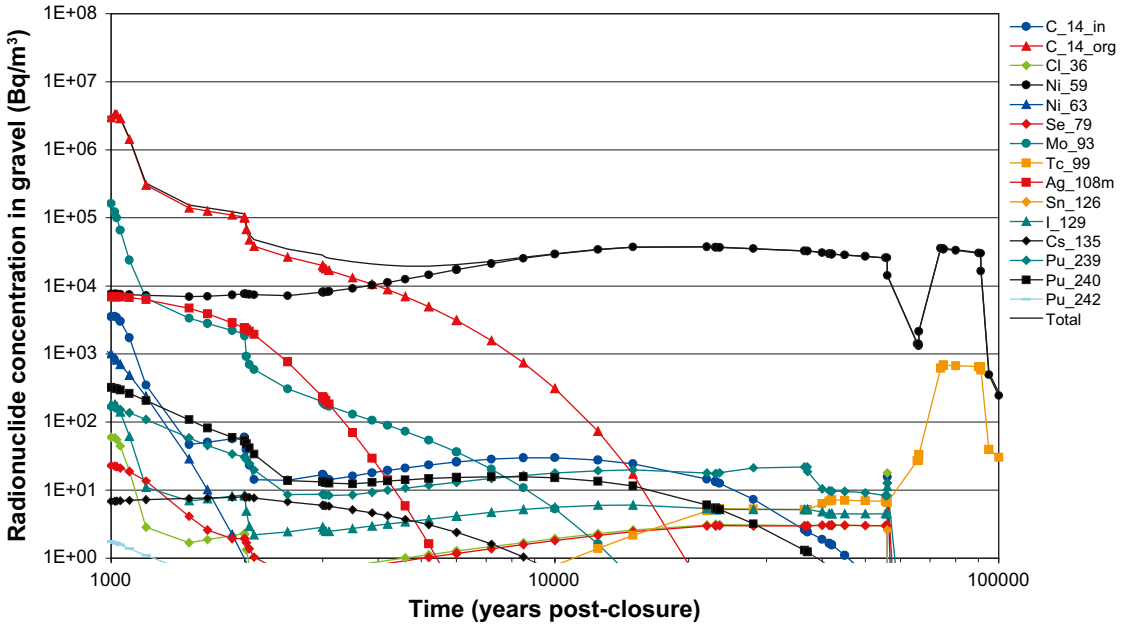

Figure 4-96. *Best estimate radionuclide concentrations within BMA gravel for CC9.*

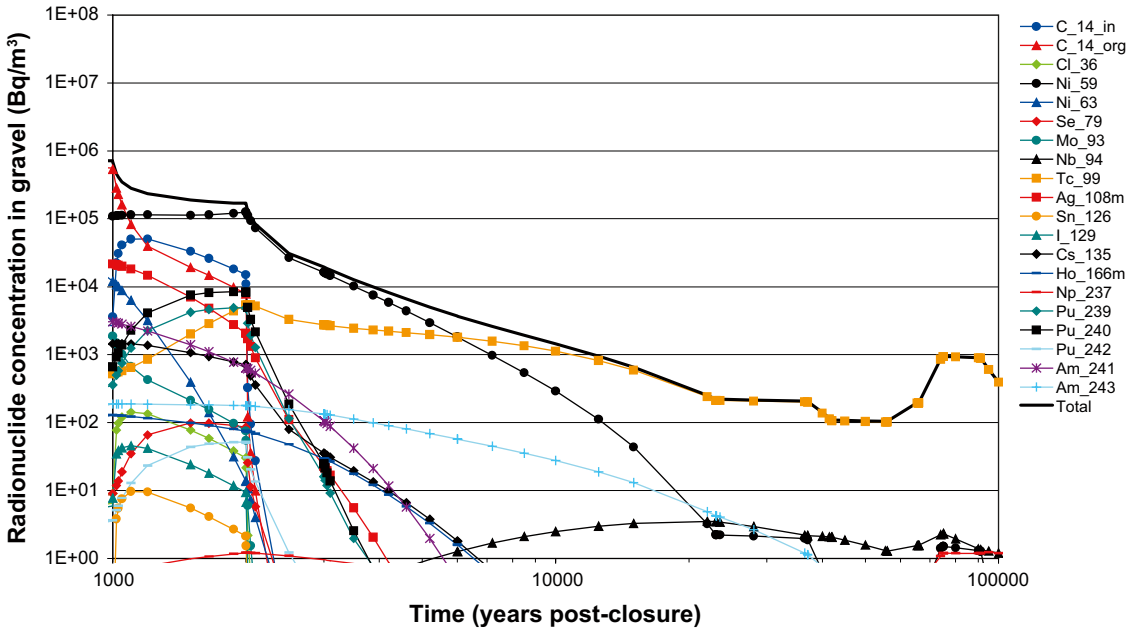

Figure 4-97. *Best estimate radionuclide concentrations within 1BTF gravel for CC9.*

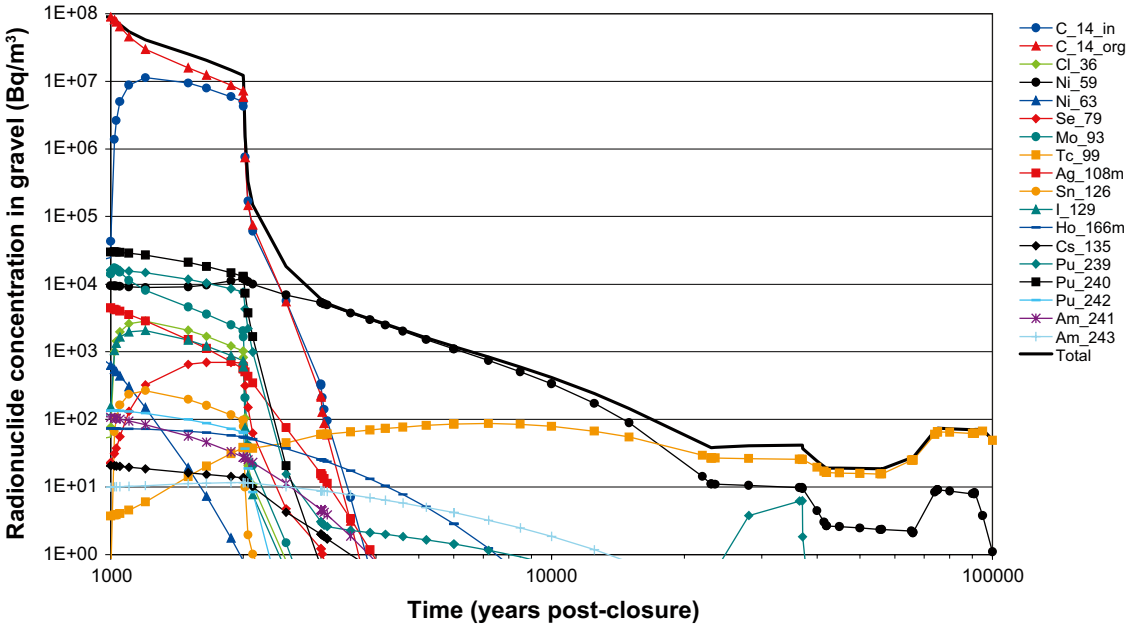

Figure 4-98. *Best estimate radionuclide concentrations within 2BTF gravel for CC9.*

4.12 Calculation Case CC12

Calculation Case CC12 is the first of two calculations to illustrate the influence of performance of near-field barriers on radionuclide releases from SFR 1. Within the Main Scenario it is assumed that radionuclides undergo retardation by sorption onto materials within the near-field[21]. Within this CC12 it is assumed that radionuclides are not retarded by sorption onto near-field materials. The remainder of CC12 follows that previously described for CC1 (e.g. sorption onto the rock matrix is still considered within the geosphere).

A summary of the results for CC12 is presented below in Table 4-15. The data provided in the table show the magnitudes and times of the maximum flux from the best estimate calculations and also from the calculations using sampled parameters (the latter is based on the mean of the individual results). Also shown is the range of the maximum fluxes obtained from the calculations using sampled parameters.

[21] The BLA is an exception in which it is conservatively assumed within CC1 that no sorption takes place. For this reason the BLA is not included within CC12.

Table 4-15. Summary of results from CC12 showing maximum flux and time of peak flux in years after closure.

	Near-field		Geosphere	
Silo	Best estimate	$3.1 \cdot 10^{8}$ Bq/y at 3,000 years	Best estimate	$3.2 \cdot 10^{8}$ Bq/y at 2,000 years
	Mean	$3.3 \cdot 10^{8}$ Bq/y at 3,400 years	Mean	$3.9 \cdot 10^{8}$ Bq/y at 12,000 years
	Range of max.	$2.4 \cdot 10^{8}$ Bq/y–$5.3 \cdot 10^{8}$ Bq/y	Range of max.	$2.2 \cdot 10^{7}$ Bq/y–$3.2 \cdot 10^{9}$ Bq/y
BMA	Best estimate	$6.6 \cdot 10^{9}$ Bq/y at 200 years	Best estimate	$1.6 \cdot 10^{9}$ Bq/y at 2,000 years
	Mean	$7.3 \cdot 10^{9}$ Bq/y at 210 years	Mean	$4.2 \cdot 10^{9}$ Bq/y at 1,200 years
	Range of max.	$4.3 \cdot 10^{9}$ Bq/y–$1.4 \cdot 10^{10}$ Bq/y	Range of max.	$3.2 \cdot 10^{9}$ Bq/y–$4.6 \cdot 10^{10}$ Bq/y
1BTF	Best estimate	$1.7 \cdot 10^{8}$ Bq/y at 150 years	Best estimate	$5.2 \cdot 10^{7}$ Bq/y at 2,000 years
	Mean	$2.9 \cdot 10^{8}$ Bq/y at 790 years	Mean	$1.4 \cdot 10^{8}$ Bq/y at 1,500 years
	Range of max.	$1.4 \cdot 10^{8}$ Bq/y–$9.0 \cdot 10^{8}$ Bq/y	Range of max.	$6.6 \cdot 10^{6}$ Bq/y–$8.4 \cdot 10^{8}$ Bq/y
2BTF	Best estimate	$4.2 \cdot 10^{8}$ Bq/y at 2,000 years	Best estimate	$4.2 \cdot 10^{8}$ Bq/y at 2,000 years
	Mean	$5.2 \cdot 10^{8}$ Bq/y at 1,400 years	Mean	$8.5 \cdot 10^{8}$ Bq/y at 1,700 years
	Range of max.	$3.6 \cdot 10^{8}$ Bq/y–$9.1 \cdot 10^{8}$ Bq/y	Range of max.	$3.9 \cdot 10^{7}$ Bq/y–$9.7 \cdot 10^{9}$ Bq/y

The results can be summarised as follows:

- Silo
  The maximum near-field radionuclide flux is increased by a factor of approximately 14 compared to CC1. The time of the near-field maximum is unchanged at approximately 3,000 years post-closure for the best estimate. The key contributor to the near-field and geosphere flux at the time of the maximum is changed from organic C-14 to inorganic C-14. The disposal inventory of inorganic C-14 is higher in the Silo than organic C-14.
- BMA
  The maximum near-field radionuclide flux is increased by a factor of approximately 24 compared to CC1. The time of the near-field maximum is earlier at approximately 200 years post-closure for the best estimate. The key contributor to the near-field flux at the time of the maximum is changed from organic C-14 to Ni-59. The disposal inventory of Ni-59 is higher in the BMA than organic C-14.
- 1BTF
  The maximum near-field radionuclide flux is increased by a factor of approximately 2 compared to CC1. The time of the near-field maximum is earlier at approximately 150 years post-closure for the best estimate. The key contributor to the near-field flux at the time of the maximum is changed to Ni-59.
- 2BTF
  The maximum near-field radionuclide flux is increased only slightly and the time of the near-field maximum is unchanged at approximately 2,000 years post-closure for the best estimate compared to CC1. The key contributor to the near-field flux at the time of the maximum is unchanged, inorganic C-14[22].

[22] These results require some additional explanation as they may seem contradictory when compared with CC1 and CC9. The near-field maximum radionuclide flux for 2BTF is associated with the flow-field changes at 2,000 years post-closure in CC1, CC9 and CC12. In CC12 the inorganic C-14 is not retained within 2BTF by sorption and there will therefore be less inorganic C-14 within the 2BTF at 2,000 years post-closure in than there is within CC9 where inorganic C-14 is still considered to undergo limited amounts of sorption

The Silo and BMA show the greatest sensitivity to near-field sorption and the maximum near-field and geosphere fluxes are increased by the largest amounts relative to CC1 for these facilities. The Silo and BMA have larger inventories than the BTF (and BLA) tunnels and also use more engineering order to retain the radionuclide. It is therefore expected that the performance of these facilities are the most sensitive to the removal of barriers.

4.13 Calculation Case CC13

Calculation Case CC13 is a residual scenario calculation case which considers the contribution of the geosphere to act as part of the barrier system and retard the release of radionuclides. Table 4-16 below summarises the best estimate results from CC1 which are to be used within CC12.

From comparison of the magnitude of the maximum fluxes from the near-field and the geosphere and the times of their occurrence effects are noted for all disposal facilities except the Silo. The change in the hydrogeological domain from a low hydraulic gradient marine discharge regime to a higher hydraulic gradient terrestrial discharge regime is an important transition at 2,000 years post-closure and this affects the majority of the results. This has been discussed previously in the presentation of the results for CC1, particularly in relation to the sensitivity of the Silo to this transition in conditions.

It can be concluded that the geosphere does contribute to safety of SFR 1 by reducing the magnitude of the fluxes of radionuclides (particularly short-lived radionuclides) and also in delaying the time of the maximum flux.

4.14 Calculation Case CC14

Calculation Case CC14 is the second of two calculations to illustrate the influence of performance of near-field barriers on radionuclide releases from SFR 1. Within this Calculation Case it is assumed that both the Silo and BMA fail at 3,000 years post-closure. The remainder of the Calculation Case follows that previously described for CC1.

Table 4-16. Summary of best estimate results from CC1 showing key radionuclide, maximum flux and time of peak flux in years after closure.

	Near-field (Maximum flux, time and key contributor)	Geosphere (Maximum flux, time and key contributor)
Silo	$2.8 \cdot 10^{7}$ Bq/y, 3,000 years	$1.0 \cdot 10^{8}$ Bq/y, 2,000 years
	Organic C-14	Organic C-14
BMA	$2.8 \cdot 10^{8}$ Bq/y, 1,100 years	$2.0 \cdot 10^{8}$ Bq/y, 2,000 years
	Organic C-14	Organic C-14
1BTF	$8.3 \cdot 10^{7}$ Bq/y, 2,000 years	$5.6 \cdot 10^{7}$ Bq/y, 2,100 years
	Inorganic C-14	Inorganic C-14
2BTF	$4.4 \cdot 10^{8}$ Bq/y, 2,000 years	$3.7 \cdot 10^{8}$ Bq/y, 2,100 years
	Inorganic C-14	Inorganic C-14
BLA	$6.4 \cdot 10^{8}$ Bq/y, 0 years	$1.5 \cdot 10^{8}$ Bq/y, 75 years
	Ni-63	Ni-63

A summary of the results for CC14 is presented below in Table 4-17. The data provided in the table show the magnitudes and times of the maximum flux from the best estimate calculations and also from the calculations using sampled parameters (the latter is based on the mean of the individual results). Also shown is the range of the maximum fluxes obtained from the calculations using sampled parameters.

The results can be summarised as follows:

- Silo
  The maximum near-field radionuclide flux is increased by a factor of approximately 6 compared to CC1. The time of the near-field maximum is delayed to approximately 4,200 years post-closure for the best estimate. The key contributor to the near-field and geosphere flux at the time of the maximum is unchanged (organic C-14). The reduction in sorption associated with degradation of the Silo combined with increases in flow rates results in increased fluxes of several radionuclides, particularly inorganic C-14.
- BMA
  The maximum near-field radionuclide flux is increased by a factor of approximately 10 compared to CC2. The time of the near-field maximum is delayed to approximately 3,000 years post-closure for the best estimate. The key contributor to the near-field flux at the time of the maximum changes to inorganic C-14. The maximum occurs at the time of the failure for similar reasons to those described previously for the 1BTF and 2BTF (i.e. reduction in sorption and increase in advective and diffusive transport).

The higher magnitude of the maximum total radionuclide flux and the earlier time of maximum for the BMA as compared to the Silo may be indicative of the suggestion previously that the parameterisation of the failure of the BMA is conservative in terms of radionuclide release.

Table 4-17. Summary of results from CC14 showing maximum flux and time of peak flux in years after closure.

	Near-field		Geosphere	
Silo	Best estimate	$1.8 \cdot 10^{8}$ Bq/y at 4,200 years	Best estimate	$1.7 \cdot 10^{8}$ Bq/y at 4,200 years
	Mean	$2.1 \cdot 10^{8}$ Bq/y at 4,000 years	Mean	$2.1 \cdot 10^{8}$ Bq/y at 4,000 years
	Range of max.	$1.0 \cdot 10^{8}$ Bq/y–$5.8 \cdot 10^{8}$ Bq/y	Range of max.	$4.4 \cdot 10^{7}$ Bq/y–$1.3 \cdot 10^{9}$ Bq/y
BMA	Best estimate	$2.9 \cdot 10^{9}$ Bq/y at 3,000 years	Best estimate	$2.3 \cdot 10^{9}$ Bq/y at 3,100 years
	Mean	$3.5 \cdot 10^{9}$ Bq/y at 3,000 years	Mean	$2.4 \cdot 10^{9}$ Bq/y at 3,500 years
	Range of max.	$7.7 \cdot 10^{8}$ Bq/y–$1.2 \cdot 10^{10}$ Bq/y	Range of max.	$8.8 \cdot 10^{8}$ Bq/y–$8.1 \cdot 10^{9}$ Bq/y

5 Overall summary

This report describes the radionuclide release calculations that have been undertaken as part of SAR-08. The information, assumptions and data used in the calculations are reported and the results are presented.

The radionuclide release calculations have been undertaken in order to quantitatively assess differing scenario variants through the use of targeted calculation cases. The calculation cases seek to address specific questions related to the assessment of the performance of the SFR 1 repository.

The following areas have been reviewed and updated following Project SAFE.

- Assessment timescales have been extended beyond 10,000 years post-closure.
- The potential impacts of climate change have been considered.
- A revised set of scenarios and calculation cases has been derived.
- An updated radionuclide disposal inventory has been estimated.
- Uncertainty in the calibration of the supporting hydrogeological models is considered.
- The time-dependent failure of the engineering barrier system is considered.
- The impact of uncertainties in key parameters is considered through undertaking calculations using parameters sampled from distributions.

The majority of the radioactive to be disposed within SFR 1 will be emplaced within the Silo and the BMA. These high specification facilities offer optimum environmental protection and their engineering components are estimated to afford considerable barrier properties for tens of millennia or more. The radionuclides that dominate the radionuclide flux from the Silo and the BMA are initially organic C-14 in the short-term and long-term and then Ni-59 in the very long-term. Relatively high inventories of radionuclides such as H-3, Co-60, Sr-90 and Cs-137 undergo significant retention and radioactive decay within the engineered containment. The peak radionuclide fluxes from the Silo are estimated to occur at around 3,000 years post-closure when the release of organic C-14 reaches its maximum. For the BMA this maximum is estimated to occur at around 1,100 years post-closure.

The performance of these facilities are assumed to be sensitive to large scale environmental change, the development of permafrost and the advance and retreat of ice sheets may result in significant degradation of these facilities in the distant future (e.g. 40,000 years AP or more). Following failure of the containment of these facilities the release rates of residual radionuclides will be increased due to increased rates of groundwater flow through the facilities and reduced sorption.

The potential for a relatively earlier failure of the BMA is not considered to result in significantly altered rates of radionuclide release (although they will occur several thousands of years earlier).

The BTF disposal facilities contain a lower radionuclide inventory and therefore require less containment. For this reason these facilities are assumed to degrade at relatively early at 1,000 years post-closure. Environmental releases from these facilities are dominated initially by organic and inorganic C-14 and in the longer term by Ni-59 and Tc-99. Maximum releases from the facilities occur shortly after failure.

The representation of the BLA in the calculation cases excludes both engineered barriers and sorption from the assessment models. This results in the peak near-field radionuclide flux being estimated to occur immediately on closure with contributions from individual radionuclides

made in proportion to their overall abundance in the disposal inventory. The dominant radionuclide is Ni-63. The highest releases of short-lived radionuclides (e.g. Co-60, Sr-90, Cs-137) are observed for the BLA due to the relative simplicity of the model.

The disposal inventory is completely removed from the BLA within the initial 5,000 year period following closure (i.e. the total radionuclide is below 1 Bq/y from this onwards). However, relatively low-level fluxes of long-lived radionuclides such as Ni-59 and Tc-99 continue from the geosphere throughout the assessment period due to retardation by matrix diffusion and sorption.

A linear relationship has been shown to exist between the amount of radionuclide disposed within a facility and the resultant maximum radionuclide release rate, i.e. the higher the disposal inventory the higher the maximum radionuclide flux.

All facilities are sensitive to assumptions on the general regional hydrogeological regime (e.g. active/in-active during continuous permafrost) and its evolution as a series of step changes. It is suggested that representing the evolution of system as a series of step changes is likely to be conservative in terms of radionuclide release.

6 References

Almkvist L, Gordon A, 2007. Low and intermediate Level Waste in SFR 1 Reference Waste Inventory 2007. SKB R-07-17, Svensk Kärnbränslehantering AB.

Bayliss S, McCrohon R, Oliver P, Pilkington N-J, Thomason HP, 1996. Near-Field Sorption Studies: January 1989 to June 1991. UKAEA. Report NSSIR277, Harwell, UK.

Bergström U, Avila R, Ekström P-A, de la Cruz I, 2008. Dose assessments for SFR 1 (*in prep*). SKB R-08-15, Svensk Kärnbränslehantering AB.

Bradbury M H, Van Loon, 1998. Cementitious near-filed sorption database for performance assessment of a L/ILW repository in a palfris host rock. PSI Bericht nr 98-1, January 1998, ISSN 1019-0643; CEM-94: Update I, June 1997.

Cronstrand P, 2005. Assessment of uncertainty intervals for sorption coefficients. SKB R-05-75, Svensk Kärnbränslehantering AB.

Cronstrand P, 2007. Modelling the long-time stability of the engineered barriers of SFR with respect to climate changes. SKB R-07-51, Svensk Kärnbränslehantering AB.

Emborg M, Jonasson J-E, Knutsson S, 2007. Långtidsstabilitet till följd av frysning och tining av betong och bentonit vid förvaring av låg- och medelaktivt kärnavfall i SFR 1. SKB R-07-60, Svensk Kärnbränslehantering AB.

Enviros Consulting Limited and Quintessa Limited, 2007. AMBER 5.1 Reference Guide. Version 1.0. 2007.

Fanger G, Skagius K, Wiborgh M, 2001. Project SAFE. Complexing agents in SFR. SKB R-01-04, Svensk Kärnbränslehantering AB.

Freeze RA, Cherry JA, 1979. Groundwater. Prentice-Hall.

Gordon A, Lindgren M, Löfgren M, 2008. Update of priority of FEPs from project SAFE. SKB R-08-12, Svensk Kärnbränslehantering AB.

Greenfield BF, Hurdus MH, Spindler MW, Thomason HP, 1997. The effect of the products from the anaerobic degradation of cellulose on the solubility and sorption of radioelements in the near field. NIREX Report NSS/R376.

Holmén JG, Stigsson M, 2001a. Modelling of future hydrogeological conditions at SFR. SKB R-01-02, Svensk Kärnbränslehantering AB.

Holmén JG, Stigsson M, 2001b. Details of predicted flow in deposition tunnels at SFR, Forsmark. SKB R-01-21, Svensk Kärnbränslehantering AB.

Holmén JG, 2005. Inverse modelling of inflow to tunnels and propagation of estimated uncertainties to predictive stages. SKB R-05-74, Svensk Kärnbränslehantering AB.

Holmén JG, 2007. SFR inverse modelling. Part 2. Uncertainty factors of predicted flow in storage tunnels and uncertainty in distribution of flow paths from storage tunnels. SKB R-07-61, Svensk Kärnbränslehantering AB.

Hummel W, Anderegg G, Puigdomenech I, Rao L, Tochiyama O, 2005. NEA/OECD Chemical Thermodynamics Series Volume: Chemical Thermodynamics of Compounds and Complexes of U, Np, Pu, Am, Tc, Se, Ni and Zr with Selected Organic Ligands.

Höglund LO, 2001. Project SAFE: Modelling of long-term concrete degradation processes in the Swedish SFR repository. SKB R-01-08, Svensk Kärnbränslehantering AB.

Höglund LO, Bengtsson A, 1991. Some chemical and physical processes related to the long-term performance of the SFR repository. SKB Progress Report SFR 91-06, Svensk Kärnbränslehantering AB.

IAEA, 2004. Safety Assessment Methodologies for Near Surface Disposal Facilities: Results of a co-ordinated research project. Volume 2 Test cases. International Atomic Energy Agency, Vienna.

Lindgren M, Pettersson M, Karlsson S, Moreno L, 2001. Project SAFE. Radionuclide release and dose from the SFR repository. SKB R-01-18, Svensk Kärnbränslehantering AB.

McEwen T, de Marsily G, 1991. The Potential Significance of Permafrost to the Behaviour of a Deep Radioactive Waste Repository. SKI Technical Report 91:8. February 1991.

Moreno L, Skagius K, Södergren S, Wiborgh M, 2001. Project SAFE. Gas related processes in SFR. SKB R-01-11, Svensk Kärnbränslehantering AB.

Moreton AD, Pilkington NJ, Tweed CJ, 2000. Thermodynamic modelling of the effect of hydroxycarboxylic acids on the solubility of plutonium at high pH. NIREX Report NSS/R339.

Ochs M, Talerico C, 2004. SR-Can Data and uncertainty assessment. Migration parameters for the bentonite buffer in the KBS-3 concept. SKB TR-04-18. Svensk Kärnbränslehantering AB.

Rai D, Rao L, Moore DA, 1998. The influence of isosaccharinic acid on the solubility of Np(IV) hydrous oxide. Radiochimica Acta, 83, 9–13.

Rai D, Hess NJ, Xia Y, Rao L, Cho HM, Moore RC, Van Loon LR, 2003. Comprehensive thermodynamic model applicable to highly acidic to basic conditions for isosaccharinate reactions with Ca(II) and Np(IV). Journal of Solution Chemistry, 32(8), 665–689.

Robinson P C, Penfold J S S, Little R H, Walke R C, 2004. AMBER 4.6 Verification: Summary. Quintessa Report QRS-1059C-1, for Enviros.

Rorif F, Valcke E Glaus M A, 2004. The effect of cellulose degradation products on the solubility and sorption of Pu and Am in alkaline-plume-affected and in unaffected Boom Clay. Mat. Res. Soc. Symp. Proc., 807, 633–638.

SKB, 1993. SSR, SFR 1 – Slutlig säkerhetsrapport. Svensk Kärnbränslehantering AB.

SKB, 1999a. SR 97 – Post-closure safety. Deep repository for spent nuclear fuel. Main report. (Two volumes), SKB Technical Report TR-99-06, Svensk Kärnbränslehantering AB.

SKB, 1999b. Deep repository for long-lived low- and intermediate level waste – Preliminary safety assessment. SKB Technical Report TR-99-28, Svensk Kärnbränslehantering AB.

SKB, 2001a. SFR-1. Slutförvar för radioaktivt driftavfall. SSR Slutlig säkerhetsrapport. Version 1.0, Juni 2001, Svensk Kärnbränslehantering AB. (in Swedish)

SKB, 2001b. Project SAFE. Compilation of data for radionuclide transport calculations. SKB R-01-14, Svensk Kärnbränslehantering AB.

SKB, 2006a. Long-term safety for KBS-3 repositories at Forsmark and Laxemar – a first evaluation. Main Report of the SR-Can project. SKB TR-06-09, Svensk Kärnbränslehantering AB.

SKB, 2006b. Climate and climate-related issues for the safety assessment SR-Can. SKB TR-06-23. Svensk Kärnbränslehantering AB.

SKB, 2006c. Data report for the safety assessment SR-Can. SKB TR-06-25, Svensk Kärnbränslehantering AB.

SKB, 2006d. The biosphere at Forsmark. Data, assumptions and models used in the SR-Can assessment. SKB R-06-82, Svensk Kärnbränslehantering AB.

SKI and SSI, 2004. SSI and SKI's Review of SKB's Updated Final Safety Report for SFR-1. Review Report. SKI Report 2004:47 (SSI Report 2004:06).

Thomson G, Miller B, 2005. SFR 1 – Post closure radionuclide release and dose calculations. SKB R-05-81, Svensk Kärnbränslehantering AB.

Thomson G, Herben M, Lloyd P, Rose D, Smith C, Barraclough I, 2008. Implementation of project Safe in Amber. Verification study for SFR 1 SAR-08. SKB R-08-13, Svensk Kärnbränslehantering AB.

Tits J, Wieland E, Bradbury M H, 2005. The effect of isosaccharinic acid and gluconic acid on the Eu(III), Am(III) and Th(IV) retention by calcite, Appl. Geochem., 20, 2082–2096.

Vercammen K, Glaus MA, Van Loon, LR, 2001. Complexation of Th(IV) and Eu(III) by α-isosaccharinic acid under alkaline conditions. Radiochimica Acta, 89, 393–401.

Vidstrand P, Näslund J-O, Hartikainen J, Svensson U, 2007. Hydrogeological flux scenarios at Forsmark. Generic numerical flow simulations and compilation of climatic information for use in the safety analysis SFR1 SAR08. SKB R-07-63, Svensk Kärnbränslehantering AB.

Warwick P, Evans N, Vines S, 2006. Studies on some divalent metal α-isosaccharinic acid complexes. Radiochimica Acta, 94, 363–368.

Wiborgh M, Lindgren M, 1987. Database for the radionuclide transport calculations for SFR. SKB Progress Report SFR 87-09, Svensk Kärnbränslehantering AB.

Wieland E, Tits J, Spieler P, Dobler J-P, 1998. Interaction of Eu(III) and Th(IV) with sulphate-resisting Portland Cement, 21st International Symposium on the Scientific Basis for Nuclear Waste Management, Davos, Sept. 28th to October 3rd 1997. Mat. Res. Soc. Symp. Proc. Vol. 506, p. 573–578.

Appendix A

Deterministic baseline models

The implementation of Project SAFE in AMBER is described in a supporting document /Thomson et al. 2008/. In configuring AMBER to represent Project SAFE and subsequently comparing the results with those obtained originally using NUCFLOW some discrepancies and inconsistencies between the documentation and implementation were noted.

This appendix briefly describes the modified models that will be used to develop the models for the SAFE Update assessment.

A1 Silo

The following modifications to the Silo model have been made /Thomson et al. 2008/:

- The point at which the advective flux exits the Silo bottom has been changed.

The NUCFLOW model of the Silo that was developed for use in Project SAFE did not consider that the radionuclides exited from the base of the model. Instead the advective flux was assumed to exit from the upper most compartment of sand/bentonite layer beneath the Silo base (Figure A-1).

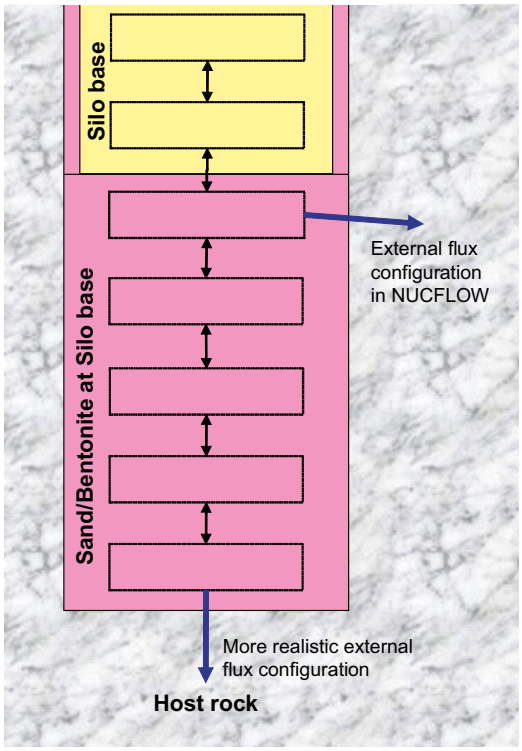

Figure A-1. *Comparison of configuration of external flows from base of Silo model.*

A more appropriate representation is considered to be the discharge of radionuclides from the bottom most compartment of sand/bentonite layer beneath the Silo base (Figure A-1). In reality it is likely that groundwater will discharge from the sand/bentonite both laterally and vertically[23]. However, information on the derivation of the groundwater flow fields used in the Silo assessment model from that reported in /Holmén and Stigsson 2001a/ is not available so the simplified approach described was adopted.

- The sorption coefficients for inorganic C, Se and Sr have been corrected.

Several discrepancies between the values used within the NUCFLOW model of the Silo and those reported in the transport calculations for project SAFE /Lindgren et al. 2001/ were noted /Thomson et al. 2008/. In order to replicate the results obtained from NUCFLOW the values used in AMBER were input to match those of the NUCFLOW model. The parameter values describing the sorption of inorganic C, Se and Sr onto gravel and sand used within NUCFLOW are considered to have resulted from rounding the values reported in /Lindgren et al. 2001/ to 3 decimal places. These have been corrected here.

The sorption values for these elements onto sand/bentonite were also required to be modified (as they are calculated as the weighted average of the values for gravel and sand and bentonite).

The sorption values utilised are summarised in Table A-1. Those that differ from the summary in /Thomson et al. 2008/ are highlighted in bold.

- The approach to representing bitumen release has been simplified.

Table A-1. Sorption coefficients [m³/kg] used in deterministic baseline models.

Element	Concrete/Cement	Gravel and sand	Bentonite	Sand-Bentonite
H	0	0	0	0.000
C (inorganic)	0.2	**0.0005**	0	**0.00045**
C (organic)	0	0	0	0.000
Cl	0.006	0	0	0.000
Co	0.04	0.01	0.02	0.011
Ni	0.04	0.01	0.02	0.011
Se	0.006	**0.0005**	0	**0.00045**
Sr	0.001	**0.0001**	0.001	**0.00019**
Zr	0.5	0.5	0.05	0.455
Nb	0.5	0.5	0	0.450
Mo	0.006	0	0	0.000
Tc	0.5	0.3	0.01	0.271
Pd	0.04	0.001	0	0.001
Ag	0.001	0.01	0	0.009
Cd	0.04	0.01	0.02	0.011
Sn	0.5	0	0.01	0.001
I	0.003	0	0	0.000
Cs	0.001	0.01	0.005	0.010
Sm	5	1	0.2	0.920
Eu	5	1	0.2	0.920
Ho	5	1	0.2	0.920
Pu	5	1	1	1.000
Am	1	1	1	1.000

[23] Within Project SAFE it was assumed that the remaining void space between the top of the Silo and host rock was back filled with Gravel and/or sand through which groundwater was assumed to discharge both laterally and vertically.

Based on a review of bitumenised waste behaviour the calculations undertaken within Project SAFE assumed that radionuclides were released from bitumen matrices over a period of 100 years /Lindgren et al. 2001/. This was implemented in NUCFLOW (and replicated in AMBER) using a constant flow rate through the bitumenised waste and deriving an effective solubility limit that results in the release of radionuclides over a 100 year period.

An alternative approach was taken whereby radionuclides were assumed to be available instantaneously for release from the bitumenised waste in a similar manner to that assumed for the cement-stabilised wastes.

Figure A-2 shows a comparison of the estimated near-field radionuclide flux from the Silo baseline and Project SAFE models. The open symbols are Project SAFE (NUCFLOW) and the lines are AMBER. Table A-2 also summarises the results for each simulation. For each radionuclide reported the first value is the maximum radionuclide flux [Bq y^{-1}] and the second

Table A-2. Summary of Silo baseline and Project SAFE near-field peak fluxes with times for selected radionuclides in parentheses.

Radionuclide	AMBER Silo baseline	Project SAFE
Inorganic C-14	$3.244 \cdot 10^{0}$ ($1.3 \cdot 10^{4}$)	$3.616 \cdot 10^{0}$ ($1.3 \cdot 10^{4}$)
Organic C-14	$5.228 \cdot 10^{7}$ ($1.6 \cdot 10^{3}$)	$5.228 \cdot 10^{7}$ ($1.6 \cdot 10^{3}$)
Cl-36	$3.267 \cdot 10^{4}$ ($1.3 \cdot 10^{4}$)	$3.263 \cdot 10^{4}$ ($1.3 \cdot 10^{4}$)
Se-79	$1.090 \cdot 10^{4}$ ($1.3 \cdot 10^{4}$)	$1.163 \cdot 10^{4}$ ($1.3 \cdot 10^{4}$)
Sr-90	$2.553 \cdot 10^{1}$ ($2.5 \cdot 10^{2}$)	$3.442 \cdot 10^{1}$ ($3.1 \cdot 10^{2}$)
Nb-93m	$1.396 \cdot 10^{3}$ ($7.2 \cdot 10^{3}$)	$1.392 \cdot 10^{3}$ ($7.2 \cdot 10^{3}$)
Mo-93	$1.199 \cdot 10^{4}$ ($7.2 \cdot 10^{3}$)	$1.198 \cdot 10^{4}$ ($7.2 \cdot 10^{3}$)
Tc-99	$2.116 \cdot 10^{-3}$ ($1.3 \cdot 10^{4}$)	$3.400 \cdot 10^{-3}$ ($1.3 \cdot 10^{4}$)
Pd-107	$8.179 \cdot 10^{0}$ ($1.3 \cdot 10^{4}$)	$8.904 \cdot 10^{0}$ ($1.3 \cdot 10^{4}$)
Ag-108m	$2.232 \cdot 10^{4}$ ($1.2 \cdot 10^{3}$)	$2.706 \cdot 10^{4}$ ($1.2 \cdot 10^{3}$)
I-129	$2.630 \cdot 10^{3}$ ($1.3 \cdot 10^{4}$)	$2.625 \cdot 10^{3}$ ($1.3 \cdot 10^{4}$)
Cs-135	$1.888 \cdot 10^{4}$ ($1.3 \cdot 10^{4}$)	$2.318 \cdot 10^{4}$ ($1.3 \cdot 10^{4}$)
Cs-137	$8.822 \cdot 10^{0}$ ($3.1 \cdot 10^{2}$)	$8.786 \cdot 10^{0}$ ($3.1 \cdot 10^{2}$)

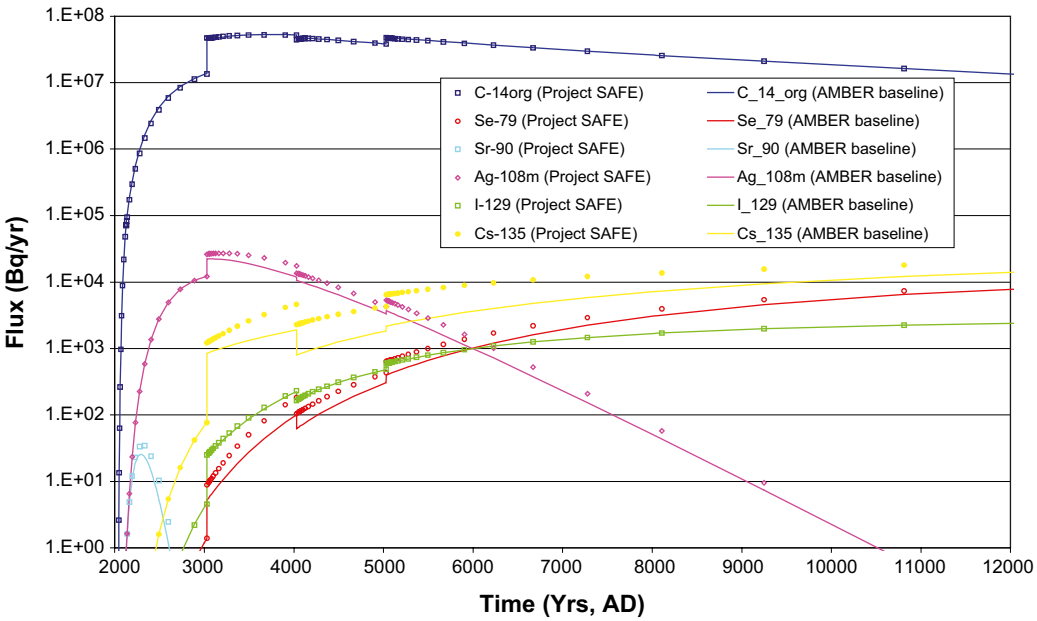

Figure A-2. *Comparison of Silo baseline and Project SAFE near-field fluxes for selected radionuclides.*

value in parentheses is the time of the maximum radionuclide flux [y]. Little difference is discernible between the two sets of model results for radionuclides with negligible sorption, except inorganic C-14. The maximum flux of inorganic C-14 is estimated to be slightly increased and this is considered to be due to the re-configured flux from the model base. The remaining radionuclides, such as Se-79, Sr-90, Tc-99 and Pd-107, tend to show reduced fluxes for the AMBER baseline relative to Project SAFE. This is due to a combination of the re-configured flux from the model base and the increased sorption coefficients for inorganic C, Se and Sr, which result in an increased level of retardation within the Silo.

A2 BMA

The following modifications to the BMA model described in /Thomson et al. 2008/ have been made:

- The sorption coefficients for inorganic C, Se and Sr have been corrected as described previously for the Silo.
- The approach to representing bitumen release has been simplified so that radionuclides are instantaneously available for leaching as described previously for the Silo.
- In contrast to Project SAFE in which it was assumed that no groundwater flows through the cemented waste leaching of radionuclides from cemented wastes is included in this model in a consistent manner with that considered for the Silo and BTF tunnels. It appears that the reason for excluding this within Project SAFE was perceived to be a high conductivity contrast arising from the lack of backfilling. Radionuclides will be subject to leaching by groundwater flowing through the BMA encapsulation but the degree of leaching is expected to be related to the surface area of the waste in contact with the groundwater, the resistance of the waste to leaching, the contact time and the magnitude of groundwater flow through the waste – all of which are subject to varying degrees of uncertainty. The approach taken here is conservative in terms of radionuclide flux.

The values of groundwater flow through the waste were derived using the same approach used for the BTF tunnels in Project SAFE (i.e. the sum of inflows to the encapsulation void) and are reported below in Table A-3.

Figure A-3 shows a comparison of the estimated flux from the BMA for AMBER and NUCFLOW. The open symbols are NUCFLOW and the lines are AMBER. Table A-4 also summarises the results for each simulation. For each radionuclide reported the first value is the maximum radionuclide flux [Bq y^{-1}] and the second value in parentheses is the time of the maximum radionuclide flux [y]. Generally it can be seen that there is little difference between the simulations, the AMBER baseline radionuclide fluxes are slightly larger when compared to those obtained from Project SAFE which is most likely to be explained as a combination of the instantaneous availability of radionuclides from bitumenised wastes and the inclusion of leaching from cemented wastes. The results for Sr-90 show a slight decrease relative to Project SAFE which is considered most likely to be due to the increased sand and gravel sorption coefficient.

Table A-3. Groundwater flow rates [m^3/y] through BMA waste.

	Parameter name	Closure	1,000 years	2,000 years	3,000 years
Rooms 1–4	q_BMA_w1	0.0108	0.09688	0.06403	0.06631
Rooms 5–9	q_BMA_w2	0.01545	0.0656	0.10682	0.11197
Rooms 10 and 11	q_BMA_w3	0.01014	0.04612	0.08748	0.09199
Room 12	q_BMA_w4	0.05001	0.05284	0.11668	0.1247
Rooms 13–15	q_BMA_w5	0.06238	0.03723	0.07872	0.08196

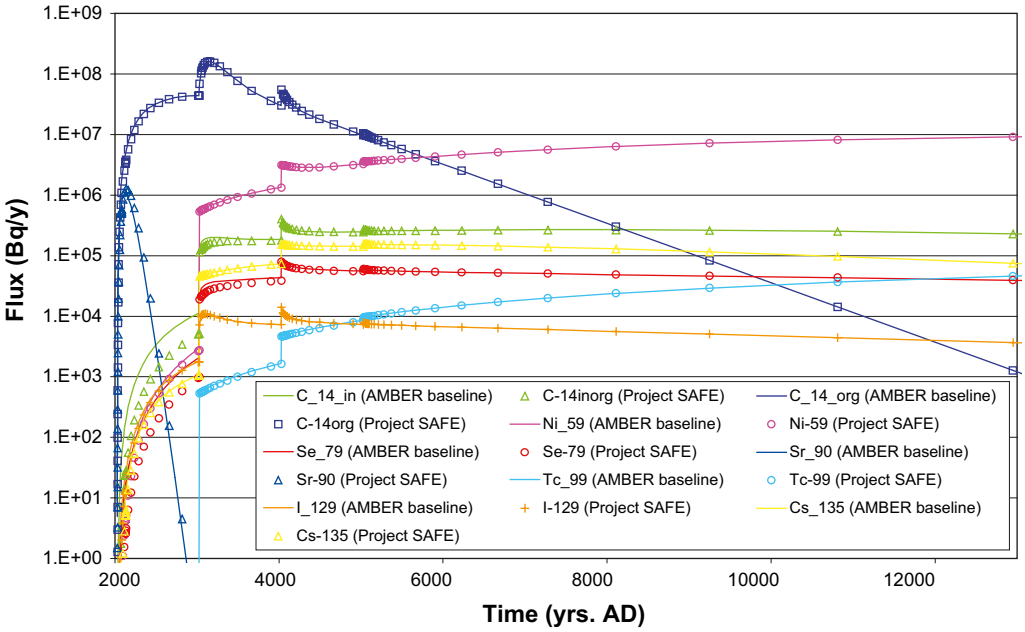

Figure A-3. *Comparison of BMA baseline and Project SAFE near-field fluxes for selected radionuclides.*

Table A-4. Summary of BMA baseline and Project SAFE near-field fluxes for selected radionuclides with times for selected radionuclides in parentheses.

Radionuclide	AMBER BMA baseline	Project SAFE
H-3	$2.971 \cdot 10^{4}$ ($3.1 \cdot 10^{1}$)	$1.592 \cdot 10^{4}$ ($4.3 \cdot 10^{1}$)
Inorganic C-14	$4.171 \cdot 10^{5}$ ($2.0 \cdot 10^{3}$)	$4.045 \cdot 10^{5}$ ($2.0 \cdot 10^{3}$)
Organic C-14	$1.604 \cdot 10^{8}$ ($1.1 \cdot 10^{3}$)	$1.612 \cdot 10^{8}$ ($1.1 \cdot 10^{3}$)
Cl-36	$2.345 \cdot 10^{5}$ ($2.0 \cdot 10^{3}$)	$2.344 \cdot 10^{5}$ ($2.0 \cdot 10^{3}$)
Ni-59	$9.759 \cdot 10^{6}$ ($1.3 \cdot 10^{4}$)	$9.740 \cdot 10^{6}$ ($1.3 \cdot 10^{4}$)
Se-79	$8.798 \cdot 10^{4}$ ($2.0 \cdot 10^{3}$)	$7.954 \cdot 10^{4}$ ($2.0 \cdot 10^{3}$)
Sr-90	$1.052 \cdot 10^{6}$ ($8.8 \cdot^{101}$)	$1.265 \cdot 10^{6}$ ($1.1 \cdot 10^{2}$)
Nb-93m	$1.637 \cdot 10^{2}$ ($2.0 \cdot 10^{3}$)	$1.635 \cdot 10^{2}$ ($2.0 \cdot 10^{3}$)
Mo-93	$5.107 \cdot 10^{5}$ ($2.0 \cdot 10^{3}$)	$5.100 \cdot 10^{5}$ ($2.0 \cdot 10^{3}$)
Tc-99	$5.533 \cdot 10^{4}$ ($1.3 \cdot 10^{4}$)	$5.543 \cdot 10^{4}$ ($1.3 \cdot 10^{4}$)
Pd-107	$2.102 \cdot 10^{3}$ ($1.3 \cdot 10^{4}$)	$2.056 \cdot 10^{3}$ ($1.3 \cdot 10^{4}$)
Ag-108m	$6.446 \cdot 10^{5}$ ($1.0 \cdot 10^{3}$)	$6.400 \cdot 10^{5}$ ($1.0 \cdot 10^{3}$)
I-129	$1.407 \cdot 10^{4}$ ($2.0 \cdot 10^{3}$)	$1.410 \cdot 10^{4}$ ($2.0 \cdot 10^{3}$)
Cs-135	$1.571 \cdot 10^{5}$ ($3.0 \cdot 10^{3}$)	$1.559 \cdot 10^{5}$ ($3.0 \cdot 10^{3}$)
Cs-137	$1.098 \cdot 10^{5}$ ($1.1 \cdot 10^{2}$)	$7.292 \cdot 10^{4}$ ($1.3 \cdot 10^{2}$)

A3 1BTF

The following modifications made to the 1BTF model have been made /Thomson et al. 2008/:

- The sorption coefficients for inorganic C, Se and Sr have been corrected as described previously for the Silo.
- The flow field imbalance was corrected.

From detailed inspection of the NUCFLOW input files /Thomson et al. 2008/ it was realised that in two particular compartments of the model an imbalance occurs in the flow fields at 1,000 years post-closure (3,000 AD), 2,000 years post-closure (4,000 AD) and 3,000 years

post-closure (5,000 AD) at the base of the second sub-division of the tunnel as shown below in Figure A-4 (the compartments which do not balance are circled). Flow balance was achieved by reversing the direction of the groundwater flows between compartments 145 and 185 at 1,000 years post-closure (3,000 AD), 2,000 years post-closure (4,000 AD) and 3,000 years post-closure (5,000 AD).

Figure A-5 shows a comparison of the estimated flux from 1BTF for AMBER and NUCFLOW. The open symbols are NUCFLOW and the lines are AMBER. Table A-5 also summarises the results for each simulation. For each radionuclide reported the first value is the maximum radionuclide flux [Bq y^{-1}] and the second value in parentheses is the time of the maximum radionuclide flux [y]. Generally it can be seen that there is little difference between the simulations. Those radionuclides which reach there maximum after 1,000 years post-closure show slightly increased radionuclide fluxes which is a result of the reconfigured flows described above. Sr-90 shows a reduced flux due to the increased sand and gravel sorption coefficient.

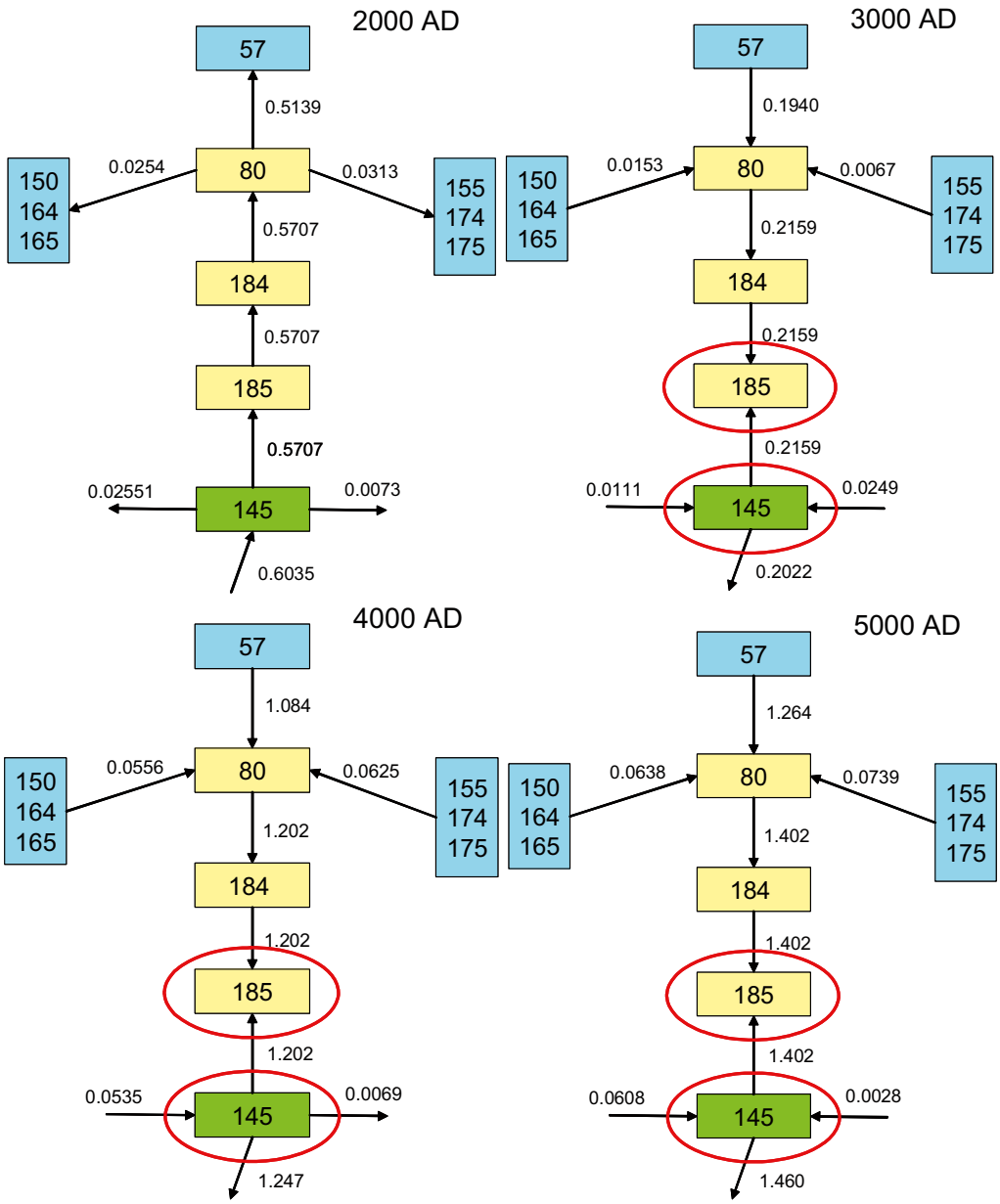

Figure A-4. *Groundwater flow components [m^3/y] in second sub-division of 1BTF.*

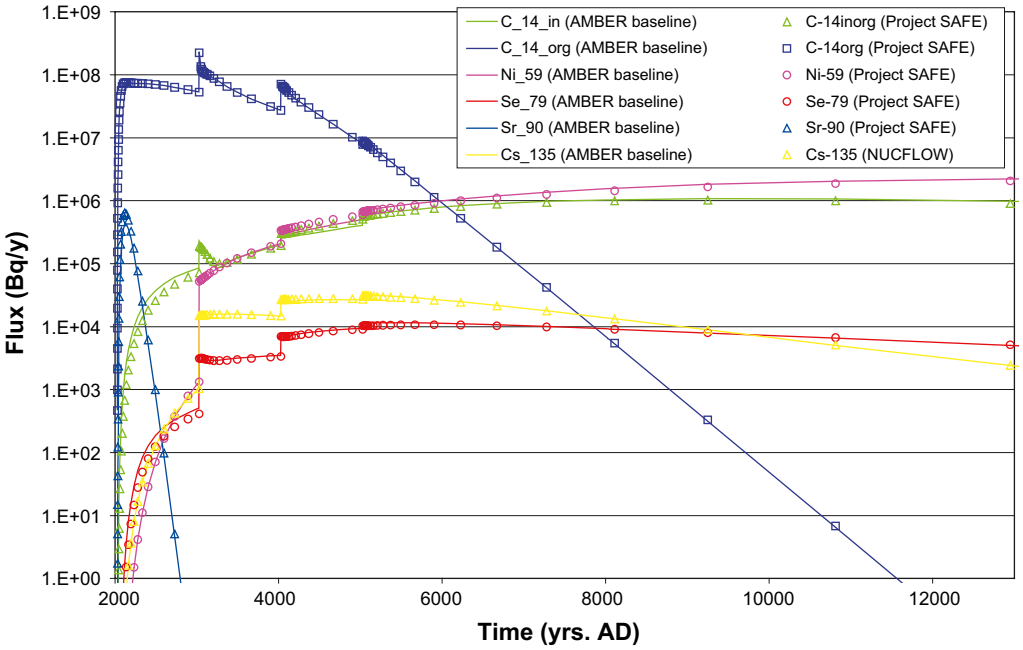

Figure A-5. *Comparison of 1BTF baseline and Project SAFE near-field fluxes for selected radionuclides.*

Table A-5. Summary of 1BTF baseline and Project SAFE near-field fluxes for selected radionuclides with times for selected radionuclides in parentheses.

Radionuclide	AMBER 1BTF baseline	Project SAFE
H-3	$1.483 \cdot 10^{4}$ ($3.9 \cdot 10^{1}$)	$1.488 \cdot 10^{4}$ ($3.9 \cdot 10^{1}$)
Inorganic C-14	$1.075 \cdot 10^{6}$ ($7.2 \cdot 10^{3}$)	$1.021 \cdot 10^{6}$ ($7.2 \cdot 10^{3}$)
Organic C-14	$2.323 \cdot 10^{8}$ ($1.0 \cdot 10^{3}$)	$2.229 \cdot 10^{8}$ ($1.0 \cdot 10^{3}$)
Cl-36	$2.945 \cdot 10^{4}$ ($3.0 \cdot 10^{3}$)	$2.699 \cdot 10^{4}$ ($3.6 \cdot 10^{3}$)
Ni-59	$2.291 \cdot 10^{6}$ ($1.3 \cdot 10^{4}$)	$2.137 \cdot 10^{6}$ ($1.3 \cdot 10^{4}$)
Se-79	$1.164 \cdot 10^{4}$ ($3.6 \cdot 10^{3}$)	$1.067 \cdot 10^{4}$ ($3.9 \cdot 10^{3}$)
Sr-90	$6.404 \cdot 10^{5}$ ($8.8 \cdot 10^{1}$)	$6.436 \cdot 10^{6}$ ($8.8 \cdot 10^{1}$)
Tc-99	$8.538 \cdot 10^{3}$ ($1.3 \cdot 10^{4}$)	$8.450 \cdot 10^{3}$ ($1.3 \cdot 10^{4}$)
Pd-107	$4.245 \cdot 10^{2}$ ($1.3 \cdot 10^{4}$)	$4.242 \cdot 10^{2}$ ($1.3 \cdot 10^{4}$)
Ag-108m	$1.917 \cdot 10^{5}$ ($1.0 \cdot 10^{3}$)	$1.914 \cdot 10^{5}$ ($1.0 \cdot 10^{3}$)
I-129	$1.618 \cdot 10^{3}$ ($3.0 \cdot 10^{3}$)	$1.506 \cdot 10^{3}$ ($3.0 \cdot 10^{3}$)
Cs-135	$3.313 \cdot 10^{4}$ ($3.0 \cdot 10^{3}$)	$3.098 \cdot 10^{4}$ ($3.0 \cdot 10^{3}$)
Cs-137	$7.406 \cdot 10^{3}$ ($1.6 \cdot 10^{2}$)	$7.331 \cdot 10^{3}$ ($1.6 \cdot 10^{2}$)

A4 2BTF

The following modifications made to the 2BTF model described in /Thomson et al. 2008/ have been made:

- The sorption coefficients for inorganic C, Se and Sr have been corrected as described previously for the Silo.
- The flow field imbalance (Figure A-6) was corrected as described previously for the 1BTF.

Figure A-7 shows a comparison of the estimated flux from 2BTF for AMBER and NUCFLOW. The open symbols are NUCFLOW and the lines are AMBER. Table A-6 also summarises the results for each simulation. For each radionuclide reported the first value is the maximum radionuclide flux [Bq y^{-1}] and the second value in parentheses is the time of the maximum

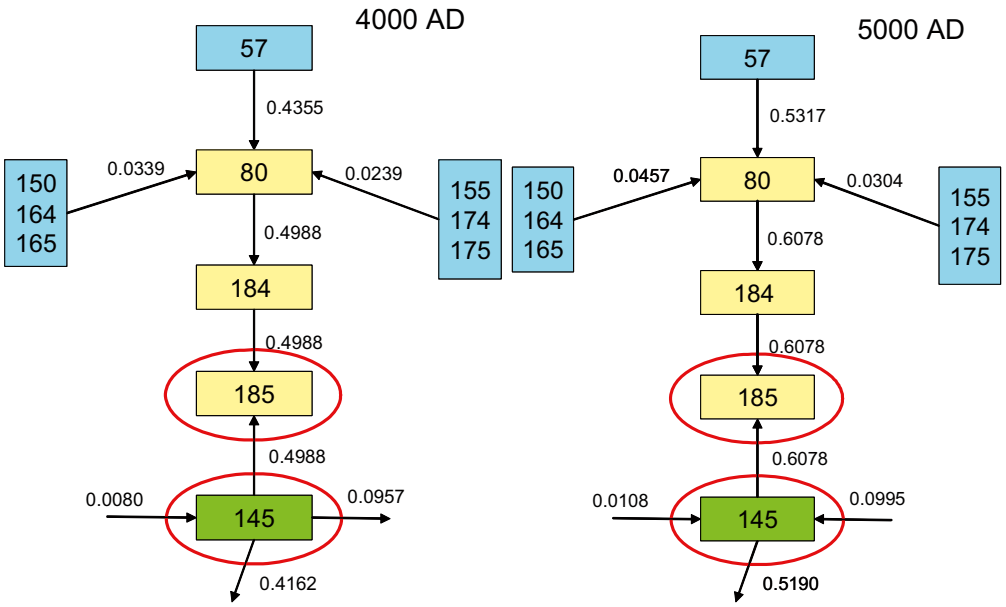

Figure A-6. *Groundwater flow components [m³/y] in second sub-division of 2BTF.*

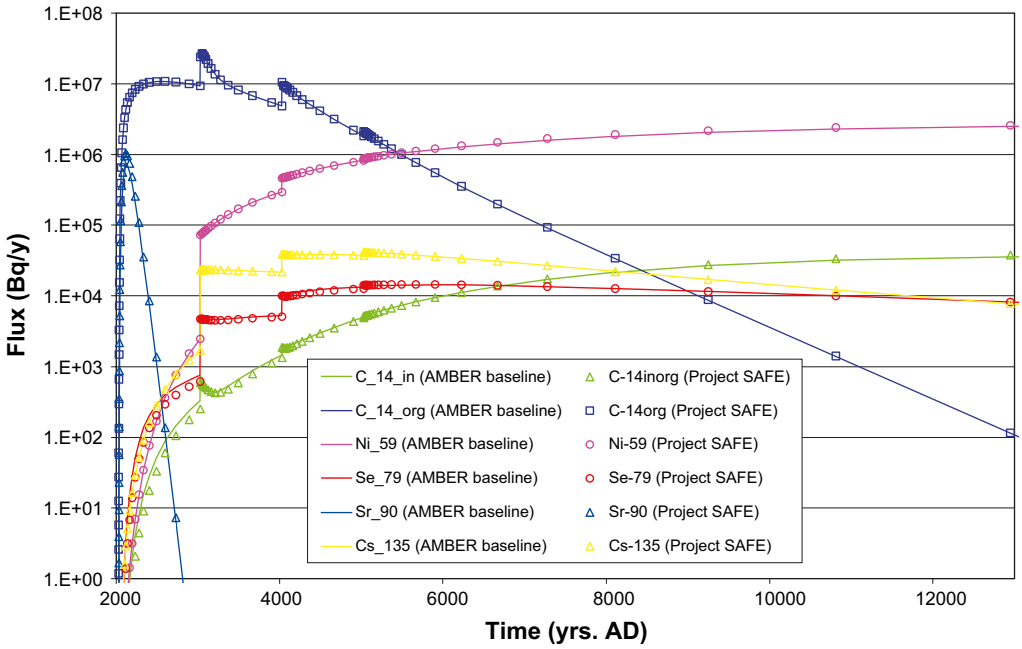

Figure A-7. *Comparison of 2BTF baseline and Project SAFE near-field fluxes for selected radionuclides.*

radionuclide flux [y]. Generally it can be seen that there is little difference between the simulations and those radionuclides which reach there maximum after 1,000 years post-closure show slightly increased radionuclide fluxes which is a result of the reconfigured flows. Sr-90 shows a reduced flux due to the increased sand and gravel sorption coefficient. The results for inorganic C-14 are influenced both by the reconfigured flows and increased sand and gravel sorption coefficient.

Table A-6. Summary of 2BTF baseline and Project SAFE near-field fluxes for selected radionuclides with times for selected radionuclides in parentheses.

Radionuclide	AMBER	NUCFLOW
H-3	$2.106 \cdot 10^{4}$ ($3.9 \cdot 10^{1}$)	$2.140 \cdot 10^{4}$ ($3.9 \cdot 10^{1}$)
Inorganic C-14	$3.607 \cdot 10^{4}$ ($1.2 \cdot 10^{4}$)	$3.810 \cdot 10^{4}$ ($1.3 \cdot 10^{4}$)
Organic C-14	$2.642 \cdot 10^{7}$ ($1.0 \cdot 10^{3}$)	$2.640 \cdot 10^{7}$ ($1.0 \cdot 10^{3}$)
Cl-36	$3.803 \cdot 10^{4}$ ($3.0 \cdot 10^{3}$)	$3.685 \cdot 10^{4}$ ($3.5 \cdot 10^{3}$)
Ni-59	$2.606 \cdot 10^{6}$ ($1.3 \cdot 10^{4}$)	$2.646 \cdot 10^{6}$ ($1.3 \cdot 10^{4}$)
Se-79	$1.500 \cdot 10^{4}$ ($3.0 \cdot 10^{3}$)	$1.450 \cdot 10^{4}$ ($3.6 \cdot 10^{3}$)
Sr-90	$7.102 \cdot 10^{5}$ ($8.8 \cdot 10^{1}$)	$1.033 \cdot 10^{6}$ ($8.8 \cdot 10^{1}$)
Tc-99	$1.186 \cdot 10^{4}$ ($1.3 \cdot 10^{4}$)	$1.182 \cdot 10^{4}$ ($1.3 \cdot 10^{4}$)
Pd-107	$5.673 \cdot 10^{2}$ ($1.3 \cdot 10^{4}$)	$5.719 \cdot 10^{2}$ ($1.3 \cdot 10^{4}$)
Ag-108m	$2.745 \cdot 10^{5}$ ($1.0 \cdot 10^{3}$)	$2.748 \cdot 10^{5}$ ($1.0 \cdot 10^{3}$)
I-129	$2.146 \cdot 10^{3}$ ($3.0 \cdot 10^{3}$)	$2.090 \cdot 10^{3}$ ($3.0 \cdot 10^{3}$)
Cs-135	$4.189 \cdot 10^{4}$ ($3.0 \cdot 10^{3}$)	$4.168 \cdot 10^{4}$ ($3.0 \cdot 10^{3}$)
Cs-137	$3.748 \cdot 10^{4}$ ($1.1 \cdot 10^{2}$)	$3.749 \cdot 10^{4}$ ($1.1 \cdot 10^{2}$)

A5 BLA

No changes were required to be made to the BLA model.

A summary of the results for the BLA simulations is given in Table A-7 /Thomson et al. 2008/. For each radionuclide reported the first value is the maximum radionuclide flux [Bq y^{-1}] and the second value in parentheses is the time of the maximum radionuclide flux [y]. There are no significant differences between the simulations.

Geosphere

In order to improve the efficiency of the model run times the discretisation in the geosphere model along fracture was reduced from 40 compartments to 11. The remainder of the model is unchanged from that described in /Thomson et al. 2008/.

Table A-7. Summary of comparisons for AMBER and NUCFLOW BLA models with times to maximum flux in parentheses.

	AMBER BLA Baseline	Project SAFE
H-3	$5.492 \cdot 10^{5}$ (0)	$5.492 \cdot 10^{5}$ (0)
C-14in	$3.230 \cdot 10^{7}$ (0)	$3.230 \cdot 10^{7}$ (0)
C-14org	$2.712 \cdot 10^{4}$ (0)	$2.712 \cdot 10^{4}$ (0)
Cl-36	$6.973 \cdot 10^{4}$ ($1.1 \cdot 10^{3}$)	$6.973 \cdot 10^{4}$ ($1.1 \cdot 10^{3}$)
Ni-59	$3.316 \cdot 10^{7}$ ($1.1 \cdot 10^{3}$)	$3.316 \cdot 10^{7}$ ($1.1 \cdot 10^{3}$)
Se-79	$2.794 \cdot 10^{4}$ ($1.1 \cdot 10^{3}$)	$2.793 \cdot 10^{4}$ ($1.1 \cdot 10^{3}$)
Sr-90	$2.989 \cdot 10^{8}$ (0)	$2.989 \cdot 10^{8}$ (0)
Tc-99	$3.482 \cdot 10^{7}$ ($1.1 \cdot 10^{3}$)	$3.482 \cdot 10^{7}$ ($1.1 \cdot 10^{3}$)
Pd-107	$6.991 \cdot 10^{3}$ ($1.1 \cdot 10^{3}$)	$6.990 \cdot 10^{3}$ ($1.1 \cdot 10^{3}$)
Ag-108m	$1.838 \cdot 10^{6}$ (0)	$1.838 \cdot 10^{6}$ (0)
I-129	$2.097 \cdot 10^{3}$ ($1.1 \cdot 10^{3}$)	$2.097 \cdot 10^{3}$ ($1.1 \cdot 10^{3}$)
Cs-135	$3.495 \cdot 10^{4}$ ($1.1 \cdot 10^{3}$)	$3.494 \cdot 10^{4}$ ($1.1 \cdot 10^{3}$)
Cs-137	$3.097 \cdot 10^{9}$ (0)	$3.097 \cdot 10^{9}$ (0)

The results of these changes are summarised in Figure A-8 and Table A-8. It can be seen that a reduction in the number of compartments results in a small increase in the dispersion but the values of maximum radionuclide flux are little altered.

Table A-8. Variation in radionuclide flux [Bq/y] from geosphere with differing longitudinal discretisation.

	Longitudinal discretisation	
	11 compartments	40 compartments
C-14 inorganic	$1.9 \cdot 10^{7}$	$1.7 \cdot 10^{7}$
C-14 organic	$2.4 \cdot 10^{4}$	$2.1 \cdot 10^{4}$
Cl-36	$6.7 \cdot 10^{4}$	$5.5 \cdot 10^{4}$
Co-60	$6.1 \cdot 10^{3}$	$2.9 \cdot 10^{3}$
Ni-59	$1.1 \cdot 10^{7}$	$1.1 \cdot 10^{7}$
Ni-63	$1.0 \cdot 10^{8}$	$9.9 \cdot 10^{7}$
Se-79	$1.9 \cdot 10^{4}$	$1.7 \cdot 10^{4}$
Sr-90	$2.7 \cdot 10^{7}$	$2.6 \cdot 10^{7}$
Nb-94	$3.3 \cdot 10^{3}$	$3.2 \cdot 10^{3}$
Tc-99	$4.2 \cdot 10^{5}$	$4.1 \cdot 10^{5}$
Ag-108m	$1.6 \cdot 10^{4}$	$1.5 \cdot 10^{4}$
Sn-126	$2.4 \cdot 10^{3}$	$2.2 \cdot 10^{3}$
I-129	$2.0 \cdot 10^{3}$	$1.7 \cdot 10^{3}$
Cs-135	$3.8 \cdot 10^{3}$	$3.4 \cdot 10^{3}$
Cs-137	$1.1 \cdot 10^{5}$	$6.3 \cdot 10^{4}$
Pu-239	$7.2 \cdot 10^{2}$	$6.2 \cdot 10^{2}$
Pu-240	$5.3 \cdot 10^{2}$	$4.5 \cdot 10^{2}$
Pu-242	$9.2 \cdot 10^{0}$	$7.9 \cdot 10^{0}$
Am-241	$6.8 \cdot 10^{0}$	$2.6 \cdot 10^{0}$

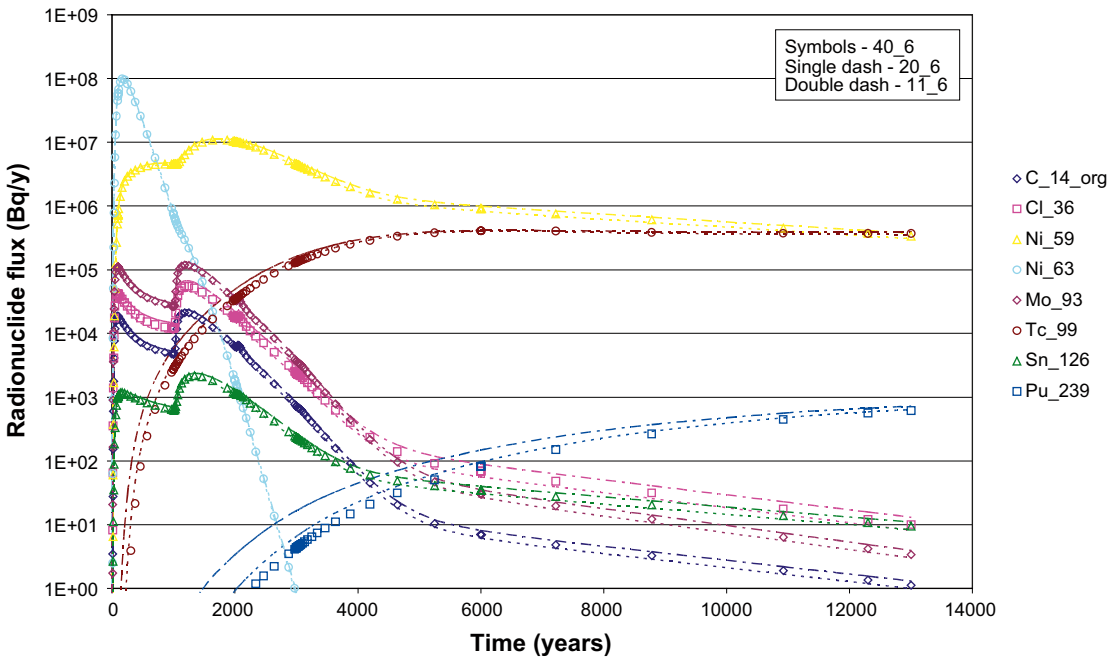

Figure A-8. *Comparison of geosphere fluxes resulting from different levels of geosphere discretisation.*

Appendix B

Disposal inventory screening

This appendix reports the results of an exercise to identify those radionuclides and decay chains that are to be included within the SAR-08 near-field and geosphere assessment calculations.

B1 Overview

Several safety assessments on SFR 1 have been undertaken to date. Disposal inventories often vary between each safety assessment as assumptions on reactor lifetime change, the efficiencies of waste management activities improve, knowledge of waste compositions is revised and regulatory expectations are reviewed. Table B-1 summarises inventories from previous safety assessments undertaken on SFR 1 and also presents that to be used within SAR-08 (based on 50 year reactor lifetime) /Almkvist and Gordon 2007/. Those radionuclides highlighted in italics were not previously included within Project SAFE or the 2005 calculations.

Generally it can be seen that the radionuclide inventory estimated for Project SAFE was higher than that in the assessment reported as SFR 87-11. However, in the majority of cases the radionuclide inventory estimated for SAR-08 is below that used in Project SAFE and more in line with that used in the assessment reported as SFR 87-11.

Another feature is that the number of radionuclides for which a disposal inventory is reported and which are included in assessment calculations increased from the assessment reported as SFR 87-11 to Project SAFE. However, not all radionuclides were considered within Project SAFE or the 2005 calculations. A subset of radionuclides was included in order to focus efforts on those considered to be more important to assessing the safety of the repository.

As the SAR-08 disposal inventory has been revised and the calculations required to be undertaken are more computationally demanding it would be beneficial to review the basis of radionuclide screening.

Table B-1. Inventories (Bq) used in safety assessments on SFR 1.

Radionuclide	Half-life (y)	SFR 87-11	Project SAFE	2005 calculations	SAR-08
H-3	$1.23 \cdot 10^{1}$	$1.3 \cdot 10^{14}$	$6.2 \cdot 10^{11}$	$3.8 \cdot 10^{10}$	$3.92 \cdot 10^{10}$
Be-10	$1.60 \cdot 10^{6}$		*$1.4 \cdot 10^{7}$*	*$1.0 \cdot 10^{6}$*	$1.22 \cdot 10^{6}$
C-14 org	$5.73 \cdot 10^{3}$	$7.2 \cdot 10^{12}$	$2.6 \cdot 10^{13}$	$4.8 \cdot 10^{12}$	$2.83 \cdot 10^{12}$
C-14 inorg	$5.73 \cdot 10^{3}$				$1.83 \cdot 10^{13}$
Cl-36	$3.01 \cdot 10^{5}$		$5.1 \cdot 10^{10}$	$3.1 \cdot 10^{9}$	$1.37 \cdot 10^{9}$
Fe-55	$2.74 \cdot 10^{0}$	$1.1 \cdot 10^{15}$	*$6.5 \cdot 10^{14}$*	*$2.1 \cdot 10^{13}$*	$2.13 \cdot 10^{13}$
Ni-59	$7.60 \cdot 10^{4}$	$8.0 \cdot 10^{12}$	$2.4 \cdot 10^{13}$	$8.5 \cdot 10^{11}$	$9.46 \cdot 10^{12}$
Co-60	$5.27 \cdot 10^{0}$	$2.1 \cdot 10^{15}$	$1.9 \cdot 10^{15}$	$9.3 \cdot 10^{13}$	$9.31 \cdot 10^{13}$
Ni-63	$1.00 \cdot 10^{2}$	$7.3 \cdot 10^{14}$	$4.0 \cdot 10^{15}$	$1.2 \cdot 10^{14}$	$1.15 \cdot 10^{15}$
Se-79	$1.13 \cdot 10^{6}$		$2.1 \cdot 10^{10}$	$1.1 \cdot 10^{9}$	$1.27 \cdot 10^{9}$
Sr-90	$2.88 \cdot 10^{2}$	$2.6 \cdot 10^{14}$	$2.6 \cdot 10^{14}$	$1.2 \cdot 10^{13}$	$1.28 \cdot 10^{13}$
Mo-93	$4.00 \cdot 10^{3}$		$1.2 \cdot 10^{11}$	$9.1 \cdot 10^{9}$	$3.47 \cdot 10^{9}$
Nb-93m	$1.61 \cdot 10^{1}$		$8.2 \cdot 10^{12}$	$5.2 \cdot 10^{11}$	$5.46 \cdot 10^{11}$
Zr-93	$1.53 \cdot 10^{6}$		$2.4 \cdot 10^{10}$	$1.6 \cdot 10^{10}$	$2.28 \cdot 10^{9}$
Nb-94	$2.03 \cdot 10^{4}$	$8.0 \cdot 10^{9}$	$2.4 \cdot 10^{11}$	$1.7 \cdot 10^{10}$	$2.03 \cdot 10^{10}$
Tc-99	$2.11 \cdot 10^{5}$	$3.4 \cdot 10^{11}$	$2.6 \cdot 10^{13}$	$1.4 \cdot 10^{12}$	$3.56 \cdot 10^{11}$
Ru-106	$1.02 \cdot 10^{0}$	$6.3 \cdot 10^{12}$	*$2.9 \cdot 10^{11}$*	*$1.9 \cdot 10^{9}$*	$1.57 \cdot 10^{9}$
Pd-107	$6.50 \cdot 10^{6}$		$5.1 \cdot 10^{9}$	$2.8 \cdot 10^{8}$	$3.18 \cdot 10^{8}$

Radionuclide	Half-life (y)	SFR 87-11	Project SAFE	2005 calculations	SAR-08
Ag-108m	$4.18 \cdot 10^{2}$		$1.4 \cdot 10^{12}$	$9.6 \cdot 10^{10}$	$1.15 \cdot 10^{11}$
Cd-113m	$1.41 \cdot 10^{1}$		*$8.7 \cdot 10^{11}$*	$3.5 \cdot 10^{10}$	$3.49 \cdot 10^{10}$
Sb-125	$2.76 \cdot 10^{0}$		*$6.6 \cdot 10^{13}$*	*$2.4 \cdot 10^{12}$*	$2.29 \cdot 10^{12}$
Sn-126	$1.00 \cdot 10^{5}$		$2.6 \cdot 10^{9}$	$1.4 \cdot 10^{8}$	$1.59 \cdot 10^{8}$
I-129	$1.57 \cdot 10^{7}$	$2.0 \cdot 10^{9}$	$1.5 \cdot 10^{9}$	$9.5 \cdot 10^{8}$	$9.03 \cdot 10^{8}$
Ba-133	$1.05 \cdot 10^{1}$		*$5.1 \cdot 10^{10}$*	*$3.1 \cdot 10^{9}$*	$3.13 \cdot 10^{9}$
Cs-134	$2.07 \cdot 10^{0}$	$6.2 \cdot 10^{14}$	*$1.1 \cdot 10^{14}$*	*$1.1 \cdot 10^{12}$*	$9.65 \cdot 10^{11}$
Cs-135	$2.30 \cdot 10^{6}$	$2.0 \cdot 10^{10}$	$2.6 \cdot 10^{10}$	$1.4 \cdot 10^{9}$	$3.09 \cdot 10^{9}$
Cs-137	$3.00 \cdot 10^{1}$	$5.1 \cdot 10^{15}$	$2.7 \cdot 10^{15}$	$1.3 \cdot 10^{14}$	$1.35 \cdot 10^{14}$
Pm-147	$2.62 \cdot 10^{0}$		$1.4 \cdot 10^{14}$	$2.1 \cdot 10^{12}$	$1.87 \cdot 10^{12}$
Sm-151	$9.00 \cdot 10^{1}$		$1.2 \cdot 10^{13}$	$6.4 \cdot 10^{11}$	$6.99 \cdot 10^{11}$
Eu-152	$1.35 \cdot 10^{1}$		$5.3 \cdot 10^{11}$	$7.4 \cdot 10^{9}$	$5.36 \cdot 10^{9}$
Eu-154	$8.59 \cdot 10^{0}$		$8.2 \cdot 10^{13}$	$2.9 \cdot 10^{12}$	$2.75 \cdot 10^{12}$
Eu-155	$4.75 \cdot 10^{0}$		$2.5 \cdot 10^{13}$	$6.4 \cdot 10^{11}$	$6.02 \cdot 10^{11}$
Ho-166m	$1.20 \cdot 10^{3}$		$9.4 \cdot 10^{10}$	$7.2 \cdot 10^{9}$	$8.93 \cdot 10^{9}$
Pb-210	$2.23 \cdot 10^{1}$		*$9.2 \cdot 10^{0}$*		$2.60 \cdot 10^{-1}$
Ac-227	$2.18 \cdot 10^{1}$		*$1.8 \cdot 10^{2}$*		$5.09 \cdot 10^{1}$
Ra-226	$1.60 \cdot 10^{3}$		*$1.8 \cdot 10^{3}$*		$6.91 \cdot 10^{0}$
Th-229	$7.34 \cdot 10^{4}$		*$2.7 \cdot 10^{2}$*		$1.05 \cdot 10^{1}$
Th-230	$7.54 \cdot 10^{4}$		*$8.0 \cdot 10^{-4}$*		$3.15 \cdot 10^{3}$
Th-232	$1.32 \cdot 10^{10}$		*$8.9 \cdot 10^{2}$*		$3.51 \cdot 10^{-3}$
Pa-231	$3.28 \cdot 10^{4}$		*$2.7 \cdot 10^{-4}$*		$1.05 \cdot 10^{3}$
U-232	$6.89 \cdot 10^{1}$		*$2.1 \cdot 10^{7}$*	*$8.7 \cdot 10^{5}$*	$7.46 \cdot 10^{5}$
U-233	$1.59 \cdot 10^{5}$		*$1.8 \cdot 10^{4}$*		$7.01 \cdot 10^{2}$
U-234	$2.46 \cdot 10^{5}$		*$8.9 \cdot 10^{8}$*	*$3.8 \cdot 10^{7}$*	$3.51 \cdot 10^{7}$
U-235	$7.00 \cdot 10^{8}$		*$1.8 \cdot 10^{7}$*	*$5.2 \cdot 10^{8}$*	$4.66 \cdot 10^{8}$
U-236	$2.30 \cdot 10^{7}$		*$2.7 \cdot 10^{8}$*	*$1.5 \cdot 10^{7}$*	$1.40 \cdot 10^{7}$
U-238	$4.50 \cdot 10^{9}$		*$3.6 \cdot 10^{8}$*	*$1.6 \cdot 10^{9}$*	$1.47 \cdot 10^{9}$
Np-237	$2.14 \cdot 10^{6}$		*$3.6 \cdot 10^{8}$*	*$1.3 \cdot 10^{8}$*	$1.58 \cdot 10^{8}$
Pu-238	$8.77 \cdot 10^{1}$	$3.8 \cdot 10^{12}$	*$3.0 \cdot 10^{12}$*	*$8.7 \cdot 10^{10}$*	$4.86 \cdot 10^{10}$
Pu-239	$2.41 \cdot 10^{4}$	$4.0 \cdot 10^{11}$	$3.0 \cdot 10^{11}$	$1.1 \cdot 10^{10}$	$3.22 \cdot 10^{10}$
Pu-240	$6.56 \cdot 10^{3}$	$8.1 \cdot 10^{11}$	$5.9 \cdot 10^{11}$	$2.1 \cdot 10^{10}$	$1.58 \cdot 10^{9}$
Pu-241	$1.44 \cdot 10^{1}$	$4.3 \cdot 10^{13}$	*$3.2 \cdot 10^{13}$*	*$1.1 \cdot 10^{12}$*	$8.19 \cdot 10^{11}$
Pu-242	$3.73 \cdot 10^{5}$		$2.9 \cdot 10^{9}$	$1.1 \cdot 10^{8}$	$1.05 \cdot 10^{8}$
Pu-244	$8.00 \cdot 10^{7}$		*$6.2 \cdot 10^{2}$*		$2.45 \cdot 10^{1}$
Am-241	$4.32 \cdot 10^{2}$	$1.0 \cdot 10^{12}$	$6.1 \cdot 10^{12}$	$5.1 \cdot 10^{11}$	$4.97 \cdot 10^{11}$
Am-242m	$1.41 \cdot 10^{2}$		*$8.0 \cdot 10^{9}$*	*$3.3 \cdot 10^{8}$*	$2.96 \cdot 10^{8}$
Am-243	$7.37 \cdot 10^{3}$		*$2.7 \cdot 10^{10}$*	*$1.2 \cdot 10^{9}$*	$1.10 \cdot 10^{9}$
Cm-243	$2.91 \cdot 10^{1}$		*$1.1 \cdot 10^{10}$*	*$3.7 \cdot 10^{8}$*	$2.90 \cdot 10^{8}$
Cm-244	$1.81 \cdot 10^{1}$	$1.2 \cdot 10^{11}$	*$1.2 \cdot 10^{12}$*	*$2.1 \cdot 10^{10}$*	$1.01 \cdot 10^{10}$
Cm-245	$8.50 \cdot 10^{3}$		*$2.7 \cdot 10^{8}$*	*$1.1 \cdot 10^{7}$*	$1.05 \cdot 10^{7}$
Cm-246	$4.73 \cdot 10^{3}$		*$7.1 \cdot 10^{7}$*	*$3.0 \cdot 10^{6}$*	$2.79 \cdot 10^{6}$

B2 Screening calculations

The two fundamental questions asked here are

- *Which radionuclides are considered the most important for SAR-08?*
- *Which decay chains are appropriate for the near-field and geosphere assessment calculations?*

In order to undertake the screening exercise a simple and cautious approach to estimating impact, represented by annual individual $Dose_{screening}$ [Sv y^{-1}], was undertaken.

$$Dose_{screening} = A_i.e^{-\lambda_i t.R_f^i} T_{geo}.BDF_i \qquad \text{Equation B-1}$$

where

A_i is the assumed disposed inventory for radionuclide i [Bq]

λ_i is the decay constant for radionuclide i [y^{-1}]

t is the geosphere travel time [y]

R_f^i is the geosphere retardation factor for radionuclide i [–]

$$R_f = 1 + a_w d_0 \theta R_m \qquad \text{Equation B-2}$$

a_w is the flow wetted surface area [120 m^2 m^{-3}]

d_0 is the thickness of the thin layer [0.0001 m], estimated using data for Pu

θ is the matrix porosity [0.005]

R_m is the retardation within the rock matrix [–], given by

$$R_m = 1 + \rho.K_d \big/ \theta \qquad \text{Equation B-3}$$

ρ is the rock matrix bulk density [2,700 kg m^{-3}]

T_{geo} is the geosphere transfer rate for a conservative radionuclide [y^{-1}] calculated from the advective rate and path length

BDF_i is the biosphere dose factor for radionuclide i [Sv y^{-1} per Bq y^{-1}].

The radionuclide disposal inventories used are those for the whole of SFR 1 for 40 years reactor operations. Illustrative geosphere data from the inverse modelling calculations for 5,000 AD were taken for travel time [40 years] and pathlength [410 m], the geosphere sorption data were those used in Project SAFE (where data for elements were not reported they were conservatively assumed to undergo no retardation).

Preliminary biosphere dose factors for this assessment were used. Three different types of ecosystems were considered:

- From year 2,000 AD–5,000 AD when the whole area is under the sea (see biosphere dose factors in Table B-2).
- From year 5,000 AD–8,000 AD when there are 2 lakes in the area and the rest is under the sea (see biosphere dose factors in Table B-3).
- From year 8,000 AD when there are 3 mires in the area and the rest in under the sea (see biosphere dose factors in Table B-4).

Table B-2. Screening dose conversion factors (SDF [Sv y^{-1} per Bq y^{-1}]) from a continuous input of 1 Bq/y during 10,000 years to a coastal part of the Öregrundsgrepen.

Radionuclide	SDF
H-3	$2.92 \cdot 10^{-22}$
Be-10	$2.7 \cdot 10^{-18}$
Cl-36	$1.57 \cdot 10^{-20}$
Fe-55	$3.61 \cdot 10^{-19}$
Co-60	$2.42 \cdot 10^{-18}$
Ni-59	$2.34 \cdot 10^{-19}$
Ni-63	$4.56 \cdot 10^{-19}$
Se-79	$1.48 \cdot 10^{-16}$
Sr-90	$6.12 \cdot 10^{-18}$
Zr-93	$1.35 \cdot 10^{-18}$
Nb-93m	$6.2 \cdot 10^{-20}$
Nb-94	$2.1 \cdot 10^{-18}$
Mo-93	$4.04 \cdot 10^{-19}$
Tc-99	$3.55 \cdot 10^{-19}$
Ru-106	$3.69 \cdot 10^{-20}$
Pd-107	$4.56 \cdot 10^{-21}$
Ag-108m	$1.34 \cdot 10^{-17}$
Cd-113m	$2.22 \cdot 10^{-17}$
Sn-126	$5.79 \cdot 10^{-17}$
I-129	$4.15 \cdot 10^{-17}$
Cs-134	$3.87 \cdot 10^{-18}$
Cs-135	$4.96 \cdot 10^{-18}$
Cs-137	$1.86 \cdot 10^{-17}$
Sb-125	$2.07 \cdot 10^{-19}$
Ba-133	$1.2 \cdot 10^{-18}$
Pm-147	$6.73 \cdot 10^{-20}$
Sm-151	$2.89 \cdot 10^{-20}$
Eu-152	$6.72 \cdot 10^{-19}$
Eu-154	$6.92 \cdot 10^{-19}$
Eu-155	$7.04 \cdot 10^{-20}$
Ho-166m	$7.26 \cdot 10^{-19}$
Th-230	$7.7 \cdot 10^{-17}$
Pa-231	$8.69 \cdot 10^{-17}$
U-232	$1.57 \cdot 10^{-16}$
U-234	$3.06 \cdot 10^{-17}$
U-235	$2.94 \cdot 10^{-17}$
U-236	$2.94 \cdot 10^{-17}$
U-238	$2.81 \cdot 10^{-17}$
Np-237	$6.77 \cdot 10^{-17}$
Pu-238	$6.74 \cdot 10^{-17}$
Pu-239	$9.16 \cdot 10^{-17}$
Pu-240	$9.14 \cdot 10^{-17}$
Pu-241	$6.92 \cdot 10^{-19}$
Pu-242	$8.8 \cdot 10^{-17}$
Pu-244	$8.8 \cdot 10^{-17}$
Am-241	$1.36 \cdot 10^{-16}$
Am-242m	$1.17 \cdot 10^{-16}$
Am-243	$1.42 \cdot 10^{-16}$
Cm-243	$5.11 \cdot 10^{-17}$
Cm-244	$3.24 \cdot 10^{-17}$
Cm-245	$1.25 \cdot 10^{-16}$
Cm-246	$4.71 \cdot 10^{-16}$

Table B-3. Screening dose conversion factors (SDF [Sv y^{-1} per Bq y^{-1}]) from a continuous input of 1 Bq/y during 10,000 years to a lake, created by landrise of a former bay at Öregrundsgrepen.

Radionuclide	SDF
Be-10	$5.24 \cdot 10^{-14}$
Cl-36	$1.18 \cdot 10^{-14}$
Ni-59	$3.25 \cdot 10^{-15}$
Se-79	$2.46 \cdot 10^{-12}$
Zr-93	$1.63 \cdot 10^{-14}$
Nb-93m	$5.9 \cdot 10^{-15}$
Nb-94	$8.68 \cdot 10^{-14}$
Mo-93	$8.34 \cdot 10^{-15}$
Tc-99	$4.92 \cdot 10^{-15}$
Pd-107	$6.28 \cdot 10^{-16}$
Ag-108m	$2.62 \cdot 10^{-13}$
Sn-126	$1.06 \cdot 10^{-12}$
I-129	$5.46 \cdot 10^{-12}$
Cs-135	$3.43 \cdot 10^{-12}$
Ho-166m	$1.52 \cdot 10^{-14}$
Th-230	$9.19 \cdot 10^{-13}$
Th-232	$1.01 \cdot 10^{-12}$
Pa-231	$3.34 \cdot 10^{-13}$
U-234	$9.24 \cdot 10^{-14}$
U-235	$8.86 \cdot 10^{-14}$
U-236	$8.86 \cdot 10^{-14}$
U-238	$8.49 \cdot 10^{-14}$
Np-237	$9.41 \cdot 10^{-13}$
Pu-239	$3.4 \cdot 10^{-13}$
Pu-240	$3.4 \cdot 10^{-13}$
Pu-242	$3.26 \cdot 10^{-13}$
Am-241	$3.39 \cdot 10^{-12}$
Am-242m	$3.21 \cdot 10^{-12}$
Am-243	$3.4 \cdot 10^{-12}$
Cm-245	$7.67 \cdot 10^{-14}$
Cm-246	$7.67 \cdot 10^{-14}$

Table B-4. Screening dose conversion factors (SDF [Sv y^{-1} per Bq y^{-1}]) from a continuous input of 1 Bq/y during 10,000 years to a mire, created by landrise of a former bay at Öregrundsgrepen.

Radionuclide	SDF
Be-10	$1.32 \cdot 10^{-14}$
Cl-36	$1.15 \cdot 10^{-14}$
Ni-59	$3.89 \cdot 10^{-15}$
Se-79	$6.28 \cdot 10^{-14}$
Zr-93	$1.88 \cdot 10^{-14}$
Nb-93m	$3.03 \cdot 10^{-16}$
Nb-94	$5.29 \cdot 10^{-13}$
Mo-93	$5.57 \cdot 10^{-14}$
Tc-99	$7.28 \cdot 10^{-16}$
Pd-107	$1.9 \cdot 10^{-14}$
Ag-108m	$7.44 \cdot 10^{-12}$
Sn-126	$3.51 \cdot 10^{-13}$
I-129	$4.56 \cdot 10^{-12}$

Cs-135	$3.76 \cdot 10^{-12}$
Ho-166m	$8.17 \cdot 10^{-13}$
Th-230	$8.05 \cdot 10^{-10}$
Th-232	$9.12 \cdot 10^{-10}$
Pa-231	$9.49 \cdot 10^{-11}$
U-234	$3.65 \cdot 10^{-13}$
U-235	$3.39 \cdot 10^{-13}$
U-236	$3.39 \cdot 10^{-13}$
U-238	$3.12 \cdot 10^{-13}$
Np-237	$2.33 \cdot 10^{-11}$
Pu-239	$5.48 \cdot 10^{-11}$
Pu-240	$5.43 \cdot 10^{-11}$
Pu-242	$5.04 \cdot 10^{-11}$
Am-241	$3.7 \cdot 10^{-11}$
Am-242m	$2.68 \cdot 10^{-11}$
Am-243	$4.35 \cdot 10^{-11}$
Cm-245	$4.53 \cdot 10^{-11}$

The relevance of a radionuclide was determined by calculating a Risk Quotient for each radionuclide which is defined as the calculated dose divided by the screening value. A value of 10^{-7} Sv/y (i.e. 0.01*Dose constraint) was used as the screening value. The factor of 0.01 is used to account for the exposure to several radionuclides. If the Risk Quotient is below 1 then a radionuclide can be excluded.

These biosphere dose factors were applied in turn and all those radionuclides with a Risk Quotient is above 1 were considered for inclusion in the calculations.

The screening calculations are summarised in Table B-5.

Table B-5. Summary of screening calculations.

Radionuclide	Half life (y)	Inventory (Bq)	Rf (–)	Geosphere flux (Bq y^{-1})	Coastal Dose (Sv/y)	RQ	Lake Dose (Sv/y)	RQ	Mire Dose (Sv/y)	RQ
H-3	$1.23 \cdot 10^{1}$	$3.92 \cdot 10^{10}$	$1.00 \cdot 10^{0}$	$1.02 \cdot 10^{8}$	$2.98 \cdot 10^{-14}$	0.00				
Be-10	$1.60 \cdot 10^{6}$	$1.22 \cdot 10^{6}$	$1.00 \cdot 10^{0}$	$3.04 \cdot 10^{4}$	$8.21 \cdot 10^{-14}$	0.00	$1.59 \cdot 10^{-9}$	0.01	$4.01 \cdot 10^{-10}$	0.00
Organic C-14	$5.73 \cdot 10^{3}$	$2.83 \cdot 10^{12}$	$1.00 \cdot 10^{0}$	$7.05 \cdot 10^{10}$						
Inorganic C-14	$5.73 \cdot 10^{3}$	$1.83 \cdot 10^{13}$	$1.03 \cdot 10^{0}$	$4.40 \cdot 10^{11}$						
Cl-36	$3.01 \cdot 10^{5}$	$1.37 \cdot 10^{9}$	$1.00 \cdot 10^{0}$	$3.44 \cdot 10^{7}$	$5.39 \cdot 10^{-13}$	0.00	$4.05 \cdot 10^{-7}$	2.53	$3.95 \cdot 10^{-7}$	2.47
Fe-55	$2.74 \cdot 10^{0}$	$2.13 \cdot 10^{13}$	$1.00 \cdot 10^{0}$	$2.10 \cdot 10^{7}$	$7.59 \cdot 10^{-12}$	0.00				
Ni-59	$7.60 \cdot 10^{4}$	$9.46 \cdot 10^{12}$	$1.65 \cdot 10^{0}$	$1.43 \cdot 10^{11}$	$3.36 \cdot 10^{-8}$	0.21	$4.66 \cdot 10^{-4}$	2,913	$5.58 \cdot 10^{-4}$	3,487
Co-60	$5.27 \cdot 10^{0}$	$9.31 \cdot 10^{13}$	$1.65 \cdot 10^{0}$	$2.42 \cdot 10^{8}$	$5.86 \cdot 10^{-10}$	0.00				
Ni-63	$1.00 \cdot 10^{2}$	$1.15 \cdot 10^{15}$	$1.65 \cdot 10^{0}$	$1.11 \cdot 10^{13}$	$5.04 \cdot 10^{-6}$	31.5				
Se-79	$1.13 \cdot 10^{6}$	$1.27 \cdot 10^{9}$	$1.03 \cdot 10^{0}$	$3.08 \cdot 10^{7}$	$4.56 \cdot 10^{-9}$	0.03	$7.58 \cdot 10^{-5}$	473.6	$1.93 \cdot 10^{-6}$	12.1
Sr-90	$2.88 \cdot 10^{1}$	$1.28 \cdot 10^{13}$	$1.01 \cdot 10^{0}$	$1.21 \cdot 10^{11}$	$7.38 \cdot 10^{-7}$	4.62				
Mo-93	$4.00 \cdot 10^{3}$	$3.47 \cdot 10^{9}$	$1.00 \cdot 10^{0}$	$8.61 \cdot 10^{7}$	$3.48 \cdot 10^{-11}$	0.00	$7.18 \cdot 10^{-7}$	4.49	$4.80 \cdot 10^{-6}$	30.0
Nb-93m	$1.61 \cdot 10^{1}$	$5.46 \cdot 10^{11}$	$3.34 \cdot 10^{1}$	$4.28 \cdot 10^{-17}$	$2.65 \cdot 10^{-36}$	0.00	$2.52 \cdot 10^{-31}$	0.00	$1.30 \cdot 10^{-32}$	0.00
Zr-93	$1.53 \cdot 10^{6}$	$2.28 \cdot 10^{9}$	$3.34 \cdot 10^{1}$	$1.70 \cdot 10^{6}$	$2.30 \cdot 10^{-12}$	0.00	$2.78 \cdot 10^{-8}$	0.17	$3.20 \cdot 10^{-8}$	0.20
Nb-94	$2.03 \cdot 10^{4}$	$2.03 \cdot 10^{10}$	$3.34 \cdot 10^{1}$	$1.45 \cdot 10^{7}$	$3.04 \cdot 10^{-11}$	0.00	$1.26 \cdot 10^{-6}$	7.86	$7.66 \cdot 10^{-6}$	47.9
Tc-99	$2.11 \cdot 10^{5}$	$3.56 \cdot 10^{11}$	$3.34 \cdot 10^{1}$	$2.65 \cdot 10^{8}$	$9.41 \cdot 10^{-11}$	0.00	$1.30 \cdot 10^{-6}$	8.15	$1.93 \cdot 10^{-7}$	1.21
Ru-106	$1.02 \cdot 10^{0}$	$1.57 \cdot 10^{9}$	$1.00 \cdot 10^{0}$	$6.13 \cdot 10^{-5}$	$2.26 \cdot 10^{-24}$	0.00				
Pd-107	$6.50 \cdot 10^{6}$	$3.18 \cdot 10^{8}$	$1.32 \cdot 10^{0}$	$6.01 \cdot 10^{6}$	$2.74 \cdot 10^{-14}$	0.00	$3.77 \cdot 10^{-9}$	0.02	$1.14 \cdot 10^{-7}$	0.71
Ag-108m	$4.18 \cdot 10^{2}$	$1.15 \cdot 10^{11}$	$2.62 \cdot 10^{0}$	$9.24 \cdot 10^{8}$	$1.24 \cdot 10^{-8}$	0.08	$2.42 \cdot 10^{-4}$	1,510	$6.87 \cdot 10^{-3}$	42,950
Cd-113m	$1.41 \cdot 10^{1}$	$3.49 \cdot 10^{10}$	$1.65 \cdot 10^{0}$	$2.07 \cdot 10^{7}$	$4.60 \cdot 10^{-10}$	0.00				
Sb-125	$2.76 \cdot 10^{0}$	$2.29 \cdot 10^{12}$	$1.00 \cdot 10^{0}$	$2.47 \cdot 10^{6}$	$5.12 \cdot 10^{-13}$	0.00				
Sn-126	$1.00 \cdot 10^{5}$	$1.59 \cdot 10^{8}$	$1.03 \cdot 10^{0}$	$3.85 \cdot 10^{6}$	$2.23 \cdot 10^{-10}$	0.00	$4.08 \cdot 10^{-6}$	25.50	$1.35 \cdot 10^{-6}$	8.44
I-129	$1.57 \cdot 10^{7}$	$9.03 \cdot 10^{8}$	$1.00 \cdot 10^{0}$	$2.26 \cdot 10^{7}$	$9.37 \cdot 10^{-10}$	0.01	$1.23 \cdot 10^{-4}$	771	$1.03 \cdot 10^{-4}$	644
Ba-133	$1.05 \cdot 10^{1}$	$3.13 \cdot 10^{9}$	$1.00 \cdot 10^{0}$	$5.64 \cdot 10^{6}$	$6.77 \cdot 10^{-12}$	0.00				
Cs-134	$2.07 \cdot 10^{0}$	$9.65 \cdot 10^{11}$	$2.62 \cdot 10^{0}$	$4.86 \cdot 10^{-6}$	$1.88 \cdot 10^{-23}$	0.00				
Cs-135	$2.30 \cdot 10^{6}$	$3.09 \cdot 10^{9}$	$2.62 \cdot 10^{0}$	$2.95 \cdot 10^{7}$	$1.46 \cdot 10^{-10}$	0.00	$1.01 \cdot 10^{-4}$	631	$1.11 \cdot 10^{-4}$	692
Cs-137	$3.00 \cdot 10^{1}$	$1.35 \cdot 10^{14}$	$2.62 \cdot 10^{0}$	$1.14 \cdot 10^{11}$	$2.13 \cdot 10^{-6}$	13.3				
Pm-147	$2.62 \cdot 10^{0}$	$1.87 \cdot 10^{12}$	$1.00 \cdot 10^{0}$	$1.20 \cdot 10^{6}$	$8.09 \cdot 10^{-14}$	0.00				
Sm-151	$9.00 \cdot 10^{1}$	$6.99 \cdot 10^{11}$	$6.58 \cdot 10^{1}$	$4.17 \cdot 10^{-1}$	$1.21 \cdot 10^{-20}$	0.00				

Radionuclide	Half life (y)	Inventory (Bq)	Rf (–)	Geosphere flux (Bq y^{-1})	Coastal Dose (Sv/y)	RQ	Lake Dose (Sv/y)	RQ	Mire Dose (Sv/y)	RQ
Eu-152	$1.35 \cdot 10^{1}$	$5.36 \cdot 10^{9}$	$6.58 \cdot 10^{1}$	$< 1 \cdot 10^{-50}$	$< 1 \cdot 10^{-50}$	0.00				
Eu-154	$8.59 \cdot 10^{0}$	$2.75 \cdot 10^{12}$	$6.58 \cdot 10^{1}$	$< 1 \cdot 10^{-50}$	$< 1 \cdot 10^{-50}$	0.00				
Eu-155	$4.75 \cdot 10^{0}$	$6.02 \cdot 10^{11}$	$6.58 \cdot 10^{1}$	$< 1 \cdot 10^{-50}$	$< 1 \cdot 10^{-50}$	0.00				
Ho-166m	$1.20 \cdot 10^{3}$	$8.93 \cdot 10^{9}$	$6.58 \cdot 10^{1}$	$7.42 \cdot 10^{5}$	$5.39 \cdot 10^{-13}$	0.00	$1.13 \cdot 10^{-8}$	0.07	$6.06 \cdot 10^{-7}$	3.79
Pb-210	$2.23 \cdot 10^{1}$	$2.60 \cdot 10^{-1}$	$1.00 \cdot 10^{0}$	$1.87 \cdot 10^{-3}$		0.00				
Ac-227	$2.18 \cdot 10^{1}$	$5.09 \cdot 10^{1}$	$1.00 \cdot 10^{0}$	$3.56 \cdot 10^{-1}$		0.00				
Ra-226	$1.60 \cdot 10^{3}$	$6.91 \cdot 10^{0}$	$1.65 \cdot 10^{0}$	$1.02 \cdot 10^{-1}$		0.00				
Th-229	$7.34 \cdot 10^{3}$	$1.05 \cdot 10^{1}$	$1.63 \cdot 10^{2}$	$8.69 \cdot 10^{-4}$		0.00				
Th-230	$7.54 \cdot 10^{4}$	$3.15 \cdot 10^{3}$	$1.63 \cdot 10^{2}$	$4.56 \cdot 10^{-1}$	$3.51 \cdot 10^{-17}$	0.00	$4.19 \cdot 10^{-13}$	0.00	$3.67 \cdot 10^{-10}$	0.00
Th-232	$1.32 \cdot 10^{10}$	$3.51 \cdot 10^{-3}$	$1.63 \cdot 10^{2}$	$5.38 \cdot 10^{-7}$		0.00	$5.43 \cdot 10^{-19}$	0.00	$4.90 \cdot 10^{-16}$	0.00
Pa-231	$3.28 \cdot 10^{4}$	$1.05 \cdot 10^{3}$	$3.34 \cdot 10^{1}$	$7.65 \cdot 10^{-1}$	$6.65 \cdot 10^{-17}$	0.00	$2.55 \cdot 10^{-13}$	0.00	$7.26 \cdot 10^{-11}$	0.00
U-232	$6.89 \cdot 10^{1}$	$7.46 \cdot 10^{5}$	$1.63 \cdot 10^{2}$	$3.73 \cdot 10^{-27}$	$< 1 \cdot 10^{-50}$	0.00				
U-233	$1.59 \cdot 10^{5}$	$7.01 \cdot 10^{2}$	$1.63 \cdot 10^{2}$	$1.05 \cdot 10^{-1}$		0.00				
U-234	$2.46 \cdot 10^{5}$	$3.51 \cdot 10^{7}$	$1.63 \cdot 10^{2}$	$5.28 \cdot 10^{3}$	$1.62 \cdot 10^{-13}$	0.00	$4.88 \cdot 10^{-10}$	0.00	$1.93 \cdot 10^{-9}$	0.01
U-235	$7.00 \cdot 10^{8}$	$4.66 \cdot 10^{8}$	$1.63 \cdot 10^{2}$	$7.15 \cdot 10^{4}$	$2.10 \cdot 10^{-12}$	0.00	$6.33 \cdot 10^{-9}$	0.04	$2.42 \cdot 10^{-8}$	0.15
U-236	$2.30 \cdot 10^{7}$	$1.40 \cdot 10^{7}$	$1.63 \cdot 10^{2}$	$2.14 \cdot 10^{3}$	$6.30 \cdot 10^{-14}$	0.00	$1.90 \cdot 10^{-10}$	0.00	$7.26 \cdot 10^{-10}$	0.00
U-238	$4.50 \cdot 10^{9}$	$1.47 \cdot 10^{9}$	$1.63 \cdot 10^{2}$	$2.25 \cdot 10^{5}$	$6.32 \cdot 10^{-12}$	0.00	$1.91 \cdot 10^{-8}$	0.12	$7.02 \cdot 10^{-8}$	0.44
Np-237	$2.14 \cdot 10^{6}$	$1.58 \cdot 10^{8}$	$1.63 \cdot 10^{2}$	$2.41 \cdot 10^{4}$	$1.63 \cdot 10^{-12}$	0.00	$2.27 \cdot 10^{-8}$	0.14	$5.62 \cdot 10^{-7}$	3.51
Pu-238	$8.77 \cdot 10^{1}$	$4.86 \cdot 10^{10}$	$1.63 \cdot 10^{2}$	$3.11 \cdot 10^{-16}$	$2.09 \cdot 10^{-32}$	0.00				
Pu-239	$2.41 \cdot 10^{4}$	$3.22 \cdot 10^{10}$	$1.63 \cdot 10^{2}$	$4.10 \cdot 10^{6}$	$3.75 \cdot 10^{-10}$	0.00	$1.39 \cdot 10^{-6}$	8.71	$2.25 \cdot 10^{-4}$	1,400
Pu-240	$6.56 \cdot 10^{3}$	$1.58 \cdot 10^{9}$	$1.63 \cdot 10^{2}$	$1.22 \cdot 10^{5}$	$1.12 \cdot 10^{-11}$	0.00	$4.15 \cdot 10^{-8}$	0.26	$6.63 \cdot 10^{-6}$	41.4
Pu-241	$1.44 \cdot 10^{1}$	$8.19 \cdot 10^{11}$	$1.63 \cdot 10^{2}$	$< 1 \cdot 10^{-50}$	$< 1 \cdot 10^{-50}$	0.00				
Pu-242	$3.73 \cdot 10^{5}$	$1.05 \cdot 10^{8}$	$1.63 \cdot 10^{2}$	$1.59 \cdot 10^{4}$	$1.40 \cdot 10^{-12}$	0.00	$5.20 \cdot 10^{-9}$	0.03	$8.03 \cdot 10^{-7}$	5.02
Pu-244	$8.00 \cdot 10^{7}$	$2.45 \cdot 10^{1}$	$1.63 \cdot 10^{2}$	$3.76 \cdot 10^{-3}$	$3.31 \cdot 10^{-19}$	0.00				
Am-241	$4.32 \cdot 10^{2}$	$4.97 \cdot 10^{11}$	$9.82 \cdot 10^{1}$	$2.32 \cdot 10^{5}$	$3.15 \cdot 10^{-11}$	0.00	$7.86 \cdot 10^{-7}$	4.91	$8.58 \cdot 10^{-6}$	53.6
Am-242m	$1.41 \cdot 10^{2}$	$2.96 \cdot 10^{8}$	$9.82 \cdot 10^{1}$	$3.09 \cdot 10^{-4}$	$3.62 \cdot 10^{-20}$	0.00				
Am-243	$7.37 \cdot 10^{3}$	$1.10 \cdot 10^{9}$	$9.82 \cdot 10^{1}$	$1.94 \cdot 10^{5}$	$2.75 \cdot 10^{-11}$	0.00	$6.58 \cdot 10^{-7}$	4.11	$8.42 \cdot 10^{-6}$	52.7
Cm-243	$2.91 \cdot 10^{1}$	$2.90 \cdot 10^{8}$	$9.82 \cdot 10^{1}$	$1.71 \cdot 10^{-36}$	$< 1 \cdot 10^{-50}$	0.00				
Cm-244	$1.81 \cdot 10^{1}$	$1.01 \cdot 10^{10}$	$9.82 \cdot 10^{1}$	$< 1 \cdot 10^{-50}$	$< 1 \cdot 10^{-50}$	0.00				
Cm-245	$8.50 \cdot 10^{3}$	$1.05 \cdot 10^{7}$	$9.82 \cdot 10^{1}$	$1.94 \cdot 10^{3}$	$2.42 \cdot 10^{-13}$	0.00	$1.49 \cdot 10^{-10}$	0.00	$8.78 \cdot 10^{-8}$	0.55
Cm-246	$4.73 \cdot 10^{3}$	$2.79 \cdot 10^{6}$	$9.82 \cdot 10^{1}$	$4.00 \cdot 10^{2}$	$1.88 \cdot 10^{-13}$	0.00	$3.06 \cdot 10^{-11}$	0.00	0.00	0.00

Table B-6 presents the radionuclides screened in. It is noted that only a very few radionuclides have any real significance. Table B-6 does not apply to intrusion scenario screening, e.g. BDFs would be different and including retardation would lead to higher impacts. This implies that it is necessary to additionally include the dominant long-lived activity radionuclides, especially alpha emitters, but they are already included in Table B-6.

Table B-7 briefly reviews those radionuclides which it was not possible to include in the main screening calculations due to a lack of a reported BDF. It is considered that only the two chemical forms of C-14 merit further consideration in the assessment, the other radionuclides have a negligible geosphere flux (due to either a modest disposal inventory or decay within the geosphere) and did not contribute to overall radionuclide fluxes or annual doses in Project SAFE.

Table B-6. Radionuclides screened in by BDFs.

Radionuclide	RQ	Comment
Cl-36	2.53	Screened in from Lake and Mire BDFs
Ni-59	2,868	Screened in from Lake and Mire BDFs
Ni-63	31.5	Screened in from Coastal BDF
Se-79	474	Screened in from Lake and Mire BDFs
Sr-90	4.62	Screened in from Coastal BDF
Mo-93	4.49	Screened in from Lake and Mire BDFs
Nb-94	7.86	Screened in from Lake and Mire BDFs
Tc-99	8.15	Screened in from Lake and Mire BDFs
Ag-108m	1,512	Screened in from Lake and Mire BDFs
Sn-126	25.5	Screened in from Lake BDF
I-129	771	Screened in from Lake and Mire BDFs
Cs-135	631	Screened in from Lake and Mire BDFs
Cs-137	13.3	Screened in from Coastal BDF
Ho-166m	3.79	Screened in from Mire BDF
Np-237	3.51	Screened in from Mire BDF
Pu-239	8.71	Screened in from Lake and Mire BDFs
Pu-240	41.4	Screened in from Mire BDF
Pu-242	5.02	Screened in from Mire BDF
Am-241	4.91	Screened in from Lake and Mire BDFs
Am-243	4.11	Screened in from Lake and Mire BDFs

Table B-7. Review of radionuclides without BDF values.

Radionuclide	Half-life (y)	Inventory (Bq)	Rf (–)	Geosphere flux (Bq y^{-1})	Comment
C-14 organic	$5.73 \cdot 10^{3}$	$2.83 \cdot 10^{12}$	$1.00 \cdot 10^{0}$	$2.82 \cdot 10^{12}$	Include due to high inventory
C-14 inorganic	$5.73 \cdot 10^{3}$	$1.83 \cdot 10^{13}$	$1.03 \cdot 10^{0}$	$1.82 \cdot 10^{13}$	Include due to high inventory
Pb-210	$2.23 \cdot 10^{1}$	$2.60 \cdot 10^{-1}$	$1.00 \cdot 10^{0}$	$7.49 \cdot 10^{-2}$	Exclude due to low geosphere flux
Ac-227	$2.18 \cdot 10^{1}$	$5.09 \cdot 10^{1}$	$1.00 \cdot 10^{0}$	$1.42 \cdot 10^{1}$	Exclude due to low geosphere flux
Ra-226	$1.60 \cdot 10^{3}$	$6.91 \cdot 10^{0}$	$1.65 \cdot 10^{0}$	$6.71 \cdot 10^{0}$	Exclude due to low geosphere flux
Th-229	$7.34 \cdot 10^{3}$	$1.05 \cdot 10^{1}$	$1.63 \cdot 10^{2}$	$5.66 \cdot 10^{0}$	Exclude due to low geosphere flux
Th-232	$1.32 \cdot 10^{10}$	$3.51 \cdot 10^{-3}$	$1.63 \cdot 10^{2}$	$3.51 \cdot 10^{-3}$	Exclude due to low geosphere flux
U-233	$1.59 \cdot 10^{5}$	$7.01 \cdot 10^{2}$	$1.63 \cdot 10^{2}$	$6.81 \cdot 10^{2}$	Exclude due to low geosphere flux

B3 Consideration of radionuclide decay chains

The majority of the radionuclides summarised in Table B-6 for inclusion in the safety assessment calculations decay directly to stable daughters with the following exceptions:

- Sr-90 decays to Y-90 which has a half-life of 64.1 hours and it is therefore not considered necessary to include this decay chain within the near-field and geosphere calculations.
- Cs-137 decays to Ba-137m which has a half-life of 2.5 minutes and it is therefore not considered necessary to include this decay chain within the near-field and geosphere calculations.
- Pu-239 is part of the 4N+3 Series (decaying to U-235, its parent is Am-243)
  Decay of Pu-239 (it would take in excess of 240,000 y to achieve 10 half-lives) adds < 1% to U-235 inventory which is insufficient to increase U-235 above the screening cut-off – inclusion of U-235 and its daughters is not considered necessary.
- Pu-240 is part of the 4N Series (decaying to U-236, its parent is Cm-244)
  Decay of Pu-240 (it would take in excess of 65,000 y to achieve 10 half-lives) adds 3% to U-236 inventory which is insufficient to increase U-236 above the screening cut-off – inclusion of U-236 and its daughters is not considered necessary.
  Decay of Cm-244 (it would take less than 200 y to achieve 10 half-lives) adds 2% to Pu-240 inventory – add the decayed Cm-244 inventory to Pu-240 inventory.
- Am-241 is part of the 4N+1 Series (decaying to Np-237, its parent is Pu-241)
  Decay of Am-241 (it would take in excess of 4,000 y to achieve 10 half-lives) adds 63% to Np-237 inventory which is insufficient to increase Np-237 above the screening cut-off – because the Np-237 in-growth was not explicitly considered in the screening calculation we propose to include it as a daughter of Am-241 in the update calculations and, therefore the initial Np-237 inventory.
  Decay of Pu-241 (it would take less than 200 y to achieve 10 half-lives) adds 5% to Am-241 inventory – add the decayed Pu-241 inventory to Am-241 inventory.
- Am-243 is part of the 4N+3 decay chain (decaying to Pu-239)
  Decay of Am-243 (> 70,000 y) adds 1% to Pu-239 inventory – include decay.

B4 Summary

A summary of 24 radionuclides recommended for inclusion within the SAR-08 calculations and a commentary on their treatment is given in Table B-8.

These recommended radionuclides compare well with those which were identified as important in recent safety assessment calculations undertaken in 2005 /Thomson and Miller 2005/ and are highlighted in bold in Table B-9 (other radionuclides reported in Table B-9 either gave a radionuclide flux greater then 1 Bq/y or an annual dose greater than 10^{-12} Sv y^{-1} but did not contribute significantly to the total).

Note that whilst Table B-8 is effective for the near-field and geosphere calculations, the biosphere calculations would need to take account of the decays chains, at least in some cases.

Table B-8. Radionuclides recommended for inclusion with SAR-08 near-field and geosphere calculations.

Radionuclide	Half-life (y)	Comment
H-3	$1.23 \cdot 10^{1}$	Included due to high inventory and mobility.
Organic C-14	$5.73 \cdot 10^{3}$	
Inorganic C-14	$5.73 \cdot 10^{3}$	Included due to high inventory and mobility.
Cl-36	$3.01 \cdot 10^{5}$	Included due to high inventory and mobility.
Ni-59	$7.60 \cdot 10^{4}$	
Co-60	$5.27 \cdot 10^{0}$	Included due to high inventory.

Radionuclide	Half-life (y)	Comment
Ni-63	$1.00 \cdot 10^{2}$	
Se-79	$1.13 \cdot 10^{6}$	
Sr-90	$2.88 \cdot 10^{2}$	Decay chain not required.
Mo-93	$4.00 \cdot 10^{3}$	
Nb-94	$2.03 \cdot 10^{4}$	
Tc-99	$2.11 \cdot 10^{5}$	
Ag-108m	$4.18 \cdot 10^{2}$	
Sn-126	$1.00 \cdot 10^{5}$	
I-129	$1.57 \cdot 10^{7}$	
Cs-135	$2.30 \cdot 10^{6}$	
Cs-137	$3.00 \cdot 10^{1}$	Decay chain not required.
Ho-166m	$1.20 \cdot 10^{3}$	
Np-237	$2.14 \cdot 10^{6}$	
Pu-239	$2.41 \cdot 10^{4}$	Decay chain not required.
Pu-240	$6.56 \cdot 10^{3}$	Add Cm-244 decayed inventory. Decay chain not required.
Am-241	$4.32 \cdot 10^{2}$	Add Pu-241 decayed inventory. Include decay to Np-237.
Am-243	$7.37 \cdot 10^{3}$	Include decay to Pu-239.

Table B-9. Summary of key radionuclides from 2005 assessment calculations.

	Most likely scenario			
	Near-field	Geosphere	RBD and River	Well
Silo	H-3, C-14 inorganic, C-14 organic, Cl-36, Ni-59, Se-79, Zr-93, Nb-93m, Mo-93, Tc-99, Pd-107, Ag-108m, I-129, Cs-135	C-14 inorganic, C-14 organic, Cl-36, Ni-59, Se-79, Zr-93, Nb-93m, Mo-93, Tc-99, Pd-107, Ag-108m, I-129, Cs-135	C-14 organic, Cl-36, Ni-59, Se-79, Mo-93, I-129, Cs-135	C-14 inorganic, C-14 organic, Cl-36, Ni-59, Se-79, Zr-93, Nb-93m, Mo-93, Tc-99, Pd-107, Ag-108m, I-129, Cs-135
BMA	H-3, C-14 inorganic, C-14 organic, Cl-36, Ni-59, Ni-63, Se-79, Sr-90, Zr-93, Mo-93, Tc-99, Pd-107, Ag-108m, I-129, Cs-135, Cs-137	H-3, C-14 inorganic, C-14 organic, Cl-36, Ni-59, Ni-63, Se-79, Sr-90, Zr-93, Mo-93, Tc-99, Pd-107, Ag-108m, I-129, Cs-135, Cs-137	C-14 inorganic, C-14 organic, Cl-36, Ni-59, Se-79, Zr-93, Mo-93, Tc-99, Ag-108m, I-129, Cs-135	C-14 inorganic, C-14 organic, Cl-36, Ni-59, Se-79, Zr-93, Nb-93m, Nb-94, Mo-93, Tc-99, Pd-107, Ag-108m, Sn-126, I-129, Cs-135, Pu-239, Pu-240, Pu-242
1BTF	H-3, C-14 inorganic, C-14 organic, Cl-36, Ni-59, Ni-63, Se-79, Sr-90, Zr-93, Nb-93m, Mo-93, Tc-99, Ag-108m, I-129, Cs-135, Cs-137	H-3, C-14 inorganic, C-14 organic, Cl-36, Ni-59, Ni-63, Se-79, Sr-90, Zr-93, Nb-93m, Mo-93, Tc-99, Pd-107, Ag-108m, I-129, Cs-135	C-14 inorganic, C-14 organic, Cl-36, Ni-59, Se-79, Mo-93, Tc-99, I-129, Cs-135	C-14 inorganic, C-14 organic, Cl-36, Ni-59, Se-79, Zr-93, Nb-93m, Nb-94, Mo-93, Tc-99, Pd-107, Ag-108m, Sn-126, I-129, Cs-135, Pu-239, Pu-242
2BTF	H-3, C-14 inorganic, C-14 organic, Cl-36, Ni-59, Ni-63, Se-79, Sr-90, Zr-93, Nb-93m, Nb-94, Mo-93, Tc-99, Pd-107, Ag-108m, I-129, Cs-135, Cs-137	H-3, C-14 inorganic, C-14 organic, Cl-36, Ni-59, Ni-63, Se-79, Sr-90, Zr-93, Nb-93m, Nb-94, Mo-93, Tc-99, Pd-107, Ag-108m, I-129, Cs-135	C-14 inorganic, C-14 organic, Cl-36, Ni-59, Se-79, Nb-93m, Mo-93, Tc-99, I-129, Cs-135	C-14 inorganic, C-14 organic, Cl-36, Ni-59, Se-79, Zr-93, Nb-93m, Nb-94, Mo-93, Tc-99, Pd-107, Ag-108m, Sn-126, I-129, Cs-135, Pu-239, Pu-242
BLA	H-3, C-14 inorganic, C-14 organic, Cl-36, Co-60, Ni-59, Ni-63, Se-79, Sr-90, Zr-93, Nb-93m, Nb-94, Mo-93, Tc-99, Ag-108m, I-129, Cs-135, Cs-137	H-3, C-14 inorganic, C-14 organic, Cl-36, Co-60, Ni-59, Ni-63, Se-79, Sr-90, Zr-93, Nb-93m, Nb-94, Mo-93, Tc-99, Ag-108m, I-129, Cs-135, Cs-137	C-14 inorganic, C-14 organic, Cl-36, Ni-59, Se-79, Nb-94, Tc-99, I-129, Cs-135, Pu-239, Pu-240, Pu-242	C-14 inorganic, C-14 organic, Cl-36, Ni-59, Ni-63, Se-79, Zr-93, Nb-93m, Nb-94, Mo-93, Tc-99, Pd-107, Ag-108m, Sn-126, I-129, Cs-135, Ho-166m, Pu-239, Pu-240, Pu-242, Am-241

Appendix C

Datasets from inverse modelling studies

This appendix provides further presentation of the data from the inverse modelling studies used within the SAR-08 near-field and geosphere calculations.

C1 U-factors

Table C-1 provides summary statistics for the uncertainty factors determined from the inverse modelling studies /Holmén 2007/.

C2 Geosphere pathlength and travel time

Tables C-2, C-3 and C-4 provides summary statistics for the geosphere pathlength and travel times in the sub-samples used in the assessment calculations which were determined from the larger dataset from the inverse modelling studies /Holmén 2007/.

Table C-1. Variation in near-field uncertainty factors.

	BMA	BLA	BTF1	BTF2	Silo
Closure					
Minimum	2.35	0.56	0.46	0.43	0.47
Maximum	6.24	2.89	2.76	2.64	1.15
Mean	3.64	1.26	1.14	1.07	0.72
Median	3.38	1.05	0.90	0.85	0.69
5th percentile	2.66	0.68	0.57	0.52	0.49
95th percentile	5.77	2.60	2.45	2.35	1.04
2,000 years post-closure					
Minimum	2.36	2.25	2.73	2.30	0.69
Maximum	6.73	9.50	12.80	10.86	1.72
Mean	3.72	4.37	5.80	4.81	1.03
Median	3.37	3.62	4.85	3.97	0.97
5th percentile	2.51	2.35	2.89	2.41	0.71
95th percentile	6.46	8.58	11.72	9.90	1.59

Table C-2. Variation in flow pathlength and travel time at closure.

Percentiles	BMA	BLA	BTF1	BTF2	Silo
Pathlength (m)					
1	66.0	71.0	77.0	71.6	61.0
5	66.0	71.0	77.0	77.0	61.0
10	66.1	71.0	77.1	77.0	61.0
20	66.2	71.1	77.1	77.1	66.1
30	66.4	71.2	77.2	77.2	66.1
40	66.6	71.4	77.4	77.3	66.2
50	67.4	71.8	77.9	77.7	66.2
60	68.5	72.7	78.7	78.5	66.4
70	69.8	74.0	79.7	79.6	66.7
80	71.2	75.6	81.0	80.9	78.4
90	73.5	77.6	82.7	82.8	104.0
95	76.2	79.1	84.1	84.2	119.6

Percentiles	BMA	BLA	BTF1	BTF2	Silo
99	80.1	81.1	85.7	86.1	132.2
P90-P10	*7.4*	*6.6*	*5.7*	*5.8*	*43.0*
Travel time (years)					
1	5	3	4	4	216
5	6	4	8	7	243
10	8	6	16	11	284
20	12	9	41	25	335
30	22	14	77	53	384
40	46	22	229	117	432
50	86	40	317	272	495
60	185	66	372	331	561
70	241	187	447	392	613
80	296	277	590	519	738
90	432	407	704	689	1,083
95	539	558	803	760	1,581
99	797	748	936	927	2,681
P90-P10	*424*	*401*	*688*	*678*	*799*

Table C-3. Variation in flow path length and travel time at 2,000 years post-closure.

Percentiles	BMA	BLA	BTF1	BTF2	Silo
Pathlength (m)					
1	151.1	153.9	114.7	141.2	165.2
5	178.8	194.8	144.7	203.9	169.8
10	237.5	260.9	169.1	249.7	174.5
20	333.4	303.5	224.7	274.9	186.0
30	358.7	350.4	255.9	298.7	303.0
40	383.6	410.7	286.9	334.6	356.5
50	425.0	503.4	314.8	412.1	387.9
60	551.0	574.4	380.0	515.0	436.2
70	608.6	621.5	498.1	590.5	707.4
80	670.6	699.3	582.6	709.9	784.8
90	748.6	812.6	940.9	944.4	891.0
95	814.7	892.3	1,332.3	1,067.3	990.9
99	984.3	1,010.0	1,557.0	1,283.2	1,148.8
P90-P10	*511*	*552*	*772*	*695*	*716*
Travel time (years)					
1	4	4	6	5	12
5	6	7	8	7	22
10	8	9	11	9	28
20	11	13	16	12	39
30	14	16	23	18	50
40	17	20	33	25	59
50	22	26	45	36	72
60	29	33	61	50	94
70	41	47	83	70	151
80	58	76	121	115	412
90	91	180	256	247	866
95	119	357	552	476	1,367
99	206	853	1,527	1,122	2,457
P90-P10	*83*	*171*	*245*	*238*	*838*

Table C-4. Comparison of geosphere datasets.

	960 sample subset		/Holmen 2007/	
	Pathlength	Travel time	Pathlength	Travel time
Silo (Closure)				
Median	66.2	490.7	66.2	495
10th percentile	66.0	285.3	61	284
90th percentile	98.6	1,007.2	104	1,083
Silo (2,000 years post-closure)				
Median	383.2	71.7	387	72
10th percentile	174.3	28.4	174	28
90th percentile	888.3	844.5	891	866
BMA (Closure)				
Median	67.3	84.0	67.4	86
10th percentile	66.1	7.8	66.1	8
90th percentile	73.2	441.4	73.5	432
BMA (2,000 years post-closure)				
Median	419.6	21.9	425	22
10th percentile	229.4	7.8	237.5	8
90th percentile	748.2	96.3	748	91
1BTF (Closure)				
Median	77.9	325.5	77.9	317
10th percentile	77.1	15.8	77.1	16
90th percentile	82.7	710.2	82.7	704
1BTF (2,000 years post-closure)				
Median	319.1	46.3	314.8	45
10th percentile	167.1	11.4	169.1	11
90th percentile	1,007.5	274.7	812.6	256
2BTF (Closure)				
Median	77.8	237.1	77.7	272
10th percentile	77.0	10.0	77	11
90th percentile	82.9	687.4	82.8	689
2BTF (2,000 years post-closure)				
Median	433.0	37.7	412.1	36
10th percentile	250.0	9.3	249.7	9
90th percentile	967.2	249.9	944.4	247
BLA (Closure)				
Median	71.9	40.8	71.8	40
10th percentile	71.0	6.0	71	6
90th percentile	77.7	402.2	77.6	407
BLA (2,000 years post-closure				
Median	489.8	25.5	503	26
10th percentile	255.1	9.1	260	9
90th percentile	802.7	183.8	812	180

Appendix D

Derivation of Silo flow-fields for failed barriers

The potential exists for situations to occur in the future in which the containment capability of the facilities at SFR 1 will have been reduced by the failure of the engineered barrier system. Such failures may arise from events such as freeze-thaw cycles or glacial washout associated with climatic variation.

There is a need to asses the potential impacts of such failure as part of the SAR-08 calculations. This section summarises the approach to estimate the consequences of failure of the containment of the Silo.

The near-field flow fields developed for the Silo as part of Project SAFE /Holmén and Stigsson 2001ab/ reflect both the general evolution of the regional groundwater system and the controlling influence of the barriers on the facility performance.

The values of hydraulic conductivity used in the models as reported in /Holmén and Stigsson 2001a/ are shown below in Table D-1.

It was estimated that when the Silo is below the sea-bed the dominant flow direction groundwater flow is vertically upwards and of small magnitude (due to low hydraulic gradients).

At 2,800 AD the ongoing uplift results in the shoreline moving so that it would be directly above SFR 1 and thereafter it would retreat further past the repository. This change results in the general groundwater flow being dominantly in a horizontal direction of a larger magnitude (due to higher hydraulic gradients). However, the low hydraulic conductivity of the bentonite backfill around the Silo walls is such that the main groundwater flow direction is still vertical.

The resulting conceptual model that was developed for implementation within Project SAFE was based on this and is shown schematically in Figure D-1. Here it is important to note that advective flow out of the Silo is only considered possible via either the gravel top filling or sand-bentonite layer beneath the base. Diffusive fluxes of radionuclides through the bentonite outside the Silo walls is included but is less than the advective fluxes previously mentioned.

This conceptual model has been adopted for the SAR-08 calculations for the initial phase of the assessment as it remains valid when the Silo containment is intact. However, as noted previously (see the initial part of this appendix) circumstances have been identified which could lead to a loss of containment and it is considered plausible that a significant proportion of advective transport could occur horizontally through the failed side walls and associated bentonite backfill.

An alternative conceptualisation for this situation is shown below in Figure D-2. Advective transport of radionuclides is also included horizontally through the breached side walls and associated bentonite backfill and vertical transport within the bentonite backfill is also possible.

Table D-1. Hydraulic conductivities [m s^{-1}] used in Silo intact base case model /Holmén and Stigsson 2001a/.

	Flow direction		
	x	y	z
Top filling	$1 \cdot 10^{-5}$	$1 \cdot 10^{-5}$	$1 \cdot 10^{-5}$
Concrete/Bentonite at top	$1 \cdot 10^{-9}$	$1 \cdot 10^{-9}$	$1 \cdot 10^{-9}$
Waste encapsulation	$4.5 \cdot 10^{-9}$	$4.5 \cdot 10^{-9}$	$7.4 \cdot 10^{-9}$
Concrete/Bentonite at base	$9.3 \cdot 10^{-10}$	$9.3 \cdot 10^{-10}$	$9.2 \cdot 10^{-10}$
Concrete/Bentonite at sides	$1.1 \cdot 10^{-11}$	$1.1 \cdot 10^{-11}$	$3.4 \cdot 10^{-10}$

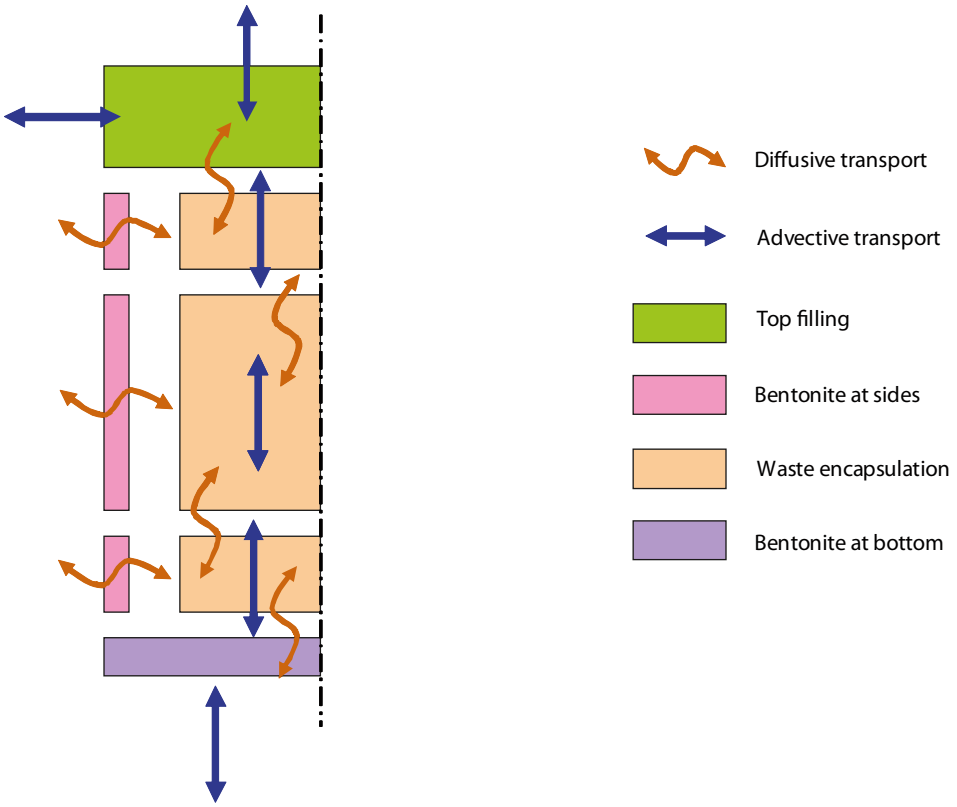

Figure D-1. *Conceptual model of radionuclide transport within intact Silo.*

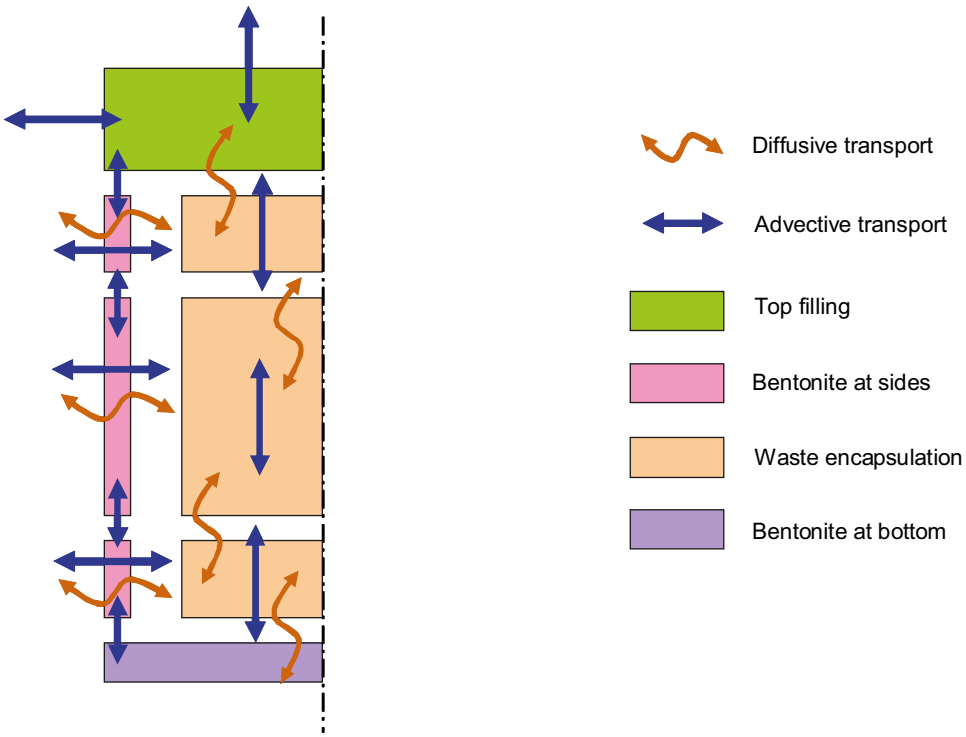

Figure D-2. *Conceptual model of radionuclide transport within degraded Silo.*

The hydrogeological modelling studies carried out in support of Project SAFE included a case in which the Silo barriers were considered to have failed (but the plugs were considered to remain intact). The side walls and associated bentonite backfill were considered to either be breached or to have collapsed. The hydraulic conductivities used in the case are shown in Table D-2.

The flow fields developed for this case could therefore be used to represent a failed Silo for the purposes of the SAR-08 assessment. However, in order to do this it is necessary to convert the flow fields reported in /Holmén and Stigsson 2001a/ to those required for input to AMBER (i.e. using a similar technique to that used to derive the NUCFLOW input).

Figure D-3 shows the original flow field developed within Project SAFE for an intact Silo at Closure. Figure D-4 shows a replication of that undertaken here using the output from /Holmén and Stigsson 2001a/. This intermediate step was carried out before introducing horizontal flow components in order to provide the basis for a technique for developing balanced flow fields for the Silo.

Figure D-3 shows a flow field for a failed Silo at Closure by extending the technique previously developed in order to include additional horizontal flow components (coloured purple). In producing this simplified flow field it has been assumed that outflow in the radial direction from the levels with waste is to the geosphere which is consistent with the treatment of gravel top fill. The horizontal subdivision of the encapsulation area suggests that the flow balances in this area must be altered to account for this.

Table D-3 provides a comparison of the axial and radial flow components through the Silo for the base case at Closure and the failed case at Closure and 3,000 years post-closure based on data from /Holmén and Stigsson 2001a/. It can be seen that for the failed Silo case the flow direction is still estimated to be dominantly in the vertical direction at Closure, whereas at 3,000 years post-closure the dominant direction appears to be horizontally. The results for the failed case at Closure seems to be consistent with the general findings that when the Silo is beneath the sea bed the small hydraulic gradients result in low magnitude groundwater flow vertically upwards. The results for the failed case at 3,000 years post-closure reflect both the changes in regional groundwater flow patterns to a more horizontal orientation with larger gradients and also the absence of the low permeability Silo structures (which moderate the regional groundwater flow in the intact base case simulation in /Holmén and Stigsson 2001a/).

Table D-2. Hydraulic conductivities [m s^{-1}] used in failed Silo case /Holmén and Stigsson 2001a/.

	Flow direction		
	X	**y**	**z**
Top filling	10^{-5}	10^{-5}	10^{-5}
Concrete/Bentonite at top	10^{-8}	10^{-8}	10^{-8}
Waste encapsulation	10^{-8}	10^{-8}	10^{-8}
Concrete/Bentonite at base	10^{-8}	10^{-8}	10^{-8}
Concrete/Bentonite at sides	10^{-8}	10^{-8}	10^{-8}

Table D-3. Comparison of flow components [m^3 y^{-1}] for intact and failed Silo.

	Axial flow		Radial flow	
	K–1	**K+1**	**Inflow (+ve)**	**Outflow (–ve)**
Intact: Closure	1.86	–2.11	0.27	–0.011
Failed: Closure	3.57	–3.80	0.53	–0.30
Failed: 3,000 years post-closure	–2.07	0.48	2.96	–1.37

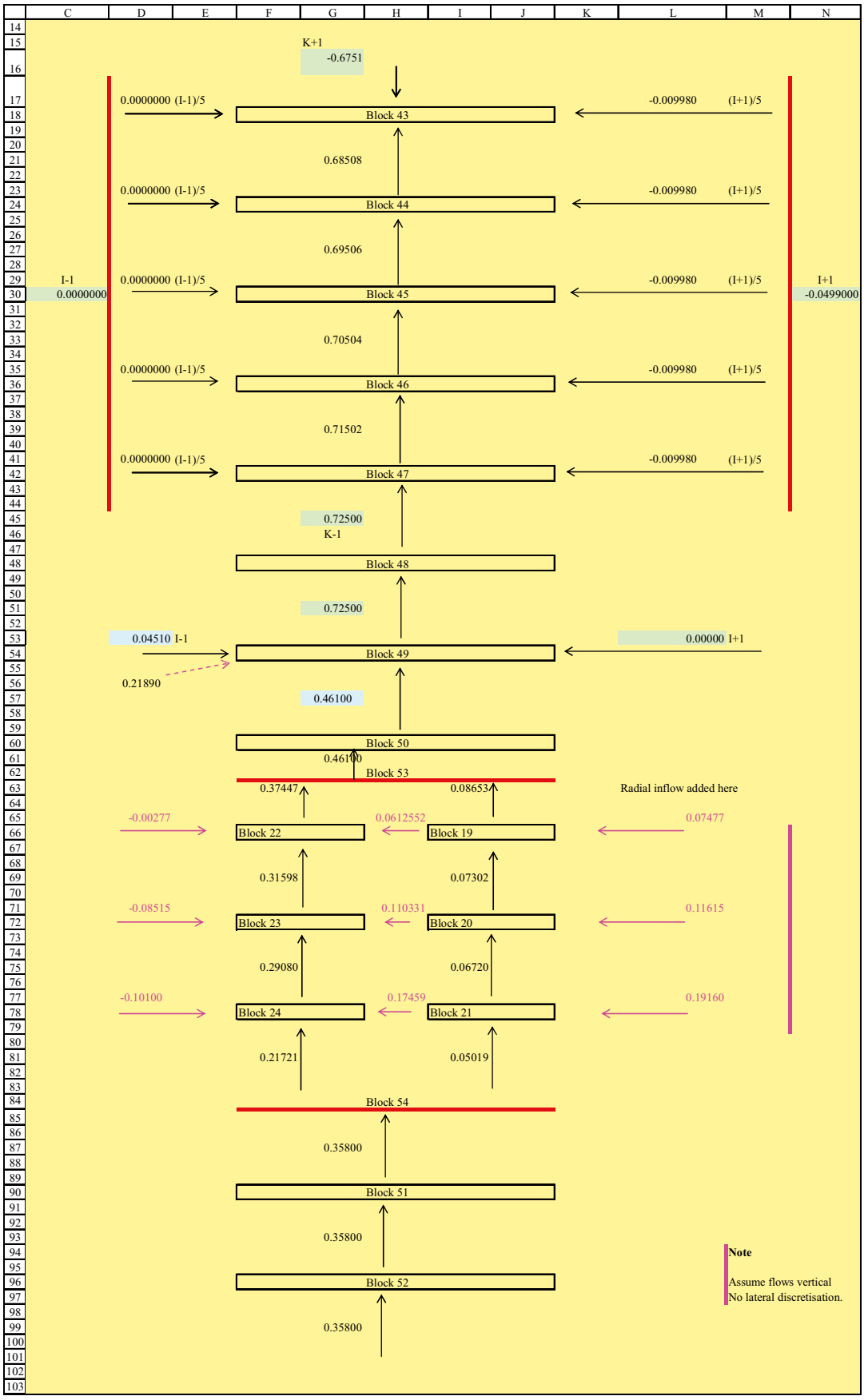

Figure D-3. *Silo flow field for failed encapsulation when submerged.*

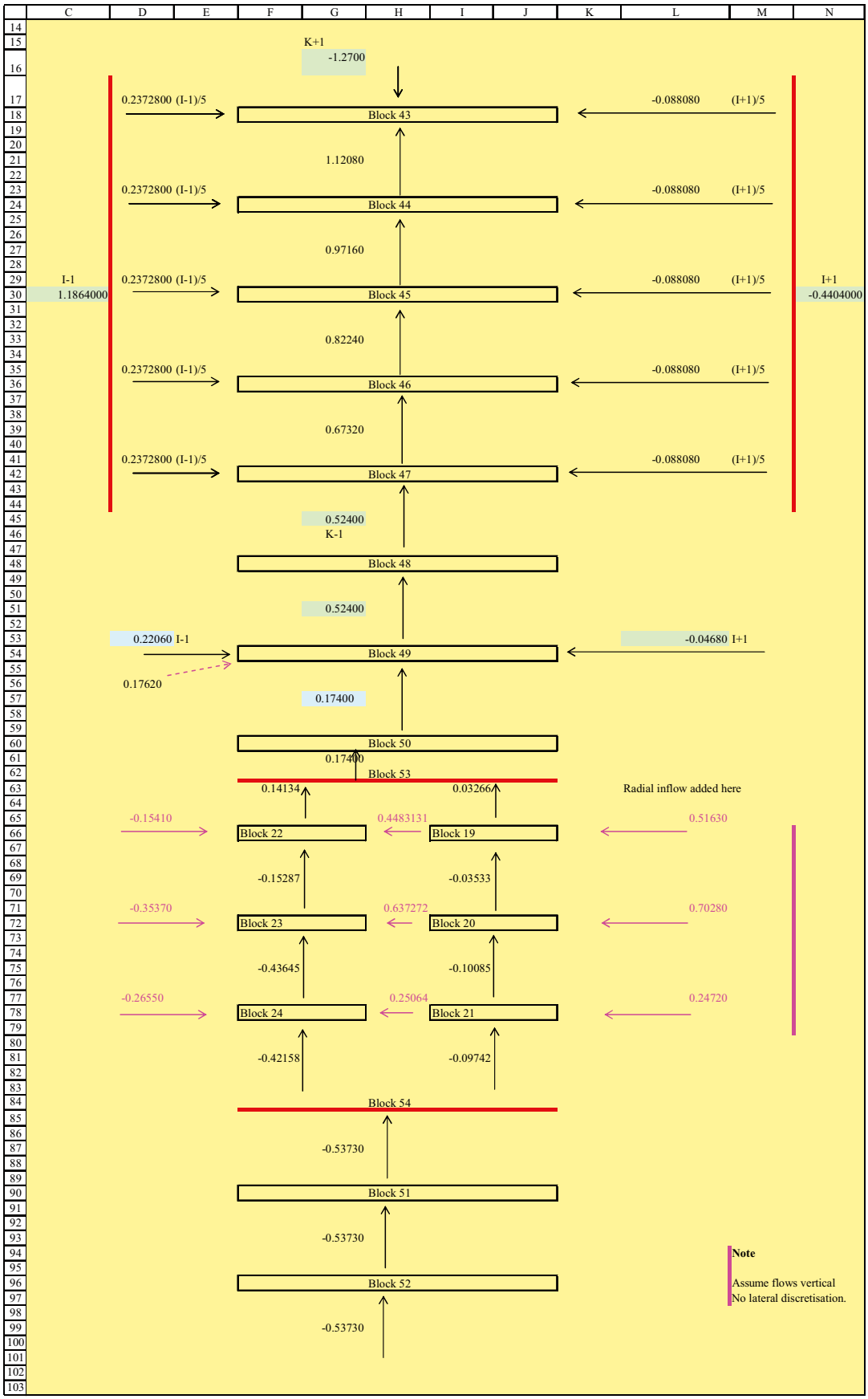

Figure D-4. *Silo flow field for failed encapsulation when emergent.*

Appendix E

Derivation of Silo flow fields for CC10

This appendix presents the derivation of the Silo groundwater flow fields for the two step release used to assess the impacts of increased levels of bulk gas generation on radionuclide release which is considered in CC10.

Figure E-1 below shows a schematic of the upper portion of the Silo encapsulation which highlights the design solution to control adopted to manage bulk gas generation.

The impact of the generation of bulk gases at an increased rates within the Silo on groundwater flows is represented as a two step process as follows /Moreno et al. 2001/.

- As the bulk gases cannot travel through the water saturated Silo materials a volume of water is expelled in order to create a means of escape for the gases. It was estimated that this would require the expulsion of 72 m^3 of porewater immediately on closure over a period of 1 year. A review of the inventory for SAR-08 suggests that sufficient gas generation is still possible for this step to take place in the initial year post-closure. The expulsion of water takes place vertically upwards from the waste through the concrete lid. The volumes of porewater are reported in Table E-1 below /Moreno et al. 2001/.
- Following this an overpressure is developed within the Silo encapsulation in order to overcome the relatively low hydraulic conductivity in the sand-bentonite layer above the Silo lid to enable the gas to escape /Moreno et al. 2001/. The overpressure required is assumed to be 15 kPa which results in a lowering of the water level within the Silo encapsulation by 1.5 m and the expulsion of 60 m^3 water through the bottom of the Silo over a period of 10 years (assuming a hydraulic conductivity of concrete of around 10^{-9} m/s). The volumes of porewater are reported in Table E-2 below and are taken from /Moreno et al. 2001/.

These flows were simply partitioned in proportion to the volume of the subdivisions of the Silo model as shown in Figures E-2 and E-3 and Tables E-3 and E-4 below.

It should also be noted that as there is no flow through the Silo lid the flows within the top-filling are reduced within this time period, as noted in Table E-4 below.

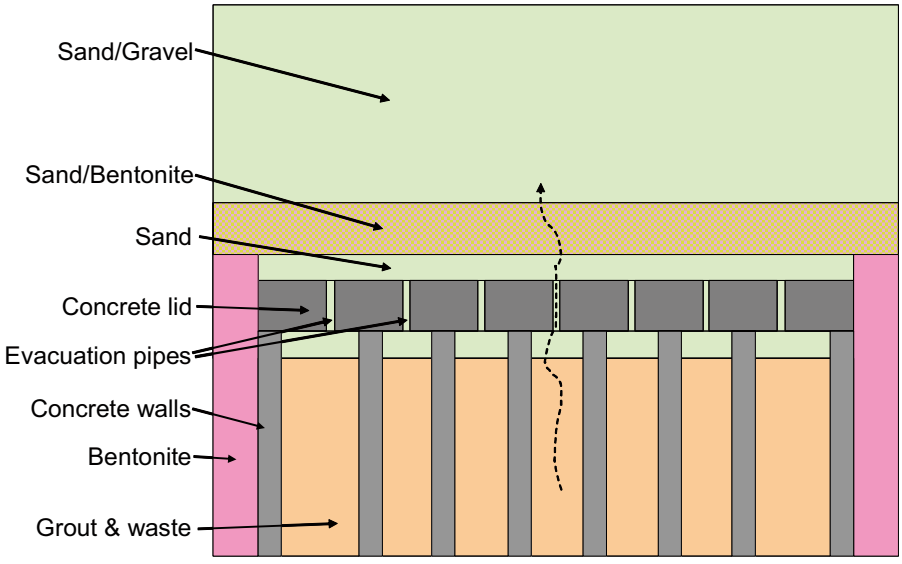

Figure E-1. *Schematic of upper portion of Silo encapsulation.*

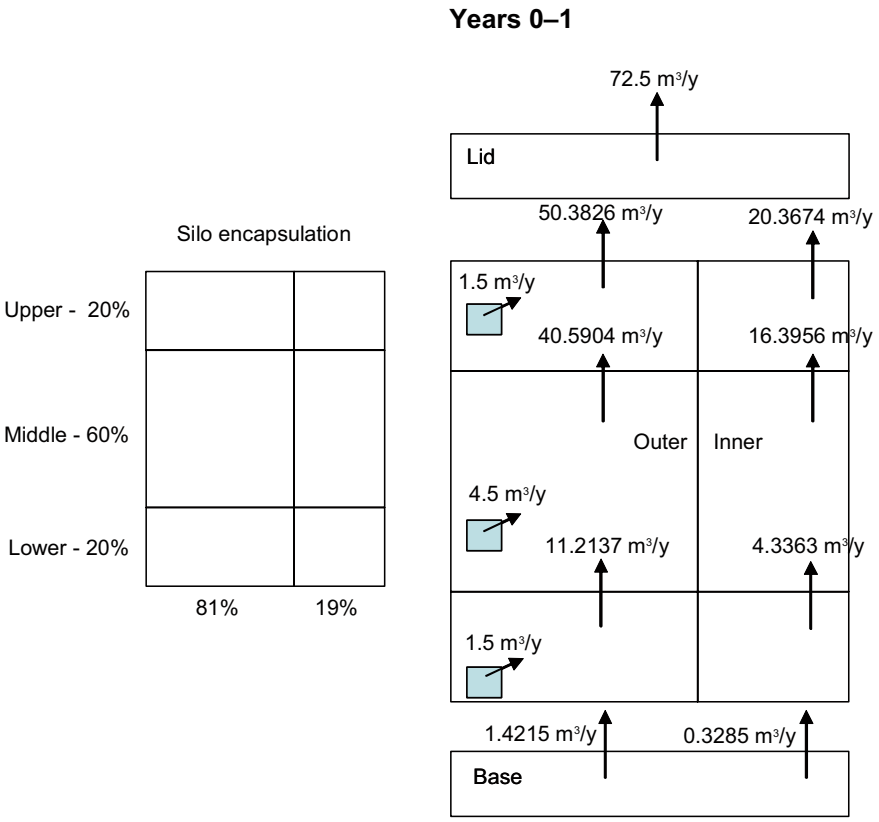

Figure E-2. *Allocation of flow fields for 1st stage.*

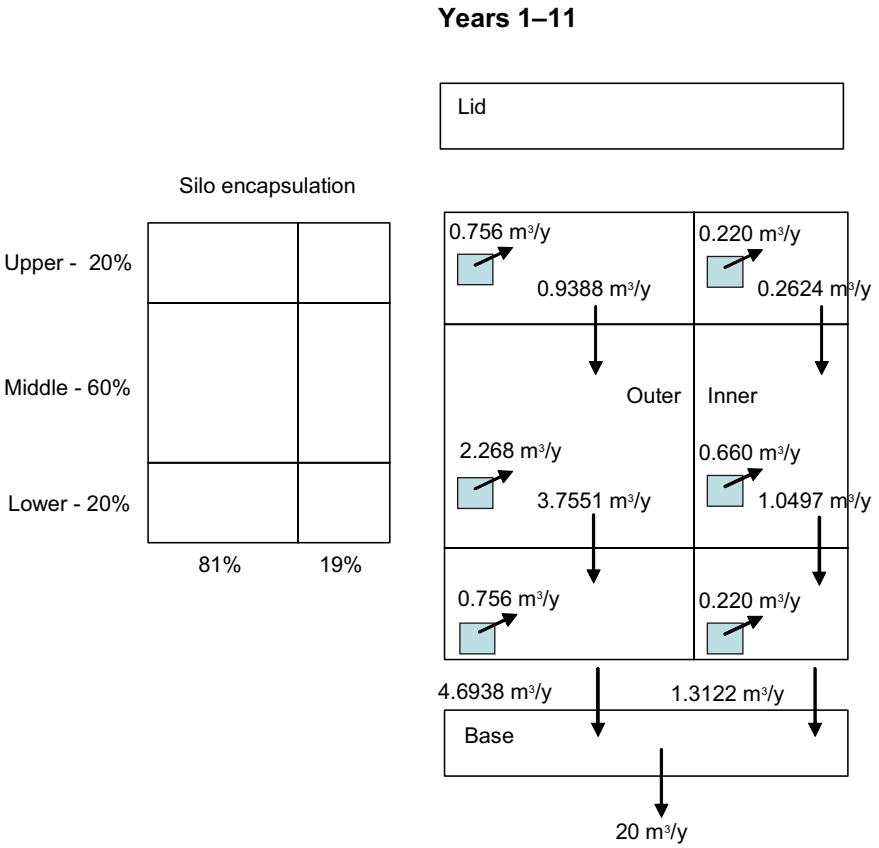

Figure E-3. *Allocation of flow fields for 2nd stage.*

Table E-1. Volume of water expelled to establish gas pathways (step 1).

Component	Volume (m^3)	Water volume expelled (m^3)
Outer Silo Wall	3,662	11.0
Bottom and lid	1,772	3.5
Inner walls	4,301	13
Porous concrete	6,254	37.5
Concrete mould walls	2,657	7.5

Table E-2. Volume of water expelled to establish overpressure (step 2).

Component	Volume (m^3)	Water volume expelled (m^3)
Concrete mould (cement)	659	23
Steel mould (cement)	802	15
Steel drum (cement)	7	0.15
Steel mould (bitumen)		4.8
Steel drum (bitumen)		6.2
Porous concrete	1,876	11.3

Table E-3. Modified groundwater flow parameters for 1st stage.

AMBER parameter	Flow description	Flowrate ($m^3\ y^{-1}$) years 0–1
q_silo_m_gas	Flow from concrete moulds**	1.5
q_silo_e1	External flow from compartment 43	72.5
q_silo_e2	External flow from compartments 44–47	0
q_silo_e3	External flow from compartment 49	0
q_silo_e4	External flow from compartment 52	0
q_silo_1a	Vertical flow through compartment 44	72.5
q_silo_2a	Vertical flow through compartment 45	72.5
q_silo_3a	Vertical flow through compartment 46	72.5
q_silo_4a	Vertical flow through compartment 47	72.5
q_silo_5a	Vertical flow through compartments 48 and 49	72.5
q_silo_6a	Vertical flow through Silo lid	72.5
q_silo_11a	Vertical flow from inner area to Silo lid	20.3674
q_silo_12a	Vertical flow into inner area of Silo top	16.3596
q_silo_13a	Vertical flow into inner area of Silo middle	4.3363
q_silo_14a	Vertical flow into inner area of Silo bottom	0.3285
q_silo_7a	Vertical flow from outer area into Silo lid	50.3826
q_silo_8a	Vertical flow into outer area of Silo top	40.5904
q_silo_9a	Vertical flow into outer area of Silo middle	11.2137
q_silo_10a	Vertical flow into outer area of Silo bottom	1.4215
q_silo_21a	Vertical flow into Silo bottom	1.75

** New parameter. Value given is for upper or bottom sections of encapsulation. Value for middle section is 4.5 $m^3\ y^{-1}$ (i.e. 3 times the value for the upper or bottom sections).

Table E-4. Modified groundwater flow parameters for 2nd stage.

AMBER parameter	Flow description	Flowrate (m^3 y^{-1}) years 1–11
q_silo_bw1**	Flow from upper/lower bitumenised wastes**	0.220
q_silo_bw2**	Flow from middle bitumenised wastes**	0.660
q_silo_cw1**	Flow from upper/lower cemented wastes**	0.756
q_silo_cw2**	Flow from middle cemented wastes**	2.268
q_silo_e1	External flow from compartment 43	0.22
q_silo_e2	External flow from compartments 44–47	0
q_silo_e3	External flow from compartment 49	0
q_silo_e4	External flow from compartment 52	6.006
q_silo_1a	Vertical flow through compartment 44	0.176
q_silo_2a	Vertical flow through compartment 45	0.132
q_silo_3a	Vertical flow through compartment 46	0.088
q_silo_4a	Vertical flow through compartment 47	0.044
q_silo_5a	Vertical flow through compartments 48 and 49	0
q_silo_6a	Vertical flow through Silo lid	0
q_silo_11a	Vertical flow from inner area to Silo lid	0
q_silo_12a	Vertical flow into inner area of Silo top	0
q_silo_12b	Vertical flow into inner area of Silo middle	0.2624
q_silo_13a	Vertical flow into inner area of Silo middle	0
q_silo_13b	Vertical flow into inner area of Silo bottom	1.0497
q_silo_14a	Vertical flow into inner area of Silo bottom	0
q_silo_14b	Vertical flow into Silo bottom	1.3122
q_silo_7a	Vertical flow from outer area into Silo lid	0
q_silo_8a	Vertical flow into outer area of Silo top	0
q_silo_8b	Vertical flow into outer area of Silo middle	0.9388
q_silo_9a	Vertical flow into outer area of Silo middle	0
q_silo_9b	Vertical flow into outer area of Silo bottom	3.7551
q_silo_10a	Vertical flow into outer area of Silo bottom	0
q_silo_10b	Vertical flow into Silo bottom	4.6938
q_silo_21a	Vertical flow into Silo bottom	0
q_silo_21b	Vertical flow into Silo base	6.006
q_silo_22a	Vertical flow into Silo base	0
q_silo_22b	Vertical flow into Silo bottom sand-bentonite	6.006

** New parameters. Values for middle section are 3 times the values for the upper or bottom sections.